Institute of Mechanical Engineering

Aalborg University

Special Report no. 37

Development of Tools for Engineering Analysis and Design of High-Performance FRP-Composite Structural Elements

Ph.D. Thesis

by

Flemming Mortensen

Printed at Aalborg University, August 1998.

ISSN 0905-2305

Preface

This thesis has been submitted to the Faculty of Technology and Science of Aalborg University, Denmark, as partial fulfilment of the requirements for the technical Ph.D. degree.

The project underlying this thesis has been carried out from August 1995 to August 1998 at the Institute of Mechanical Engineering, Aalborg University. The project has been supervised by Associate Professor, Ph.D. Ole Thybo Thomsen, to whom I express my sincere graditude for his inspiring and supporting guidance and for his huge efforts in providing good research conditions.

Furthermore, I would like to thank Professor Y. Frostig, Israel Institute of Technology, Faculty of Civil Engineering, Hafia, Israel, for our joint work on adhesive bonded joints, and Associate Professor, Ph.D. Jens H. Andreasen for many inspiring and encouraging discussions. I would also like to thank my colleagues and friends, M.Sc. Jacob Foldager & M.Sc. Søren Tørholm for discussions and advices given during this work, and to the other colleagues at the Institute of Mechanical Engineering.

The cooperation with the ESAComp team, at the Helsinki University of Technology, Laboratory of Lightweight Structures, is also gratefully acknowledged.

The present work has been co-sponsored by the Danish Technical Research Council's, 'Programme of Research on Computer-Aided Engineering Design', and by the Danish Research Council under the 'Programme of Research Associated with the European Space Agency'.

Flemming Mortensen

Aalborg, August 1998

Abstract

The objective of the present Ph.D. project has been to develop three analysis and design modules for implementation in the software program ESAComp. ESAComp is a software program for the analysis and design of composite laminates and laminated structures, which combines advanced analysis features with well-established design guidelines in an interactive computer envionment. The three modules developed for the program contain:

- **Adhesive bonded joints** including linear elastic and non-linear adhesive behaviour of adhesive bonded joints between composite laminates. The module includes facilities for the analysis of typically used standard joints as well as advanced joints.
- **Layer drop-offs** in sandwich panels and monolithic/solid laminates including exterior and embedded ply drops.
- **Sandwich plates with Inserts** including 'through-the-thickness' and 'fully-potted' inserts.

The analyses of adhesive bonded joints are based on a new approach, where the adherends are modelled as beams or plates in cylindrical bending, and are considered as generally orthotropic laminates using classical lamination theory. Consequently, adherends made as asymmetric and unbalanced composite laminates are included in the analysis. The adhesive layers are modelled as continuously distributed linear tension/compression and shear springs. The possibility that the adhesive layers can display non-linear plastic effects is included in the analysis.

In the modelling of the ply drop problems an interface/'resin-rich' layer between the plies is assumed, and the ply drop problems are therefore modelled in the same way as the adhesive bonded joints. In case the ply drops occur in the face sheets of a sandwich panel the core material is modelled using a 'two-parameter' foundation model.

For the analysis of sandwich plates with inserts a high-order sandwich plate theory, adopted especially for the purpose of studying sandwich plates with inserts and other 'hard points', is used. The theory, which accounts for the transverse flexibility of the core material, includes separate descriptions of the face sheets and the core materials as well as general specification of loads and boundary conditions.

For all the structural problems addressed, the analyses are carried out following the same principal approach, which is based on an explicit formulation of the governing set of differential equations. The governing differential equations are formulated in terms of sets of coupled first-order ordinary differential equations, which are solved numerically using a direct integration-scheme known as the 'multi-segment method of integration'.

For all the structural problems addressed solution procedures have been developed for the implementation in ESAComp. The solution procedures for the adhesive bonded joints have been used to conduct a parametric study, where the influence of using laminated adherends has been investigated. Based on this, a set of general design guidelines has been given in order to improve the structural performance and strength for joints with laminated adherends. The guidelines are also valid for the ply drop problems, since their mechanical behaviour are very similar.

The results obtained for adhesive bonded joints, ply drops and insert problems have been compared with finite element analysis results. The results obtained for the insert problems has also been compared with interferometric measurements obtained using electronic speckle pattern interferometry (ESPI) on test specimens.

Abstrakt

Formålet med dette projekt har været at udvikle tre analysemoduler til implementering i softwareprogrammet ESAComp. ESAComp er en en ny softwarepakke til preliminær analyse og design af letvzgtskonstruktioner fremstillet i avancerede komposit- og sandwichstrukturer. De tre moduler der er udviklet til programmet indeholder:

- **Limsamlinger** imellem kompositlaminater udformet som standard eller avancerede samlinger, hvor det adhæsive materiale er modelleret som lineært elastisk eller ikke-lineært.
- **Aftrapningseffekter** omkring ydre og indre aftrappede plies i monolitiske FRP-laminater samt FRP-laminater virkende som dæklag i sandwichpaneler.
- **Sandwichplader med Inserts** inkluderende 'through-the-thickness' og 'fully-potted' inserts.

Analyserne af limsamlingerne er baseret på en ny metode, hvor adherenderne er modelleret som bjælker eller plader i cylindrisk bmjning og er betragtet som generelle orthotrope laminater baseret på klassisk laminatteori. Pa baggrund af dette vil effekten af at have ikke balancerede og usymmetriske laminater være inkluderet i analysen. De adhæsive lag er modelleret som en kontinuert fordeling af lineære træk/tryk- og forskydningsfjedre, med muligheden for inkludering af ikke-lineære plastiske effekter i de adhesive lag.

I modelleringen af aftrapningsproblemerne er det antaget at der eksisterer et lag af resin mellem de enkelte plies i laminatet, og aftrapningsproblemerne kan derfor modelleres på samme made som limsamlingerne. Hvis aftrapningen forkommer i dæklagene af et sandwichpanel modelleres interaktionen med kærnematerialet vha. en 'to-parameter' funderingsmodel.

Analyserne af sandwich plader med 'inserts' er baseret på en højre-ordens sandwich plade teori udviklet specielt til undersøgelser af inserts i sandwichplader. Teorien, der tager hensyn til den transverse fleksibilitet af kærnematerialet, inkluderer separat beskrivelse af dæklagene og kærnematerialerne, lige som det er muligt at specificere generelle last og randbetingelser.

For alle de strukturelle problemer er der formuleret en matematisk model, der resulterer i et sæt af styrende differentialligninger. De styrende differentialligninger er formuleret som sæt af koblede første ordens differentialligninger, som løses ved direkte integration vha. en metode kendt som 'the multi-segment method of integration'.

For alle de strukturelle problemer er der udviklet algoritmer til implementation i ESAComp. Det udviklede modul til analyse af limsamlinger er anvendt til et parameterstudie for at belyse effekten af at have laminerede adherender. Med udgangspunkt i dette parameterstudie er der givet et generelt set af retningslinier til at forbedre den strukturelle opførsel og styrke for limsamlinger med laminerede adherender. Disse retningslinier er også gyldige for aftrapningsproblemerne, idet disses mekaniske opføsel, samt måden de modelleres pi, er ækvivalent med limsamlinger.

Resulteterne fra analyserne i de tre moduler er sammenlignet med finite element reultater for verifikation af modellerne. Analyserne af sandwichplader med inserts er desuden sammenlignet med interferometriske malinger på forskellige testemner udføert ved anvendelse af 'electronic speckle pattern interferometry' (ESPI).

Contents

Chapter

1

Introduction

THE USE OF polymeric fibre reinforced composite materials, abbreviated FRP-materials (FRP = fibre reinforced plastics), has gained widespread acceptance as an excellent way to obtain stiff, strong and very lightweight structural elements. FRP-materials have long been accepted for structural applications where properties as maximum stiffness to weight, maximum strength to weight, dimensional stability and corrosion resistance are important design features. The use of FRP-material has been initiated and developed by the aerospace and aircraft industries, with the purpose of making lighter and more cost effective space- and aircraft structures. The use of FRP-materials has since vigorously been expanded and accepted for many other structural applications such as wind turbine blades, high-speed ferries, trains etc.

Alongside with the increasing use of FRP-materials a number of critical structural design features appear. As an illustration of some of these critical features a schematic 'cut-out' of the central thrust cylinder of a telecommunications satellite designed and manufactured for the European Space Agency (ESA) under the ESA-ASTP3 programme is shown in Figure 1.1. The thrust cylinder is made as a sandwich with a honeycomb core and CFRP-face sheets (CFRP = carbon fibre reinforced plastics). Inside the thrust cylinder a propellant tank is placed, and in order to fasten the tank to the thrust cylinder and to introduce the loads of the tank into the cylinder, a number of inserts are mounted along the inner circumference of the sandwich cylinder. Around the inserts the face sheets of the sandwich panel are reinforced by adding extra plies to provide for the load transfer from the inserts into the sandwich cylinder. These extra plies have only been added to the face sheets in the near vicinity of the inserts, and a distance away from the inserts a ply drop zone occurs. The inserts have been bonded to the sandwich cylinder and the cylinder has been bonded to the aluminium endring. Thus, the chosen example displays at least three critical details in the structural design of sandwich structures and FRP-materials:

- Adhesive bonded joints.
- Ply drop effects.
- Load introduction into sandwich elements using inserts.

The reason why these structural design details can be very critical is the layered structure of composite laminates, which results in poor strength properties with respect to loading by inter-laminar shear and transverse normal stresses. Thus, the interaction between composite elements and adjoining parts often proves to be among the most critical areas of a structural assembly,

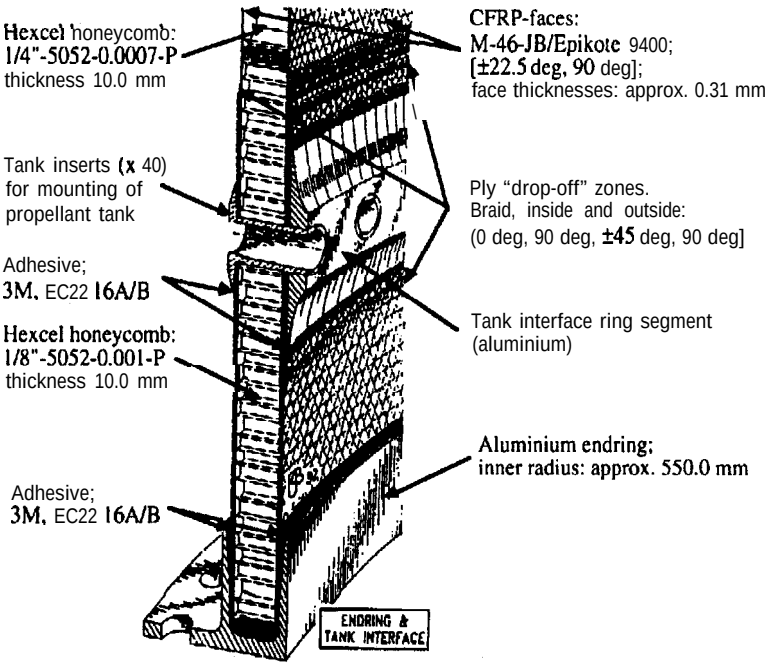

Figure 1.1: *Design* details *of lower end ring* and tank interface *of CFRP* sandwich satellite thrust cylinder, *ESA-ASTP3 program*, demonstrator model *(courtesy of Stork* Products Engineering BV, *The* Netherlands).

since severe local stress concentrations can appear there. These local stress concentrations might lead to a premature failure since sandwich panels and monolithic laminates are susceptible to failure due to local stress concentrations.

Joining of composite structures can be achieved through the use of bolted, riveted or adhesive bonded joints, but generally the use of adhesive bonded joints provides a much more efficient load transfer than mechanically fastened joints. The load applied to an adhesive bonded joint will be distributed over the entire adhesive bonded area, even though the load will not be distributed evenly over the area and severe stress concentrations will appear at the ends of the adhesive layers. However, these stress concentrations will be much less severe than the stress concentrations appearing in joints made with mechanical fasteners.

The ply drop zones appearing from increasing the face sheet thickness locally to provide for the load transfer around highly loaded locations, such as inserts or joints, induce local bending effects in the face sheets. These local bending effects, in which the face sheet/core interaction plays an important role, induce interlaminar and bending stresses in the face sheet laminates, as well as stresses in the core/face sheet interface. In the use of FRP-materials ply drops are also very often used in monolithic composite laminates (as opposed to sandwich laminates). Ply drops are considered beneficial in monolithic composite laminates in zones where the load carried by the laminate is decreased, and fewer plies are needed as a consequence of this.

When inserts are used in sandwich elements, the 'ideal' load transfer mechanism is disturbed significantly in the regions close to inserts. In the areas of such disturbances the face sheets will

tend to bend locally about their own middle surface rather than about the middle surface of the sandwich panel. This results in severe local stress concentrations in the face sheets, in the core material and in the interface between the face sheets and the core.

Due to the increasing and successful use of advanced fibre reinforced materials with polymeric resins, there is a well-documented need for the development of improved analysis tools, as well as for the development of computerized analysis and design programs. Accurate analysis of composite structures or structural elements, such as adhesive bonded joints, ply drop problems or sandwich elements with inserts, as described above, using for instance the finite element method, is an elaborate and computationally demanding task, and there is a specific need for analysis and design tools that can provide accurate results with little computational efforts involved. Such tools would be very useful for preliminary design purposes, i.e. in the stages of design where fast estimates of stress and strain distributions as well as strengths are needed. The need for such tools has been recognized by, among others, the European Space Agency (ESA), which has initiated the development of ESAComp, a computerized analysis and design tool for composite elements that combines advanced analysis features with well-established design guidelines in an interactive computer environment.

Based on these considerations, it has been decided to develop three analysis and design modules addressing the topics described above, i.e. adhesive bonded joints, ply drops and sandwich plates with inserts, and to implement these modules within the framework of ESAComp.

1.1 ESAComp

ESAComp is a computerized analysis and design tool for composite laminates and laminated structural elements that combines advanced analysis features with well-established design guidelines in an interactive computer environment. The development work was initiated by the European Space Research and Technology Centre (ESTEC) of the European Space Agency (ESA) with a vision of creating an open software combining all necessary composites analysis and design capabilities under one unified user interface. Despite its origin in the aerospace field, ESAComp has been developed as a general tool that serves people dealing with composites, both in industry and in research.

ESAComp has been developed for ESTEC by the Helsinki University of Technology, Laboratory of Lightweight Structures (HUT/LLS) and by Helsoft Corporation, Helsinki, Finland. HUT/LLS also serves as the distributor and the support organization of ESAComp. The first version of ESAComp (version 1.0) was released in February 1998.

The program is primarily coded in C. Some functionalities, including the design tools and the possibility to add user extensions, have been implemented using the expert system development tool CLIPS (C Language Integrated Production System) developed by the Software Technology Branch, NASA/Lyndon B. Johnson Space Center, USA.

ESAComp is available for UNIX workstations with the X Window/Motif environment and for personal computers (PC) with the Windows 95/98 operation system.

In this section an overview of the program will be given first, and then a more thorough description of the program architecture and the capabilities will be given. The description is primarily based on the ESAComp System Manual for ESAComp Version I.0 (ESAComp System Manual 1998).

1.1.1 The Program

The ESAComp Version 1.0 program is schematically illustrated in Figure 1.2, and the tools included in the program are the following:

- **Micromechanical analysis tools** evaluate the mechanical behaviour of plies from a fiber and matrix material.
- **Macromechanical analysis tools** evaluate the mechanical behaviour and load carrying capability of plies and laminated structural elements such as continuous laminates, notched laminates, bars/beams, plates and joints.
- **Design tools** search for efficient plies and laminates for structural elements.
- **Interfaces** import and export data. The most important of these are interfaces to the most commonly used FE programs.
- **User extensions** are possible.

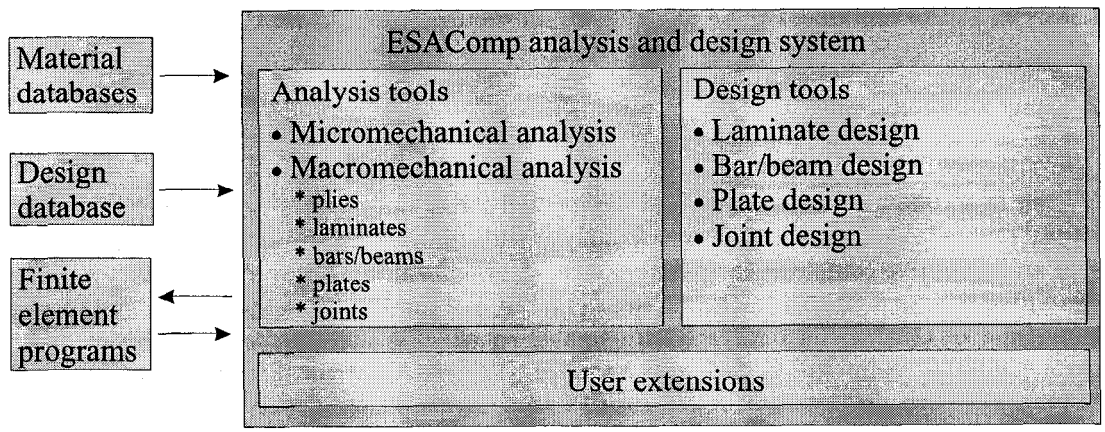

Figure 1.2: ESAComp program.

Figure 1.2 serves to give an overview of the program and its capabilities. However to give a more thorough understanding, the program architecture and capabilities will be described in the following sections.

1.1.2 The Architecture of the Program

The architecture of ESAComp is based on the two concepts **objects** and **cases** which are introduced and defined as:

- An **object** is a laminated structural element, a constituent part of an element, or a load applied to an element. An object may be independent or a **sub-object** for another object.
- A **case** is a design study formed by a set of objects.

Based on these concepts, and with reference to Figure 1.3, the program structure is defined by:

- Specification *Tools* allow to create objects in the working area. The design study in the working area is called the **Active case.**
- *Analysis* and Design *Tools* allow to perform analysis and design tasks related to objects of the active case.
- Cases are stored in the **Database.** Its support system allows to save the active case to a case in the database, and to export/import data from/to the program. The database is divided into three levels: user levels, company levels and the ESAComp Data Bank, which includes data for commonly used aerospace materials and material systems.
- Knowledge in the **Knowledge Base** defines the design tools. The Knowledge *Base* Support System allows to edit the knowledge.
- Option Settings define which of the alternative approaches the program uses.
- The Online *Help* provides guidence to the use of the program and to the task of designing with the program.

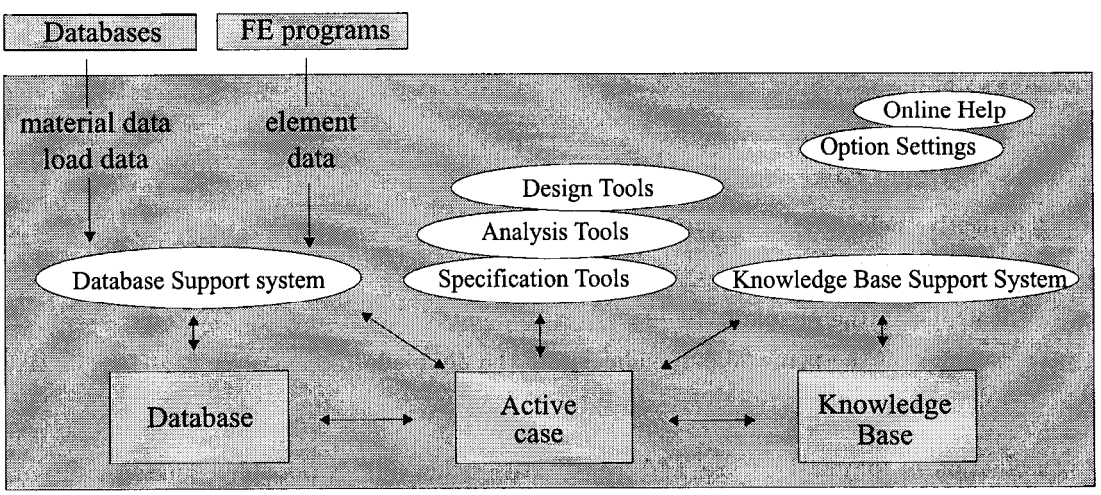

Figure 1.3: ESAComp architecture.

Based on this general description of the program structure the capabilities of the program can be described.

1.1.3 The Capabilities of the Program

The capabilities of the program are divided into four areas, which are Objects, Analysis tools, Design tools and Interfaces.

Objects

The objects available in the current program version are (1) plies, (2) laminates and (3) laminate loads as described in Section 1.1.1. According to Figure 1.4:

- Laminates in a case are always formed from plies of the case.
- Laminate loads are sub-objects of laminates.

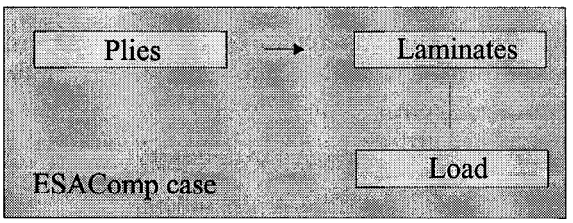

Figure 1.4: ESAComp case.

Plies:

Plies are classified based on their physical nature and constitutive behaviour. The classes are:

- 'Physical nature':
  - fiber-reinforced
  - homogeneous
  - homogeneous core
  - honeycomb core
- 'Constitutive behaviour':
  - orthotropic
  - isotropic in the ply plane 12
  - isotropic in the plane 23 perpendicular to the ply plane
  - isotropic

Any combination of 'physical nature' and 'constitutive behaviour' is possible. Thus, the user can specify any of these combinations for a ply in the program.

Laminates:

Laminates may contain any types of plies. Based on their general arrangement, the laminates are classified into three groups:

- **solid laminates** do not contain core plies
- **sandwich laminates** are 'classical' sandwich panels formed by a core layer (or a stack of identically oriented core layers) in between two face sheets composed of homogeneous and/or fiber-reinforced plies
- **mixed laminates** contain core plies but do not fulfil the conditions described above for a 'classical' sandwich laminate.

When a laminate is created in ESAComp, the program identifies the different types of plies included in the laminate and classify the laminate according to the types described above. Besides laminates with fixed lay-ups, the so-called O-laminates can be specified. These are laminates in which the orientation angle of one or several layers is not defined.

Laminate loads:

Loads applied to a laminate are defined with load vectors. One laminate load may contain two load vectors called the variable load vector and the constant load vector. The concept of two vectors is used to enable a realistic description of loads that are independent of each other, i.e. of different origin and applied simultaneously. An example of structures experiencing such loads is a spacecraft that can be subjected to a constant thrust load and to variable loads resulting from wind gusts. Also, mechanical and hygrothermal loads are often independent of each other.

A load vector consists of load components. These are divided into two groups, to external loads and to internal loads. Mechanical forces, moments and forced deformations are examples of the external loads that can be specified. Thermal loads and moisture loads are internal by their nature, and thus referred to as the internal loads. It should be noted that a load vector may contain any combination of external and internal loads.

Analysis Tools

The analysis tools are divided into ply and laminate analysis capabilities.

Ply analyses:

The following ply analysis tools are available:

- **2/3D behaviour:** The tool computes mechanical and hygrothermal properties of a ply in a specified coordinate system.
- **Carpet plots:** The tool plots a selected mechanical, hygrothermal or strength value for a symmetrical $[0°/\pm\theta/90°]$-laminate as a function of the proportion of Slayers for selected constant proportions of 0°- and 90°-layers.

Laminate analyses:

The following laminate analysis tools are available:

- **2.5D behaviour:** The tool computes mechanical and hygrothermal properties of a laminate.
- **Strength:** The tool computes the strength of a laminate.
- **Load response/failure:** The tool computes how a laminate responds to an applied load. Margin to failure can also be computed when ply strengths are known.
- **Failure/design envelopes:** The tool plots charts that display combinations of two load components that a laminate can withstand.
- **Sensitivity to ply properties:** The tool computes how tolerances applied to ply properties affect laminate performance.
- **Sensitivity to layer orientations:** The tool computes how tolerances applied to layer orientations affect laminate performance.
- **Layer drop-off:** The tool provides analysis facilities, which enable the study of layer drop-off induced local bending effects in solid laminates and in face sheets of sandwich laminates (presented in this thesis work).

- **Free edge:** The tool computes how the free edge of a laminate responds to an applied load.

More **Analysis Tools** will be added to the above list for ESAComp version 2.0, which will be released in 1999. Among the Analysis Tools to be included in ESAComp version 2.0 can be mentioned the Adhesive Bonded Joint Module, which is described in this thesis.

Design Tools

The following tool is available for the design of continuous laminates:

- **Laminate evaluation:** The tool evaluates how selected laminates satisfy specified constraints and objectives.

Interfaces

Interfaces are provided as follows:

- **FE Export:** Allows to export laminate data to the following finite element programs:
  - ANSYS, I-DEAS, MSC/NASTRAN

More FE programs will be added to this list for ESAComp version 2.0, as well as the possibility to import load data from the FE software for detailed analysis in ESAComp.

The system is an open system, which enables user extensions. The user can specify new failure criteria for laminate analyses and create tailored result displays. Version 2.0 introduces general capabilities for adding new analyses as user extensions.

This ends the general description of the ESAComp system.

1.1.4 Demonstration of ESAComp

To give an impression of the program a short demonstration of how to specify a laminate lay-up based on data from the ESAComp Data Bank, and how to perform a calculation of the mechanical laminate properties, are shown.

This demo shows how to specify a monolithic/solid laminate in ESAComp. The laminate is composed of 5 carbon/epoxy plies with the lay-up [0”, 30°, −30°, 30°, −30°]. Figure 1.5 illustrates the procedure. From the ESAComp *Main* window the ply is imported into the active case from the *ESAcomp* Data *Bank* by selecting Import and then reinforced ply, abbreviated *ReinfPly*. A new window then appears showing different elements from the *ESAComp Data Bank* and by selecting *Typical* a number of carbon/epoxy plies stored in the data bank are shown. One or more of the plies can then be selected and stored in the active case.

After a ply has been imported into the active case a laminate can be created. This is illustrated in Figure 1.6.

From the ESAComp main window *Laminates* is selected. In the *Laminates* window, under *edit,* new is selected and a *Laminate specification* window appears. From this window *Lay-up*

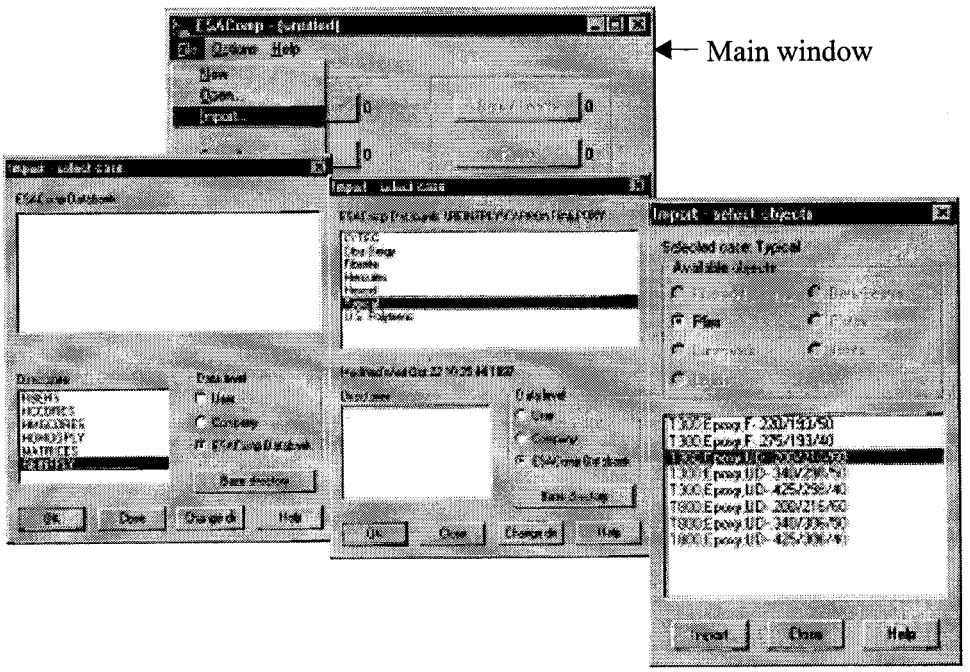

Figure 1.5: Importing a carbon/epoxy ply from the ESAComp Data Bank into an active case.

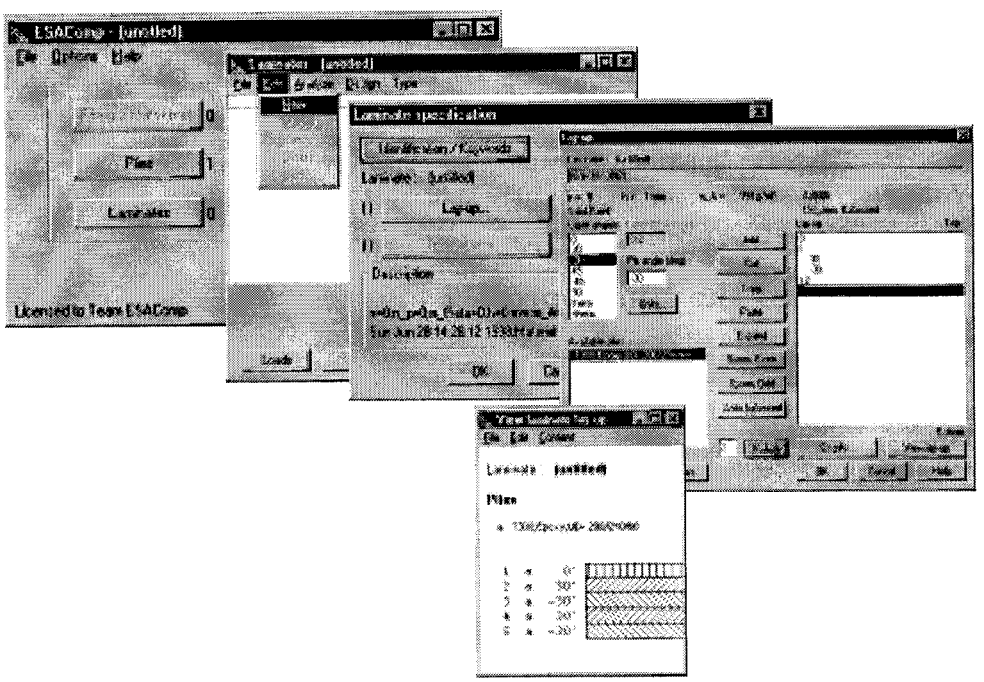

Figure 1.6: Creation of a laminate in ESAComp.

is selected and the laminate lay-up window appears, where the lay-up can be specified. After specification of the laminate, the lay-up of the laminate can be viewed as shown in Figure 1.6.

After the laminate has been created different analyses can be performed. Figure 1.7 illustrates how the mechanical laminate properties can be calculated.

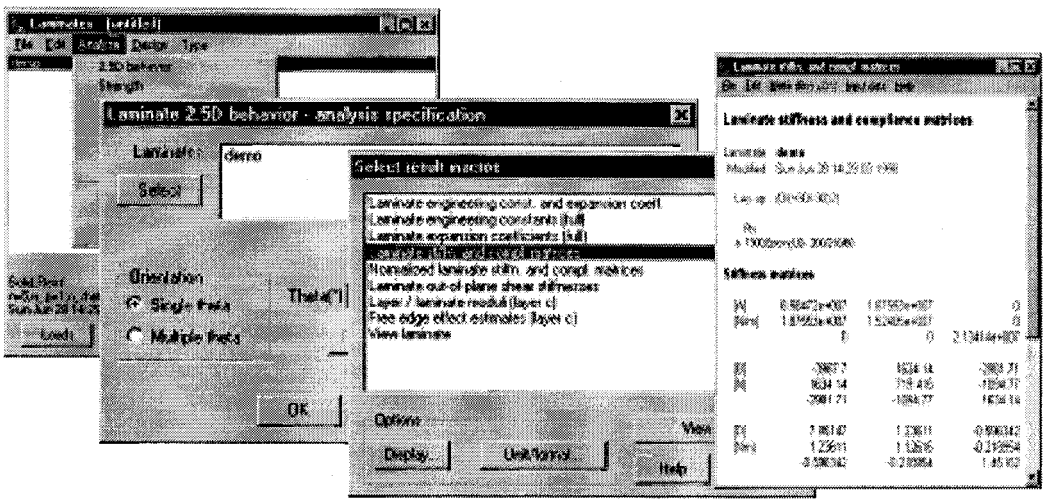

Figure 1.7: Calculation of mechanical laminate properties *in* ESAComp.

In the Laminate window, under *Analyze*, *Laminate 2.5D* behaviour is selected, and the laminate *2.50* behaviour *analysis specification* window appear, from which a normal stiffness analysis of the laminate or a multiple analysis can be selected. A multiple analysis gives the possibility to analyse the laminate mechanical behaviour as a function of the laminate orientation. If a normal stiffness analysis is selected, a window containing the different possibilities for the laminate to be displayed appear, and from this the laminate stiffness matrix can be shown for instance.

This demonstration serves as an introduction to the ESAComp system. For an elaborate demonstration of the program see the ESAComp System Manual (1998).

1.2 Objectives of the Ph.D. project

Based on the considerations presented and the description of the ESAComp system, the objectives for the Ph.D. project have been defined as follows:

The objectives for the present Ph.D. project is to develop and validate methods for the analysis and design of:

- **Adhesive bonded joints** including *linear elastic* and *non-linear* adhesive *behaviour* ***of*** standard and *advanced* ***joints.***
- **Layer drop-offs** *in sandwich* panels and *monolithic/solid* laminates including exterior *and embedded ply drops.*
- **Sandwich plates with Inserts** *including 'through-the-thickness' and 'fully-potted' in-*serts.

In addition the objectives ***for*** *the present Ph.D. project* have *been to implement this work* as *three analysis and design modules* in *the ESAComp system.*

The adhesive bonded joint module includes analysis of typically used standard and advanced joints. The analyses are modelled following a new approach where the adherends are modelled as beams or plates in cylindrical bending, and are considered as generally orthotropic laminates using classical lamination theory. Consequently, adherends made as asymmetric and unbalanced composite laminates can be included in the analysis. The adhesive layers are modelled as continuously distributed linear tension/compression and shear springs. The possibility that the adhesive layers can display non-linear plastic behaviour is included in the analysis.

The layer drop-off module includes analysis of exterior and embedded ply drops in sandwich panels and monolithic/solid laminates. An interface/resin-rich layer between the plies is assumed to exsist, and the ply drop problems are therefore modelled in the same way as the adhesive bonded joints. In case the ply drops occur in the face sheets of a sandwich panel the core material is modelled using a 'two-parameter' foundation model.

The third module includes analysis of inserts in sandwich panels. A high-order sandwich plate theory, adapted especially for the purpose of studying sandwich plates with inserts and other 'hard points', is used. The theory, which accounts for the transverse flexibility of the core material, includes separate descriptions of the face sheets and the core materials as well as general specification of loads and boundary conditions.

For all the structural problems addressed the analyses are carried out following the same principal approach, which is based on an explicit formulation of the governing set of differential equations. The governing differential equations are formulated in terms of sets of coupled first-order ordinary differential equations, which are solved numerically using a direct integration-scheme known as the 'multi-segment method of integration'.

The project was defined and settled under the auspices of an ESA research fellowship awarded to my supervisor Associate Professor, Ph.D., Ole Thybo Thomsen in the Mechanical Systems Department, Structures and Mechanisms Division, Structural Engineering Section at the European Space Research and Technology Centre (ESTEC) in Noordwijk, The Netherlands.

The project is defined so that the responsibility for the full development and documentation of the modules described is held by Aalborg University (AAU), Institute of Mechanical Engineering (IME), whereas responsibility for the development of the Windows interfaces in the ESAComp system is held by Helsinki University of Technology (HUT), Laboratory of Lightweight Structures (LLS). The implementation of the developed analysis modules and the Windows interfaces is done in cooperation between AAU/IME and HUT/LLS according to the time schedule agreed between HUT/LLS, AAU/IME and ESTEC. Within ESAComp version 1.0 the Layer drop-off module has been implemented. The adhesive layer module has been planned for the ESAComp version 2.0 and the inserts module for a later version.

The development of the three analysis modules commenced August 1995 at the Institute of Mechanical Engineering, Aalborg University. The work reported in this thesis has been co-sponsored by the Danish Technical Research Council's, 'Programme of Research on Computer-Aided Engineering Design', and by the Danish Research Council under the 'Programme of Research Associated with the European Space Agency'.

1.3 Outline of thesis

In Chapter 2, the adhesive bonded module is presented. The different types of adhesive bonded joints included are presented. The mathematical formulation of the structural problems, the derivation of the governing equations as well as the numerical solution procedure, the 'multi-

segment method of integration', are stated. Parametric effects and comparison between the joint types are shown, and the adopted adhesive layer model is validated through comparison with results derived by elaborate finite element modelling and a high-order theory approach. Finally, it is described how the module will be implemented into ESAComp.

Chapter 3 contains a description of the ply drop problems. The adopted restrictive assumptions, the implications and the limitations of the modelling are presented. As for the adhesive bonded joints, numerical examples, parametric effects and comparison with finite element analysis are performed. In addition the implementation into ESAComp is described.

Chapter 4 contains a description of the inserts module. The different types of inserts and the structural problems connected with the use of inserts for load introduction in sandwich panels are described. The chapter contains a short description of the structural modelling and a few numerical examples. A validation of the theory is presented by comparison with finite element analysis results and interferometric measurements on test specimens obtained using electronic speckle pattern interferometry (ESPI). Finally, it is described how the module will be implemented into ESAComp.

Finally, in Chapter 5 general conclusions are drawn from the present work.

Chapter

2

Adhesive Bonded Joints

JOINING OF COMPOSITE structures can be achieved through the use of bolted, riveted or adhesive bonded joints. The performances of the mentioned joint types are severely influenced by the characteristics of the layered composite materials, but adhesive bonded joints provide a much more efficient load transfer than mechanically fastened joints. Accurate analysis of adhesive bonded joints, for instance using the finite element method, is an elaborate and computationally demanding task, see Crocombe and Adams (1981), Harris and Adams (1984) and Frostig et al. (1997), and there is a specific need for analysis and design tools that can provide accurate results with little computational efforts involved for preliminary design purposes.

2.1 Introduction to Adhesive Bonded Joints

The terminology used for adhesive bonded joints is shortly defined according to Adams and Wake (1984). An *adhesive* is defined as a substance, a polymeric material, capable of joining two surfaces together, and capable of preventing them from separating. An adhesive is called a structural *adhesive* when the load required to separate the joined parts is substantial, i.e. such that the adhesive provides for the major strength of the structure. The structural members joined together by the adhesive layer are called adherends.

The advantages and limitations of adhesive bonded joints can be exposed by comparison with alternative types of joints such as mechanical fastened joints.

The **advantages** (selected) of using adhesive bonded joints are:

- Very good fatigue resistance.
- Dissimilar materials may be joined together.
- Lighter joints may be achieved.
- The joints are completely sealed.
- Smooth surfaces may be obtained.

The load applied to an adhesive bonded joint will be distributed over the entire adhesive bonded area, even though the load will not be distributed evenly over the bonded area. Thus, significant

stress concentrations appear at the ends of the adhesive bond lines, but these stress concentrations are much less severe than the stress concentrations appearing in mechanical joints. This is the reason why adhesive bonded joints generally display outstanding fatigue resistance. Adhesives are particularly suitable for the joining of dissimilar materials, and many structural adhesives also have the flexibility to absorb stresses induced by differences in stiffness and thermal expansion of the adherends.

Although there are a lot of advantages in using adhesive bonded joints, there are also some **disadvantages:**

- The joints should be designed such that peeling stresses are minimized.
- The surfaces joined together must be prepared very carefully.
- The adhesive may be degraded by the environment.
- No easy and reliable non-destructive test methods are available to verify the integrity and performance of adhesive bonded joints.
- Limited capability to resist elevated temparatures (usally the maximum temperature is $100 - 150°$ C).
- Adhesive joints are permanent.
- The adhesive material may creep.

Structural adhesives are very strong in shear, but weak when transverse normal stresses, called 'peeling' stresses, are present, and it is therefore of paramount importance to design the joints so that these stresses are minimized. In general the complexity of adhesive bonded joints are often inversely proportional to the existence of these undesirable peeling stresses, i.e. by increasing the complexity of the joint, the eccentricity of the load path can be reduced, and the undesirable transverse normal stresses can thereby be reduced, see Mortensen and Thomsen (1997a) and Mortensen and Thomsen (1997b).

2.1.1 Adhesive Materials

The strength of most properly made adhesive bonded joints is directly related to the strength of the adhesives, with which they are made. The mechanical response of adhesive bonded joints depends on the modulus of elasticity of the structural adhesive polymer layers, which again is strongly depending on the temperature. There are several important temperatures which characterize the polymers used as adhesives. These temperatures are the *glass transition temperature,* the *melting* temperature, the crystal *melting* temperature and the decomposition *temperature,* although not all polymeric adhesives will show all four.

The most important temperature is the *glass* transition temperature, usually written T_g which is exhibited by all polymers. The glass transition is a 'second order' transition, which means that there are no abrupt changes in any physical or mechanical properties, but instead changes in the derivatives of the fundamental quantities with respect to temperature are seen. There is a marked change in the mechanical properties exhibited above and below the glass transition, and the range of temperatures below T_g is called the glassy-state, as a consequence of the brittleness shown by most polymers in this range, Adams and Wake (1984). Properties as the modulus of elasticity, the tensile strength and the ultimate strain show only slight variations when exposed to temperatures below T_g. Many polymers exhibit approximately elastic behaviour, but not

necessarily linear elastic behaviour in this range. Above the glass transition temperature T_g the mechanical properties such as the modulus of elasticity and the tensile strength decrease in an approximately linear manner, which results in an approximately linear increase in the ultimate strain, Adams and Wake (1984). As an example epoxy has a glass transition temperature of $T_g = 100°C$.

Amorphous polymers have a melting temperature above the glass transition temperature where they become liquid, and crystalline polymers have a *crystal* melting temperature, at which the mechanical properties change very abruptly, i.e. the modulus of elasticity and the tensile strength decrease very fast.

At some temperature above the melting or the crystal melting temperature the decomposition temperature is reached, and many polymers revert to the monomers from which they are derived, while others char and give of gasses, Adams and Wake (1984). It should be emphasized that continuous exposure to temperatures much less than the decomposition temperature causes deterioration and shortens the lifetime of adhesive bonded joints.

Usually polymeric adhesives are used at temperatures below their glass transition temperature. The mechanical properties of interest are therefore those of the material in its glassy condition. In this range the strains from which recovery is virtually complete can be about 5 %, although there may be a considerable delay in reaching complete recovery. Strains at break of glassy polymers can also be very high, compared to structural metals, but this is very sensitive to the strain rate.

If the temperature is raised and approaches T_g, the modulus of elasticity decreases, and the viscous effects become important. The specification of viscoelastic materials properties can be made in many different ways, see Adams and Wake (1984), but will not be considered any further in this thesis.

The properties of polymeric structural adhesives are also sensitive to oxygen and moisture, which are capable of degrading the mechanical properties of the adhesives. The chemical changes that accompany slow atmospheric oxidation, or rapid changes which occur when used in air at elevated temperatures, vary with the nature of the polymer, but generally adhesives such as polyurethanes and epoxies are quite unsuitable for use under hot and wet conditions, Adams and Wake (1984).

Finally it should be mentioned that the tensile stress-strain relation very often is far from linear, and the strain range over which linearity can be assumed is frequently small compared with the ultimate strain.

2.1.2 Adhesive Bonded Joint Types

The most commonly used joint types and the joints included in the ESAComp Adhesive Bonded Module are presented below:

- Single lap joint with straight and scarfed adherends in the overlap zone;
- Bonded doubler joint;
- Double lap joint;
- Single sided stepped and scarfed lap joint;
- Double sided stepped and scarfed lap joint;

The joint configurations described above, and composed of similar or dissimilar generally orthotropic laminates subjected to general loading conditions, are shown in Figure 2.1 - 2.8.

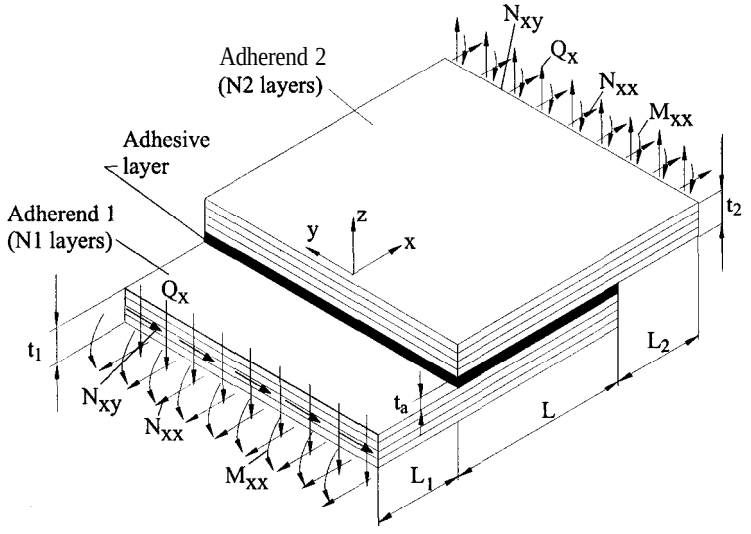

Figure 2.1: Schematic illustration of adhesive single lap joint with straight adherends in the overlap zone subjected to general loading conditions.

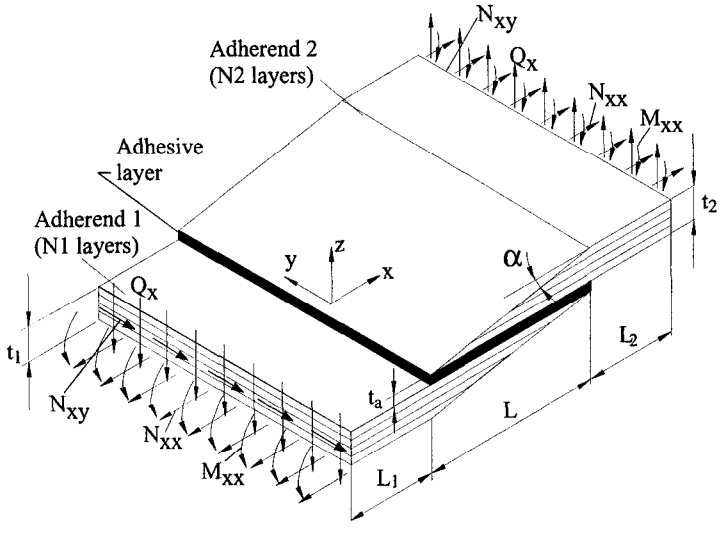

Figure 2.2: Schematic illustration *of* adhesive single lap joint *with* scarfed adherends in *the* overlap zone subjected to general loading conditions.

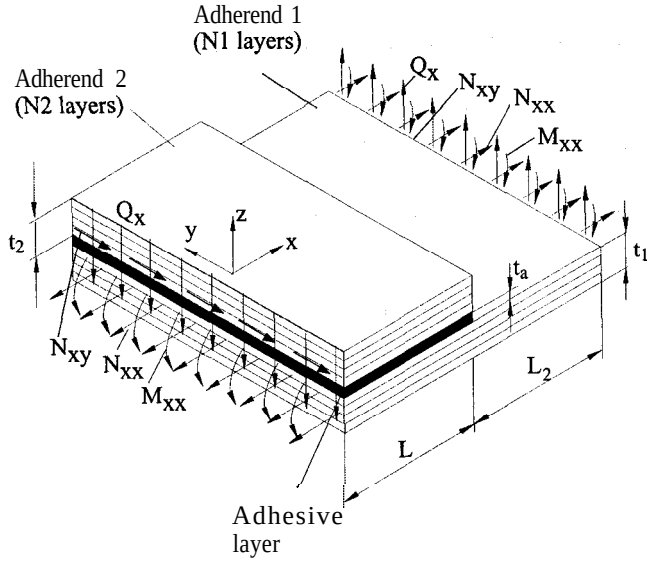

Figure 2.3: Schematic illustration of adhesive bonded doubler joint subjected to general loading conditions.

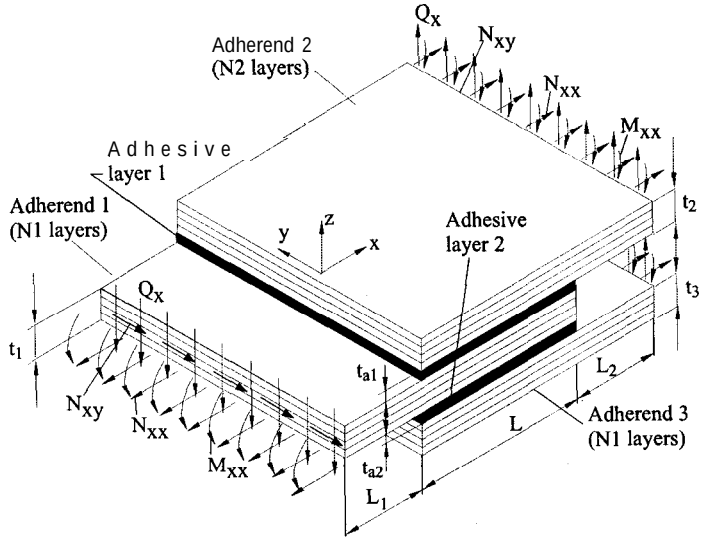

Figure 2.4: Schematic illustration of adhesive double lap joint subjected to general loading conditions.

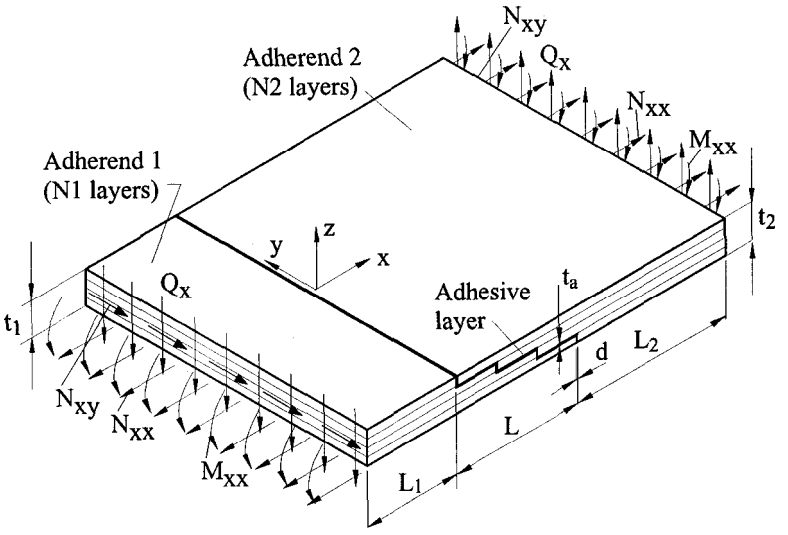

Figure 2.5: Schematic illustration of adhesive single sided stepped lap joint subjected to general loading conditions.

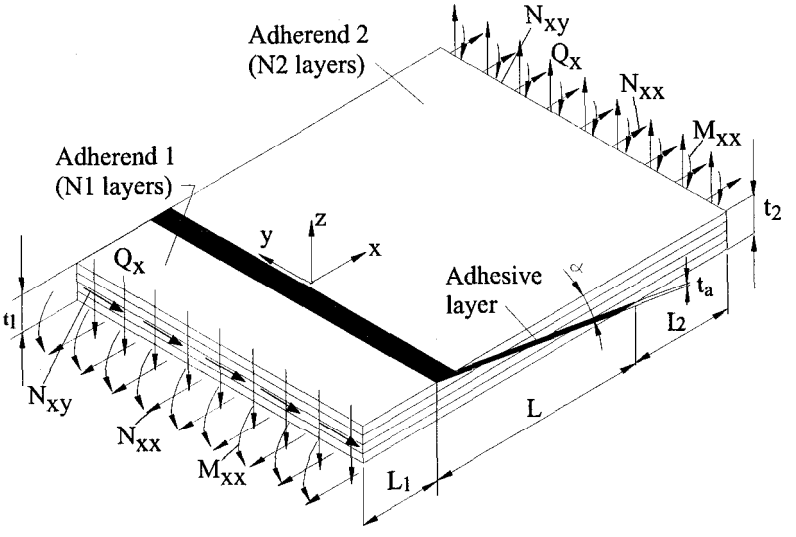

Figure 2.6: Schematic illustration of adhesive single sided scarfed lap joint subjected to general loading conditions.

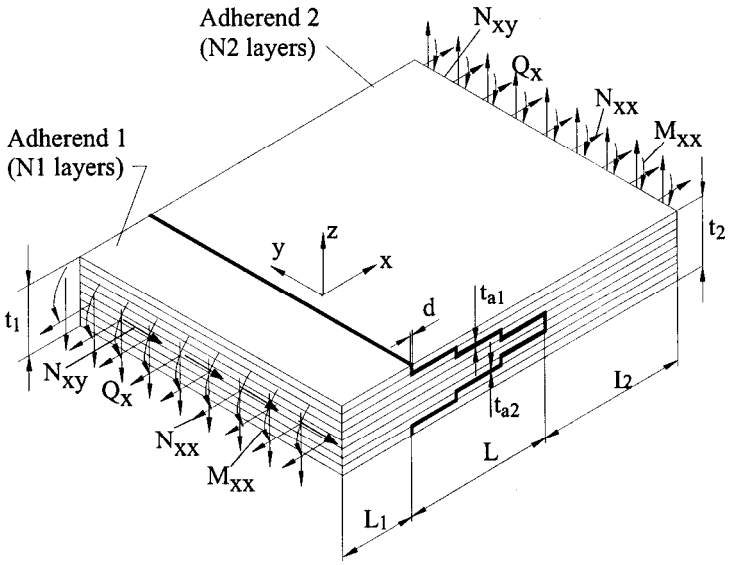

Figure 2.7: Schematic illustration of adhesive double sided stepped lap joint subjected to general loading conditions.

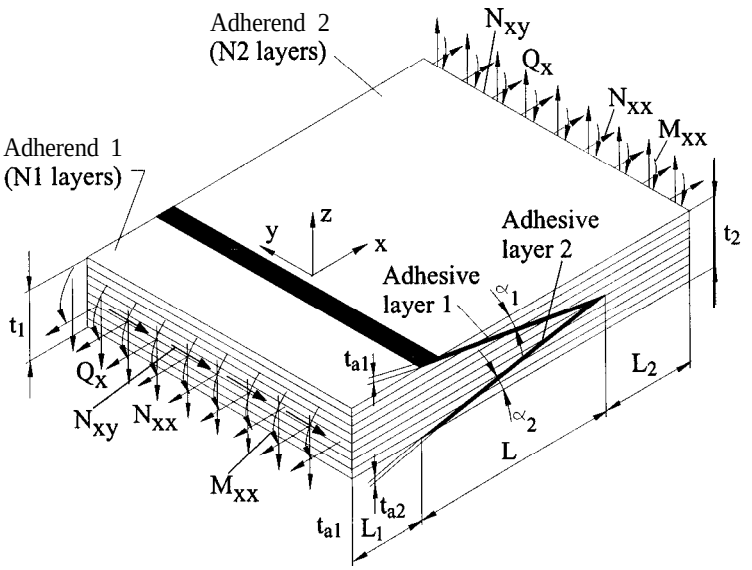

Figure 2.8: Schematic illustration of adhesive double sided scarfed lap joint subjected to general loading conditions.

The first four types of adhesive bonded joints, shown in Figure 2.1 - 2.4, are called standard *joints,* and the last four, shown in Figure 2.5 - *2.8,* are called *advanced joints* with reference to the complexity of the joints. The advanced joints are more efficient than the standard joints, due to the reduced eccentricity of the load path, but the advanced joints are also much more

expensive to manufacture, and they are only used for high-performance joints.

2.1.3 State-of-the-Art of the Modelling of Adhesive Bonded Joints

The first attempt of analyzing adhesive bonded joints was carried out by Volkersen (1938) who modelled the adhesive layer as continuously distributed shear springs, thus ignoring adhered bending effects as well as transverse straining of the adhesive layer (also known as the so called shear lag analysis). The modelling was later refined by adopting a two-parameter elastic foundation approach, in which, the adherends are considered as narrow or wide beams, and the adhesive layer is described in terms of uniformly distributed transverse normal and shear springs. This type of model was originally suggested by Goland and Reissner (1944) for the analysis of single lap joints, but has later formed the basis for many investigations of the structural response of adhesive bonded single lap joints such as Hart-Smith (1973c), who refined the analysis and also considered an ideal plasticity model for the adhesive layer, since non-linear effects in the form of adhesive plasticity play an important role in the load transfer. More recently analysis of single lap joints has been made by Tong (1996). Following the same approach as for the single lap joint Hart-Smith also developed the analysis for double lap joints (Hart-Smith 1973a) and scarfed and stepped lap joints (Hart-Smith 197313). Yuceoglu and Updike later extended the analysis to account also for the transverse shear deformations of the adherends (Yuceoglu and Upclike (1975a), Yuceoglu and Updike (1975b), Yuceoglu and Updike (1981)) and Renton and Vinson accounted for both normal and shear deformations in the transverse direction of the adherends (Renton and Vinson (1975a), Renton and Vinson (1975b)). Yuceoglu and Updike (1981) however, showed that these deformations only will affect the adhesive layer stresses when the adherends are strongly anisotropic and deformable in shear. Adhesive bonded joints between composite circular shells have been treated among others by Pickett (1983), Pickett and Hollaway (1985), Thomsen (1989) and Thomsen (1992).

In all the references mentioned above for standard and advanced joints, the joints have been modelled as plane strain models, where the width direction (y-direction according to Figure 2.1 - 2.8) has been neglected. Consequently the problems have been reduced to two-dimensional problems. The adhesive layers have been considered to be homogeneous, isotropic and to have a thickness much smaller than the adhered thicknesses. From that it has been assumed that the adhesive layer stresses are constant in the transverse direction, and that only the transverse normal and shear stresses are significant and must be included in the analysis. Based on these assumptions the adhesive layers have been modelled as continuously distributed linear tension/compression and shear springs rather than as elastic continua. The limitations of this formulation are:

- The inability to control the boundary/continuity conditions of the adhesive layer at the edges of the overlap zone. The joints are normally idealized so that the edges of the adhesive layer at the ends of the overlap zones are free. As a consequence of this the adhesive layer shear stresses must be zero there, but using the spring model approach the adhesive layer stresses will be maximum there.
- The assumption that the transverse normal stresses in the adhesive layer are uniform through the thickness.

As a consequence of this, the stress field in the adhesive layer does not fulfil point equilibrium although global equilibrium is maintained.

A different approach that overcomes the limitations of the elastic foundation formulation has been suggested by Frostig et al. (1997) following a high-order theory approach, where the

adhesive layer is modelled as a 2-D or 3-D (in case of cylindrical bending) elastic continuum capable of transferring transverse normal and shear stresses. If the analysis is carried out following the approach suggested by Frostig et al. (1997), it is possible to fulfil the requirements that the edges of the adhesive layer at the ends of the overlap zones are free, and that the adhesive layer shear stresses at that location must be zero. The results from the analysis show that there will be tremendous variations of the adhesive layer transverse normal stresses over the thickness of the adhesive layer close to the end of the overlap zone. The assumption that the transverse normal stresses should be constant over the thickness of the adhesive layer, adopted by using the spring model approach, is therefore not correct. However, in real adhesive joints no free edges at the ends of the overlap zone are present. Surplus adhesive material is always 'squeezed out' at the ends of the overlap zone. This surplus adhesive known as a *spew-fillet,* is an inherent part of the manufacturing process. The differences between the idealised and 'real' joint is illustrated in Figure 2.9.

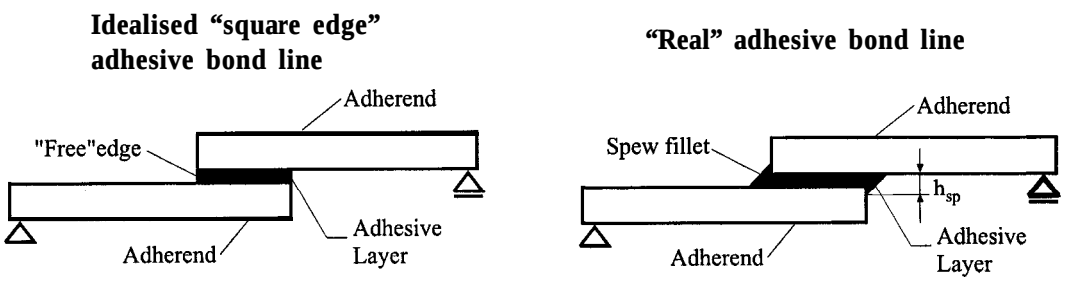

Figure 2.9: Illustration *of a model* joint and *a* real joint.

This spew fillet allows the transfer of shear stresses in the adhesive layer at the overlap ends, and the shear stresses will therefore not be zero at this location, see Frostig et al. (1997). Frostig et al. (1997) also interpreted and modelled the spew-fillet as an elastic bar, and showed that the results obtained, by doing this, approaches the results obtained by modelling the adhesive layer by the spring model approach. This is discussed and illustrated in Section 2.5.

Most of the references reviewed, except for Hart-Smith (1973a), Pickett (1983), Thomsen (1989) and Thomsen (1992) assume the adhesive layer to behave as a linear elastic material. Analyses based on this assumption do provide useful information about the intensities of stress concentrations and their location, but as previously mentioned most polymeric structural adhesives behave non-linearly, and many of them show pronounced viscous and plastic effects even at temperatures below their glass transition temperature. Thus, the results do not reflect the true stress distribution at appreciable levels of loading because of the non-linear behaviour of the polymeric structural adhesives.

A full treatment of the visco-elastic-plastic behaviour of the polymeric structural adhesives, characterized by their sensitivity towards strain rate and environmental effects such as temperature and moisture, is a very difficult task, and not many investigations have been carried out on this topic. Instead, several investigations using an elasto-plastic approach which neglects strain rate and temperature effects and includes plastic residual strains have been carried out, see Hart-Smith (1973a), Hart-Smith (1973b), Hart-Smith (1973c), Pickett (1983), Pickett and Hollaway (1985), Adams et al. (1978) Gali and Ishai (1978), Thomsen (1989) and Thomsen (1992). The first 6 of the references are using an elastic ideal plastic material model for the adhesive behaviour. The last three references are using a model which allows adhesive plasticity to depend upon the hydrostatic as well as the deviatoric stress components. This approach is conducted by using a modified von Mises criterion incorporated in a finite element or semi-analytical solution

procedure, and is more realistic than the elastic ideal plastic model.

2.1.4 Objectives of the Adhesive Bonded Joint Module for ESAComp

The main objective of this module is to make ESAComp capable of determining the stress and displacement fields in the most commonly used adhesive bonded joint configurations. The joint configurations included in the module are those presented in Section 2.1.2 (Figures 2.1-2.8).

The analyses are developed based on a new unified approach. In the analysis the adherends are modelled as beams or plates in cylindrical bending and are considered as generally orthotropic laminates using classical lamination theory (CLT). Consequently, adherends made as asymmetric and unbalanced composite laminates can be included in the analysis. The adhesive layer is modelled as continuously distributed linear tension/compression and shear springs. As non-linear effects in the form of adhesive plasticity play an important role in the load transfer, the analysis allows inclusion of non-linear adhesive properties. The load and boundary conditions can be chosen arbitrarily.

In this thesis, the developed solution procedures are used to conduct a parametric study on the influence of certain important parameters on the stress distributions in the adhesive layer and the adherends. A comparison of linear and non-linear solutions is presented, and a comparison between the different joint types is performed. Finally, a comparison with finite element analysis and a high-order theory approach is carried out in order to validate the adhesive layer model adopted (i.e. distributed spring model versus high-order and continuum models).

2.2 Structural Modelling and Solution Procedure

The structural modelling is carried out by adopting a set of basic restrictive assumptions for the behaviour of bonded joints. Based on those the constitutive and kinematic relations for the adherends are derived, and constitutive relations for the adhesive layers are adopted. Finally, the equilibrium equations for the joints are derived, and by combination of all these equations and relations, the set of governing equations is obtained. This results in a set of first order ordinary differential equations, called the governing system equations, describing the system behaviour. The governing system equations are solved numerically using a method called the 'multi-segment method of integration'.

The adhesive bonded joint configurations composed of similar or dissimilar generally orthotropic laminates subjected to general loading conditions are all shown in Section 2.1.2, Figures 2.1 - 2.8.

The adhered thicknesses are t_1 and t_2 for all the joints outside the overlap zone (see Figures 2.1 - 2.8). For the double lap joint the thickness of the third adhered (lower adhered) is t_3 (see Figure 2.4).

Inside the overlap zone ($0 \leq x \leq L$) the thicknesses are:

- Single lap joint and bonded doubler (see Figure 2.1 and Figure 2.3):

$$t_1(x) = t_1,\ t_2(x) = t_2 \tag{2.1}$$

- Double lap (see Figure 2.4):

$$t_1(x) = t_1,\ t_2(x) = t_2,\ t_3(x) = t_3 \tag{2.2}$$

- Single lap joint with scarfed adherends and single sided scarfed lap joint (see Figure 2.2 and Figure 2.6):

$$t_1(x) = t_1 - \frac{t_1 - t_1^{end}}{L}x, \; t_2(x) = t_2^{end} - \frac{t_2^{end} - t_2}{L}x \tag{2.3}$$

where the superscript *end* in t_1^{end} and t_2^{end} refers to the thicknesses of the adherends at the free ends of the overlap, see Figures 2.10 and 2.11.

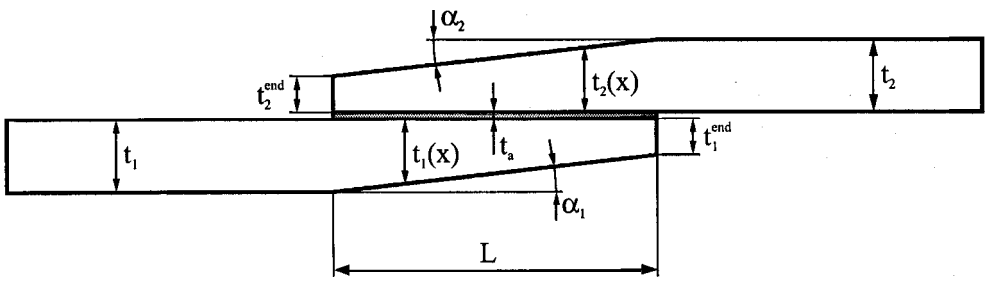

Figure 2.10: Thicknesses and scarf angles *for* single *lap* joint with scarfed adherends.

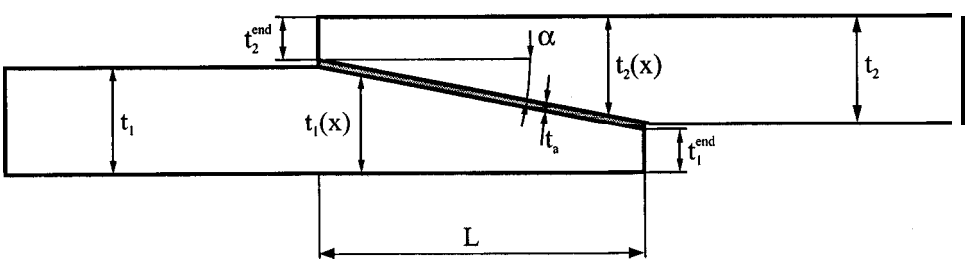

Figure 2.11: Thicknesses and scarf *angle for* single sided scarfed *lap* joint.

- Single sided stepped lap joint (see Figure 2.5):

$$t_1(x) = t_1^m; \quad t_2(x) = t_2^m; \quad m = Step\ number, \quad 0 \leq x \leq L \tag{2.4}$$

where t_1^m and t_2^m refer to the thicknesses of the adherends within the m'th step, see Figure 2.12

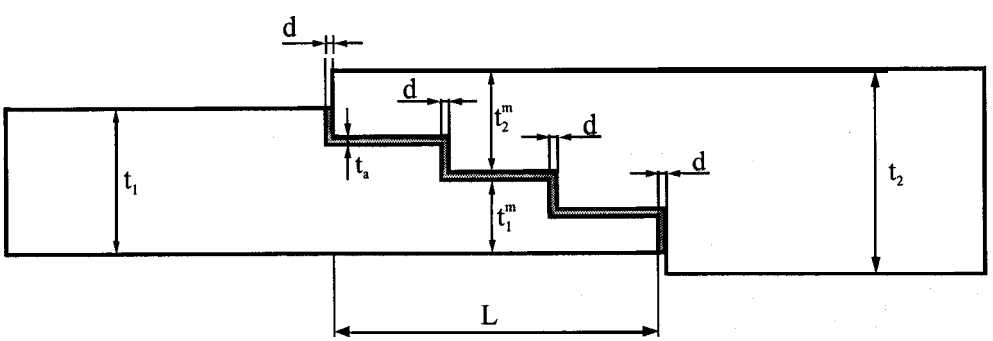

Figure 2.12: Thicknesses *for single* sided stepped lap joint.

- Double sided stepped lap joint (see Figure 2.7):

$$t_1(x) = t_1^m; \quad t_{2a}(x) = t_{2a}^m; \quad t_{2b}(x) = t_{2b}^m; \quad m = Step\ number, \quad 0 \leq 2 \leq L \tag{2.5}$$

where the subscripts a and *b* in t_{2a} and t_{2b} refer to the thicknesses of adherend 2 *above* and *below* adherend 1, see Figure 2.13

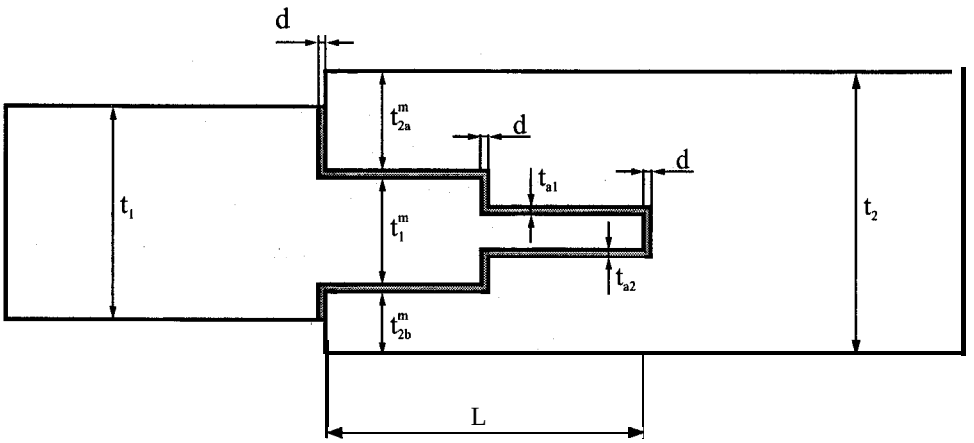

Figure 2.13: Thicknesses for double sided stepped lap joint.

- Double sided scarfed lap joint (see Figure **2.8):**

$$\begin{aligned} t_{1a}(x) &= t_1/2 - \tfrac{t_{2a}^{end,R} - t_{2a}^{end,L}}{L} x; \quad t_{1b}(x) = t_1/2 - \tfrac{t_{2b}^{end,R} - t_{2b}^{end,L}}{L} x; \\ t_{2a}(x) &= t_{2a}^{end,L} - \tfrac{t_{2a}^{end,L} - t_{2a}^{end,R}}{L} x; \quad t_{2b}(x) = t_{2b}^{end,L} - \tfrac{t_{2b}^{end,L} - t_{2b}^{end,R}}{L} x; \end{aligned} \qquad 0 \leq x \leq L \tag{2.6}$$

where the subscripts *a* and *b* and the superscript *end* in $t_{2a}^{end,L}$ and $t_{2b}^{end,L}$ refer to the thicknesses of the adherend 2 at the left (L) and right (R) ends of the overlap *above* and *below* adherend 1, see Figure 2.14.

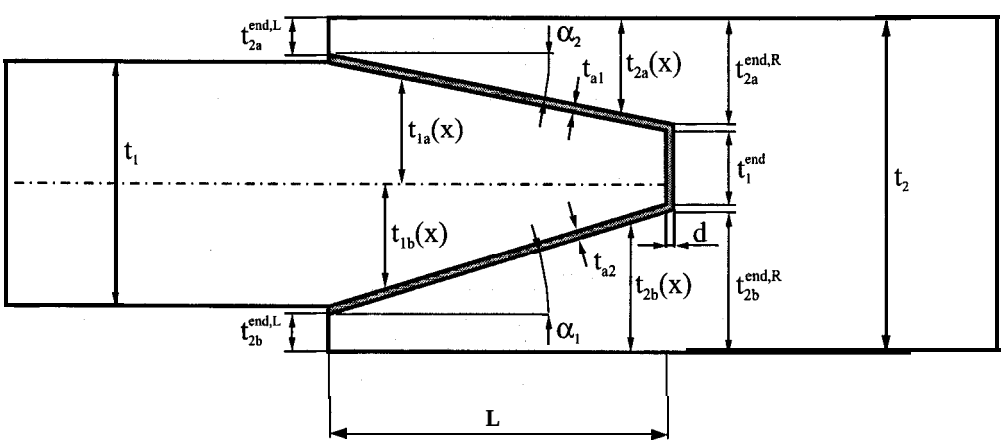

Figure 2.14: Thicknesses for double sided scarfed lap *joint.*

2.2.1 Basic Assumptions for the Structural Modelling

The basic restrictive assumptions adopted for the structural modelling are the following:

- The adherends:
  - Beams or plates in cylindrical bending, which are described by use of ordinary 'Kirchhoff' plate theory ('Love-Kirchhoff' assumptions).
  - Generally orthotropic laminates using classical lamination theory (e.g. asymmetric and unbalanced composite laminates can be included in the analysis).
  - The laminates are assumed to obey linear elastic constitutive laws.
  - The strains are small, and the rotations are very small.
- The adhesive layer:
  - Modelled as continuously distributed linear tension/compression and shear springs.
  - Inclusion of non-linear adhesive properties, by using a secant modulus approach for the nonlinear tensile stress-strain relationship in conjunction with a modified von Mises yield criterion.
- Load and Boundary Conditions:
  - Can be chosen arbitrarily.

The system of governing equations is set up for two different cases, i.e. the adherends are modelled as plates in cylindrical bending or as wide beams. In the following the case where the adherends are modelled as plates in cylindrical bending will receive the primary attention, since the modelling of the adherends as beams can be considered as a reduced case of this.

2.2.2 Modelling of Adherends as Plates in Cylindrical Bending

For the purposes of the present investigation, and with references to Figures 2.15 and Figures 2.1-2.8, cylindrical bending can be defined as a wide plate (in the y-direction), where the displacement field can be described as a function of the longitudinal coordinate only. As a consequence of this, the displacement field in the width directions will be uniform. Thus, the **displacement field** can be described as:

$$u_0^i = u_0^i(x), \qquad v_0^i = v_0^i(x), \qquad w^i = w^i(x) \tag{2.7}$$

where u_0 is the midplane displacement in the longitudinal direction (r-direction), v_0 is the midplane displacement in the width direction (y-direction), and w is the displacement in the transverse direction (z-direction). The displacement components u_0, v_0, w are all defined relative to the middle surfaces of the laminates, and $i = 1, 2, 3$ corresponds to the laminates 1, 2 and 3, respectively (see Figures 2.1-2.8 in Section 2.1.2).

As a consequence of this, the following holds true:

$$u_{0,y}^i = v_{0,y}^i = w_{,y}^i = w_{,yy}^i = 0 \tag{2.8}$$

In the concept of 'cylindrical bending' the boundary conditions at the boundaries in the width direction are not well defined. However, it is assumed that there are some restrictive constraints

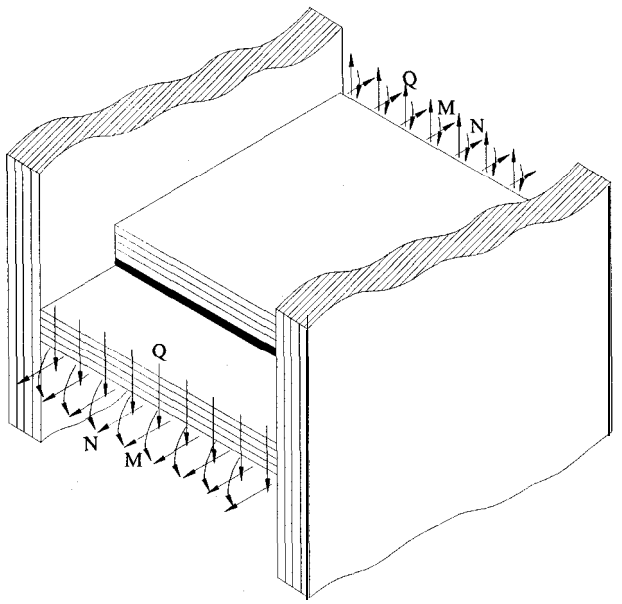

Figure 2.15: Schematic *illustration of* adhesive single lap joint 'clamped' between two vertical laminates, *which prevent the* adherends *of the single* lap joint *of* moving and rotating freely *in the* width direction. *This* represents *the* conceptual interpretation *of* cylindrical bending *as* defined in *the* present formulation.

on the boundaries, such that they not are capable of moving and rotating freely. This is illustrated conceptually in Figure 2.15. It should be noted that the concept of 'cylindrical bending' is not unique, and that other definitions than the one used in the present formulation can be adopted, see Whitney (1987).

Substitution of the quantities in Equation 2.8 into the constitutive relations for a laminated composite material (Whitney (1987)) gives the **constitutive relations** for a laminate (i) in cylindrical bending:

$$\begin{aligned} N^i_{xx} &= A^i_{11}u^i_{0,x} + A^i_{16}v^i_{0,x} - B^i_{11}w^i_{,xx} \\ N^i_{yy} &= A^i_{12}u^i_{0,x} + A^i_{26}v^i_{0,x} - B^i_{12}w^i_{,xx} \\ N^i_{xy} &= A^i_{16}u^i_{0,x} + A^i_{66}v^i_{0,x} - B^i_{16}w^i_{,xx} \\ M^i_{xx} &= B^i_{11}u^i_{0,x} + B^i_{16}v^i_{0,x} - D^i_{11}w^i_{,xx} \\ M^i_{yy} &= B^i_{12}u^i_{0,x} + B^i_{26}v^i_{0,x} - D^i_{12}w^i_{,xx} \\ M^i_{xy} &= B^i_{16}u^i_{0,x} + B^i_{66}v^i_{0,x} - D^i_{16}w^i_{,xx} \end{aligned} \tag{2.9}$$

where A^i_{jk}, B^i_{jk} and D^i_{jk} (j,k = 1,2,6) are the extensional, coupling and the flexural rigidities. N^i_{xx}, N^i_{yy} and N^i_{xy} are the in-plane stress resultants and M^i_{xx}, M^i_{yy} and M^i_{xy} are the moment resultants. In accordance with classical lamination theory A^i_{jk}, B^i_{jk} and D^i_{jk} (i = 1,2,3 and j, k = 1,2,6) for a laminate with m plies are defined by (Jones (1975)):

$$A^i_{jk} = \sum_{m=1}^{N} \left\{\overline{Q}^i_{jk}\right\}_m \{z^i_m - z^i_{m-1}\}$$

$$B^i_{jk} = \frac{1}{2}\sum_{m=1}^{N}\left\{\overline{Q}^i_{jk}\right\}_m\{(z^i_m)^2 - (z^i_{m-1})^2\}; \quad (j,k = 1,2,6) \tag{2.10}$$

$$D^i_{jk} = \frac{1}{3}\sum_{m=1}^{N}\left\{\overline{Q}^i_{jk}\right\}_m\{(z^i_m)^3 - (z^i_{m-1})^3\}$$

where $\left\{\overline{Q}^i_{jk}\right\}_m$ are the transformed elastic stiffnesses of the m'th ply in the i'th laminate.

For the stepped lap joints (see Figures 2.5 and 2.7) the rigidities A^i_{jk}, B^i_{jk} and D^i_{jk} $(j, k = 1,2,6)$ have different values within each step depending on the thickness of the adherends and the plies within each step. For the joints with scarfed adherends (see Figures 2.2, 2.6 and 2.8) the rigidities within the overlap zone are interpolated as continuous functions of the longitudinal direction in accordance with their definition (see Equations 2.10), i.e. A^i_{jk} is changed linearly, B^i_{jk} is changed parabolically and D^i_{jk} is changed cubically $(j, k = 1,2,6)$ between their values at the ends of the overlap zone. This is of course an approximation since the actual stiffnesses of the laminates will change discontinuously each time a ply is dropped (see Figure 2.16).

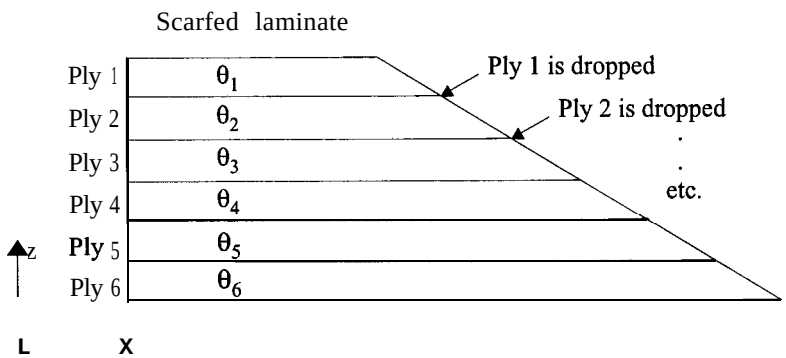

Figure 2.16: Illustration of scarfed laminate.

To model the discontinuous change of stiffness occuring at each ply drop would require that the end points of each of the plies were known, and that the stiffness of each ply should be included in the analysis. This would require a large amount of input from the user, and it is believed that the benefits, compared with the adopted interpolation of the stiffnesses between the end points of the overlap zone, would be small.

From the 'Love-Kirchhoff' assumptions, the following **kinematic relations** for the laminates are derived:

$$u^i = u^i_0 + z\beta^i_x, \qquad \beta^i_x = -w^i_{,x}, \qquad \beta^i_y = 0 \tag{2.11}$$

where u^i is the longitudinal displacement, u^i_0 is the longitudinal displacement of the midplane, and w^i is the vertical displacement of the i'th laminate.

2.2.3 Modelling of Adherends as Beams

Modelling of the adherends as wide beams can be considered as a special case of cylindrical bending. When the adherends are modelled as beams the width direction displacements are not considered, and only the longitudinal and vertical displacements are included. Thus, the **displacement field** in Equation 2.7 is reduced to:

$$u_0 = u_0(x), \qquad \text{w} = \text{w(z)} \tag{2.12}$$

For this case the **constitutive relations** for a composite beam are reduced to:

$$\begin{aligned} N^i_{xx} &= A^i_{11} u^i_{0,x} - B^i_{11} w^i_{,xx} \\ M^i_{xx} &= B^i_{11} u^i_{0,x} - D^i_{11} w^i_{,xx} \end{aligned} \tag{2.13}$$

The kinematic relations (Equation 2.11) are the same as for the cylindrical bending case except that all variables associated with the width direction are nill.

2.2.4 Constitutive Relations for the Adhesive Layer

The coupling between the adherends is established through the constitutive relations for the adhesive layer, which as a first approximation is assumed to be homogeneous, isotropic and linear elastic. The constitutive relations for the adhesive layer are established by use of a two-parameter elastic foundation approach, where the adhesive layer is assumed to be composed of continuously distributed shear and tension/compression springs. The constitutive relations of the adhesive layer are suggested in accordance with Thomsen (1989), Thomsen (1992), Thomsen et al. (1996a) and Tong (1996):

$$\left.\begin{aligned} \tau_{ax} &= \frac{G_a}{t_a}(u^i - u^j) = \frac{G_a}{t_a}\left(u^i_0 - \frac{t_i(x)}{2}\beta^i_x - u^j_0 - \frac{t_j(x)}{2}\beta^j_x\right) \\ \tau_{ay} &= \frac{G_a}{t_a}(v^i - v^j) = \frac{G_a}{t_a}(v^i_0 - v^j_0) \\ \sigma_a &= \frac{E_a}{t_a}(w^i - w^j) \end{aligned}\right\} \begin{aligned} &(i,j = 1,2,3), \\ &(i \neq j) \end{aligned} \tag{2.14}$$

where i and j are the numbers of the adherends, G_a is the shear modulus, and E_a is the elastic modulus of the adhesive layer.

As described in Section 2.1.3, the consequence of using the simple spring model approach for the modelling of the adhesive layers is, that it is not possible to satisfy the equilibrium conditions at the edges (free) of the adhesive. However, in real adhesive joints no free edges are present at the ends of the overlap, since a fillet of surplus adhesive, a so-called spew-fillet, is formed at the ends of the overlap zone. This spew fillet allows for the transfer of shear stresses at the overlap ends. Modelling of the adhesive layer by spring models has been compared with other known analysis methods such as finite element analysis (Crocombe and Adams (1981) and Frostig et al. (1997)) and a higher order theory approach including spew fillets (Frostig et al. (1997)), and the results show that the overall stress distribution as well as the predicted values are in very good agreement. The discussion of the justification and the validity of the adhesive layer spring model approach is continued in greater detail in Section 2.5.

2.2.5 Equilibrium Equations

The equilibrium equations are derived based on equilibrium elements in- and outside the overlap zone for each of the considered joint types. The equilibrium equations are derived for plates in cylindrical bending, since the equilibrium equations for the beam modelling can be considered as a reduced case of this. The general equilibrium equations outside the overlap zone for each of the adherends, i.e. in the regions $-L_1 \leq x \leq 0$ and $L \leq x \leq L + L_2$, are all the same (see

Figure 2.1 - 2.8) and are derived based on Figure 2.17:

$$\left.\begin{aligned} N^i_{xx,x} + N^i_{yx,y} &= 0 \\ N^i_{xy,x} + N^i_{yy,y} &= 0 \\ Q^i_{x,x} + Q^i_{y,y} &= 0 \\ M^i_{xx,x} + M^i_{yx,y} - Q^i_x &= 0 \\ M^i_{xy,x} - M^i_{yy,y} - Q^i_y &= 0 \end{aligned}\right\} \quad -L_1 \le x \le 0 \text{ and } L \le x \le L + L_2. \qquad (2.15)$$

where i corresponds to the adherends $i = 1, 2, 3$ and , x and , y corresponds to the derivatives with respect to the x and y direction.

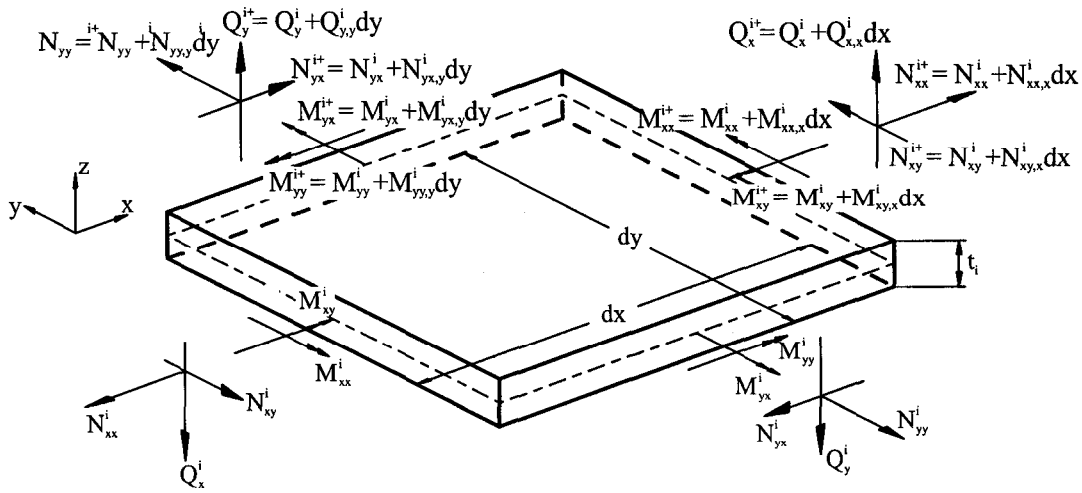

Figure 2.17: Equilibrium elements *of* adherend outside *the overlap zone;* $-L_1 \le x \le 0$ *or* $L \le x \le L + L_2$.

In cylindrical bending the stress and moment resultants are only a function of the longitudinal coordinate x, and the derivatives with respect to the width direction y are all equal to zero. The equilibrium equations outside the overlap zone for each of the adherends in cylindrical bending are therefore derived from Equation 2.15 by setting the derivatives with respect to y equal to zero:

$$\left.\begin{aligned} N^i_{xx,x} &= 0 \\ N^i_{xy,x} &= 0 \\ Q^i_{x,x} &= 0 \\ M^i_{xx,x} &= Q^i_x \\ M^i_{xy,x} &= Q^i_y \end{aligned}\right\} \quad -L_1 \le x \le 0 \text{ and } L \le x \le L + L_2. \qquad (2.16)$$

where i corresponds to the adherends i = $1, 2, 3$.

The equilibrium equations derived inside the overlap zones can be divided into the following two groups:

- Joints with one adhesive layer inside the overlap zone.
- Joints with two adhesive layers inside the overlap zone.

Equilibrium Equations for Joints with one Adhesive Layer inside the Overlap Zone

According to Section 2.1.2 the joint configurations considered with one adhesive layer and two adherends are:

- Single lap joint (Figure 2.1);
- Bonded doubler joint (Figure 2.3);
- Single sided stepped lap joint (Figure 2.5 and Figure 2.12);
- Single lap joint with scarfed adherends in the overlap zone (Figure 2.2 and Figure 2.10);
- Single sided scarfed lap joint (Figure 2.6 and Figure 2.11);

The general equilibrium equations inside the overlap zone for the first three joint types are identical, and they are derived based on Figure 2.18:

$$\left.\begin{aligned}
N^1_{xx,x} + N^1_{yx,y} + \tau_{ax} &= 0\\
N^1_{xy,x} + N^1_{yy,y} + \tau_{ay} &= 0\\
Q^1_{x,x} + Q^1_{y,y} + \sigma_a &= 0\\
M^1_{xx,x} + M^1_{yx,y} - Q^1_x + \tau_{ax}\tfrac{t_1(x)+t_a}{2} &= 0\\
M^1_{xy,x} - M^1_{yy,y} - Q^1_y + \tau_{ay}\tfrac{t_1(x)+t_a}{2} &= 0\\
N^2_{xx,x} + N^2_{yx,y} - \tau_{ax} &= 0\\
N^2_{xy,x} + N^2_{yy,y} - \tau_{ay} &= 0\\
Q^2_{x,x} + Q^2_{y,y} - \sigma_a &= 0\\
M^2_{xx,x} + M^2_{yx,y} - Q^2_x + \tau_{ax}\tfrac{t_2(x)+t_a}{2} &= 0\\
M^2_{xy,x} - M^2_{yy,y} - Q^2_y + \tau_{ay}\tfrac{t_2(x)+t_a}{2} &= 0
\end{aligned}\right| \quad 0 \le x \le L. \tag{2.17}$$

where $t_1(x)$ and $t_2(x)$ are the adherend thicknesses according to Equations 2.1 and 2.4, and t_a is the adhesive layer thickness. For the single lap joint and for the bonded doubler the adherend thicknesses will remain the same in the entire overlap zone as specified by Equations 2.1. For the single sided stepped lap joint the adherend thicknesses will change inside the overlap zone, as specified by Equation 2.4.

The equilibrium equations inside the overlap zone for the first three joint types with the adherends in cylindrical bending, are derived based on Equation 2.17 by setting the derivatives with respect to y equal to zero, since the variables are independent with respect to the width direction:

$$\left.\begin{aligned}
N^1_{xx,x} &= -\tau_{ax}, & N^2_{xx,x} &= \tau_{ax}\\
N^1_{xy,x} &= -\tau_{ay}, & N^2_{xy,x} &= \tau_{ay}\\
Q^1_{x,x} &= -\sigma_a, & Q^2_{x,x} &= \sigma_a\\
M^1_{xx,x} &= Q^1_x - \tau_{ax}\tfrac{t_1(x)+t_a}{2}, & M^2_{xx,x} &= Q^2_x - \tau_{ax}\tfrac{t_2(x)+t_a}{2}\\
M^1_{xy,x} &= Q^1_y - \tau_{ay}\tfrac{t_1(x)+t_a}{2}, & M^2_{xy,x} &= Q^2_y - \tau_{ay}\tfrac{t_2(x)+t_a}{2}
\end{aligned}\right\} \quad 0 \le x \le L. \tag{2.18}$$

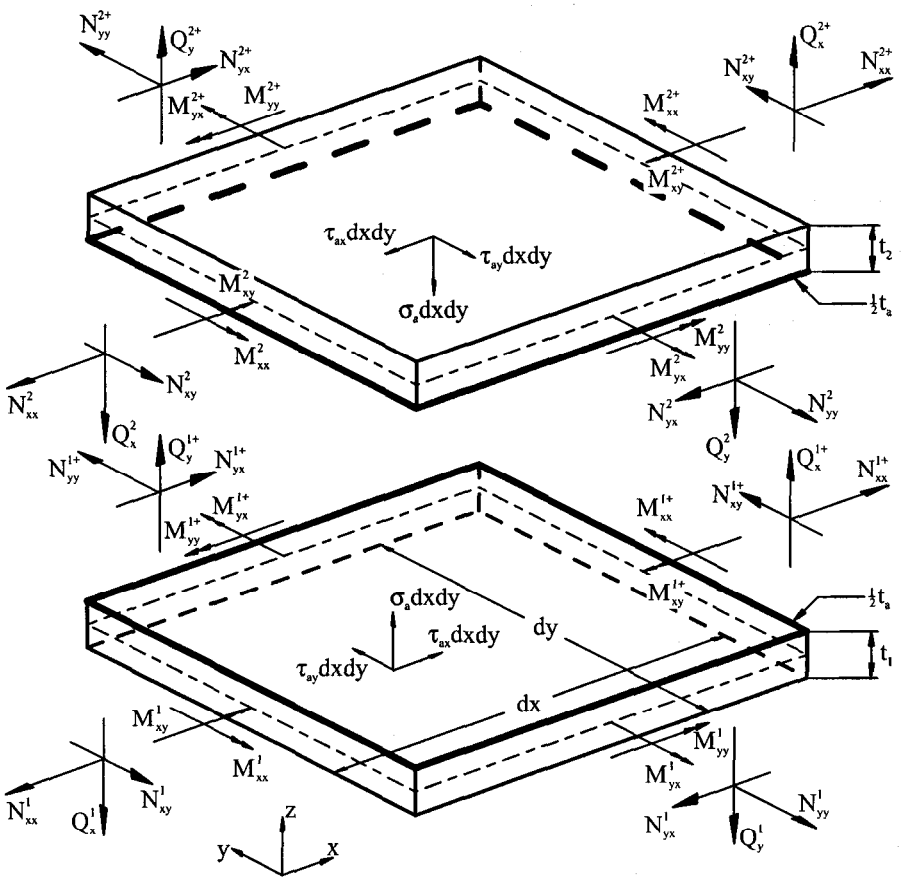

Figure 2.18: Equilibrium element of adherends inside *the overlap* zone *for* joints with one ad*hesive* layer and straight adherends; $0 \leq x \leq L$ *(see also Figure 2.1, Figure 2.3,* Figure 2.5 and Figure 2.12).

The general equilibrium equations inside the overlap zone for the single lap joint with scarfed adherends (with scarf angle α) are derived based on Figure 2.19, and are different from the previous ones, due to the linear change of the adherend thicknesses:

$$\left.\begin{aligned}
N^1_{xx,x} + N^1_{yx,y} + \tau_{ax} &= 0\\
N^1_{xy,x} + N^1_{yy,y} + \tau_{ay} &= 0\\
Q^1_{x,x} + Q^1_{y,y} + \sigma_a &= 0\\
M^1_{xx,x} + M^1_{yx,y} - Q^1_x + \tau_{ax}\tfrac{t_1(x)+t_a}{2} + N^1_{xx}\tfrac{t_1 - t_1^{end}}{2L} &= 0\\
M^1_{xy,x} - M^1_{yy,y} - Q^1_y + \tau_{ay}\tfrac{t_1(x)+t_a}{2} + N^1_{xy}\tfrac{t_1 - t_1^{end}}{2L} &= 0\\
N^2_{xx,x} + N^2_{yx,y} - \tau_{ax} &= 0\\
N^2_{xy,x} + N^2_{yy,y} - \tau_{ay} &= 0\\
Q^2_{x,x} + Q^2_{y,y} - \sigma_a &= 0\\
M^2_{xx,x} + M^2_{yx,y} - Q^2_x + \tau_{ax}\tfrac{t_2(x)+t_a}{2} + N^2_{xx}\tfrac{t_2 - t_2^{end}}{2L} &= 0\\
M^2_{xy,x} - M^2_{yy,y} - Q^2_y + \tau_{ay}\tfrac{t_2(x)+t_a}{2} + N^2_{xy}\tfrac{t_2 - t_2^{end}}{2L} &= 0
\end{aligned}\right\}, \quad 0 \leq x \leq L. \tag{2.19}$$

where $t_1(x)$ and $t_2(x)$ are the adherend thicknesses according to Equations 2.3.

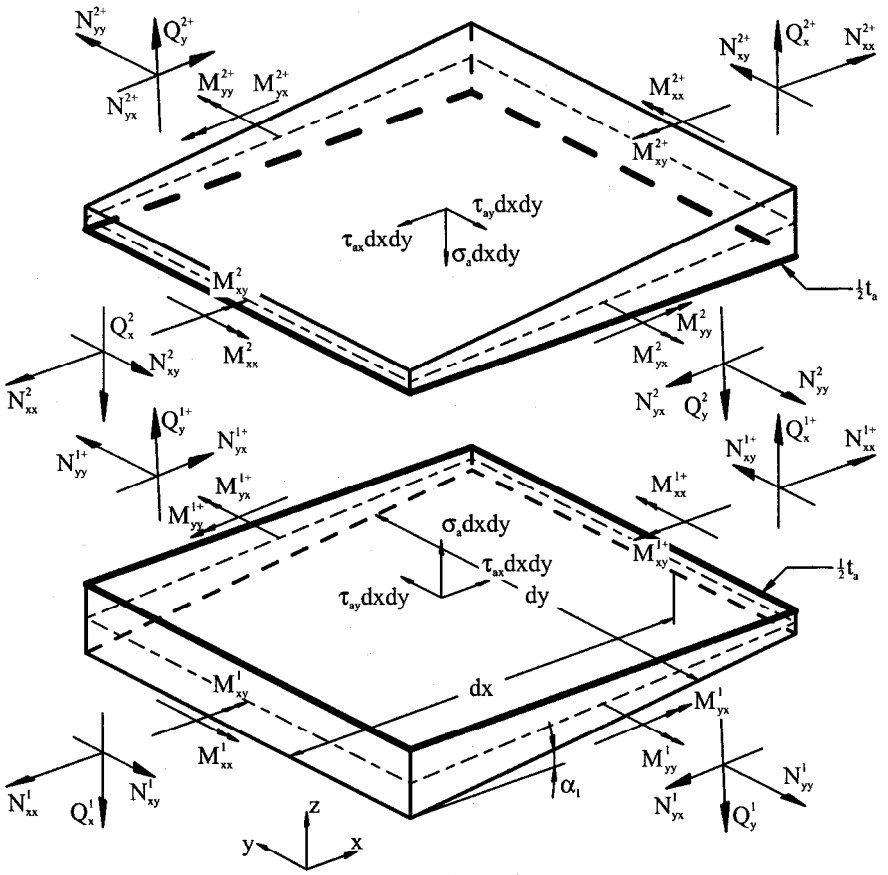

Figure 2.19: Equilibrium *elements in the* overlap zone *for* a *single* lap *joint with* scarfed *adherends (scarf angles* α_1 *and* α_2*);* $0 \leq x \leq L$ *(see* also *Figure 2.2* and Figure 2.10).

The equilibrium equations inside the overlap zone for the single lap joint with scarfed adherends (with scarf angle α) in cylindrical bending are derived based on Equation 2.19 by setting the derivatives with respect to y equal to zero:

$$\left.\begin{aligned}
N^1_{xx,x} &= -\tau_{ax}, & N^2_{xx,x} &= \tau_{ax} \\
N^1_{xy,x} &= -\tau_{ay}, & N^2_{xy,x} &= \tau_{ay} \\
Q^1_{x,x} &= -\sigma_a, & Q^2_{x,x} &= \sigma_a \\
M^1_{xx,x} &= Q^1_x - \tau_{ax}\left(\tfrac{t_1(x)+t_a}{2}\right) - N^1_{xx}\tfrac{t_1-t_1^{end}}{2L}, & M^2_{xx,x} &= Q^2_x - \tau_{ax}\left(\tfrac{t_2(x)+t_a}{2}\right) - N^2_{xx}\tfrac{t_2-t_2^{end}}{2L} \\
M^1_{xy,x} &= Q^1_y - \tau_{ay}\left(\tfrac{t_1(x)+t_a}{2}\right) - N^1_{xy}\tfrac{t_1-t_1^{end}}{2L}, & M^2_{xy,x} &= Q^2_y - \tau_{ay}\left(\tfrac{t_2(x)+t_a}{2}\right) - N^2_{xy}\tfrac{t_2-t_2^{end}}{2L}
\end{aligned}\right\} \quad 0 \leq x \leq L. \quad (2.20)$$

where $t_1(x)$ and $t_2(x)$ are the adherend thicknesses according to Equations 2.3.

The general equilibrium equations inside the overlap zone for the single sided scarfed lap joint are derived based on Figure 2.20, and are different due to the linear change of the adherend

thicknesses and to the sloping bond line:

$$\left.\begin{aligned}
N^1_{xx,x} + N^1_{yx,y} + \tau_{ax} &= 0\\
N^1_{xy,x} + N^1_{yy,y} + \tau_{ay} &= 0\\
Q^1_{x,x} + Q^1_{y,y} + \sigma_a &= 0\\
M^1_{xx,x} + M^1_{yx,y} - Q^1_x + \tau_{ax}\tfrac{t_1(x)+t_a}{2} - N^1_{xx}\tfrac{t_1-t_1^{end}}{2L} &= 0\\
M^1_{xy,x} - M^1_{yy,y} - Q^1_y + \tau_{ay}\tfrac{t_1(x)+t_a}{2} - N^1_{xy}\tfrac{t_1-t_1^{end}}{2L} &= 0\\
N^2_{xx,x} + N^2_{yx,y} - \tau_{ax} &= 0\\
N^2_{xy,x} + N^2_{yy,y} - \tau_{ay} &= 0\\
Q^2_{x,x} + Q^2_{y,y} - \sigma_a &= 0\\
M^2_{xx,x} + M^2_{yx,y} - Q^2_x \;\mathrm{t}\; \tau_{ax}\tfrac{t_2(x)+t_a}{2} - N^2_{xx}\tfrac{t_2-t_2^{end}}{2L} &= 0\\
M^2_{xy,x} - M^2_{yy,y} - Q^2_y + \tau_{ay}\tfrac{t_2(x)+t_a}{2} - N^2_{xy}\tfrac{t_2-t_2^{end}}{2L} &= 0
\end{aligned}\right\} \quad 0 \le x \le L. \qquad (2.21)$$

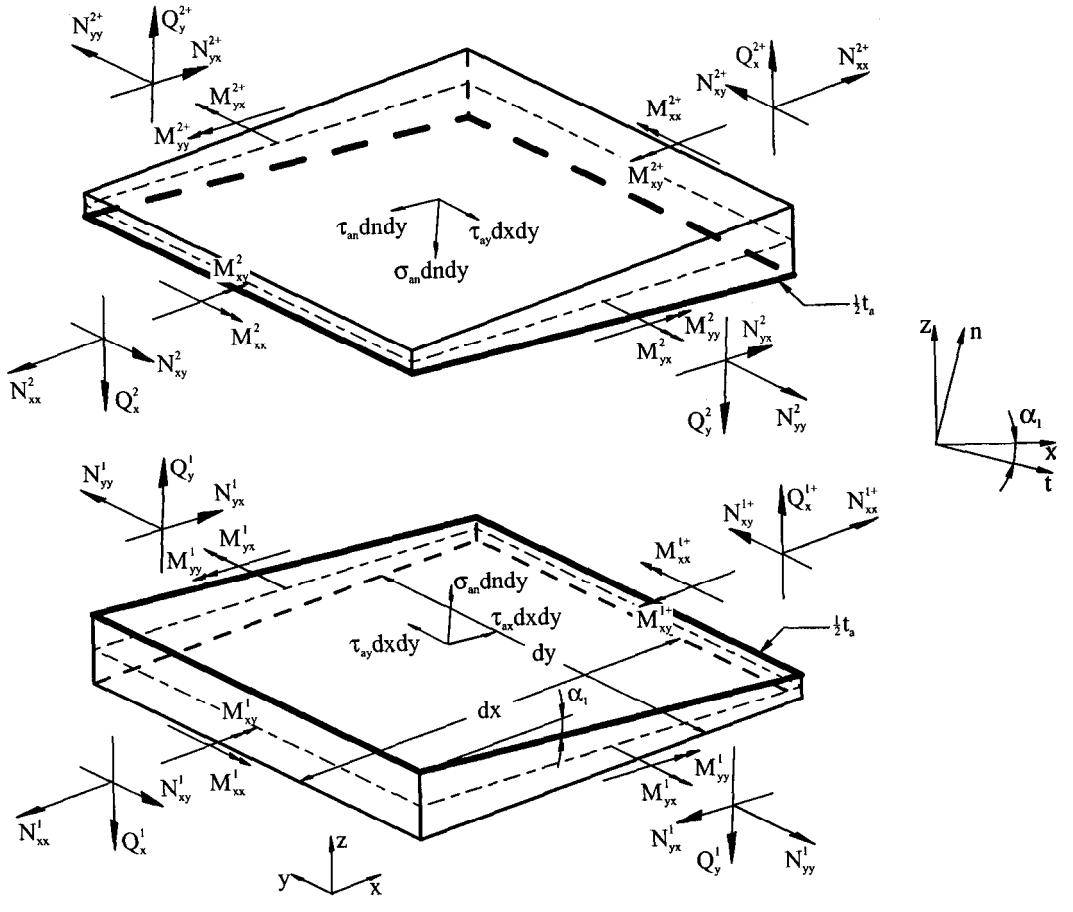

Figure 2.20: Equilibrium elements in the overlap zone for a single sided scarfed lap joint (scarf angles *a); $0 \le x \le L$ (see also Figure* 2.6 and Figure 2.11).

The equilibrium equations inside the overlap zone for the single sided scarfed lap joint with the adherends in cylindrical bending are derived based on Equation 2.21 by setting the derivatives with respect to y equal to zero:

$$\left.\begin{aligned}
N^1_{xx,x} &= -\tau_{ax} \\
N^1_{xy,x} &= -\tau_{ay} \\
Q^1_{x,x} &= -\sigma_a \\
M^1_{xx,x} &= Q^1_x - \tau_{ax}\left(\tfrac{t_1(x)+t_a}{2}\right) + N^1_{xx}\tfrac{t_1-t_1^{end}}{2L} \\
M^1_{xy,x} &= Q^1_y - \tau_{ay}\left(\tfrac{t_1(x)+t_a}{2}\right) + N^1_{xy}\tfrac{t_1-t_1^{end}}{2L} \\
N^2_{xx,x} &= \tau_{ax} \\
N^2_{xy,x} &= \tau_{ay} \\
Q^2_{x,x} &= \sigma_a \\
M^2_{xx,x} &= Q^2_x - \tau_{ax}\left(\tfrac{t_2(x)+t_a}{2}\right) + N^2_{xx}\tfrac{t_2-t_2^{end}}{2L} \\
M^2_{xy,x} &= Q^2_y - \tau_{ay}\left(\tfrac{t_2(x)+t_a}{2}\right) + N^2_{xy}\tfrac{t_2-t_2^{end}}{2L}
\end{aligned}\right\}, \quad 0 \le x \le L. \qquad (2.22)$$

where the relationship between τ_{ax}, σ_a in Equation 2.22 and τ_{an}, σ_{an} shown in Figure 2.20 is established through equilibrium:

$$\begin{aligned}
\tau_{an} &= \tau_{ax}cos^2\alpha \; t \; \sigma_a sin\alpha cos\alpha, \\
\sigma_{an} &= \tau_{ax}sin\alpha cos\alpha \; \mathbf{t} \; \sigma_a cos^2\alpha
\end{aligned} \qquad (2.23)$$

where α is the scarf angle of the adherends in the overlap zone (see Figure 2.11)

The adherend thicknesses $t_1(x)$, $t_2(x)$ vary linearly through the overlap length as specified by Equation 2.3.

Equilibrium Equations for Joints with two Adhesive Layers inside the Overlap Zone

According to Section 2.1.2 the joint configurations with two adhesive layers considered are:

- Double lap joint (Figure 2.4);
- Double sided stepped lap joint (Figure 2.7 and Figure 2.13);
- Double sided scarfed lap joint (Figure 2.8 and Figure 2.14);

The general equilibrium equations inside the overlap zone for the double lap joint and for the double sided stepped lap joint are derived based on Figure 2.21:

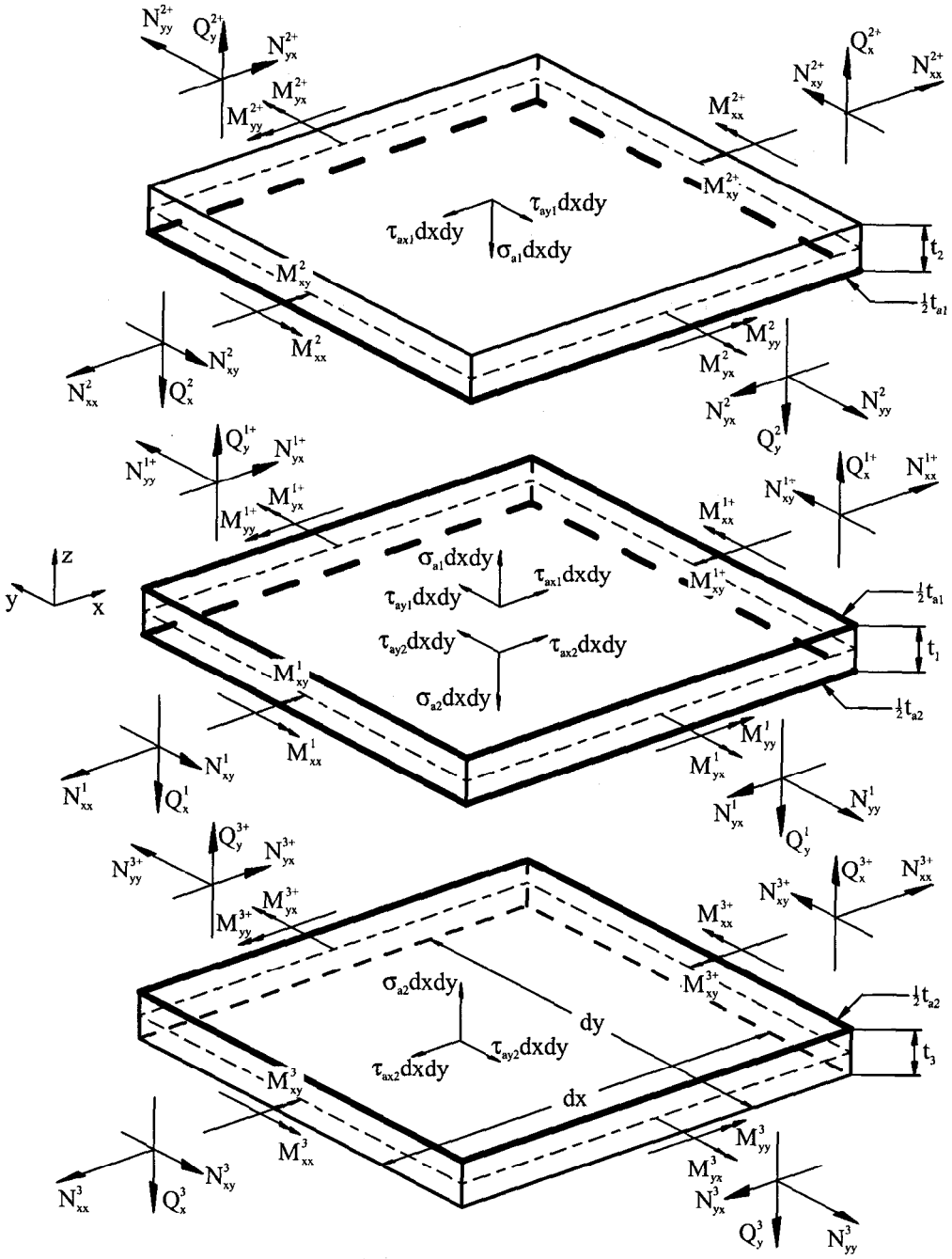

Figure 2.21: Equilibrium element of adherends inside the overlap zone for joints with two adhesive layer and straight adherends; $0 \leq x \leq L$ (see also Figure 2.4, Figure 2.7 and Figure 2.13).

$$
\left.
\begin{aligned}
&N^1_{xx,x} + N^1_{yx,y} + \tau_{ax1} + \tau_{ax2} = 0\\
&N^1_{xy,x} + N^1_{yy,y} + \tau_{ay1} + \tau_{ay2} = 0\\
&Q^1_{x,x} + Q^1_{y,y} - \sigma_{a1} + \sigma_{a2} = 0\\
&M^1_{xx,x} + M^1_{yx,y} - Q^1_x + \tau_{ax1}\tfrac{t_1(x)+t_{a1}}{2} - \tau_{ax2}\tfrac{t_1(x)+t_{a2}}{2} = 0\\
&M^1_{xy,x} - M^1_{yy,y} - Q^1_y + \tau_{ay1}\tfrac{t_1(x)+t_{a1}}{2} - \tau_{ay2}\tfrac{t_1(x)+t_{a2}}{2} = 0\\
&N^i_{xx,x} + N^i_{yx,y} - \tau_{ax1} = 0\\
&N^i_{xy,x} + N^i_{yy,y} - \tau_{ay1} = 0\\
&Q^i_{x,x} + Q^i_{y,y} - \sigma_{a1} = 0\\
&M^i_{xx,x} + M^i_{yx,y} - Q^i_x + \tau_{ax1}\tfrac{t_i(x)+t_{a1}}{2} = 0\\
&M^i_{xy,x} - M^i_{yy,y} - Q^i_y + \tau_{ay1}\tfrac{t_i(x)+t_{a1}}{2} = 0\\
&N^j_{xx,x} + N^j_{yx,y} - \tau_{ax2} = 0\\
&N^j_{xy,x} + N^j_{yy,y} - \tau_{ay2} = 0\\
&Q^j_{x,x} + Q^j_{y,y} - \sigma_{a2} = 0\\
&M^j_{xx,x} + M^j_{yx,y} - Q^i_x + \tau_{ax2}\tfrac{t_i(x)+t_{a2}}{2} = 0\\
&M^j_{xy,x} - M^j_{yy,y} - Q^i_y + \tau_{ay2}\tfrac{t_i(x)+t_{a2}}{2} = 0
\end{aligned}
\right\} \quad 0 \le x \le L. \qquad (2.24)
$$

The equilibrium equations inside the overlap zone for the double lap joint and for the double sided stepped lap joint with the adherends in cylindrical bending are derived based on Equation 2.24 by setting the derivatives with respect to y equal to zero:

$$
\left.
\begin{aligned}
&N^1_{xx,x} = -\tau_{ax1} - \tau_{ax2}\\
&N^1_{xy,x} = -\tau_{ay1} - \tau_{ay2}\\
&Q^1_{x,x} = \sigma_{a1} - \sigma_{a2}\\
&M^1_{xx,x} = Q^1_x - \tau_{ax1}\tfrac{t_1(x)+t_{a1}}{2} + \tau_{ax2}\tfrac{t_1(x)+t_{a2}}{2}\\
&M^1_{xy,x} = Q^1_y - \tau_{ay1}\tfrac{t_1(x)+t_{a1}}{2} + \tau_{ay2}\tfrac{t_1(x)+t_{a2}}{2}\\
&N^i_{xx,x} = \tau_{ax1}, \qquad N^j_{xx,x} = \tau_{ax2}\\
&N^i_{xy,x} = \tau_{ay1}, \qquad N^j_{xy,x} = \tau_{ay2}\\
&Q^i_{x,x} = \sigma_{a1}, \qquad Q^j_{x,x} = \sigma_{a2}\\
&M^i_{xx,x} = Q^i_x - \tau_{ax1}\tfrac{t_i(x)+t_{a1}}{2}, \qquad M^j_{xx,x} = Q^j_x - \tau_{ax2}\tfrac{t_j(x)+t_{a2}}{2}\\
&M^i_{xy,x} = Q^i_y - \tau_{ay1}\tfrac{t_i(x)+t_{a1}}{2}, \qquad M^j_{xy,x} = Q^j_y - \tau_{ay2}\tfrac{t_j(x)+t_{a2}}{2}
\end{aligned}
\right\} \quad 0 \le x \le L. \qquad (2.25)
$$

where $i = 2$ and $j = 3$ for the double lap joint (see Figure 2.4), and $i = 2a$ and $j = 2b$ for the double sided stepped lap joint (see Figure 2.13). t_{a1} and t_{a2} are the adhesive layer thicknesses and $t_1(x)$, $t_i(x)$ and $t_j(x)$ are the adherend thicknesses. For the double lap joint the equilibrium equations will remain the same thoughout the entire overlap zone. For the double sided stepped lap joint the equilibrium equations will vary in the overlap zone, since the thicknesses within each step vary according to Equation 2.5.

Finally, the general equilibrium equations inside the overlap zone for the double sided scarfed lap joint are derived based on Figure 2.22:

$$
\left.
\begin{aligned}
&N^1_{xx,x} + N^1_{yx,y} + \tau_{ax1} + \tau_{ax2} = 0\\
&N^1_{xy,x} + N^1_{yy,y} + \tau_{ay1} + \tau_{ay2} = 0\\
&Q^1_{x,x} + Q^1_{y,y} - \sigma_{a1} + \sigma_{a2} = 0\\
&M^1_{xx,x} + M^1_{yx,y} - Q^1_x + \tau_{ax1}\left(t_{1a}(x) + \tfrac{t_{a1}}{2}\right) - \tau_{ax2}\left(t_{1b}(x) + \tfrac{t_{a2}}{2}\right)\\
&M^1_{xy,x} - M^1_{yy,y} - Q^1_y + \tau_{ay1}\left(t_{1a}(x) + \tfrac{t_{a1}}{2}\right) - \tau_{ay2}\left(t_{1b}(x) + \tfrac{t_{a2}}{2}\right) = 0\\
&N^{2a}_{xx,x} + N^{2a}_{yx,y} - \tau_{ax1} = 0\\
&N^{2a}_{xy,x} + N^{2a}_{yy,y} - \tau_{ay1} = 0\\
&Q^{2a}_{x,x} + Q^{2a}_{y,y} + \sigma_{a1} = 0\\
&M^{2a}_{xx,x} + M^{2a}_{yx,y} - Q^{2a}_x + \tau_{ax1}\frac{t_{2a}(x)+t_{a1}}{2} - N^{2a}_{xx}\frac{t^{end,R}_{2a} - t^{end,L}_{2a}}{2L} = 0\\
&M^{2a}_{xy,x} - M^{2}_{yy,y} - Q^{2a}_y + \tau_{ay1}\frac{t_{2a}(x)+t_{a1}}{2} - N^{2a}_{xy}\frac{t^{end,R}_{2a} - t^{end,L}_{2a}}{2L} = 0\\
&N^{2b}_{xx,x} + N^{2b}_{yx,y} - \tau_{ax2} = 0\\
&N^{2b}_{xy,x} + N^{2b}_{yy,y} - \tau_{ay2} = 0\\
&Q^{2b}_{x,x} + Q^{2b}_{y,y} + \sigma_{a2} = 0\\
&M^{2b}_{xx,x} + M^{2b}_{yx,y} - Q^{2b}_x + \tau_{ax2}\frac{t_{2b}(x)+t_{a2}}{2} + N^{2b}_{xx}\frac{t^{end,R}_{2b} - t^{end,L}_{2b}}{2L} = 0\\
&M^{2b}_{xy,x} - M^{2b}_{yy,y} - Q^{2b}_y + \tau_{ay2}\frac{t_{2b}(x)+t_{a2}}{2} + N^{2b}_{xy}\frac{t^{end,R}_{2b} - t^{end,L}_{2b}}{2L} = 0
\end{aligned}
\right\} \quad 0 \le x \le L. \qquad (2.26)
$$

The equilibrium equations inside the overlap zone for the double sided scarfed lap joint with the adherends in cylindrical bending are derived based on Equation 2.26 by setting the derivatives with respect to y equal to zero:

$$
\left.
\begin{aligned}
N^1_{xx,x} &= -\tau_{ax1} - \tau_{ax2}\\
N^1_{xy,x} &= -\tau_{ay1} - \tau_{ay2}\\
Q^1_{x,x} &= \sigma_{a1} - \sigma_{a2}\\
M^1_{xx,x} &= Q^1_x - \tau_{ax1}\left(t_{1a}(x) + \tfrac{t_{a1}}{2}\right) + \tau_{ax2}\left(t_{1b}(x) + \tfrac{t_{a2}}{2}\right)\\
M^1_{xy,x} &= Q^1_y - \tau_{ay1}\left(t_{1a}(x) + \tfrac{t_{a1}}{2}\right) + \tau_{ay2}\left(t_{1b}(x) + \tfrac{t_{a2}}{2}\right)\\
N^{2a}_{xx,x} &= \tau_{ax1}\\
N^{2a}_{xy,x} &= \tau_{ay1}\\
Q^{2a}_{x,x} &= \sigma_{a1}\\
M^{2a}_{xx,x} &= Q^{2a}_x - \tau_{ax1}\frac{t_{2a}(x)+t_{a1}}{2} + N^{2a}_{xx}\frac{t^{end,R}_{2a} - t^{end,L}_{2a}}{2L}\\
M^{2a}_{xy,x} &= Q^{2a}_y - \tau_{ay1}\frac{t_{2a}(x)+t_{a1}}{2} + N^{2a}_{xy}\frac{t^{end,R}_{2a} - t^{end,L}_{2a}}{2L}\\
N^{2b}_{xx,x} &= \tau_{ax}\\
N^{2b}_{xy,x} &= \tau_{ay}\\
Q^{2b}_{x,x} &= \sigma_a\\
M^{2b}_{xx,x} &= Q^{2b}_x - \tau_{ax2}\frac{t_{2b}(x)+t_{a2}}{2} - N^{2b}_{xx}\frac{t^{end,R}_{2b} - t^{end,L}_{2b}}{2L}\\
M^{2b}_{xy,x} &= Q^{2b}_y - \tau_{ay2}\frac{t_{2b}(x)+t_{a2}}{2} - N^{2b}_{xy}\frac{t^{end,R}_{2b} - t^{end,L}_{2b}}{2L}
\end{aligned}
\right\} \quad 0 \le x \le L. \qquad (2.27)
$$

where $t_1(x)$, $t_{2a}(x)$ and $t_{2b}(x)$ are the adherend thicknesses, according to Equation 2.6, and t_{a1} and t_{a2} are the adhesive layer thicknesses.

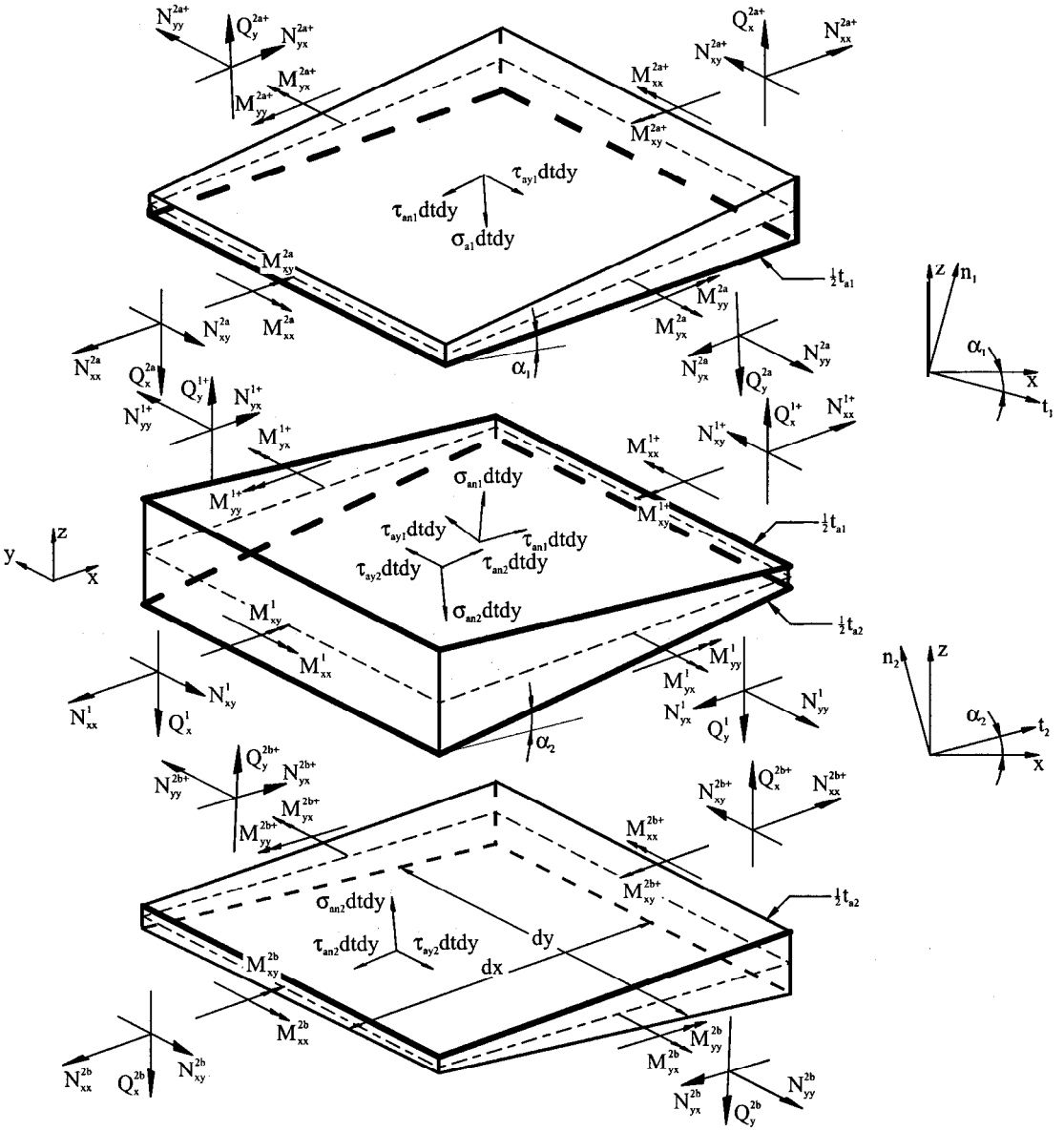

Figure 2.22: Equilibrium element of adherends inside the overlap zone for double sided scarfed lap joints; $0 \leq x \leq L$ (see also Figure 2.8 and Figure 2.14).

The relationship between τ_{ax1}, σ_{a1} in Equation 2.27 and τ_{an1}, σ_{an1} shown in Figure 2.20 as well as the relationship between τ_{ax2}, σ_{a2} in Equation 2.27 and τ_{an2}, σ_{an2} shown in Figure 2.20 is established through equilibrium:

$$\tau_{ani} = \tau_{axi}cos^2\alpha_i - \sigma_{ai}sin\alpha_i cos\alpha_i, \quad \sigma_{ani} = \tau_{axi}sin\alpha_i cos\alpha_i + \sigma_{ai}cos^2\alpha_i, \ (i = 1,2) \qquad (2.28)$$

where α_i (i = 1, 2) is the scarf angles of the adherends in the overlap zone (see Figure 2.14).

2.2.6 The Complete Set of System Equations

From the equations derived it is possible to form the complete set of system equations for each of the bonded joint configurations. Thus, combination of the constitutive and kinematic relations, i.e. Equations 2.9 and 2.11, together with the constitutive relations for the adhesive layers, i.e. Equations 2.14, and the equilibrium equations lead to a set of 8 linear coupled first-order ordinary differential equations describing the system behaviour of each of the adherends. The total set of coupled first-order ordinary differential equations within the overlap zone is therefore 16 for joints with 2 adherends inside the overlap zone, and 24 for the joints with 3 adherends inside the overlap zone. Outside the overlap zones the system behaviour for all the joints is described by 8 linear coupled first-order ordinary differential equations, except for the double lap joint which has two adherends in the region $L \leq x \leq L$ •t L_2 (see Figure 2.4) and therefore is described by a set of 16 linear coupled first-order ordinary differential equations in this region. The actual derivation of the governing equations for the bonded joint types included in this study is quite lengthy and tedious (although also straight forward). Therefore the derivation is not included in this thesis, but the resulting sets of governing equations are shown in Appendix A. The governing equations for all the bonded joint types considered can be expressed in the following general form within each region:

$$\Psi^n\{\{y^i(x^r)\}\}_{,x} = \begin{bmatrix} [\boldsymbol{A}^r_{11}(x^r)] & \cdots & [\boldsymbol{A}^r_{1n}(x^r)] \\ \vdots & & \\ [\boldsymbol{A}^r_{n1}(x^r)] & \cdots & [\boldsymbol{A}^r_{nn}(x^r)] \end{bmatrix} \Psi^n\{\{y^i(x^r)\}\} + \Upsilon^n\{\{\boldsymbol{B}^r_i(x^r)\}\} \tag{2.29}$$

$$\Psi^n\{\{y^i(x^r)\}\} = \{\{y^1(x^r)\},\{y^2(x^r)\},.....,\{y^n(x^r)\}\}$$

$$\Upsilon^n\{\{\boldsymbol{B}^r_i(x^r)\}\} = \{\{\boldsymbol{B}^r_1(x^r)\},\{\boldsymbol{B}^r_2(x^r)\},....,\{\boldsymbol{B}^r_n(x^r)\}\}$$

where n is the number of adherends within the region considered. The values of n are between 1 and 3 (both included) depending on the type of joint and the region considered. The system of governing equations are solved within a number of sub-regions r, see Figure 2.24 Section *2.2.8.* $\left[\boldsymbol{A}^r_{ij}(x^r)\right]$ $(i,j = 1, ..,n)$ is a (m,m) sub-coefficient matrix for the system of governing equations, and $\{\boldsymbol{B}^r_i(x^r)\}$ is a (m, 1) sub-matrix of non-homogeneous load terms, where m is the number of equations for each adherend, i.e. 8 for the cylindrical bending case and 6 for the beam case. For the cylindrical bending case the vector $\{y^i\}$ is the vector containing the fundamental variables, which are those quantities that appear in the natural boundary conditions at an edge x =constant defined by:

$$\left\{y^i\right\} = \left\{u^i_0, w^i, \beta^i_x, v^i_0, N^i_{xx}, N^i_{xy}, M^i_{xx}, Q^i_x\right\} \quad i = 1,2,3. \tag{2.30}$$

These variables will be determined through the analysis. In addition, the quantities

$$\left\{y^i_{res}\right\} = \left\{N^i_{yy}, M^i_{yy}, M^i_{xy}, Q^i_y\right\} i = 1,2,3 \tag{2.31}$$

can be determined from the equilibrium equations and the constitutive relations. These quantities can be seen as stress and moment resultants necessary to keep the structure in a state of cylindrical bending.

For the beam case the problem is reduced to a set of 6 coupled first-order ordinary differential equations for each adherend. The solution vector containing the fundamental variables for each adherend for this problem is defined by:

$$\left\{y^i\right\} = \left\{u^i_0, w^i, \beta^i_x, N^i_{xx}, M^i_{xx}, Q^i_x\right\} \quad i = 1,2,3. \tag{2.32}$$

In this case no additional quantities need to be determined.

2.2.7 The Boundary Conditions

To solve the adhesive bonded joint problems the boundary conditions and continuity conditions have to be stated. The continuity conditions must be stated at the ends of the regions, in which the joint is divided, as shown in Figures 2.1 - 2.8. In the following the boundary conditions and continuity conditions are stated for the different joint types:

Single lap joint (Figures 2.1 and 2.2)

$$x = -L_1,\ L + L_2 : \textit{prescribed} : \quad \left.\begin{matrix} u_0^i \textit{ or } N_{xx}^i,\ w^i \textit{ or } Q_x^i, \\ \beta_x^i \textit{ or } M_{xx}^i,\ v_0^i \textit{ or } N_{xy}^i \end{matrix}\right\} \quad i = 1,2$$

$$\begin{aligned} x = 0 &: \quad \textit{adherend } 1 : \text{Continuity across } \textit{junction} \\ &\quad \textit{adherend } 2 : N_{xx}^2 = N_{xy}^2 = M_{xx}^2 = Q_x^2 = 0 \\ x = L &: \quad \textit{adherend } 1 : N_{xx}^1 = N_{xy}^1 = M_{xx}^1 = Q_x^1 = 0 \\ &\quad \textit{adherend } 2 : \textit{Continuity across junction} \end{aligned} \tag{2.33}$$

The boundary and continuity conditions are the same for both the single lap joint with straight and scarfed adherends. The boundary conditions for adherend 2 at x = 0 and for adherend 1 at x = L are derived from the assumption that the adherend edges are free, see Figures 2.1 and 2.6. This assumption is discussed further in Section 2.5 as previously mentioned.

Bonded doubler joint (Figure 2.3)

$$x = 0,\ L \bullet t\ L_1 : \textit{prescribed} : \quad \left.\begin{matrix} u_0^i \textit{ or } N_{xx}^i,\ w^i \textit{ or } Q_x^i, \\ \beta_x^i \text{ or } M_{xx}^i,\ v_0^i \text{ or } N_{xy}^i \end{matrix}\right\} \quad i = 1,2$$

$$\begin{aligned} x = L &: \quad \textit{adherend } 1 : \textit{Continuity across junction} \\ &\quad \textit{adherend } 2 : N_{xx}^2 = N_{xy}^2 = M_{xx}^2 = Q_x^2 = 0 \end{aligned} \tag{2.34}$$

The boundary conditions for adherend 2 at x = L are derived from the assumption that the adherend edge is free, see Figure 2.3.

Double lap joint (Figure 2.4)

$$x = -L_1,\ L + L_2 : \textit{prescribed} : \quad \left.\begin{matrix} u_0^i \textit{ or } N_{xx}^i,\ w^i \textit{ or } Q_x^i, \\ \beta_x^i \textit{ or } M_{xx}^i,\ v_0^i \textit{ or } N_{xy}^i \end{matrix}\right\} \quad i = 1,2,3$$

$$\begin{aligned} x = 0 &: \quad \textit{adherend } 1 : \textit{Continuity across junction} \\ &\quad \textit{adherend } 2 : N_{xx}^2 = N_{xy}^2 = M_{xx}^2 = Q_x^2 = 0 \\ &\quad \textit{adherend } 3 : N_{xx}^3 = N_{xy}^3 = M_{xx}^3 = Q_x^3 = 0 \\ x = L &: \quad \textit{adherend } 1 : N_{xx}^1 = N_{xy}^1 = M_{xx}^1 = Q_x^1 = 0 \\ &\quad \textit{adherend } 2 : \textit{Continuity across junction} \\ &\quad \textit{adherend } 3 : \textit{Continuity across junction} \end{aligned} \tag{2.35}$$

The boundary conditions for adherend 2 and 3 at x = 0 and for adherend 1 at x = L are derived from the assumption that the adherend edges are free, see Figure 2.4.

Single sided stepped lap joint (Figure 2.5)

The boundary and continuity conditions at the ends of the joint and at the ends of the overlap zone are the same as for the single lap joint, i.e. Equations 2.33, and the only conditions which still need to be specified for the stepped lap joint are the continuity conditions across each step within the overlap zone:

Continuity ***across each step within the overlap*** *zone*:

$$\begin{array}{lll} \text{adherend 1}: & u_0^{1*} = u_0^1 - \beta_x^1 t_1^* & \textbf{adherend 2}: \quad u_0^2 = u_0^2 - \beta_x^2 t_2^* \\ & M_{xx}^{1*} = M_{xx}^1 \text{ t } N_{xx}^1 t_1^* & M_{xx}^{2*} = M_{xx}^2 + N_{xx}^2 t_2^* \\ & M_{xy}^{1*} = M_{xy}^1 + N_{xy}^1 t_1^* & M_{xy}^{2*} = M_{xy}^2 + N_{xy}^2 t_2^* \end{array} \tag{2.36}$$

where t_1^* and t_2^* are the distances between the centerlines of the adherend laminates at each step as shown in Figure 2.23.

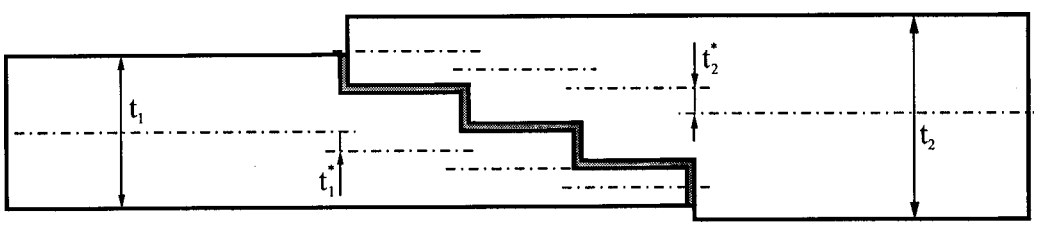

Figure 2.23: Distances between the centerlines ***of*** the adherend laminates at the ***steps*** for single sided stepped lap joint

Single sided scarfed lap joint (Figure 2.6)

The boundary and continuity conditions at the ends of the joint and at the ends of the overlap zone are the same as for the single lap joint, i.e. Equation 2.33.

Double sided stepped lap joint (Figure 2.7)

The boundary conditions at the ends of the joint are the same as for the single lap joint, i.e. Equation 2.33. The boundary and continuity conditions at the left end of the overlap zone, i.e. at $x = 0$ are the same as for the double lap joint at the same location, i.e. Equation 2.35. The only thing still needed in order to solve the problem is to specify the boundary and continuity conditions at the right end of the overlap zone, i.e. at x = ***L,*** and the continuity conditions at each step within the overlap zone.

Continuity ***across each step within the overlap*** *zone*:

$$\begin{array}{lll} \textbf{adherend 2a}: & u_0^{2a*} = u_0^{2a} - \beta_x^{2a} t_{2a}^* & \textbf{adherend 2b}: \quad u_0^{2b*} = u_0^{2b} + \beta_x^{2b} t_2^* \\ & M_{xx}^{2a*} = M_{\sim xx}^{2a} + N_{xx}^{2a} t_{2a}^* & M_{xx}^{2b*} = M_{\sim xx}^{2b} - N_{xx}^{2b} t_{2b}^* \\ & M_{xy}^{2a*} = M_{\sim xy}^{2a} + N_{xy}^{2a} t_{2a}^* & M_{xy}^{2b*} = M_{\sim xy}^{2b} - N_{xy}^{2b} t_{2b}^* \end{array} \tag{2.37}$$

$$
\begin{aligned}
x = L: \quad & \textbf{\textit{adherend}}\ 1: N^1_{xx} = N^1_{xy} = M^1_{xx} = Q^1_x = 0 \\
& \textbf{\textit{Continuity across junction}}: \\
& u^2_0 = u^{2a}_0 - t^*_{2a}\beta^{2a}_x, \qquad u^2_0 = u^{2b}_0 + t^*_{2b}\beta^{2b}_x \\
& w^2 = w^{2a}, \qquad w^2 = w^{2b} \\
& \beta^2_x = \beta^{2a}, \qquad \beta^2_x = \beta^{2b}_x \\
& v^2_0 = v^{2a}_0, \qquad v^2_0 = v^{2b}_0 \\
& N^2_{xx} = N^{2a}_{xx}\ \mathrm{t}\ N^{2b}_{xx} \\
& N^2_{xy} = N^{2a}_{xy} + N^{2b}_{xy} \\
& M^2_{xx} = M^{2a*}_{xx} + M^{2b*}_{xx} + \\
& \qquad N^{2a}_{xx}t^*_{2a} - N^{2b}_{xx}t^*_{2b} \\
& Q^2_x = Q^{2a}_x + Q^{2b}_x
\end{aligned}
\tag{2.38}
$$

where t^*_{2a} and t^*_{2b} are the distances between the centerlines of the adherend laminates at each step as for the single sided stepped lap joint, see Figure 2.23.

Double sided scarfed lap joint (Figure 2.8)

The boundary and continuity conditions are the same as for the double sided stepped lap joint, i.e. Equation 2.37, except that no continuity conditions within the overlap zone are required for the double sided scarfed lap joint.

2.2.8 Multi-Segment Method of Integration

Each set of governing equations, together with the appropriate boundary conditions for the particular bonded joint problem considered, constitutes a multiple-point boundary value problem to which no general closed-form solution is obtainable. Thus, a numerical solution procedure must be used to solve the bonded joint problems. In general, this can be done by using methods such as ***finite** difference* methods or direct ***integration*** methods. The use of a normal direct integration approach will involve some disadvantages, where the most important is that a complete loss of accuracy inevitably will occur, if the length of the integration interval is increased beyond a certain value. The loss of accuracy is caused by subtraction of almost equal and very large numbers in the process of determination of the unknown boundary values. The use of a finite difference approach instead of a direct integration approach can overcome such a loss of accuracy, but finite difference methods involve other difficulties which make them somewhat less attractive in the present context. However, the use of a modified direct integration method, called the *'multi-*segment ***method*** of integration', can overcome the loss of accuracy experienced with the 'normal' direct integration methods. Moreover, the 'multi-segment method of integration' display some advantages compared with finite difference methods, where the most significant ones are:

- It can be applied conveniently to systems of first order equations.
- It can be applied equally well to beam, plate and shell problems.
- It is especially well suited for solving 'multiple-point' boundary value problems.

The method is based on a transformation of the original 'multiple-point' boundary value problem into a series of initial value problems. The principle behind the method is to divide the original problem into a finite number of segments, where the solution within each segment can

be accomplished by means of direct integration. Fulfilment of the boundary conditions, as well as fulfilment of continuity requirements across the segment junctions, is assured by formulating and solving a set of linear algebraic equations.

The method was originally developed by Kalnins (1964a) who applied it to the solution of elasto-static shell problems, formulated as two-point boundary value problems, governed within an interval by a system of m first order linear ordinary differential equations, together with m/2 boundary conditions prescribed at each end of the interval. Kalnins also applied the multi-segment method of integration to problems of free vibrations of rotationally symmetric shells (Kalnins 1964b) and to problems of free and forced vibrations of rotationally symmetric layered shells (Kalnins 1965).

Yuceoglu and Updike (1975a), Yuceoglu and Updike (1975b) and Yuceoglu and Updike (1981) used the method to analyse different types of standard and advanced adhesive bonded joints and Thomsen (1989) and Thomsen (1992) used the method to analyse adhesive bonded tubular lap joints.

In the present work the method is adopted and adjusted to solve the multi-point boundary value problems defined for all the considered adhesive bonded joint types.

General Description of the Method Applied for the Joint Problems

The joint configuration is first divided into a number of regions within which the number of adherends is the same, i.e. regions within which the number of governing equations are the same. As an example the single lap joint configuration shown in Figure 2.24 is divided into three regions.

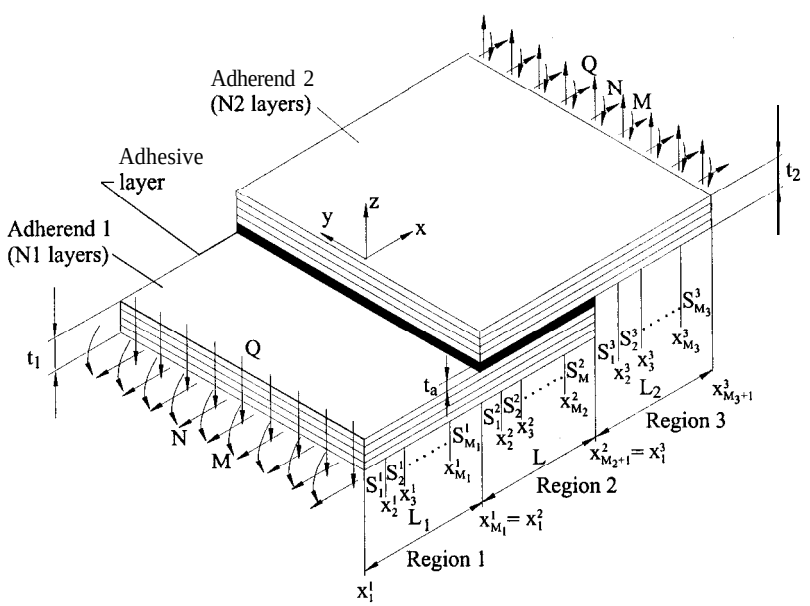

Figure 2.24: Schematic illustration of adhesive single lap joint divided into (Mr + M_2 + M_3) ***segments.***

According to Figure **2.24** the three regions are:

- The region to the left side of the overlap zone, i.e. $-L_1 \leq x \leq 0$;
- The overlap zone, i.e. $0 \leq x \leq L$;
- The region to the right side of the overlap zone, i.e. $\boldsymbol{L \leq x \leq L + L_2}$.

Each of the regions r (r = $1, 2, .., n_r$) are then divided into a finite number of segments M_r, ***see*** Figure 2.24. The segments within a region are denoted by S_j^r, ($j = 1, 2, \ldots . M_r$) and the j'th segment extends from x_j^r to x_{j+1}^r.

The solution procedure adopted in the 'multi-segment method of integration' includes four steps:

- Solution of the governing equation within each segment S_j^r in each region r.
- Specification of continuity conditions between each segment within each region r.
- Specification of boundary and continuity conditions at the ends of the regions.
- Formulation and solution of a set of linear algebraic equations containing the unknown variables.

In the following the solution procedure containing the four steps presented above will be described.

The governing equations derived for the different bonded joint configurations in the specified regions are shown in Appendix A. The corresponding boundary conditions are defined in Section **2.2.2.**

Solution of the governing equations within each segment S_j^r in each region r:

The solution within a region r, $x_1^r \leq x^r \leq x_{M_r}^r$, can in general form be written as (Kalnins (1964a)):

$$\begin{aligned} \Psi^n\{\{y^i(x^r)\}\} &= \left[\boldsymbol{Y}_j^r(x^r)\right]\ \Psi^n\{\{y(x_j^r)\}\} + \{\boldsymbol{Z}_j^r(x^r)\} \\ \Psi^n\{\{y^i(x^r)\}\} &= \{\{y^1(x^r)\},\{y^2(x^r)\},\ldots..,\{y^n(x^r)\}\} \end{aligned} \tag{2.39}$$

where $\{y^i(x^r)\}$ is the solution vector for the i'th adherend as described in Equations 2.30 or 2.32, n is the number of adherends within the considered region r. $\left[\boldsymbol{Y}_j^r(x^r)\right]$, $\{\boldsymbol{Z}_j^r(x^r)\}$ denotes (n $*$ m, n $*$ ***m)*** complementary and (n $*$ m, 1) particular solution matrices in each segment S_j^r, $x_j^r \leq x^r \leq x_{j+1}^r$, given by:

$$\frac{d}{dx}\left[\boldsymbol{Y}_j^r(x^r)\right] = \begin{vmatrix} [\boldsymbol{A}_{11}^r(x^r)] \ldots . [\boldsymbol{A}_{1n}^r(x^r)] \\ \\ [\boldsymbol{A}_{n1}^r(x^r)] \ldots . [\boldsymbol{A}_{nn}^r(x^r)] \end{vmatrix} \left[\boldsymbol{Y}_j^r(x^r)\right] \tag{2.40}$$

$$\frac{d}{dx}\{\boldsymbol{Z}_j^r(x^r)\} = \begin{vmatrix} [\boldsymbol{A}_{11}^r(x^r)] \ldots . [\boldsymbol{A}_{1n}^r(x^r)] \\ \\ [\boldsymbol{A}_{n1}^r(x^r)] \ldots . [\boldsymbol{A}_{nn}^r(x^r)] \end{vmatrix} \{\boldsymbol{Z}_j^r(x^r)\} + \Upsilon^n\{\{\boldsymbol{B}_i^r(x^r)\}\}$$

with initial conditions given by:

$$\begin{aligned} \left[\boldsymbol{Y}_j^r(x_j^r)\right] &= [\boldsymbol{I}] \\ \{\boldsymbol{Z}_j^r(x_j^r)\} &= 0 \end{aligned} \qquad \textit{(2.41)}$$

The solution within each segment can therefore be accomplished by means of direct integration of the set of first order differential equations in Equations 2.40 with the initial conditions given by Equations 2.41. From this it can be seen, that if the adherends properties and thicknesses are independent of the longitudinal coordinate x, and if each of the segments j within the region r have the same length, then it is only necessary to perform the integration of the governing equations within the considered region once. The reason for this is that the governing equations are then independent of the longitudinal coordinate x, and consequently the solution within segments of equal length will be the same. The solution for joints with straight adherends (i.e. adherends with constant stiffness properties) is therefore much faster than for joints with scarfed adherends (i.e. adherends where the stiffness properties vary with the longitudinal coordinate x) where integration within each segment must be performed.

Specification of continuity between ***each*** segment within ***the*** *region r:*

The continuity across the junctions between the segments $(x_j^r; j = 2, 3, \ldots, M_r + 1)$ within the region ***r (see*** Figure 2.24) is ensured by fulfilment of the following M_r matrix equations:

$$\Psi^n\left\{\{y^i(x_{j+1}^r)\}\right\} = \left[\boldsymbol{Y}_j^r(x_{j+1}^r)\right]\Psi^n\left\{\{y^i(x_j^r)\}\right\} + \left\{\boldsymbol{Z}_j^r(x_{j+1}^r)\right\}, \quad j = 1, 2, \ldots\ldots, M_r \qquad (2.42)$$

Equation 2.42 can be written in a partitioned form, where, for the purpose of rearranging the variables in the solutions vectors to satisfy the boundary conditions, the solution vector for each adherend is divided into two parts. In partitioned form equation 2.42 can form be written as follows :

$$\Psi^n\begin{Bmatrix}\{y_1^i(x_{j+1}^r)\}\\ \{y_2^i(x_{j+1}^r)\}\end{Bmatrix} = \begin{bmatrix} \left[\boldsymbol{Y}_{11j}^r(x_{j+1}^r)\right] & \cdots & \left[\boldsymbol{Y}_{1nj}^r(x_{j+1}^r)\right] \\ \vdots & & \\ \left[\boldsymbol{Y}_{n1j}^r(x_{j+1}^r)\right] & \cdots & \left[\boldsymbol{Y}_{nnj}^r(x_{j+1}^r)\right] \end{bmatrix} \Psi^n\begin{Bmatrix}\{y_1^i(x_j^r)\}\\ \{y_2^i(x_j^r)\}\end{Bmatrix} + \chi^{2*n}\left\{\{\boldsymbol{Z}_{ij}^r(x_{j+1}^r)\}\right\} \qquad \textit{(2.43)}$$

where

$$\begin{aligned} \Psi^n\begin{Bmatrix}\{y_1^i(x_{j+1}^r)\}\\ \{y_2^i(x_{j+1}^r)\}\end{Bmatrix} &= \left\{\{y_1^1(x_{j+1}^r)\}, \{y_2^1(x_{j+1}^r)\}, , \ldots, \{y_1^n(x_{j+1}^r)\}, \{y_2^n(x_{j+1}^r)\}\right\} \\ \chi^{2*n}\left\{\{\boldsymbol{Z}_{ij}^r(x_{j+1}^r)\}\right\} &= \left\{\{\boldsymbol{Z}_{1j}^r(x_{j+1}^r)\}, \{\boldsymbol{Z}_{2j}^r(x_{j+1}^r)\}, \ldots, \{\boldsymbol{Z}_{(2*n)j}^r(x_{j+1}^r)\}\right\} \end{aligned} \qquad \textit{(2.44)}$$

Thus, a system of $2nM_r$ linear $(m/2, 1)$ matrix equations is obtained in which the known coefficients $\left[\boldsymbol{Y}_{ikj}^r(x_{j+1}^r)\right]$, $\{\boldsymbol{Z}_{ij}^r(x_{j+1}^r)\}$ are $(m/2, m/2)$ and ***(m/2,1)*** matrices respectively, and the unknowns $\{y_1^i(x_{j+1}^r)\}$ and $\{y_2^i(x_{j+1}^r)\}$ are (m/2,1) matrices.

Specification of boundary and continuity conditions ***at the*** ends of ***the*** regions:

To solve the boundary value problems it is necessary to specify $m/2$ of the fundamental variables at the ends of the adherends. With references to Figure 2.24 the boundary conditions at the ends of the structural assembly, as well as the continuity conditions at the junctions between the regions, can be specified as:

$$\begin{aligned} x = x_1^r \quad &: \quad [\,T_L^r\,]\Psi^n\{\{y^i(x_1^r)\}\} = \{U_L^r\} \\ x = x_{M_r+1}^r \quad &: \quad [\,T_R^r\,]\Psi^n\left\{\{y^i(x_{M_r+1}^r)\}\right\} = \{U_R^r\} \end{aligned} \qquad \textit{(2.45)}$$

where $[\,T_L^r\,]$ and $[\,T_R^r\,]$ are non-singular (n * m, n * m) transformation matrices, and $\{U_L^r\}$, $\{\,U_R^r\}$ are $(n*m,\,1)$ matrices containing rearranged sets of the fundamental variables at $x = x_1^r$ and $x = x_{M_r+1}^r$. The transformation matrix $[\,T_L^r\,]$ 'performs' a rearrangement such that the first (m/2) * $n_{bc\_sp\_L}$ elements of $\{\,U_L^r\}$ denoted by $\Psi^{n_{bc\_sp\_L}}\{\{u_1^i(x_1^r)\}\}$ are the specified boundary conditions at $x = x_1^r$, where $n_{bc\_sp\_L}$ is the number of adherends with specified boundary conditions at the left end of the region, and where $\{u_1^i(x_1^r)\}$ is a (m/2, 1) matrix containing the m/2 specified boundary conditions for the i'th adherend at x = x_1^r. In the same way the transformation matrix $[\,T_R^r\,]$ 'performs' a rearrangement such that the last (m/2) * $n_{bc\_sp\_R}$ elements of $\{U_R^r\}$ denoted by $\Psi^{n_{bc\_sp\_R}}\{\{u_2^i(x_{M_r+1}^r)\}\}$ are the specified boundary conditions at x = $x_{M_r+1}^r$, where $n_{bc\_sp\_R}$ is the number of adherends with specified boundary conditions at the right end of the considered region, and where $\{u_2^i(x_{M_r+1}^r)\}$ is a $(m/2,1)$ matrix containing the m/2 specified boundary conditions for the i'th adherend at x = $x_{M_r+1}^r$.

To obtain control of the position of the unknown elements at the boundaries it is necessary to conduct some manipulations with Equations 2.42. The first of Equations 2.45 can be written as:

$$\Psi^n\left\{\{y^i(x_1^r)\}\right\} = [T_L^r]^{-1}\{U_L^r\} \tag{2.46}$$

Substitution of 2.46 into 2.42 with j = 1; $x_1^r \le$ x $\le x_2^r$ gives

$$\Psi^n\left\{\{y^i(x_2^r)\}\right\} = [\boldsymbol{Y}_1^{r*}(x_2^r)]\{U_L^r\} + \{\boldsymbol{Z}_1^r(x_2^r)\} \tag{2.47}$$

where

$$[\boldsymbol{Y}_1^{r*}(x_2^r)] = [\boldsymbol{Y}_1^r(x_2^r)][T_L^r]^{-1} \tag{2.48}$$

In partitioned form Equations 2.47 can be written as:

$$\Psi^n\begin{Bmatrix}\{y_1^i(x_2^r)\}\\ \{y_2^i(x_2^r)\}\end{Bmatrix} = \begin{bmatrix}[\boldsymbol{Y}_{111}^r(x_2^r)] & \cdots & [\boldsymbol{Y}_{1n1}^r(x_2^r)]\\ \vdots & & \\ [\boldsymbol{Y}_{n11}^r(x_2^r)] & \cdots & [\boldsymbol{Y}_{nn1}^r(x_2^r)]\end{bmatrix}\Psi^n\begin{Bmatrix}\{u_1^i(x_1^r)\}\\ \{u_2^i(x_1^r)\}\end{Bmatrix} + \chi^{2*n}\{\{\boldsymbol{Z}_{i1}^r(x_2^r)\}\} \tag{2.49}$$

where the (m/2) * $n_{bc\_sp\_L}$ matrices $\Psi^{n_{bc\_sp\_L}}\{\{u_1^i(x_1^r)\}\}$ contain the (m/2) * $n_{bc\_sp\_L}$ boundary conditions specified at x = x_1^r.

To place the (m/2) * $n_{bc\_sp\_R}$ specified boundary conditions at x = $x_{M_r+1}^r$, i.e. at the right end of the region, as the last (m/2) * $n_{bc\_sp\_R}$ elements of the (n * **m,** 1) matrix U_R^r, it is necessary to perform the same manipulations to the solution vector in the last segment S_{M_r}; $x_{M_r}^r \le$ x $\le x_{M_r+1}^r$. By multiplying the solution, i.e. Equations 2.42, in this interval with the (n * m, n * m) transformation matrix $[T_R^r]$ defined in Equations 2.45 the following relations are obtained:

$$\begin{aligned}&[T_R^r]\Psi^n\left\{\{y^i(x_{M_r+1}^r)\}\right\} = [T_R^r]\,[\boldsymbol{Y}_{M_r}^r(x_{M_r+1}^r)]\,\Psi^n\left\{\{y^i(x_{M_r}^r)\}\right\} + [T_R^r]\{\boldsymbol{Z}_{M_r}^r(x_{M_r+1}^r)\}\\ \Updownarrow\\ &[U_R^r] = [\boldsymbol{Y}_{M_r}^{r*}(x_{M_r+1}^r)]\,\Psi^n\left\{\{y^i(x_{M_r}^r)\}\right\} + \{\boldsymbol{Z}_{M_r}^{r*}(x_{M_r+1}^r)\}\end{aligned} \tag{2.50}$$

where

$$\begin{aligned}[\boldsymbol{Y}_{M_r}^{r*}(x_{M_r+1}^r)] &= [T_R^r]\,[\boldsymbol{Y}_{M_r}^r(x_{M_r+1}^r)]\\ \{\boldsymbol{Z}_{M_r}^{r*}(x_{M_r+1}^r)\} &= [T_R^r]\{\boldsymbol{Z}_{M_r}^r(x_{M_r+1}^r)\}\end{aligned} \tag{2.51}$$

In partitioned form Equation 2.50 can be written as:

$$\Psi^n \begin{Bmatrix} \{u_1^i(x^r_{M_r+1})\} \\ \{u_2^i(x^r_{M_r+1})\} \end{Bmatrix} = \begin{bmatrix} \left[Y^r_{11M_r}(x^r_{M_r+1})\right] & \cdots & \left[Y^r_{1nM_r}(x^r_{M_r+1})\right] \\ \vdots & & \\ \left[Y^r_{n1M_r}(x^r_{M_r+1})\right] & \cdots & \left[Y^r_{nnM_r}(x^r_{M_r+1})\right] \end{bmatrix} \Psi^n \begin{Bmatrix} \{y_1^i(x_{M_r})\} \\ \{y_2^i(x_{M_r})\} \end{Bmatrix} + X^{2*n}\left\{\{Z^r_{iM_r}(x^r_{M_r+1})\}\right\} \tag{2.52}$$

where the (m/2) $*$ $n_{bc\_sp\_R}$ matrices $\Psi^{n_{bc\_sp\_R}}\{\{u_2^i(x^r_{M_r+1})\}\}$ contain the (m/2) $*$ $n_{bc\_sp\_R}$ boundary conditions specified at $x = x_{M_r+1}$. This procedure is performed for each region r.

Formulation and solution of a set of linear algebraic equations containing the unknown variables:

The continuity requirements specified at the junctions between the sub-segments within each region r, i.e. Equations 2.43, together with the continuity and boundary conditions specified at the joint ends and at the junctions between the regions, i.e. Equations 2.49 and 2.52, constitute a set of linear algebraic equations. All the unknown variables at the joint ends, and at the junctions between the segments are determined by solution of the complete set of linear algebraic equations.

Solution of the Bonded Joint Problems

The number of equations and unknown variables for all the bonded joint configurations are shown in Appendix A, Section A.9.

When the set of linear algebraic equations is solved for a particular joint problem all the unknown variables at the outer boundaries and the segment region junctions are known. The fundamental variables can then be determined from Equation 2.39 at any value of x, at which solutions $\left[Y^r_j(x^r)\right]$ and $\{Z^r_j(x^r)\}$ are stored during the integration of the initial value problems defined in Equations 2.40 and Equations 2.41.

The direct integration of the initial value problems defined by Equations 2.40 and Equations 2.41 is performed by an ***embedded*** Runge-Kutta ***method,*** with adaptive step size control based on a prescribed accuracy, Press et al. (1992).

The set of linear algebraic equations derived for the different bonded joint configurations (shown in Appendix A, Section A.9), are all band diagonal equation systems. Only the components in the diagonal are therefore stored, and the systems are solved by LU-factorisation.

When the unknown (m, 1) matrices $\{y^i(x^r)\}$ for the adherends i are determined in the regions r for the adherends modelled as plates in cylindrical bending, the remaining variables, according to Equation 2.31:

$$\left\{y^i_{res}\right\} = \left\{N^i_{yy}, M^i_{yy}, M^i_{xy}, Q^i_y\right\} \quad \mathbf{i} = 1,2,3 \tag{2.53}$$

are determined from the constitutive relations in Equations 2.9 and the equilibrium equations. The quantities given in Equation 2.53 can be seen as stress and moment resultants necessary to keep the structure in cylindrical bending as mentioned previously.

Finally the adhesive layer stresses

$$\{\tau_{ax}, \tau_{ay}, \sigma_a\} \tag{2.54}$$

are determined by use of Equation 2.14.

This completes the description of the structural modelling for the adhesive bonded joint configurations and the adopted general solution procedure.

2.3 Examples and Discussion

To show the applicability of the developed linear solution procedures several examples will be presented, and the effect of varying different important parameters will be investigated.

Examples of all the bonded joint configurations will be presented in the following. Firstly examples of all the joint configurations with one adhesive layer are presented and compared, i.e. (see Figures 2.1-2.3, 2.5 and 2.6)

- Single lap joint with straight and scarfed adherends in the overlap zone (see Figure 2.1 and 2.2);
- Bonded doubler joint (see Figure 2.3);
- Single sided stepped lap joint (see Figure 2.5);
- Single sided scarfed lap joint (see Figure 2.6);

and secondly examples of all the joint configurations with two adhesive layers are presented and compared, i.e. (see Figure 2.4, 2.7 and 2.8)

- Double lap joint;
- Double sided stepped lap joint;
- Double sided scarfed lap joint.

The adherends used in the examples are all chosen to be laminates, and the lay-ups are made such that asymmetric laminates, and thereby coupling effects, appear in all the examples presented. This is chosen to show the capabilities of the approach, i.e. the modelling of the adherends as plates in cylindrical bending including coupling effects.

The basic adherend and adhesive properties assumed in the examples are shown in Table 2.1.

Plies	graphite/epoxy E_1 = 164.0 GPa, $E_2 = E_3 = 8.3$ GPa, $G_{12} = G_{31} = G_{23}$ = 2.1 GPa, $\nu_{12} = \nu_{13} = \nu_{23}$ = 0.34, t = 0.125 mm
Adhesive	epoxy AY103 (Ciba Geigy), E_a = 2800 MPa, ν_a = 0.4

Table 2.1: Specification ***of*** plies and adhesive material properties ***used for all*** the joint examples.

The adhesive used, AY103 from Ciba-Geigy, is a two-component plasticized epoxy, which is considered to be a general structural adhesive forming strong semi flexible bonds.

The lay-up of the adherends, the dimensions as well as the boundary conditions for the joints with two adherends and one adhesive layer (see Figures 2.1-2.3, 2.5 and 2.6), used in the examples, are shown in Table 2.2.

Laminate 1	graphite/epoxy $[0°, 30°, 60°]_4$, $t_1 = 1.5$ mm
Laminate 2	graphite/epoxy $[60°, 30°, 0°]_4$, $t_2 = 1.5$ mm
Lengths	$L_1 = L_2 =$ ***30.0*** mm, $\boldsymbol{L} =$ ***20.0*** mm
Adhesive	$t_a = 0.05$ mm
Modelling	Wide plates in cylindrical bending.
Load & B.C.	x = $-L_1$: $u_0^1 = w^1 = v_0^1 = M_{xx}^1 = \boldsymbol{0}$, $\boldsymbol{x = L + L_2}$: $w^2 = v_0^2 = M_{xx}^2 = \boldsymbol{0}$, $N_{xx}^2 =$ ***100*** N/mm Bonded doubler joint: $x = 0$: $u_0^1 = u_0^2 = w^1 = w^2 = v_0^1 = v_0^2 = M_{xx}^1 = M_{xx}^2 = 0$, $\boldsymbol{x = L + L_2}$: $w^1 = v_0^1 = M_{xx}^1 = \boldsymbol{0}$, $N_{xx}^1 = 100$ N/mm

Table 2.2: Laminate lay-ups, thicknesses, lengths and boundary conditions ***used for the*** joints with one adhesive layer and two adherends (see Figure 2.1-2.3, 2.5 and 2.6).

The overlap length is $\boldsymbol{L} = 20$ mm for all the joints considered, see Figures 2.1-2.3, 2.5 and 2.6 for reference, and the adherends are all modelled as plates in cylindrical bending. The difference between modelling of the adherends as beams or plates will be shown in the parametric studies, Section 2.3.9.

The lay-up of the adherend laminates is made such that the joints are symmetric seen from the adhesive layer midplane, and such that the plies facing the adhesive layers are 0" plies. The last statement is of course not fulfilled for the single sided scarfed lap joint. When joining of composite laminates is made through adhesive layers, the laminates should always be made such that the 0" plies are facing the adhesive layers in the longitudinal direction since these plies will transfer the load from the adhesive layers to the laminates (and vice versa) through the fibres instead of through the matrix material. Joing the two laminates (Table 2.2) together as a double sided stepped or double sided scarfed lap joint will not be appropiate, since it is not possible to fulfil the requirements that the 0° plies should be facing the adhesive layers in the longitudinal direction.

The joints are assumed to be simply supported at both ends, and, additionally, prevented from moving in the width direction, i.e. $v_0^i = 0$ for $(i = 1, 2)$ at $x = -L_1$ and $x = L + L_2$.

The lay-up of the adherends, the dimensions as well as the boundary conditions for the double lap joint (see Figure 2.4) used in the example, are shown in Table 2.3.

Laminate 1	graphite/epoxy $[[O", 30°, 60°]_4]_s$, $t_1 = 3$ mm;
Laminate 2	graphite/epoxy $[60°, 30°, 0°]_4$, $t_2 = 1.5$mm;
Laminate 3	graphite/epoxy $[0°, 30°, 60°]_4$, $t_1 = 1.5$ mm;
Lengths	$L_1 = L_2 =$ ***30.0*** mm, $\boldsymbol{L} =$ ***20.0*** mm;
Adhesive	$t_a = 0.0625$ mm;
Modelling	Wide plates in cylindrical bending.
Load & B.C.	$x = -L_1$: $u_0^1 = w^1 = v_0^1 = M_{xx}^1 = \boldsymbol{0}$, $N_{xx}^1 = 100$ N/mm; $\boldsymbol{x = L + L_2}$: $u_0^2 = u_0^3 = w^2 = w^3 = v_0^2 = v_0^3 = M_{xx}^2 M_{xx}^3 = \boldsymbol{0}$

Table 2.3: Laminate lay-ups, thicknesses, lengths and boundary conditions ***used*** for the double ***lap*** joints (see Figure 2.4).

Laminate 1 used for the double lap joint is symmetric. Laminates 2 and 3 are the same asymmetric laminates as used in the previous examples for the joints with one adhesive layer and two adherends. Thus, coupling effects are included in the analysis. The joint is symmetric about the

centerline of laminate 1, see Figure 2.4, and the stresses in the two adhesive layers will therefore be the same.

The laminates used for the double sided stepped and scarfed lap joints are shown in Table 2.4.

Laminate 1	graphite/epoxy $[[0°, 30°, 60°]_4]_s$, t_1 = 3 mm;
Laminate 2	graphite/epoxy $[[60°, 30°, 0°]_4, 0, [0°, 30°, 60°]_4]$, t_2 = 3.125 mm;
Lengths	$L_1 = L_2 =$ ***30.0*** mm, L = 20.0 mm;
Adhesive	t_a = ***0.0625*** mm;
Modelling	Wide plates in cylindrical bending.
Load & B.C.	$x = -L_1$: $u_0^1 = w^1 = v_0^1 = M_{xx}^1 = 0$, $x = L + L_2$: $w^2 = v_0^2 = M_{xx}^2 =$ ***0,*** $N_{xx}^2 =$ ***100*** N/mm;

Table 2.4: Laminate Jay-ups, thicknesses, lengths and boundary conditions ***used for the*** double sided stepped and scarfed *lap* joints (see Figure 2.7-2.8).

Laminate 1 used for the double sided stepped and scarfed lap joints is the same as laminate 1 used for the double lap joint example. Laminate 2 is obtained by joining laminate 2 and 3 used for the double lap joint around a 0° ply. This is done to compare the three joints. Double sided stepped or scarfed lap joints can be an alternative to a double lap joint, but are normaly more an alternative to for instance a single lap joint. The two laminates used for the examples of the double sided stepped and scarfed lap joints are both symmetric, but in the overlap zone, the sub-laminates of adherend 2 are asymmetric since plies have been removed, and coupling effects are thus included in the analysis, see Figures 2.7 and 2.8.

In the examples only in-plane normal loading has been applied, and the adhesive layer stresses are therefore normalized with respect to the prescribed load on the loaded edge, which is given by:

$$\sigma_{N_i} = N_i/t_i, \ (i = 1,2) \qquad (2.55)$$

where N_i is in-plane normal stress resultant applied.

The first results presented are the results obtained from the analysis of the single lap joint. In this example all the fundamental variables for the single lap joint problem are presented to show the output from the analysis, where the adherends are asymmetric and unbalanced laminates modelled as plates in cylindrical bending. For all the other joint configurations only selected results are presented.

It should be noted that no restrictions are imposed on the laminate lay-up of the adherends. The adherends can all be different, and in the same way no restrictions are imposed on the boundary conditions and the external loads, which can all be chosen arbitrarily.

After the presentation of the examples, and the comparison between the different joint configurations in terms of their performance characteristics, a parametric study is presented.

2.3.1 Single Lap Joint

The single lap joint configuration assumed in the example is shown in Figure 2.25.

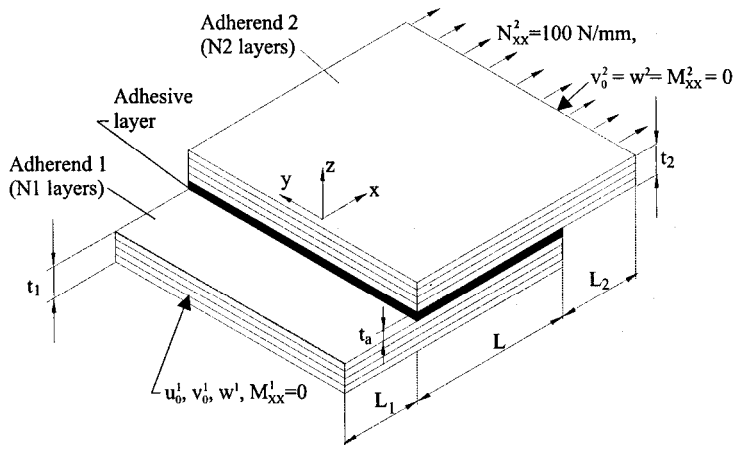

Figure 2.25: Single *lap* joint simply supported at ***both*** ends (clamped in ***the*** width direction), $t_1 = t_2 =$ **1.5** ***mm,*** $t_a =$ ***0.05 mm,*** $L_1 = L_2 =$ ***30 mm,*** $L =$ ***20 mm,*** $N^2_{xx} = 100\ N/\text{mm} \Leftrightarrow \sigma_N = 67\ MPa$.

The vertical and the width direction displacements **of** the adherends are shown in Figure 2.26 and 2.27 respectively.

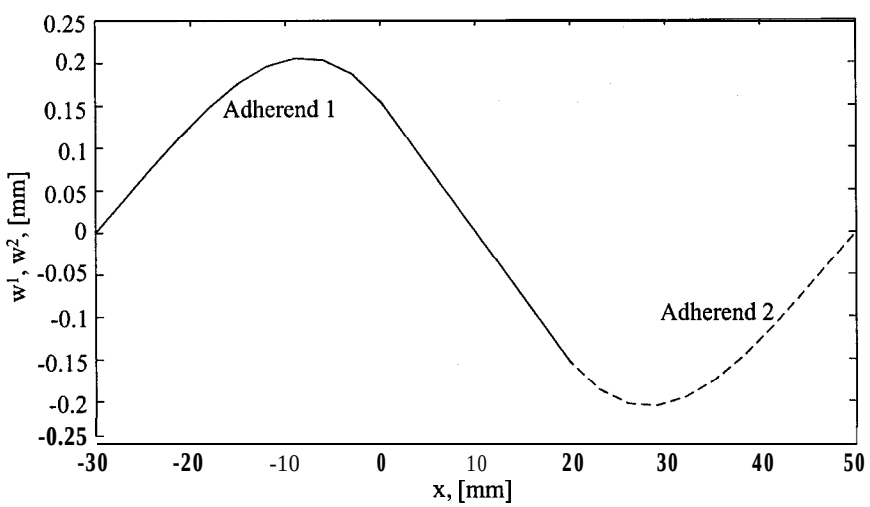

Figure 2.26: Vertical displacements w^1, w^2 ***of the*** adherends.

From Figure 2.26 it is seen that relatively large deflections occur due to the eccentricity in the load path, and that the joint rotates around the centre of the overlap zone, i.e. at $x = 10$ mm. As described previously the joint configuration is symmetric seen from the adhesive layer midplane, and this is the reason for the perfect skew-symmetric deflection pattern displayed.

The width direction displacements v^1_0 and v^2_0, shown in Figure 2.27, occur because of the coupling effects in the laminates. Comparison of the lateral deflections in Figure 2.26 and the width direction displacements in Figure 2.27 shows that the displacements in the width direction are

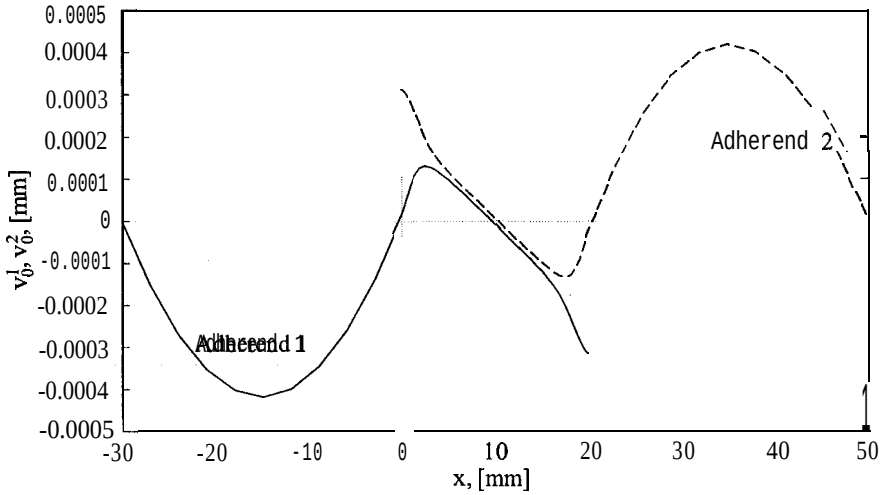

Figure 2.27: Width direction displacements v_0^1, v_0^2 ***of the*** adherends.

much smaller. It should be noticed that the concept of cylindrical bending adopted in the analysis impose restrictions on the displacements in the width direction. This can also be seen from Figure 2.32, which displays the in-plane normal stress resultants (N_{yy}) in the width direction.

The in-plane normal stress resultants in the longitudinal direction (x-direction) for the adherends are shown in Figure 2.28.

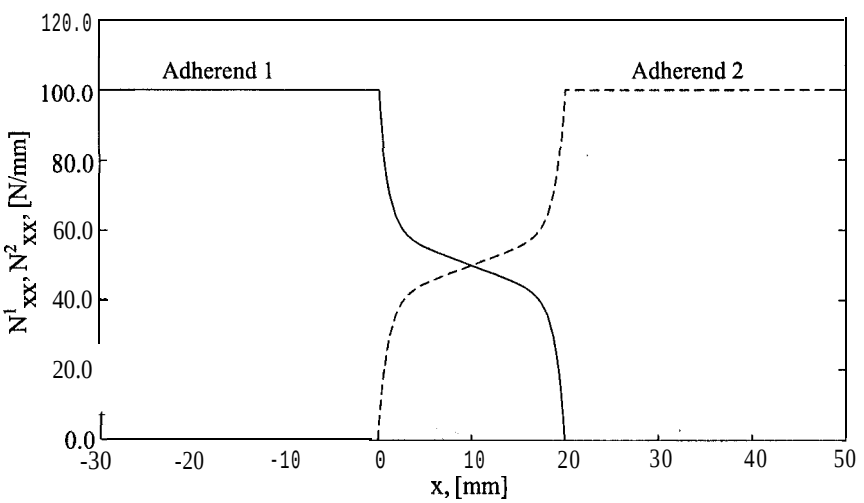

Figure 2.28: In-plane normal ***stress*** resultants N^1_{xx}, N^2_{xx} ***in the*** adherends in ***the*** longitudinal ***direction x.***

From Figure 2.28 it is observed that the in-plane normal stress resultants are constant outside the overlap zone, and that the load is transferred between the adherends through the adhesive layer in the overlap zone.

The in-plane shear stress resultants for the adherends are shown in Figure 2.29.

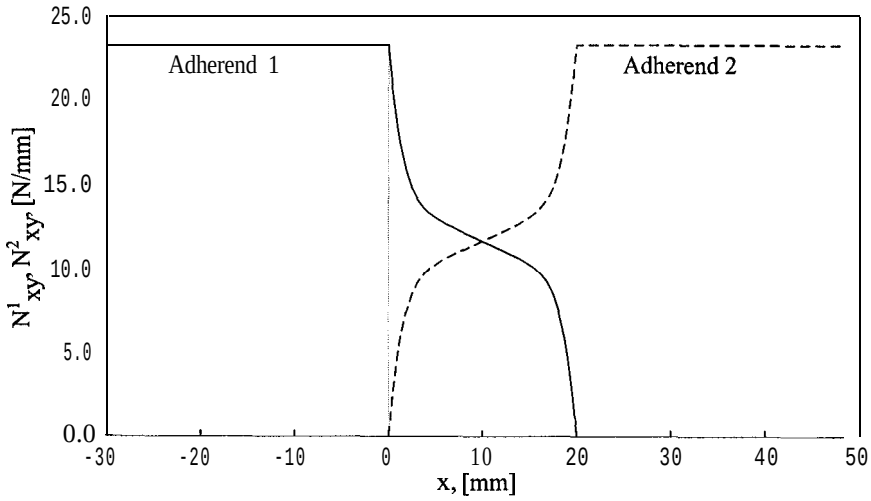

Figure 2.29: In-plane shear stress resultants N^1_{xy}, N^2_{xy} in *the* adherends.

Figure 2.29 shows a similar pattern of the in-plane shear stress resultants as for the in-plane normal stress resultants shown in Figure 2.28. The shear stress resultants occur since the adherends are asymmetric and unbalanced laminates, and since displacements and rotations are prevented in the width direction at the boundaries at both ends (see Figure 2.15). The peak values of the shear stress resultants are about 24% of the in-plane normal stress resultants applied to the bonded joint.

The bending moment resultants in the adherends in the longitudinal direction are shown in **Figure 2.30**

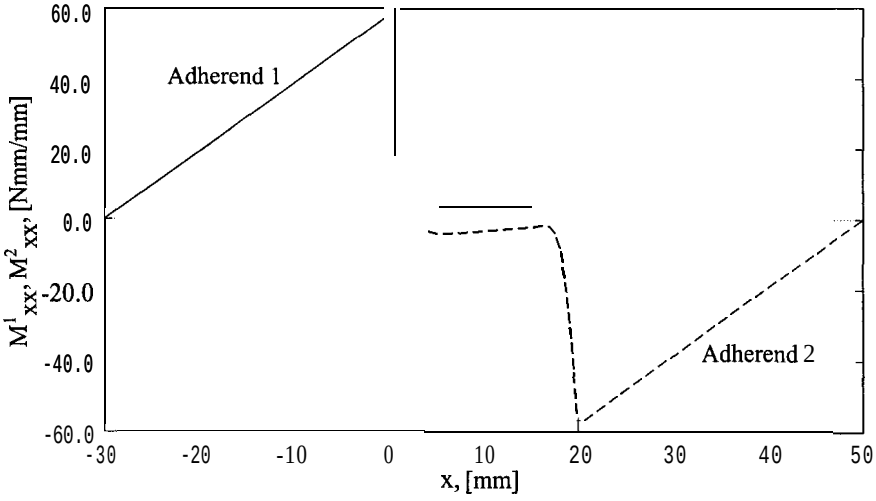

Figure 2.30: Bending moment stress resultants M^1_{xx}, M^2_{xx} *in* the adherends.

From 2.30 it is observed that the maximum bending moment resultants occur at the ends of the overlap. The large bending moment resultants occur due to the eccentricity of the load path.

Figure 2.31 shows the out-of-plane shear stress resultants.

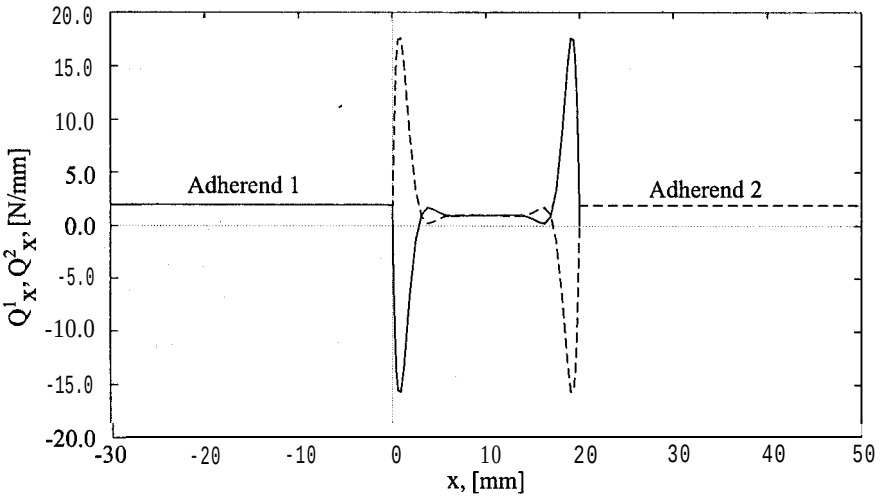

Figure 2.31: Out-of-plane shear stress resultants Q_x^1, Q_x^2 ***in the*** adherends.

It is observed from Figure 2.31 that highly localized shear stress resultants are present at the ends of the overlap zone, and this demonstrates the presence of strong local bending effects. The peak values of the out-of-plane shear stress resultants are about 17% of the in-plane normal stress resultants applied to the structure.

The results shown in Figures 2.26 - 2.31 are the fundamental variables determined through the analysis according to Equation 2.30. In addition the quantities shown in Figures 2.32 - 2.35 are determined, and they should be considered as the stress and moment resultants necessary to keep the bonded joint in a state of cylindrical bending.

The in-plane normal stress resultants for the adherends in the width direction (y-direction) are shown in Figure 2.32.

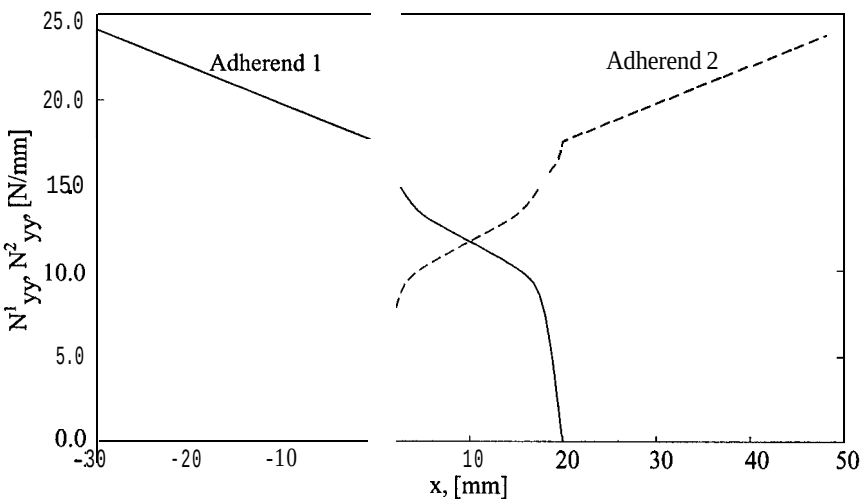

Figure 2.32: In-plane normal stress resultants N_{yy}^1, N_{yy}^2 ***in the adherends.***

The peak values of the in-plane normal stress resultants for the adherends in the width direction are 24% of the in-plane normal stress resultants (N_{xx}^i) applied to the structure. The peak values of N_{yy}^i are of about the same magnitude as the peak values of the shear stress resultants N_{xy}^i displayed in Figure 2.29.

The adherend bending moment resultants about the o-axis (M_{yy}) are shown in Figure 2.33.

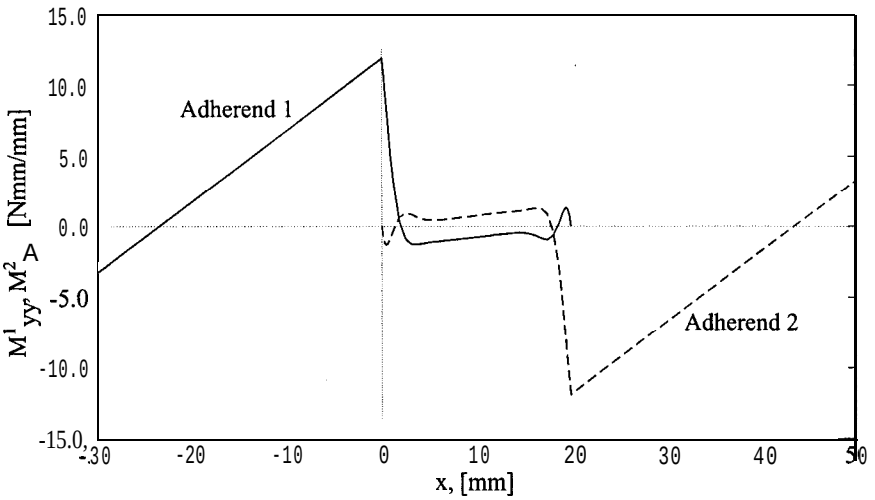

Figure 2.33: Bending moment stress resultants M_{yy}^1, M_{yy}^2 in the adherends.

By comparison of Figures 2.33 and 2.30, it seen that M_{yy} and M_{xx} display similar patterns. It is also observed that the peak values of M_{yy} are smaller than the peak values of M_{xx}, and that M_{yy} does not become equal to zero at the boundaries. The reason for this is that the adherend edges are supported uniformly in the entire width direction, i.e. $w(-L) = w(L_1 + L_2) = 0$, and the adherends are therefore prevented from rotating along the adherend edges.

The twisting moment resultants M_{xy} in the adherends are shown in Figure 2.34.

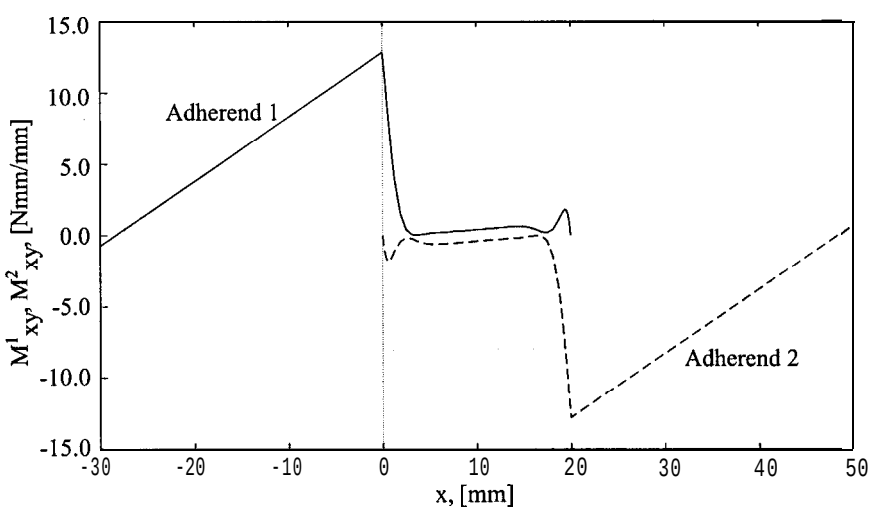

Figure 2.34: Twisting moment stress resultants M_{xy}^1, M_{xy}^2 in the adherends.

Comparison of M_{xy} shown in Figure 2.34, with the bending moment resultants M_{xx} and M_{yy}, shown in Figures 2.30 and 2.33, shows a similar pattern, and it is further observed that the peak values of M_{xy} are about the same size as the peak values of M_{yy} .

Figure 2.35 shows the out-of-plane shear stress resultants in the width direction (y-direction).

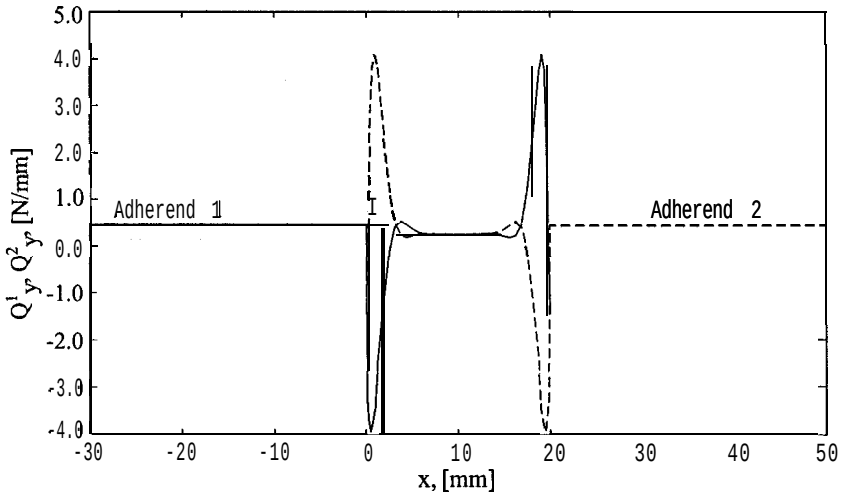

Figure 2.35: Out-of-plane shear stress resultants Q_y^1, Q_y^2.

The pattern of the out-of-plane shear stress resultants Q_y^1, Q_y^2 is the same as the pattern of the out-of-plane shear stress resultants in the longitudinal direction Q_x^1, Q_x^2, although the peak values of Q_y^1, Q_y^2 are only about about 25% of the peak values of Q_x^1, Q_x^2.

In Figure 2.36 the distributions of the normalized adhesive layer stresses are shown.

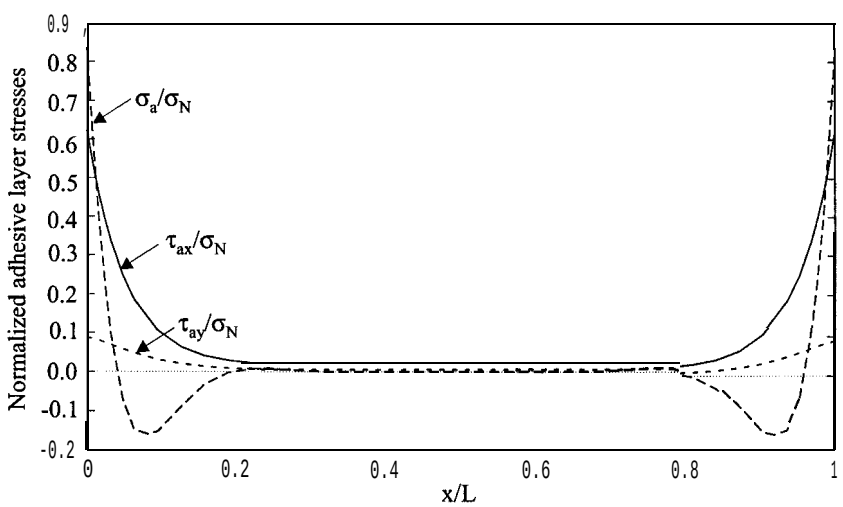

Figure 2.36: *Normalized* adhesive layer stresses, τ_{ax}/σ_N, τ_{ay}/σ_N, σ_a/σ_N.

From Figure 2.36 it is seen that the peek stresses are located at the ends of the overlap. As a consequence of the coupling effects in the laminates, it is seen that width direction shear

stresses (τ_{ay}) are non-zero (although of minor magnitude). Considering Figure 2.26 it is difficult to notice any differences between the deflections of the adherends, but from the adhesive layer stress distribution displayed in Figure 2.36, it is seen that significant transverse normal stresses do occur. These stresses are induced from differences in the lateral deflections of the adherends.

The results shown in Figures 2.32 - 2.35 as well as the width direction shear stresses (τ_{ay}) shown in Figure 2.36 will only appear if the analysis is carried out with the adherends modelled as plates in cylindrical bending. If the adherends of a bonded joint fulfil the assumptions for cylindrical bending, i.e. if the width of the bonded joint is considerable or if the movement of the sides of the bonded joint is subjected to restraints, the analysis should be carried out following this approach. The 'width direction' variables under such conditions are of considerable magnitude, as displayed in Figures 2.32 - 2.35, and they should not be ignored.

2.3.2 Single Lap Joint with Scarfed Adherends

The single lap joint configuration with scarfed adherends assumed in the example is shown in Figure 2.37.

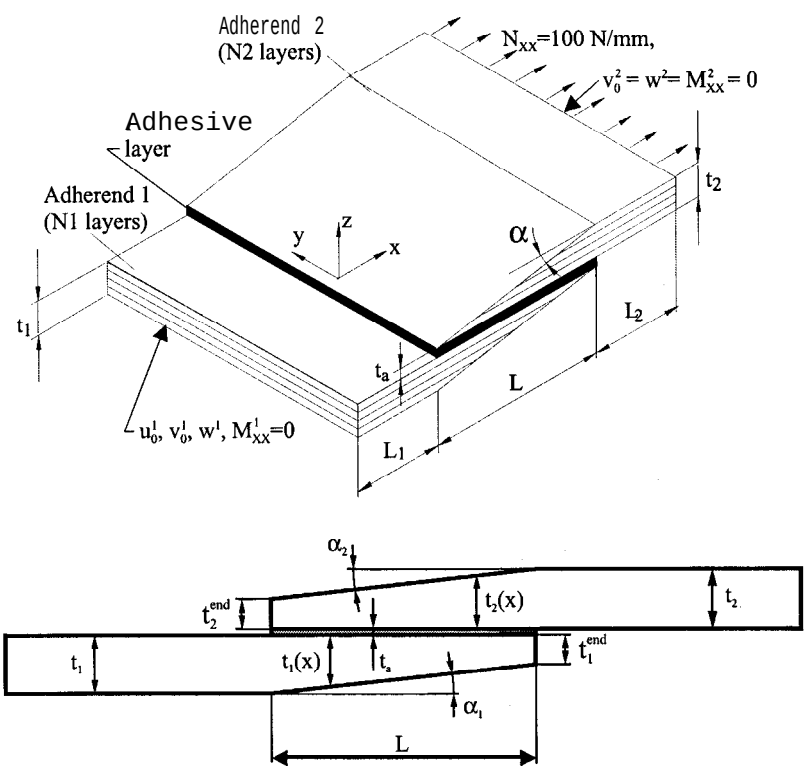

Figure 2.37: Single lap joint with scarfed ***adherends simply supported at both ends (clamped in the width direction),*** $t_1 = t_2 =$ ***1.5 mm,*** $t_1^{end} = t_1^{end} = 0.375$ ***mm,*** $t_a =$ ***0.05 mm,*** $\alpha_1 = \alpha_2 = \alpha = 3.22°$, $L_1 = L_2 =$ ***30 mm, L = 20 mm,*** $N = 100$ N/mm $\Leftrightarrow \sigma_N = 67$ MPa.

In this example the adherends are scarfed within the entire overlap zone, see Figure 2.37. The thickness of adherend 1 at the beginning of the overlap zone is t_1 = 1.5 mm with the laminate lay-up [0", $30°$, $60°]_4$. The adherend is then scarfed within the overlap zone with an scarf angle $\alpha_1 = \alpha_2$ = a = 3.22' to the end of adherend 1. At the end of adherend 1 the laminate the lay-up is [0", $30°$, $60°$] and the laminate thickness is t_1^{end} = 0.375 mm. Adherend 2 is scarfed in the same way.

By scarfing the adherends in the overlap zone the bending stiffness of the adherends towards the ends of the overlap is reduced, and the joint flexibility is increased. However, comparison of the fundamental variables obtained for the single lap joints with scarfed and straight adherends do not display any appreciable differences. The only comparison displaying interesting differences is for the adhesive layer stresses. The normalized adhesive layer stresses for the single lap joint with scarfed adherends are shown in Figure 2.38.

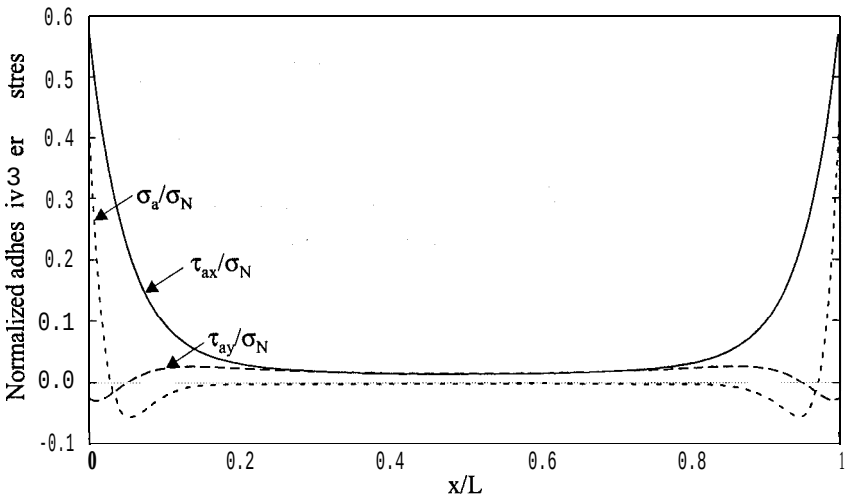

Figure 2.38: *Normalized* ***adhesive*** layer ***stresses,*** $\tau_{ax}/\sigma_N, \tau_{ay}/\sigma_N, \sigma_a/\sigma_N$.

Comparison of the adhesive layers stresses for the single lap joint with straight and scarfed adherends shown in Figure 2.36 and 2.38, shows that the peak transverse normal peak stress σ_a is reduced by about 45%, whereas the shear stresses in the longitudinal direction are almost unchanged. The shear stresses in the width direction are reduced with about 50%. Thus it is seen, that the scarfing of the single lap joint primarly provides a simple and efficient way to reduce the adhesive layer transverse normal stresses. If the scarf angle α is increased further, the adhesive layer transverse normal stresses will decrease even more.

2.3.3 Bonded Doubler Joint

The bonded doubler joint configuration assumed in the example is shown in Figure 2.39.

The vertical displacements of the adherends are shown in Figure 2.40.

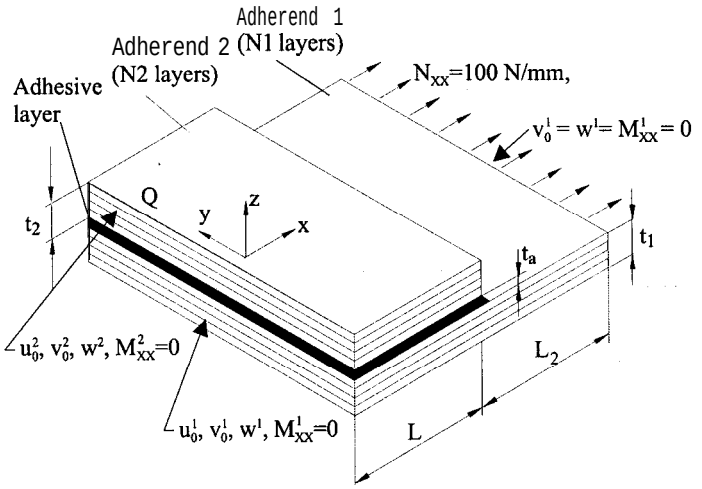

Figure 2.39: Bonded doubler joint simply supported at both ends (clamped in the width direction), $t_1 = t_2 = 1.5$ mm, $t_a = \mathbf{0.05\ mm}$, $L_2 = \mathbf{30}$ mm, $\mathbf{L = 20}$ mm, $N = 100$ N/mm $\Leftrightarrow \sigma_N = 67\ MPa$.

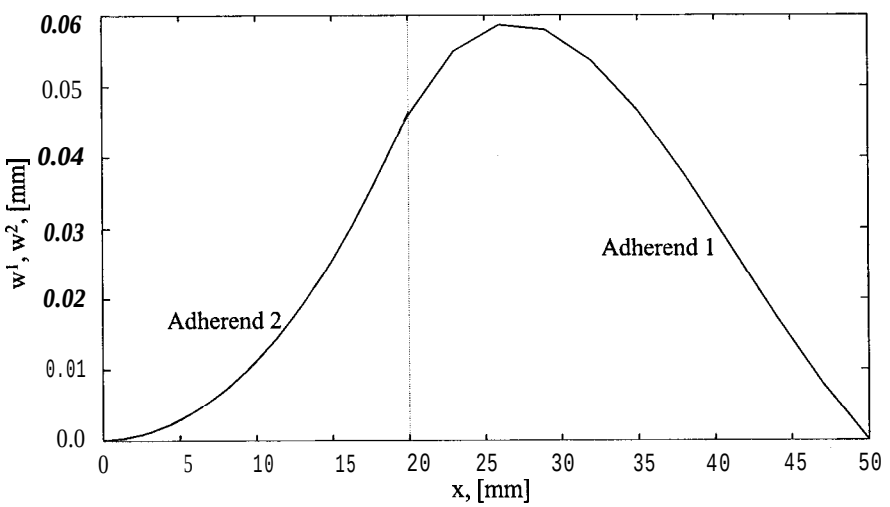

Figure 2.40: Vertical displacements w^1, w^2 ***of*** the adherends.

By comparison with the vertical displacements for the single lap joint, Figure 2.26, it is seen that the displacements are much smaller. The reasons for this are of course that the length of adherend 2 is reduced, and that adherend 1 is not free to move at the left end of the overlap zone (it is simply supported).

The bending moment resultants in the adherends in the longitudinal direction are shown in Figure 2.41.

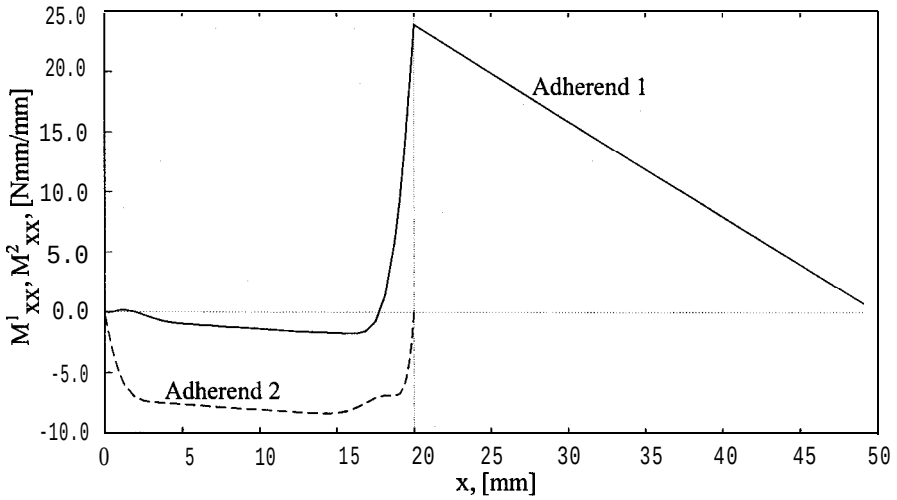

Figure 2.41: Bending moment stress resultants M_{xx}^{1}, M_{xx}^{2} in ***the*** adherends.

The maximum bending moments in adherend 1 occur at the right end of the overlap zone.

The normalized adhesive layer stresses for the bonded doubler joint are shown in Figure 2.42.

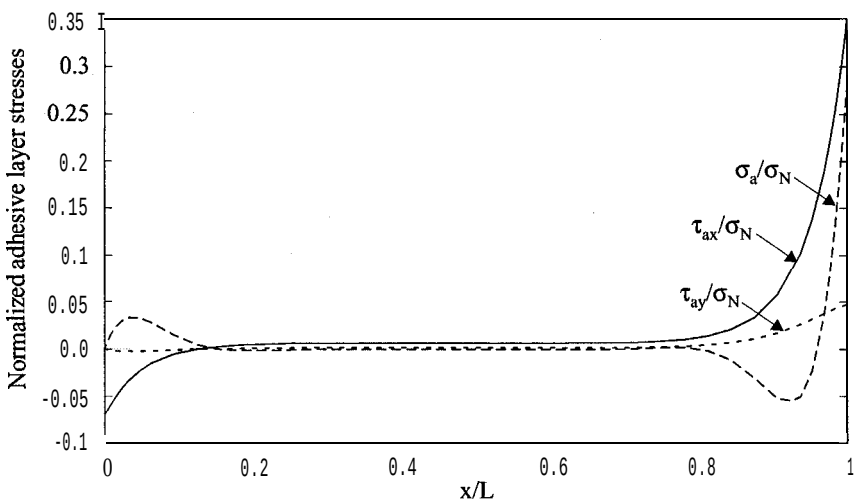

Figure 2.42: *Normalized* adhesive *layer* stresses, τ_{ax}/σ_N, τ_{ay}/σ_N, σ_a/σ_N.

The adhesive layer stresses for the bonded doubler joint are of course much lower than for the single lap joint with straight adherends, again due to the changed length of adherend 2 and the imposed boundary conditions.

2.3.4 Single Sided Stepped Lap Joint

In the assumed example the joint is made with three steps within the overlap zone, and three plies are dropped within each step. The laminate lay-up for adherend 1 is $[0°, 30°, 60°]_4$ with a thickness t_1 = 1.5 mm. The laminate lay-up for adherends 2 is $[60°, 30°, 0°]_4$ and t_2 = 1.5

mm. At each step a ply sequence $[0°, 30°, 60°]$ is dropped, thus reducing the thickness with $t_{1drop} = 0.375$ mm. Similarly a ply sequence [60°, 30°, 0"] is dropped at each step of adherend 2 and consequently t_{2drop} = 0.375 mm. In this way 0" plies are facing the adhesive layer in the entire overlap zone for both adherends. The overlap length is ***L*** = 20 mm as for the other examples, however, in the gaps d between each step, see Figure 2.43, the adhesive is not assumed to carry any load. Therefore the actual bond line which transfers the load is reduced to 18 mm, since ***d = 1*** mm.

The single sided stepped lap joint configuration used in the example is shown in Figures 2.43.

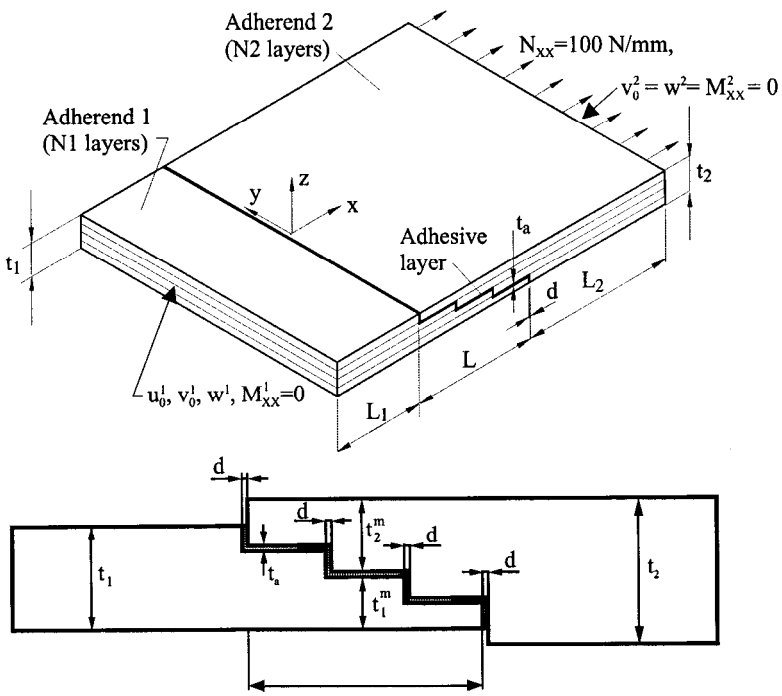

Figure 2.43: ***Single*** sided stepped ***lap*** joint ***simply*** supported in both ***ends*** (clamped ***in*** the width direction), $t_1 = t_2 = 1.5$ ***mm,*** $t_a = 0.05$ mm, $L_1 = L_2 = 30$ ***mm, L = 20 mm, d = 1.0*** mm, N = 100 ***N/mm*** $\Leftrightarrow \sigma_N$ = 67 MPa.

The vertical displacements of the adherends are shown in Figure 2.44.

Comparison between Figure 2.44 and Figure 2.26 shows, that by joining the two laminates together as a single sided stepped lap joint instead of as a single lap joint, the lateral deflections are reduced by about 85%. This is owing to the reduced eccentricity in the load path.

The bending moment resultants M_{xx} in the adherends are shown in Figure 2.45.

From 2.45 it is again observed that the maximum bending moments occur at the ends of the overlap. Compared with the bending moment resultants induced in the single lap joint shown in Figure 2.30, however, the maximum bending moments are reduced by about 60%.

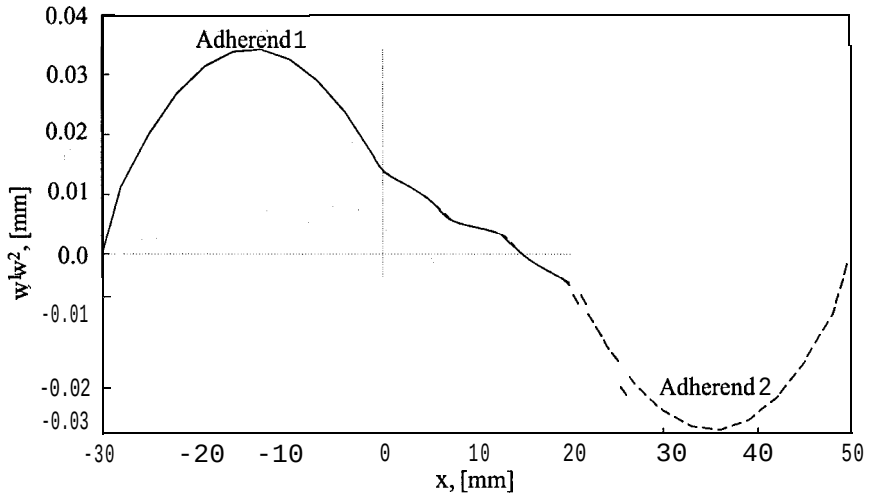

Figure 2.44: Vertical displacements w^1, w^2 ***of*** the adherends.

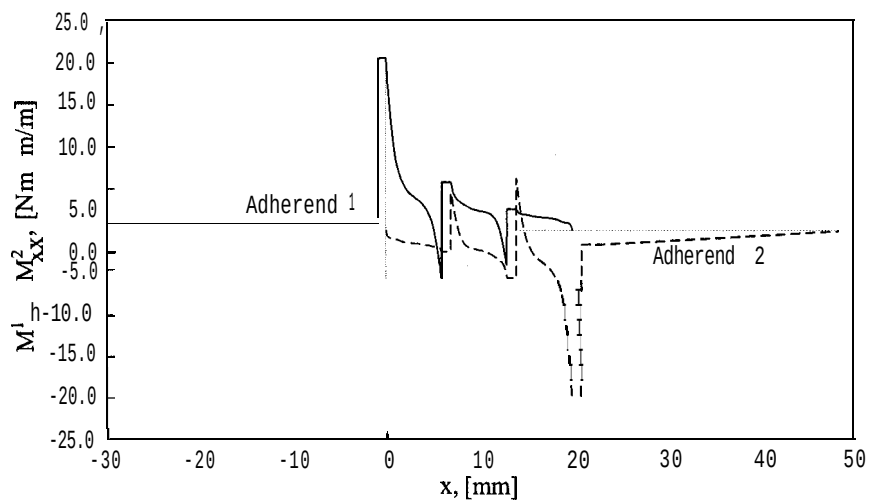

Figure 2.45: Bending moment stress resultants M^1_{xx}, M^2_{xx} in ***the*** adherends.

The normalized adhesive layer stresses for the single sided stepped lap joint are shown in Figure 2.46.

From Figure 2.46 it is seen that the adhesive layer stresses have peak values at the ends of each step, and that the maximum adhesive layer stresses occur at the ends of the overlap zone. Compared with the adhesive layer stresses for the single lap joint (Figure 2.36), however, the maximum adhesive layer shear stresses τ_{ax} have been reduced by about 35% and the maximum transverse normal stresses σ_a have been reduced by about 65%. Assuming that the structural performance (in terms of strength) is determined by the adhesive layer stresses (which is not always the case), it has thus been demonstrated, that the structural performance is strongly increased by the joining of two adherends through a stepped lap joint rather than through a single lap joint.

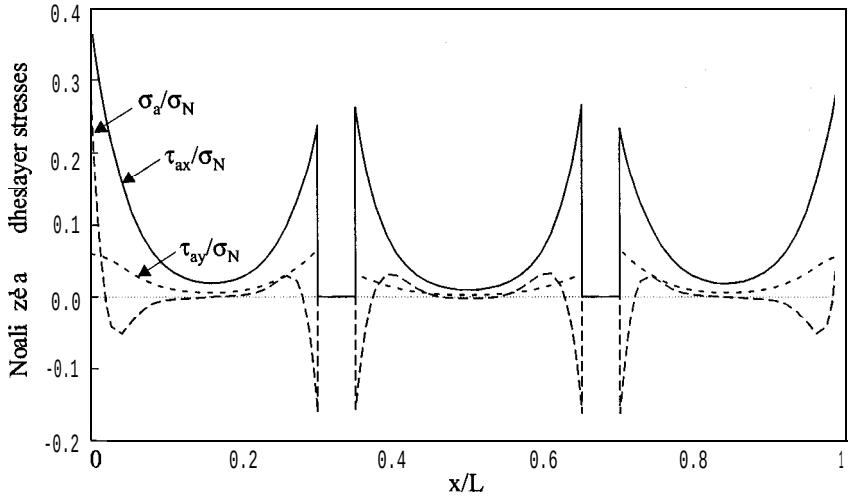

Figure 2.46: *Normalized* adhesive layer stresses, τ_{ax}/σ_N, τ_{ay}/σ_N, σ_a/σ_N.

2.3.5 Single Sided Scarfed Lap Joint

The single sided scarfed lap joint configuration assumed in the example is shown in Figure 2.47.

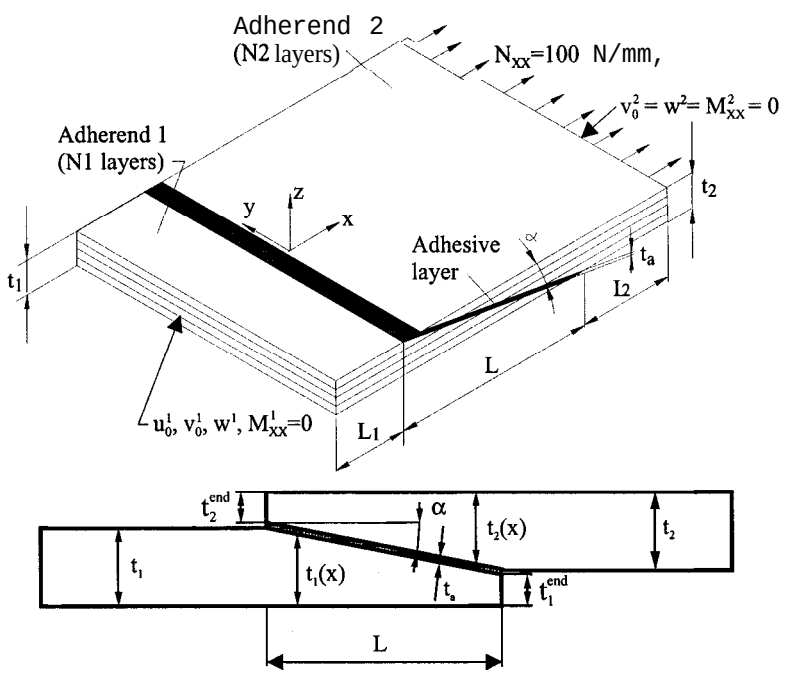

Figure 2.47: Single sided scarfed lap joint simply supported at both ends (clamped in the width direction), $t_1 = t_2 = 1.5$ mm, $t_1^{end} = t_2^{end} = 0.0$ mm, $t_a = 0.05$ mm, $\alpha = 4.33°$, L_1 = L_2 = 30 mm, L = 20 mm, N = 100 N/mm $\Leftrightarrow$ σ_N = 67 MPa.

In this example the adherends are scarfed within the overlap zone with an angle $\alpha = 4.33°$, see Figure 2.47.

The vertical displacements of the adherends are shown in Figure 2.48.

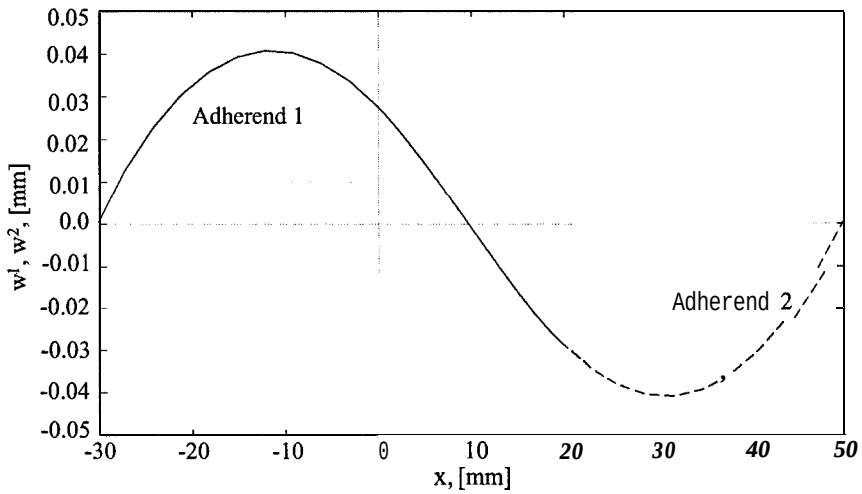

Figure 2.48: Vertical displacements w^1, w^2 of the adherends.

Compared with the vertical displacements for the single lap joint (Figure 2.26) the maximum displacements have been reduced by about 90%. The adherend bending moment resultants M_{xx} are shown in Figure 2.49, and are reduced by about the same amount.

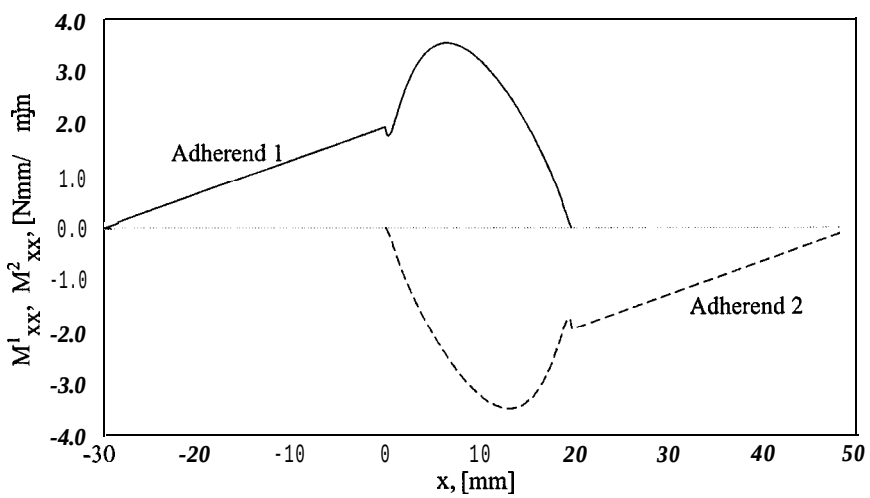

Figure 2.49: Bending moment stress resultants M^1_{xx}, M^2_{xx} in the adherends.

The normalized adhesive layer stresses for the single sided scarfed lap joint are shown in Figure 2.50.

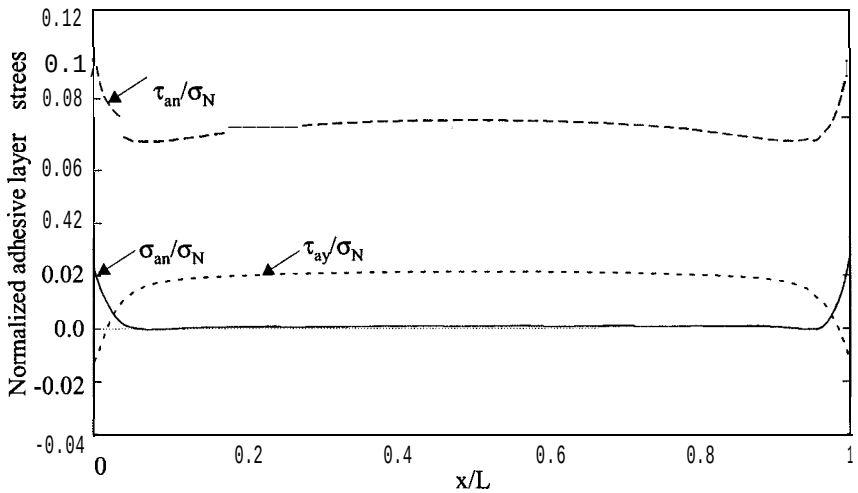

Figure 2.50: *Normalized* ***adhesive*** layer stresses, τ_{an}/σ_N, τ_{ay}/σ_N, σ_{an}/σ_N.

Joining the adherends through a single sided scarfed lap joint instead of through a single lap joint (Figure 2.36) reduces the maximum adhesive layer shear stresses by about 83% and the maximum adhesive layer peeling stresses with approximately 97%. Thus, if two adherends should be jointed together using only one adhesive layer the most effective joint configuration is the single sided scarfed lap joint as expected.

Comparison of the results obtained for the single sided stepped lap joint, Figure 2.48-2.50, and the single sided scarfed lap joint it is seen that the scarfed joint is superior to the stepped joint. If the number of steps in the stepped lap joint is increased, however, the performance will be improved considerably (the stress peaks will be reduced). For the limiting case where the number of steps approach infinity, the solution for the single sided stepped lap joint will converge to the solution for the single sided scarfed lap joint.

2.3.6 Double Lap Joint

The previous examples have all considered the joining of two adherends through one adhesive layer. If three adherends are to be bonded a double lap joint configuration appears.

The double lap joint configuration assumed in the example is shown in Figure 2.51.

The vertical displacements of the adherends are shown in Figure 2.52.

As described previously the joint is symmetric about the midplane of adherend 1, which results in the displayed symmetric deflection pattern. The deflection pattern in Figure 2.52 shows that adherend 2 and 3 tries to peel off adherend 1 at the beginning of the overlap zone, i.e. at x = 0 mm, and that they bend toward each other at the right end of the overlap zone and in the region to the right of the overlap zone.

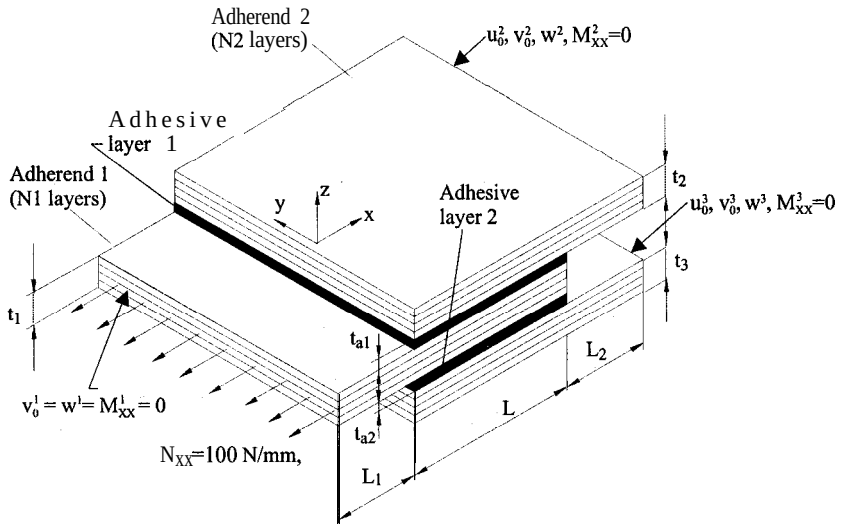

Figure 2.51: Double lap joint simply supported at both ends (clamped in the width direction), t_1 = ***3.0*** *mm*,$t_2 = t_3$ = 1.5 mm, $t_{a1} = t_{a2}$ = 0.0625 mm, $L_1 = L_2$ = ***30 mm, L = 20*** mm, N = 100 ***N/mm*** $\Leftrightarrow \sigma_N = 33$ *MPa*.

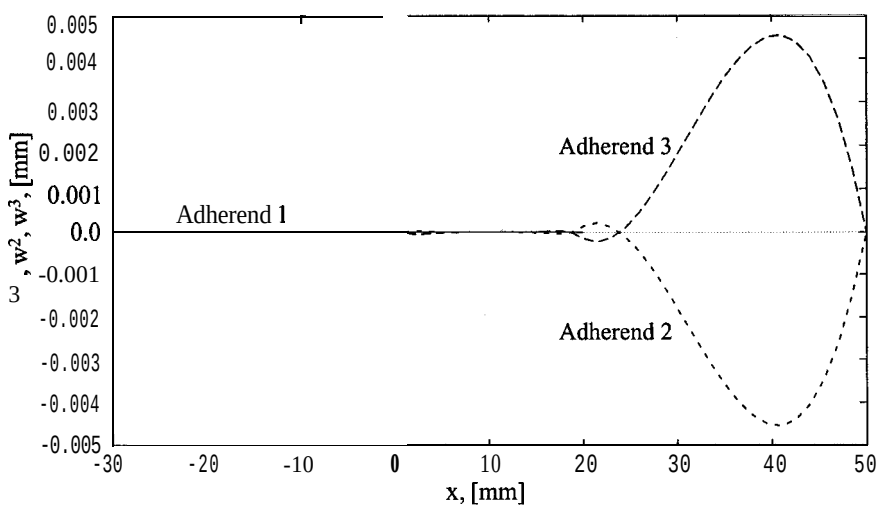

Figure 2.52: Vertical displacements w^1, w^2 ***of the*** adherends.

The adherend bending moment resultants M_{xx} are shown in Figure 2.53

From 2.53 it is observed that the maximum bending moments occur at the ends of the overlap as for all the other joints, and that no bending moment resultants occur in adherend 1, due to the symmetry.

The normalized adhesive layer stresses for the double lap joint are shown in Figure 2.54. Since the joint is symmetric about the midplane of adherend 1 the adhesive layer stresses in the two adhesive layers are identical.

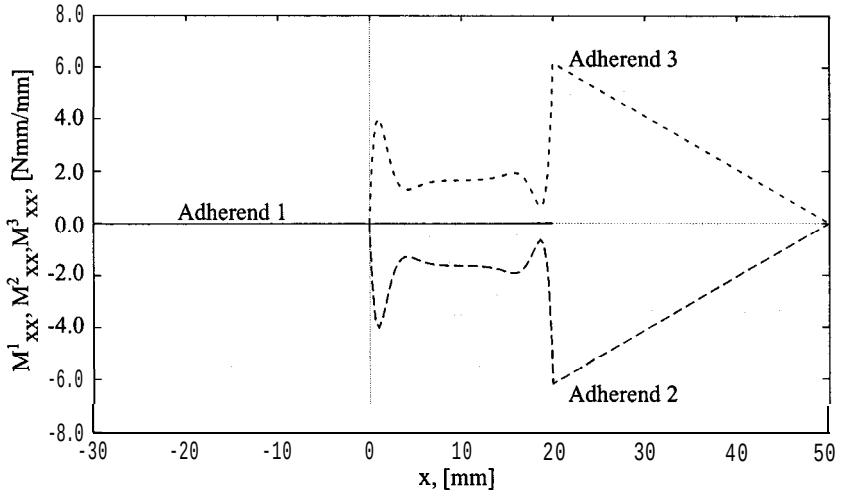

Figure 2.53: Bending moment stress resultants M^1_{xx}, M^2_{xx} in the adherends.

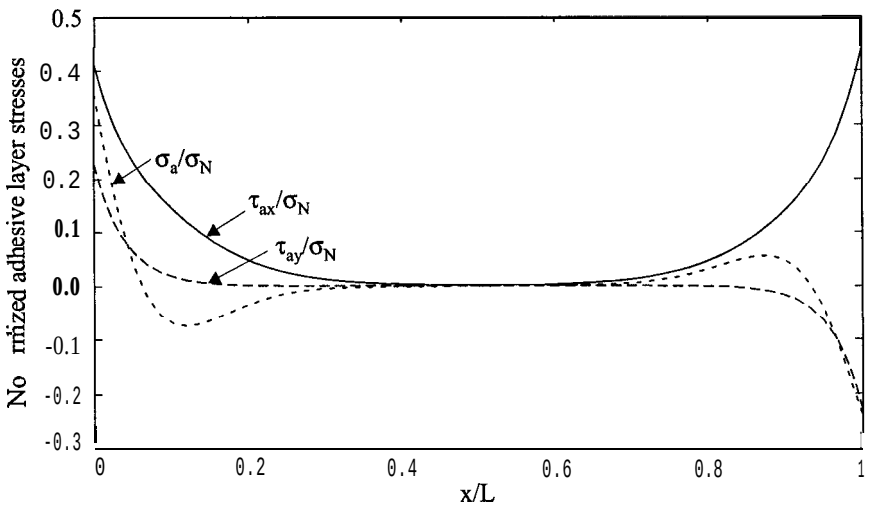

Figure 2.54: *Normalized* adhesive layer stresses, τ_{ax}/σ_N, τ_{ay}/σ_N, σ_a/σ_N.

From Figure 2.54 it is seen that the transverse normal stresses σ_a are tensile at the left end of the overlap zone, i.e. at x = 0 mm, and compressive at the right end of the overlap. This is in accordance with the deflection pattern displayed in Figure 2.52.

2.3.7 Double Sided Stepped Lap Joint

The double sided stepped lap joint is used to join two adherends together using two adhesive bond layers. However, joining of the two laminates used for the single lap joint example (Section 2.3.1) by use of a double sided stepped lap joint would not be desirable, since one of the bond lines would be located between plies with an angle different from zero.

The laminates used for the double sided stepped lap joint example is therefore chosen to have 0° plies facing the adhesive layers, as shown in Table 2.4. The double sided stepped lap joint in this

example have three steps within the overlap zone, and within each step three plies are dropped on each side of the midplane. The laminate lay-up for laminate 1 is $[[0°, 30°, 60°]_4]_s$ with a thickness t_1 = 3.0 mm. Within each step two ply sequences $[0°, 30°, 60°]$ and $[60°, 30°, 0"]$ are dropped above and below the laminate midplane, thus reducing the laminate thickness with t_{1drop} = 0.75 mm at each step. The laminate lay-up for laminate 2 is $[[0°, 30°, 60°]_4, 0°, [60°, 30°, 0°]_4]$ with a thickness t_1 = 3.125 mm. Within each step two sequences $[60°, 30°, 0"]$ and $[0°, 30°, 60°]$ are dropped above and below the midplane, and are thus reducing the thickness with t_{2drop} = 0.75 mm. This way 0" plies are facing the adhesive layers on both sides of the joint. The overlap length is L = 20 mm as for the other examples. In the gaps d between each step, see Figure 2.55, the adhesive is assumed not to carry any load, and therefore the actual bond line capable of transfering the load is reduced to 18 mm, since d = 1 mm. Laminate 1 is the same as assumed for the double lap joint example (Section 2.3.6), and laminate 2 is composed of the double lap joint example laminates 2 and 3 assembled around a 0" ply.

The double sided stepped lap joint configuration assumed in the example is shown in Figure 2.55.

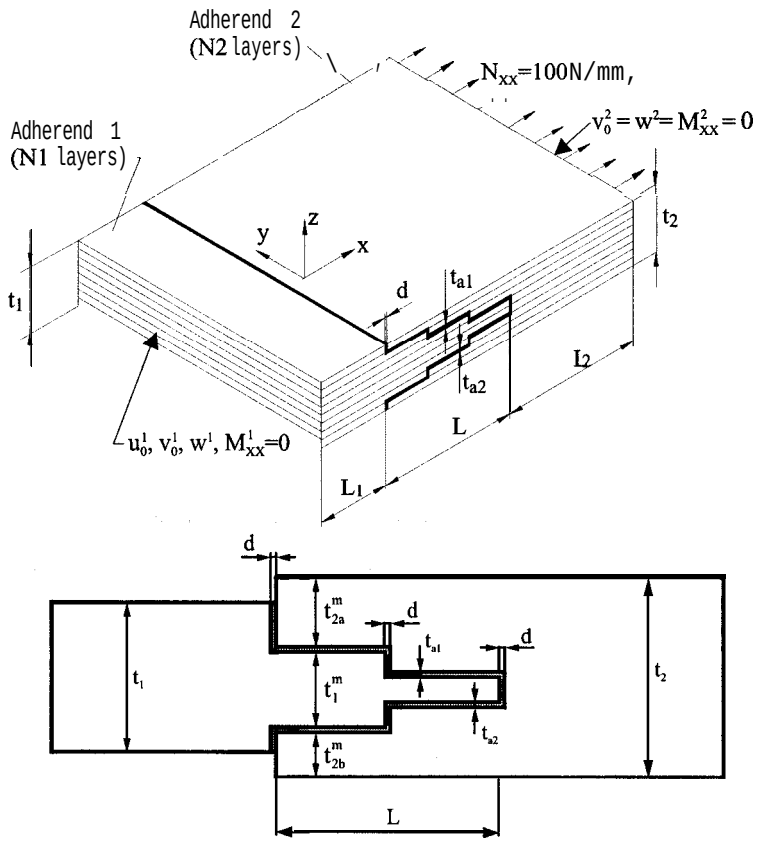

Figure 2.55: Double sided stepped lap joint simply supported at both ends (clamped in the width direction), t_1 = 3.0 mm, t_2 = 3.125 ***mm,*** $t_{a1} = t_{a2} = 0.0625$ mm, $L_1 = L_2 = 30$ mm, L = 20 ***mm,*** d = 1.0 mm, N = 100 N/mm $\Leftrightarrow \sigma_N = 33$ MPa.

The vertical displacements of the adherends are shown in Figure 2.56.

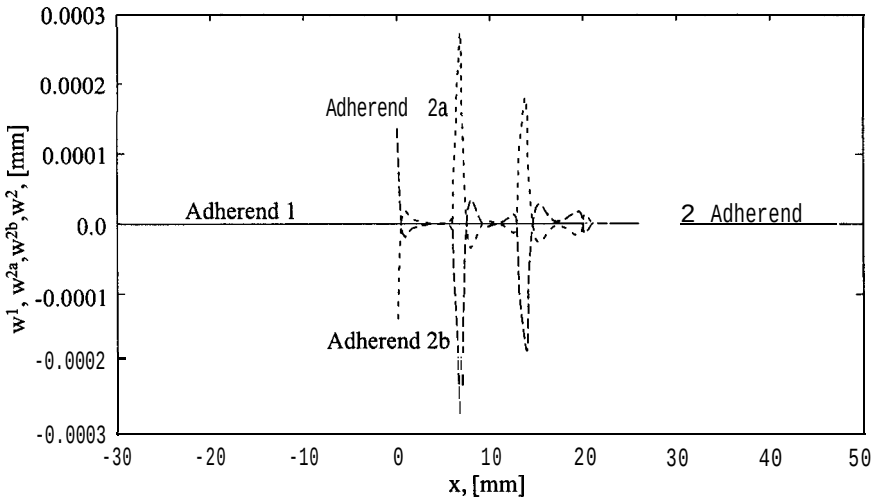

Figure 2.56: Vertical displacements w^1, w^2 *of the* adherends.

As described previously, the joint is symmetric about the midplane, which results in the symmetric lateral deflection pattern displayed in Figure 2.56.

The normalized adhesive layer stresses for the double sided stepped lap joint are shown in Figure 2.57. Since the joint is symmetric about the midplane the adhesive layer stresses in the two layers are identical.

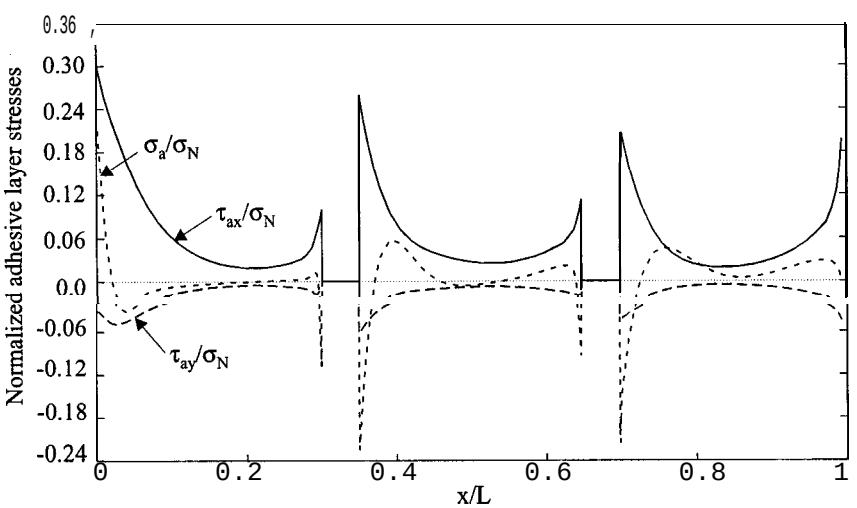

Figure 2.57: *Normalized* adhesive layer stresses, τ_{ax}/σ_N, τ_{ay} / σ_N, σ_a / σ_N.

As for the single sided stepped lap joint, the adhesive layer stresses increase towards the ends of each step, and the maximum adhesive layer stresses occur at the left end of the overlap zone. Compared with the double-lap joint the maximum adhesive layer shear stresses are reduced by approximately 25% and the maximum adhesive layer transverse normal stresses are reduced by about 40%. The peak adhesive stresses could be reduced even further by increasing the number of steps in the joint. In the limiting case where the number of steps approaches infinity, the double sided stepped lap joint will converge towards the double sided scarfed lap joint.

2.3.8 Double Sided Scarfed Lap Joint

The double sided scarfed lap joint configuration assumed in the example is shown in Figure 2.58.

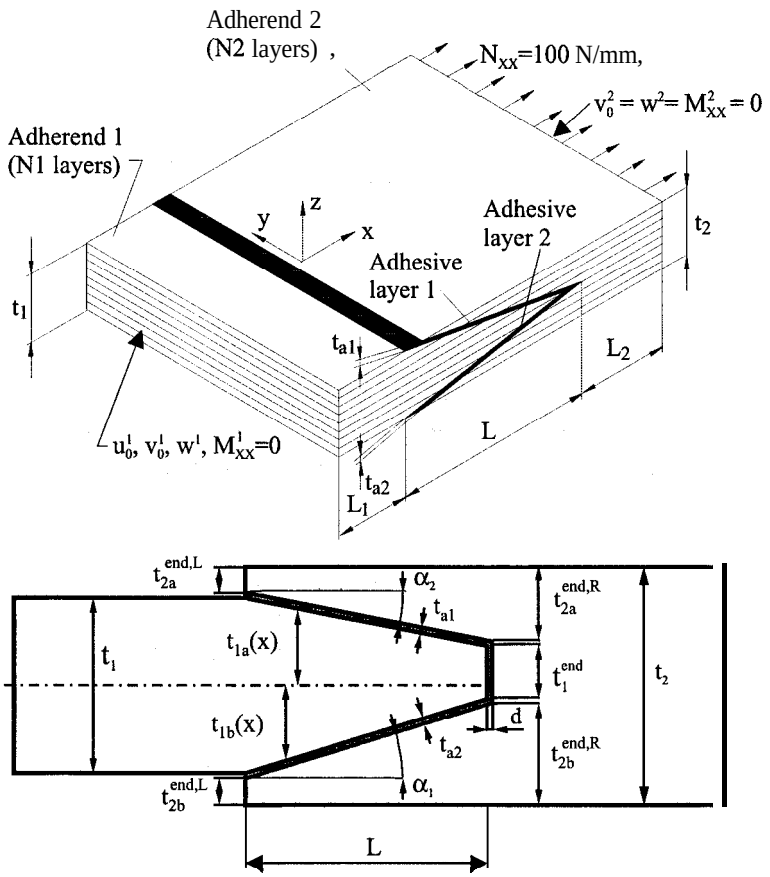

Figure 2.58: Double sided scarfed ***lap*** joint *simply* supported at both ends (clamped in the *width* direction), t_1 = 3.0 ***mm,*** t_2 = 3.125 mm, $t_1^{end,L} = t_2^{end,L} = 0.0$ mm, $t_1^{end,R} = t_2^{end,R} =$ ***3.0*** mm, t_1^{end} = ***0.0 mm,*** $t_{a1} = t_{a2} =$ ***0.0625 mm,*** $L_1 = L_2 =$ ***30 mm, L = 20 mm,*** α = 4.29°, N = 100 ***N/mm*** $\Leftrightarrow \sigma_N$ = 33 *MPa.*

The laminates assumed in this example are the same as for the double. sided stepped lap joint example (Section 2.3.7), and the adherends are scarfed within the overlap zone with the same scarf angle α on both sides of the centerline, i.e. $\alpha_1 = \alpha_2 = \alpha$ = 4.29'.

The vertical displacements of the adherends are shown in Figure 2.59.

Compared with the lateral deflection for the stepped lap joint (Figure 2.56) the maximum deflection is reduced by about 60%.

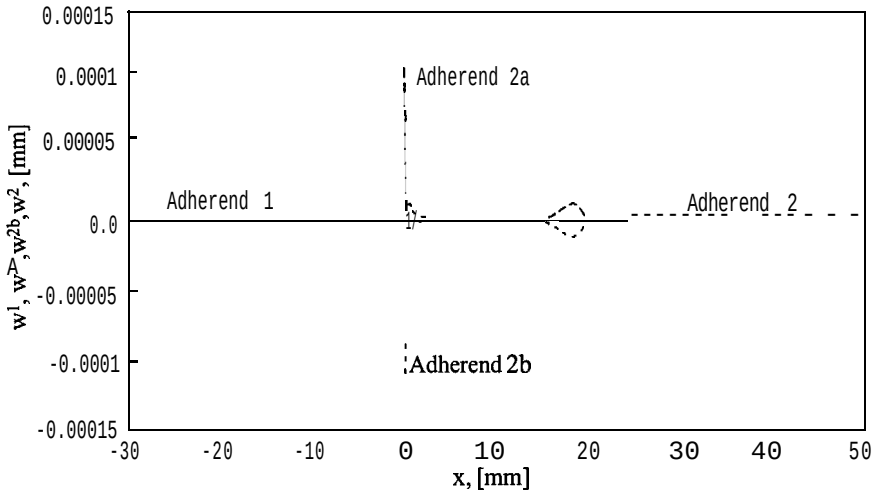

Figure 2.59: Vertical displacements w^1, w^2 *of* the adherends.

The normalized adhesive layer stresses are shown in Figure 2.60.

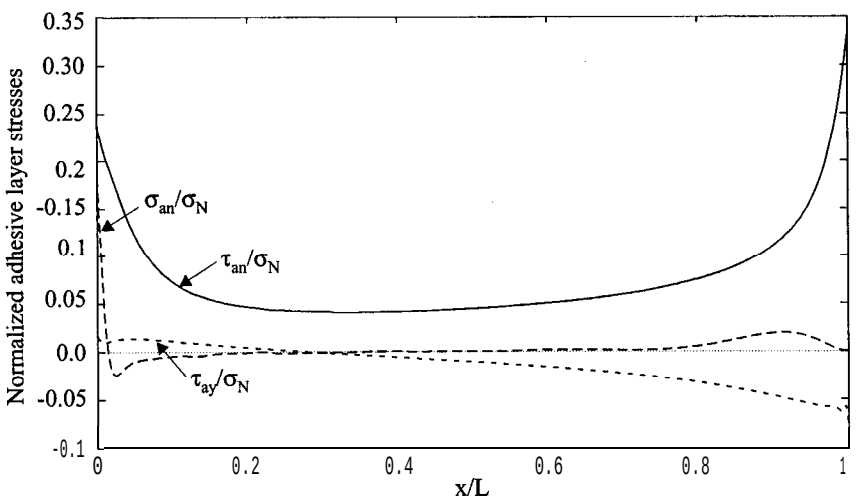

Figure 2.60: *Normalized* adhesive layer stresses, τ_{an}/σ_N, τ_{ay}/σ_N, σ_{an}/σ_N.

Compared with the adhesive layer stresses for the double lap joint shown in Figure 2.54, the maximum shear stresses are reduced by approximately 15%, and the maximum transverse normal stresses are reduced by 50%. Compared with the adhesive layer stresses for the double sided stepped lap joint shown in Figure 2.57 the maximum adhesive layer shear stresses are actually a bit higher, whereas the undesirable peeling stresses are lower.

2.3.9 Parametric Effects

For most of the bonded joint configurations presented in Section 2.1.2 several authors such as Hart-Smith (1973a) - Hart-Smith (1973c), Adams and Wake (1984) and Renton and Vinson

(1975b) have conducted parametric studies on the performances of these joints. However, in the analyses used in the quoted references, the adherends have been modelled as isotropic materials or symmetric laminates only including the extensional and bending stiffnesses. The classical characteristic parameters used for parametric studies of adhesive bonded joints are:

- The overlap length.
- The thickness of the adherends.
- The primary extensional and bending stiffnesses of the adherends.
- The thickness of the adhesive layer.
- The stiffness of the adhesive layer.

The influence of varying these parameters has been exposed in previous studies (e.g. the quoted references) of adhesive bonded joints. In the parametric studies presented in this thesis it is therefore considered important to investigate the influence of parameters, which have not been considered before. The characteristic parameters to be included in the parametric study are:

- The influences of coupling effects induced in asymmetric and unbalanced laminated adherends.
- The stacking sequence of the plies in the laminated adherends.
- The influence of modelling the adherends as plates in cylindrical bending contra wide beams.

The parametric studies will primarily be carried out for the adhesive bonded single lap joint configuration, since the parametric effects experienced for the other bonded joint configurations are similar. The effects of varying the selected parameters are less pronounced for advanced joint types, however.

The material properties for the adherends and the adhesive layers assumed for the purpose of the parametric studies are the same as assumed in the examples presented in Sections 2.3.1-2.3.8 and shown in Table 2.1.

The Influence of Coupling Effects Induced in Asymmetric and Unbalanced Laminated Adherends

The influence of coupling effects in the laminated adherends are investigated by using two laminates $[\alpha, 0°]$ $[0", \alpha]$ as adherend 1 and 2 respectively, where a $\in [0°, 45°]$. For α = 0" there is no coupling in the laminates, whereas for α = 45" strong coupling effects are induced in the laminates. To show the change of the structural response as a function of the increasing coupling effects the analysis has been performed for different values of the angle α. As a measure of the coupling effects in the laminates the following non-dimensional coupling parameter is adopted:

$$C_P = \frac{C_P^1 + C_P^2}{2}, \quad C_P^i = \left| \frac{(B_{11}^i + B_{22}^i)^2}{A_{11}^i D_{11}^i} \right|, \quad (i = 1, 2) \tag{2.56}$$

where A_{11}^i, B_{11}^i, B_{22}^i and D_{11}^i are the principal extensional, coupling and flexural stiffnesses for each of the laminates. The value of C_P^i is the same for both adherend laminates in this example.

Laminate 1	graphite/epoxy [0", $\alpha°$], t_1 = 0.25 mm, $\alpha \in [0°, 45°]$;
Laminate 2	graphite/epoxy [$0°$, $\alpha°$], t_2 = 0.25 mm, $\alpha \in [0°, 45°]$;
Lengths	$L_1 = L_2 = 30.0$ mm, $L = 20.0$ mm;
Adhesive	$t_a = 0.05$ mm;
Modelling	Wide plates in cylindrical bending.
Load & B.C.	$x = -L_1$: $u_0^1 = w^1 = v_0^1 = M_{xx}^1 = 0$, $x = L + L_2$: $w^2 = v_0^2 = M_{xx}^2 = 0$, $N_{xx}^2 = 100$ N/mm;

Table 2.5: Laminate lay-ups, thicknesses, lengths and boundary conditions used for investigation of coupling effects induced in the adherends of a single lap adhesive bonded joint.

The lay-up of the adherends, the dimensions and the boundary conditions for the bonded single lap joints assumed are shown in Table 2.5.

In the following, only the variables which display significant dependency of coupling effects are shown. The in-plane normal stress resultants N_{xx} and the bending moment resultants M_{xx} are virtually unaffected by the change of coupling parameters, and are therefore used as normalization parameters in the following.

In Figure 2.61 the maximum normalized vertical displacements as function of the coupling parameters C_P are shown.

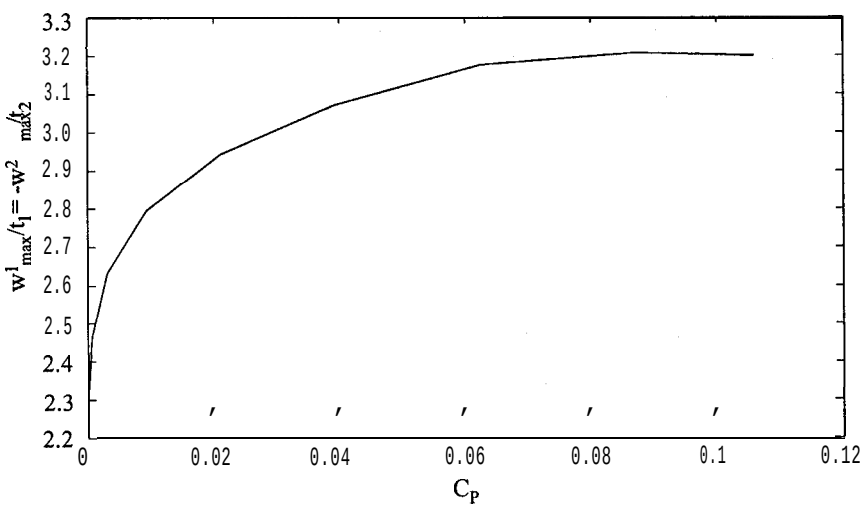

Figure 2.61: *Normalized* vertical displacements $w_{max}^1/t_1 = -w_{min}^2/t_2$ of the adherends as function of the coupling effects C_P.

From Figure 2.61 it is seen that vertical displacements are increased tremendously for small values of the coupling effects norm C_P, whereas the increase tends to smooth out for larger values of C_P.

Figure 2.62 displays the maximum adhesive layer stresses as a function of the coupling parameter C_P.

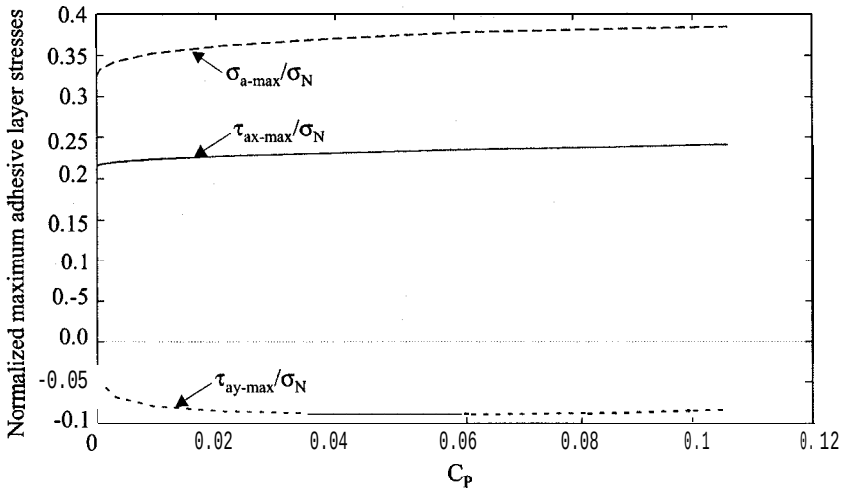

Figure 2.62: Maximum normalized adhesive layer stresses, τ_{ax-max}/σ_N, τ_{ay-max}/σ_N, σ_{a-max}/σ_N as function of the coupling effects C_P.

It is observed from Figure 2.62 that the adhesive layer stresses are only significantly affected by the coupling effects for small values of C_P.

Figure 2.63 displays the maximum normalized laminate shear stress resultants N^i_{xy-max}/N^i_{xx} and in-plane normal stress resultants N^i_{yy-max}/N^i_{xx} as a function of the coupling parameter C_P.

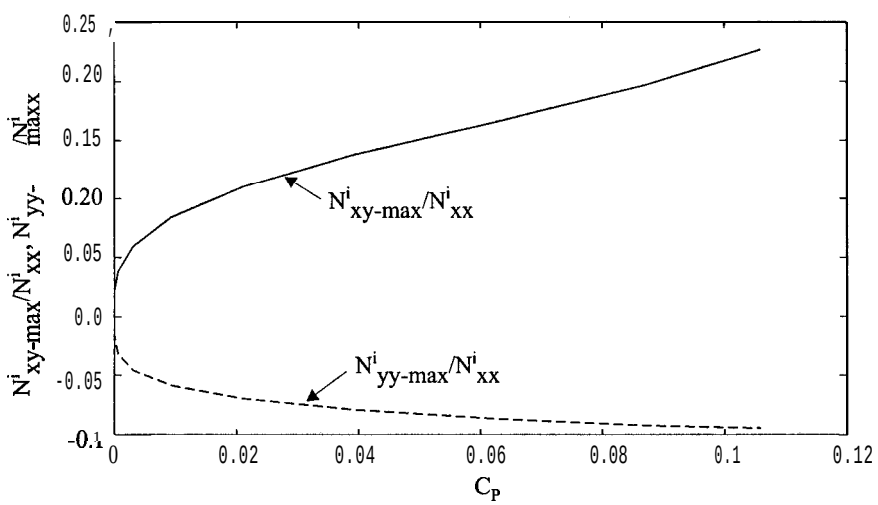

Figure 2.63: Maximum normalized shear stress resultants N^i_{xy-max}/N^i_{xx} and in-plane normal stress resultants N^i_{yy-max}/N^i_{xx} in the adherends as function of the coupling parameter C_P.

From Figure 2.63 it is observed that both the shear and in-plane stress resultants increase significantly for small values of the coupling parameter C_P. After this strong increase they both tend to increase linearly. The peak shear stress resultants reach a value of about 20% of the applied load, and the in-plane normal stress resultants reach a value of about 10% of the applied load.

Figure 2.64 shows the maximum normalized twisting moment resultants $M^i_{xy-max}/M^i_{xx-max}$ and bending moment resultants $M^i_{yy-max}/M^i_{xx-max}$ as functions of the coupling parameter C_P.

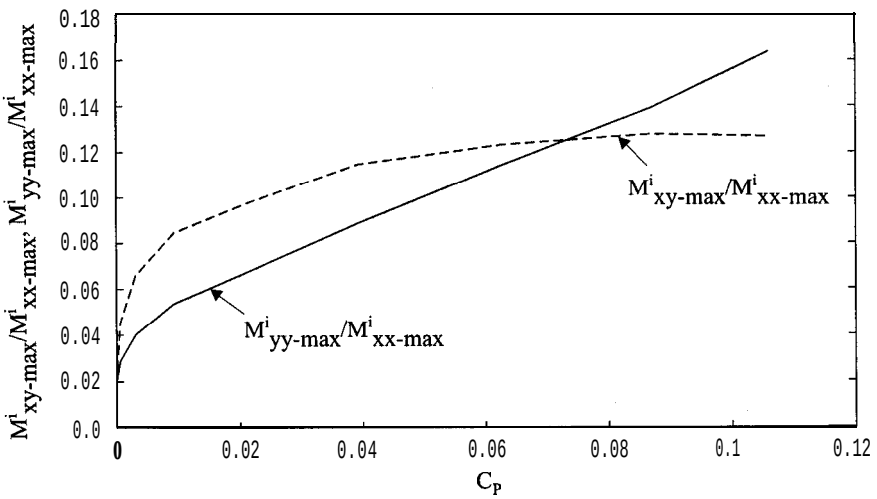

Figure 2.64: Maximum normalized twisting moment resultants $M^i_{xy-max}/M^i_{xx-max}$ and bending moment resultants *in the width* direction $M^i_{yy-max}/M^i_{xx-max}$ *of the* adherends as function *of the* coupling parameter C_P.

From Figure 2.64 it is seen that the bending moment resultants $M^i_{yy-max}/M^i_{xx-max}$ increase almost linearly as function of C_P. The twisting moment resultants increase significantly for lower values of the coupling parameter C_P, and they reach a steady state level for higher values of C_P.

The structural performances as a function of the coupling parameter C_P is not unique and Figures 2.61 - 2.64 display only general tendencies. Thus, two joints with different adherend laminates can have the same value of the coupling parameter C_P but can display different structural performance characteristics.

The Stacking Sequence of the Plies in the Laminated Adherends

Changing the stacking sequence of the plies in a laminate can change the coupling stiffnesses B_{ij} and the bending stiffnesses D_{ij} of the laminate. To investigate the influence of the stacking sequence in laminated adherends two cases have been considered. In the first case the stacking sequence is changed such that only the coupling stiffnesses B_{ij} are changed, and in the second case the stacking sequence is changed such that only the bending stiffnesses D_{ij} are changed.

A_{ij} and D_{ij} constant, B_{ij} changed:

To investigate the influence of changing the stacking sequence such that only the coupling stiffnesses B_{ij} are changed two laminates, $[0°, 45°]$ and $[45°, 0"]$, are used as aclherencl 1 and 2, respectively. Then the laminates are exchanged such that aclherencl 1 is a $[45°, 0°]$ laminate and aclherencl 2 is a $[0°, 45°]$ laminate. Thus, in the first case the 0" plies are facing the adhesive layer and in the second case the $45°$ plies are facing the adhesive layer. The laminate stiffnesses for these two laminates are identical except for the signs of the coupling stiffnesses B_{ij}, which are opposite. It should be noted that the coupling parameter C_P introduced before remains unchanged. The boundary conditions, dimensions and the loading are the same as used before.

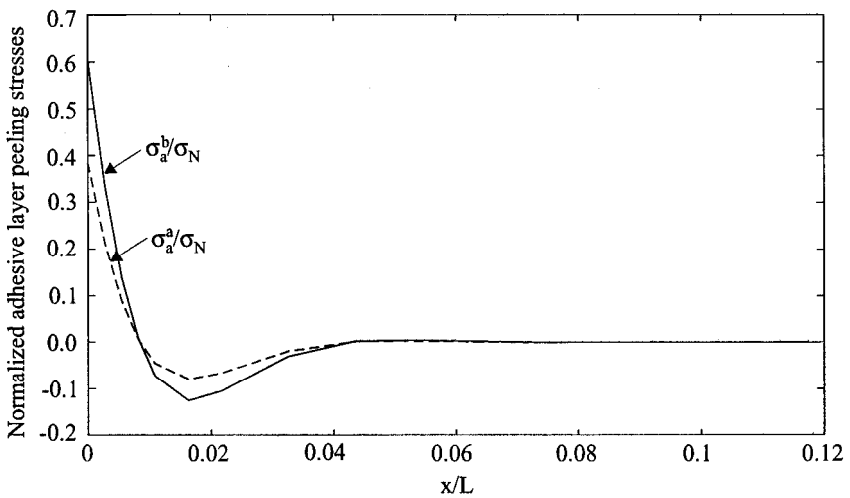

Figure 2.65: Normalized adhesive layer transverse *normal* stresses, σ_a/σ_N, *for a) Adherend 1:* $[0°, 45°]$, Adherend 2: $[45°, 0°]$ *b)* Adherend *1:* $[45°, 0°]$, Adherend 2: $[0°, 45°]$.

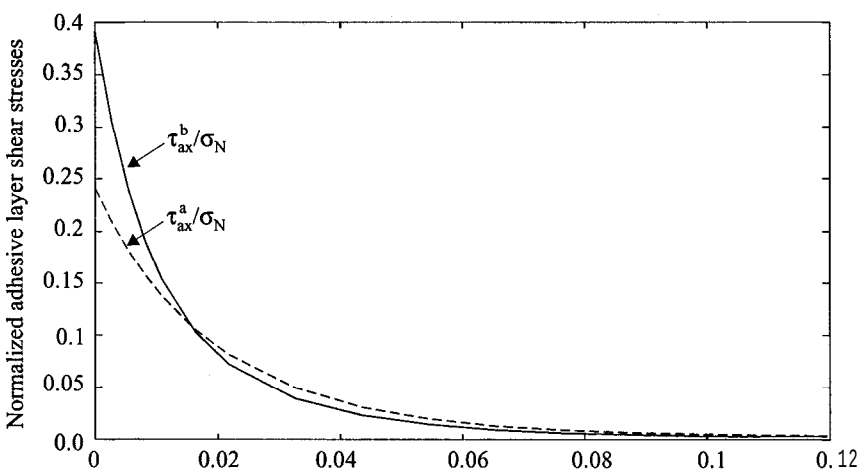

Figure 2.66: *Normalized* adhesive layer longitudinal shear stresses, τ_{ax}/σ_N, *for a)* Adherend 1: $[0°, 45°]$, Adherend 2: $[45°, 0°]$ b) Adherend *1:* $[45°, 0°]$, Adherend 2: $[0°, 45°]$.

In Figure 2.65 the normalizecl adhesive layer transverse normal stresses are shown for both cases, and the normalized adhesive layer shear stresses in the longitudinal direction are shown in Figure 2.66. In the figures only a zoom of the adhesive layer stresses at the left end of the overlap is shown, since the stresses are symmetric about the centre of the overlap zone. From Figure 2.65 it is observed that the transverse normal stresses increase by approximately 58% at $x = 0$ as the stacking sequences of the adherends are interchanged, and from Figure 2.66 it is seen that the adhesive layer longitudinal shear stresses increase by approximately 39% at x = 0 as the adherend stacking sequences are interchanged. The changes only appear due to the change in the sign of the coupling stiffnesses B_{ij} for the two laminates as mentioned previously. The reason for the increase in the adhesive layer stresses as the 45° ply is facing the adhesive layer instead of the 0° is that the deformations in the 45° are larger than in the 0°. This introduce also larger deformations in the adhesive layer and thereby larger adhesive layer stresses. Thus, it observed from Figures 2.65 and 2.66 that it is important to have the 0° plies facing the adhesive layers. This has been stipulated previously, but is demonstrated quantitatively in Figures 2.65 and 2.66.

The adhesive layer shear stresses in the width direction are not shown since the peak stresses remain almost unchanged.

A_{ij} *and* B_{ij} constant, D_{ij} changed:

To investigate the influence of changing the stacking sequence such that only the flexural stiffnesses D_{ij} are changed two symmetric and identical laminates are assumed for the two adhere&. The laminates used are in the first case: $[0°, 0°, 0°, 90°, 90°, 0°]_s$, and in the second case: [0”, 90°, 90°, 0°, 0°, O”],. The boundary conditions, dimensions as well as the loading are the same as used before.

In Figure 2.67 the normalizecl adhesive layer transverse normal stresses are shown for both cases.

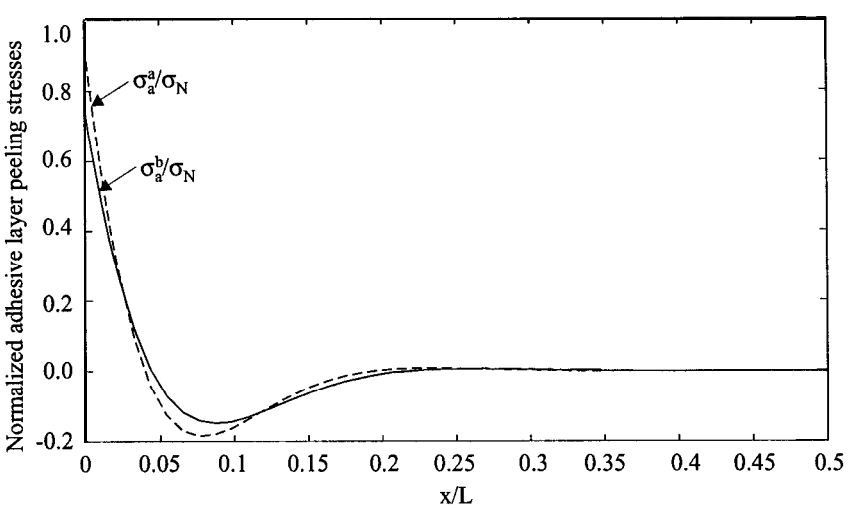

Figure 2.67: *Normalized* adhesive layer transverse normal stresses, σ_a/σ_N, for a) Adherend ***1*** = Adherend 2: $[0°,0°,0°,90°,90°,0°]_s$, b) Adherend 1 = Adherend 2: $[0°,90°,90°,0°,0°,0°]_s$.

Again, only a zoom of the adhesive layer stresses at the left end of the overlap is shown in Figure 2.67, since the stresses are symmetric about the centre of the overlap zone. It is seen from Figure

2.67 that the transverse normal stresses are increased by about 25% as the 0” plies are moved towards the midsurface of the laminated adherends. The reason for this is of course that the principal bending stiffness (D_{11}) is thereby decreased.

The adhesive layer shear stresses are not shown since the shear stresses in the longitudinal direction remain almost unchanged, and since the shear stresses in the width direction are nil. The reason why the shear stresses in the longitudinal direction remain almost unchanged is that they primarily depend on the extensional and coupling stiffnesses, which do not change.

The Influence of Modelling the Adherends as Plates in Cylindrical Bending or as Beams

An interesting property to investigate by use of the approach developed in the present work is the possibility to model the adherends as plates in cylindrical bending or as beams. The major differences in the modelling are the laminate stiffnesses. In the modelling of the adherends as beams, only the principal stiffness parameters are included, i.e. A^i_{11}, B^i_{11} and D^i_{11}. In the modelling of the adherends as plates in cylindrical bending most of the extensional, coupling and bending stiffnesses are included. Thus, if other stiffness parameters than A^i_{11}, B^i_{11} and D^i_{11} are of significant magnitude the cylindrical bending case will provide different results than the beam solution. It should also be noted, however, that in choosing between the two solution procedures the actual boundaries in the width direction should be considered with respect to the proper boundary conditions. The major difference in the output from the two different approaches is, that the ‘cylindrical bending approach’ also provides information about the variables in the width direction of the laminates as well as the adhesive layer shear stresses in the width direction.

To investigate the differences between the two approaches the same laminates and investigations as used in the evaluation of the influence of coupling effects are adopted. Thus, the laminates assumed are [a, 0°], [0”, α] as adherend 1 and 2 respectively, where $\alpha \in [0°, 45°]$. The boundary conditions, dimensions and the loading are the same as used before.

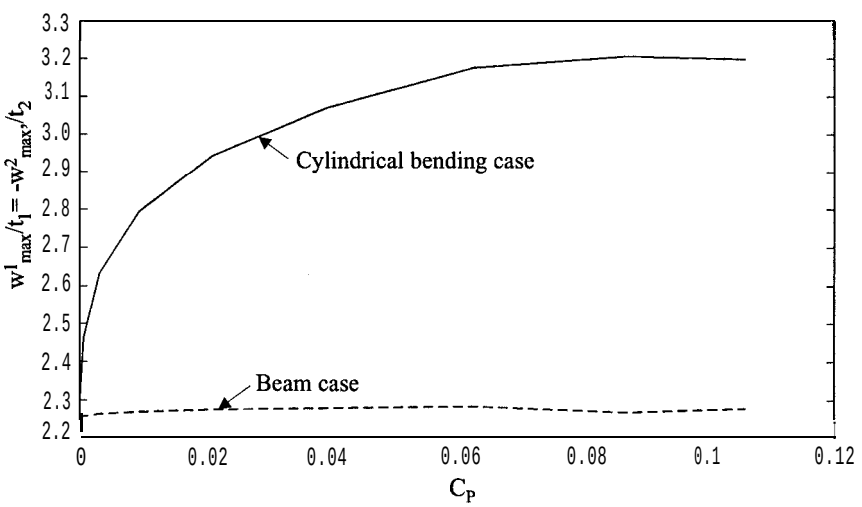

Figure 2.68: Normalised vertical displacements $w^1_{max}/t_1 = -w^2_{min}/t_2$ ***of*** the adherends as func- ***tion of the*** coupling parameter C_P ***for the*** ‘cylindrical bending’ and the ***‘beam’ cases.***

In Figure 2.68 the maximum normalized vertical displacements, again as a function of the coupling effects ***Cp,*** are shown for the 'cylindrical bending' and 'beam' cases.

Figure 2.68 displays that the vertical displacements of the adherends are almost unaffected by the coupling effects when the adherends are modelled as 'wide beams', whereas the difference between the maximum and minimum values is about 35% when the adherends are modelled as plates in 'cylindrical bending'.

Figure 2.69 displays the maximum normalized adhesive layer stresses as a function of the coupling parameter ***Cp.***

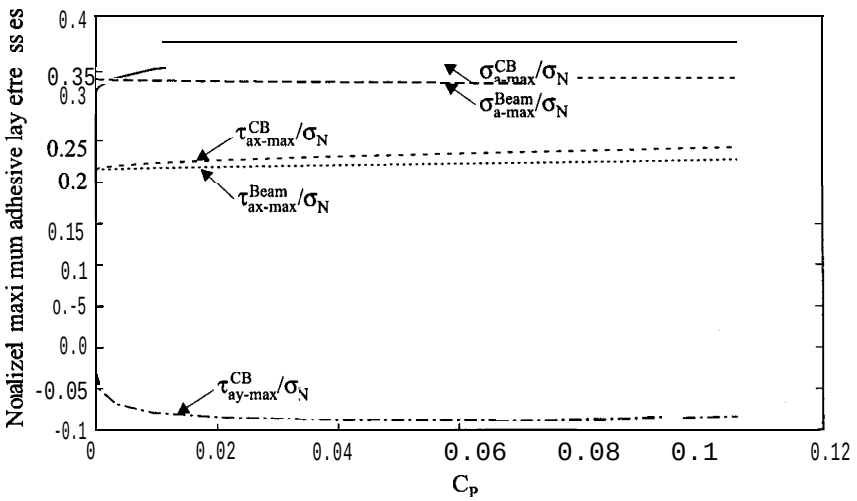

Figure 2.69: Maximum normalized adhesive layer stresses, τ_{ax-max}/σ_N, τ_{ay-max}/σ_N, σ_{a-max}/σ_N as function ***of the*** coupling parameter C_P ***for the*** 'cylindrical bending' and ***the*** 'beam' cases.

It is observed from Figure 2.69 that the maximum adhesive layer stresses are almost constant when the adherends are modelled as 'wide beams'. The maximum shearing stresses in the longitudinal direction (τ_{ax-max}) are also nearly constant when the adherends are modelled as plates in cylindrical bending, and are only a few percent larger than for the beam case. The maximum transverse normal stresses for the 'cylindrical bending' case are about 20% larger than the for the 'beam' case. In addition the cylindrical bending case also predicts the existence of shearing stresses in the width direction (τ_{ay}), whereas these shear stresses are not predicted by the beam modelling. The maximum shear stresses in the width direction (τ_{ay}) in this case reach a value of about 9% of the applied load, which should be compared with the maximum shear stresses in the longitudinal direction (i.e τ_{ax}) that reach a value of about 22% of the applied load.

2.3.10 Summary

The objective of this section has been to show the applicability of the developed linear solution procedures for the analysis of adhesive bonded joints, with adherends composed of asymmetric and unbalanced laminates. The different bonded joint configurations have been compared to

expose their different performance characteristic. In addition, a parametric study has been performed to investigate the influence of certain important parameters on the stress distributions in the adhesive layers and in the adherend laminates.

For all the bonded joint configurations it has been observed that the peaks of the bending moment and transverse shear stress resultants in the adherend appear at the ends of the overlap zone. The same observation has been done for the adhesive layer stresses, i.e. the peak stresses also appear at the ends of the overlap zone. For the stepped lap joints local peaks of the adhesive layer stresses, as well as the bending moment and transverse shear stress resultants, are present at the ends of each step. Thus it has been demonstrated, that the primary load transfer in adhesive bonded joints takes place in the regions close to the ends of the overlap zone. However this phenomenon is more pronounced for the standard joint types than for the advanced joint types, where the load transfer in the adhesive layer is more evenly distributed over the entire adhesive layer length.

The comparison of the adhesive bonded joint configurations included in this section is summa-, rized in Tables 2.6 and 2.7. Table 2.6 shows the comparison of the normalized adhesive layer stresses of the joints with one adhesive layer as shown and compared in Sections 2.3.1 - 2.3.5. In Table 2.6 the adhesive layer stresses are normalized with respect to the adhesive layer stresses obtained for the single lap joint example.

Joint Type:	$\tau_{ay-max}/\tau_{ay-max/slj}$	$\tau_{ax-max}/\tau_{ax-max/slj}$	$\sigma_{a-max}/\sigma_{a-max/slj}$
Single lap	1.0	1.0	1.0
Single lap w. scarf. adh.	0.5	0.95	0.55
Single sided stepped lap	0.5	0.65	0.35
Single sided scarfed lap	0.15	0.17	0.03

Table 2.6: Comparison ***of the*** adhesive ***layer*** peak stresses normalized ***with respect*** to ***the*** adhesive ***layer stresses*** obtained ***for the single lap joint*** for ***the joint configurations with*** one adhesive ***layer.***

Table 2.7 shows the comparison of the normalized adhesive layer stresses of the joints with two adhesive layers as shown and compared in Section 2.3.1 - 2.3.5. In Table 2.7 the adhesive layer stresses are normalized with respect to the adhesive layer stresses from the double lap joint example.

Joint Type:	$\tau_{ay-max}/\tau_{ay-max/slj}$	$\tau_{ax-max}/\tau_{ax-max/slj}$	$\sigma_{a-max}/\sigma_{a-max/slj}$
Double lap joint	1.0	1.0	1.0
Double sided stepped lap	0.35	0.75	0.60
Double sided scarfed lap	0.30	0.85	0.50

Table 2.7: Comparison ***of the*** adhesive ***layer*** peak stresses normalized ***with respect*** to ***the*** adhesive layer stresses obtained for the double lap joint for ***the joint configurations with*** two adhesive ***layers as shown in the examples.***

From Table 2.6 and 2.7 it can be concluded that the use of advanced *joint* configurationsinstead of ***standard joint*** configurations causes a significant relief of the adhesive layer stress concentrations. The primary cause of this is the reduced eccentricity of the load path, which improves the joint strength and thereby the structural performance tremendously.

From the study of the different parametric effects it can be concluded that coupling effects caused by the use of asymmetric and unbalanced laminates can exerts a strong influence on the performance of the joint. The laminate stacking sequence also exert a significant influence on the joint performance. In addition, the results obtained by modelling the adherends as plates in 'cylindrical bending' or as 'wide beams' can be quite different if the adherend laminates display strong coupling effects.

From the examples and the parametric study results, the following general design guidelines for adhesive bonded joints with laminated adherends can be specified to maximize the adhesive bonded joint performance:

- Use advanced joint configurations instead of standard joint configurations.
- Use symmetric laminates, i.e. the use of asymmetric and unbalanced laminates with significiant coupling stiffness components B_{ij} should be avoided.
- Use adherends with high bending stiffness D_{ij}. This minimizes the bending of the adherends and thereby decreases the adhesive layer transverse normal stresses.
- Use $0°$ plies adjacent to face the adhesive layers. This will provide the best load transfer from the adhesive to the adherends and reduces the adhesive layer stresses.

These design guidelines should be added to the known guidelines for adhesive bonded joints derived by other authors. To give a complete picture of the design guidelines for adhesive bonded joints the design guidelines specified by authors such as (Hart-Smith (1973a), Hart-Smith (1973b), Hart-Smith (1973c) and Thomsen (1989), Thomsen (1992)) are given below:

- Use identical or nearly identical adherends.
- Use an overlap length of minimum ten times the minimum adherend thickness.
- Use an adhesive with relatively low values of the elastic shear and tensile moduli.
- For stepped lap joints, the overlap length of the steps close to the ends of the overlap zone should be longer than in the middle of the overlap zone.

2.4 Non-linear Adhesive Formulation

2.4.1 Introduction

The structural modelling described in Section 2.2 is based on the assumption that the adhesive layer behaves as a linear elastic material. This is a good approximation for most brittle adhesives, especially at low load levels, and the approach is useful to predict the stress distribution and the location of peak stress values.

However, most polymeric structural adhesives exhibit inelastic behaviour, in the sense that plastic residual strains are induced even at low levels of external loading. It is generally accepted, that adhesive plastic yielding will appear in most adhesive bonded joints as the load is increased to failure, see Hart-Smith (1973a), Hart-Smith (1973b), Hart-Smith (1973c), Pickett (1983), Pickett and Hollaway (1985), Adams et al. (1978) Gali and Ishai (1978), Gali et al. (1981), Thomsen (1989) and Thomsen (1992). Many structural adhesives behave in a non-linear manner at moderate and higher load levels, but the plastic strains are usually large compared to the

creep strains at normal loading rates. Thus, the assumption of linear elasticity of the adhesive is clearly an approximation, and based on this the structural analysis, described in Section 2.2, has been extended to include adhesive plasticity. However, non-linear time and temperature dependent effects including viscoelasticity, creep and thermal straining are not included.

2.4.2 Non-linear Formulation and Solution Procedure

The concept of effective stress/strain is one way of approaching this problem, and it assumes, for a ductile material, that the plastic residual strains are large compared with the creep strains at normal loading rates. Therefore, a plastic yield hypothesis can be applied, and the multidirectional state of stress can be related to a simple unidirectional stress state through a function similar to that of von Mises.

However, it is widely accepted that the yield behaviour of polymeric structural adhesives is dependent on both deviatoric and hydrostatic stress components. A consequence of this phenomenon is a difference between the yield stresses in uniaxial tension and compression, see Adams et al. (1978), Gali et al. (1981), Adams (1981), Harris and Adams (1984), Thomsen (1989) and Thomsen (1992).

This behaviour has been incorporated into the analysis by the application of a modified von Mises criterion suggested by Gali et al. (1981):

$$s = C_S (J_{2D})^{1/2} + C_V J_1, \quad C_S = \frac{\sqrt{3}(1+\lambda)}{2\lambda}, \; C_V = \frac{\lambda - 1}{2\lambda}, \; \lambda = \frac{\sigma_c}{\sigma_t} \tag{2.57}$$

where s is the effective stress, J_{2D} is the second invariant of the deviatoric stress tensor, J_1 is the first invariant of the general stress tensor and λ is the ratio between the compressive and tensile yield stresses. J_{2D} and J_1 are defined by:

$$\begin{aligned} J_{2D} &= \frac{1}{6}\left((\sigma_1 - \sigma_2)^2 + (\sigma_2 - \sigma_3)^2 + (\sigma_3 - \sigma_1)^2\right) \\ J_1 &= \sigma_1 + \sigma_2 + \sigma_3 \end{aligned} \tag{2.58}$$

For $\lambda = 1$, Equation 2.57 is reduced to the ordinary von Mises criterion. At the failure load level, the first of Equations 2.57 is transformed into the expression:

$$s_{ult} = C_{S,ult} (J_{2D})_{ult}^{1/2} + C_{V,ult} (J_1)_{ult} \tag{2.59}$$

where the subscript 'ult' denotes 'ultimate'. Equation 2.59 describes the failure envelope for the general case of a ductile material, and in three-dimensional stress space Equation 2.59 represents a paraboloid with its axis coincident with the line $\sigma_1 = \sigma_2 = \sigma_3$.

The effective strain e is given by Gali et al. (1981):

$$e = C_S \frac{1}{1+\nu} (I_{2D})^{1/2} + C_V \frac{1}{1-2\nu} (I_1) \tag{2.60}$$

where ν is Poisson's ratio, I_{2D} is the second invariant of the deviatoric strain tensor and I_1 is the first invariant of the general strain tensor. I_{2D} and I_1 are defined by:

$$\begin{aligned} I_{2D} &= \frac{1}{6}\left((\epsilon_1 - \epsilon_2)^2 + (\epsilon_2 - \epsilon_3)^2 + (\epsilon_3 - \epsilon_1)^2\right) \\ I_1 &= \epsilon_1 + \epsilon_2 + \epsilon_3 \end{aligned} \tag{2.61}$$

The non-linear adhesive properties are included by implementing an effective stress-strain relationship derived experimentally from tests on adhesive bulk specimens (Thomsen (1989), Thomsen (1992), Tong (1996)). Thus it is assumed that the bulk and 'in-situ' mechanical properties of the structural adhesive are closely correlated as discussed by Gali et al. (1981) and shown experimentally by Lilleheden (1994).

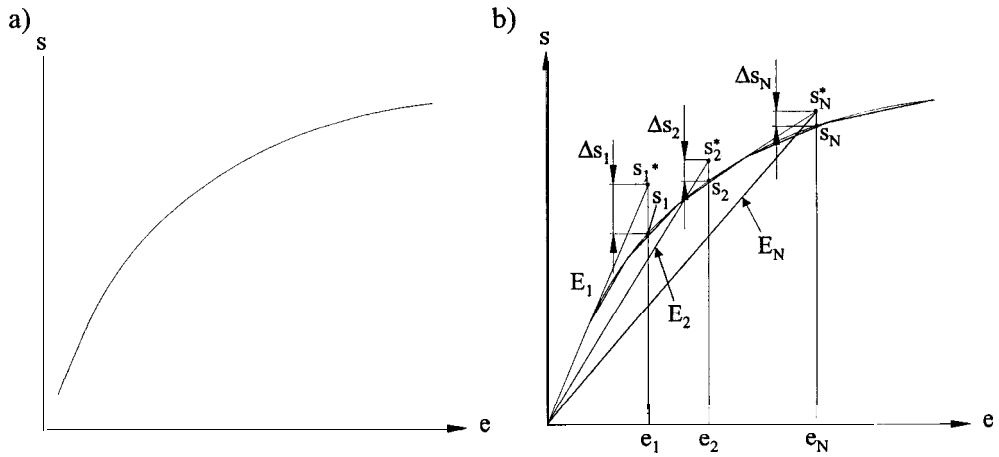

Figure 2.70: a) Effective stress-strain relationship obtained from tensile test on ***bulk*** specimen. *b)* Illustration of piece-wise linear approximation to the ***curve and the*** solution procedure ***for the*** stress analysis in ***the*** non-linear range.

Based on a secant modulus approach for the non-linear effective stress-strain relationship for the adhesive, as shown in Figure 2.70, the solution procedure for determining the stress distribution in the adhesive layer can be described by the following steps:

(1) Calculate the effective strains e_1 and stresses s_1^* (Equation 2.57 and 2.60) for each point of the adhesive layer, using the linear elastic solution procedure, assuming a uniform elastic modulus E_1 for the adhesive.

(2) If the calculated effective stresses s_1^* are above the proportional limit denoted by s_{prop}, determine the effective stresses s_1 for each point of the adhesive layer according to the corresponding effective strains e_1 (using the experimental relationship given in Figure 2.70) calculated in step (1).

(3) Calculate the difference $\Delta s_1 = s_1^* - s_1$ between the 'calculated' and the 'experimental' effective stresses, and determine the specific secant-modulus E_2^t defined by:

$$E_2^t = \{1 - \delta(\Delta s_1 / s_1)\} E_1 \qquad \textbf{(2.62)}$$

δ is a weight-factor, which determines the change of the modulus in each iteration.

(4) Rerun the procedure (steps (1)-(2)) with the elastic modulus E_1 for each adhesive point modified as per step (3).

(5) Compare the 'calculated' effective stresses s^* for each adhesive point with the 'experimental' values s obtained from the effective stress-strain curve (2.70).

(6) Repeat steps (4)-(5) until the difference between the 'calculated' and 'experimental' stresses (As) drops below a specified fraction (2%) of the 'experimental' stress value.

Convergence is usually achieved within a few iterations. The non-linear stress-strain relationship

obtained from a tensile test on a bulk specimen as illustrated in Figure 2.70 a) is in ESAComp defined by a piece-wise linear approximation to the curve as illustrated in Figure 2.70 b).

The procedure described above has previously been used for the analysis of non-linear adhesive behaviour in tubular lap joints by Thomsen (1989) and Thomsen (1992).

Failure

If the calculated maximum effective stresses or strains, depending on the applied failure criterion, reach the ultimate values, i.e. s_{ult} or e_{ult}, or lie above these values, the solution procedure will predict that the bonded joint has failed as a result of a cohesive failure in the adhesive layer.

The maximum effective stress and strain criteria have been investigated by Adams et al. (1978) and Harris and Adams (1984) by incorporating the two criteria in a finite element analysis of double and single lap joints. Their investigations showed that for brittle adhesives there was a very close correlation with experimental results by using the maximum effective stress criterion. For toughened ductile adhesives they found that the maximum effective strain criterion gave the best prediction of the joint strength. From the finite element analyses it was also possible to predict the failure mode fairly accurately.

Following the approach suggested in Section 2.2, it is not possible to predict the failure mode, due to the simple way of modelling the adhesive layer (the adhesive layer is not modelled as a continuum). However, it should be possible to predict the joint strength with reasonable accuracy by applying the maximum effective stress or strain criteria, since equally simple models of the adhesive layer have been used successfully for the prediction of the joint strength by Hart-Smith (1973a), Hart-Smith (1973b), Hart-Smith (1973c). However, the predictions should be used for comparative purposes only. For a realistic evaluation of the predicted results they should be compared with experimental results.

It should be noted here that the cohesive failure mode described above is only one failure mode, and that adherend failure may be encountered before adhesive failure. In general, a joint can fail in the following ways:

- The adhesive may fail due to high shear and transverse normal stresses (cohesive failure).
- The adhesive/adherend interfaces may fail due to high shear and transverse normal stresses.
- The adherends may fail due to the external loads coupled with the large bending moment concentrations induced in the regions near to the ends of the overlap.
- If the adherends are made of composite material they may fail due to ply-failure caused by high interlaminar shear stresses (Renton and Vinson 1975a).

The three last failure modes will not be treated any further in this thesis, but they cannot be ignored in real joints.

Finally, the ultimate load-bearing capability of the bonded joints can be calculated by an iterative use of the non-linear solution procedure, where the external loads are modified between each iteration. The iteration scheme is repeated until the calculated maximum effective stress or strain, dependent on the applied failure criterion, reaches the ultimate value (s_{ult} or e_{ult}).

2.4.3 Examples and Discussion

The effects of non-linear adhesive behaviour is illustrated by an example. The parametric effects presented in Section 2.3.9 for the linear elastic analysis, retain their validity when the non-linear adhesive behaviour is included in the analysis. The basic differences between the linear and non-linear analysis is that the adhesive stresses, at higher levels of loading, are reduced and smoothed out in the regions adjacent to the ends of the overlap zone.

To illustrate the effects of non-linear adhesive behaviour the single lap joint example shown in Section 2.3.1 will be used. Therefore, the results obtained can be compared with the results shown in Section 2.3.1. The dimensions, laminates, loads etc. are all shown in Table 2.2 in Section 2.3.

The adhesive used in the example is AY103 from Ciba-Geigy, which is a two-component plasticized epoxy adhesive as described in Section 2.3. The tensile stress/strain curve for this adhesive has been obtained from bulk specimens (Adams et al. (1978), Adams (1981), Harris and Adams (1984)), which have been subjected to the cure cycle usually used for joints bonded with this adhesive. The stress/strain relation for the used adhesive material is shown in Figure 2.71 and the material properties are given in Table 2.8.

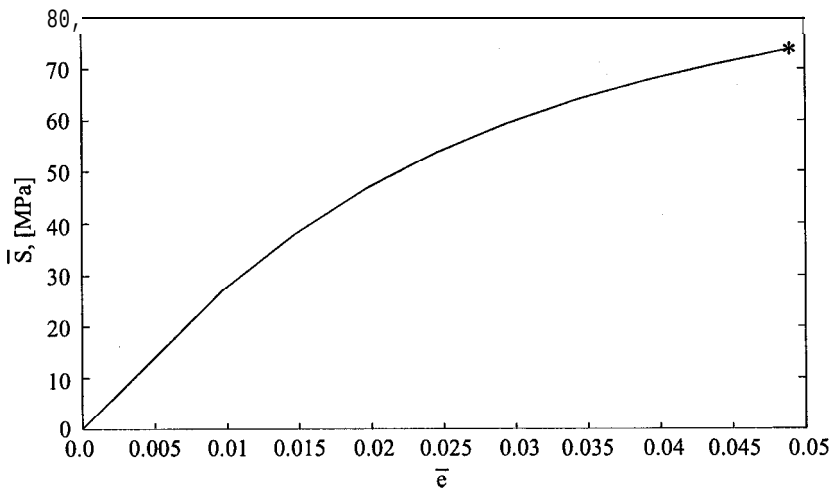

Figure 2.71: Tensile stress/strain ***curve for the*** adhesive AY103 obtained from bulk specimen, load controlled: 20.0 $[MPa/min]$.

Adhesive	epoxy AY103 (Ciba Geigy), E_a = 2800 MPa, ν_a = 0.4, λ = 1.3 ($\lambda = \frac{\sigma_c}{\sigma_t}$) s_{prop} = 27.0 MPa, s_{ult} = 71.5 MPa, e_{ult} = 0.049 MPa

Table 2.8: Specification adhesive ***material properties.***

Analysis of the single lap joint example shown in Section 2.3.1 by use of the non-linear solution procedure, based on the adhesive properties given in Table 2.1 and the non-linear adhesive stress/strain relation shown in Figure 2.71, results in the adhesive layer stress distribution shown in Figure 2.72.

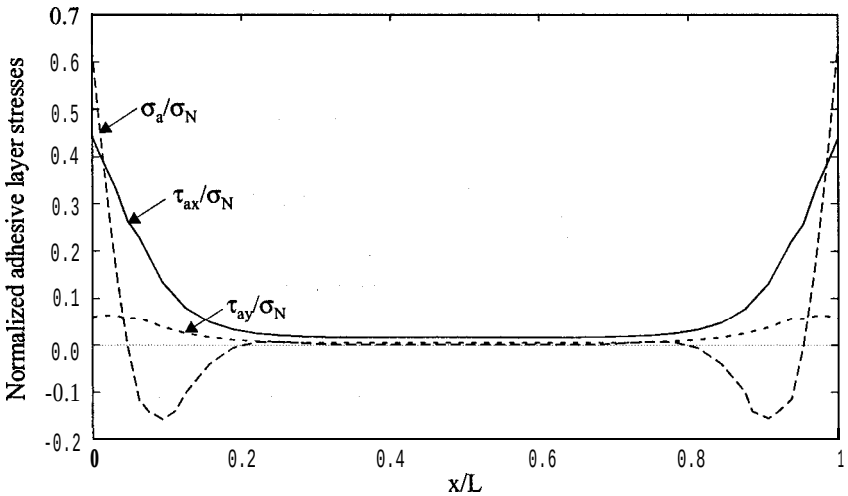

Figure 2.72: *Normalized* adhesive layer stresses, τ_{ax}/σ_N, τ_{ay}/σ_N, σ_a/σ_N for a single lap joint obtained by use of the non-linear solution procedure.

Comparison of the adhesive layer stress distribution obtained for the linear case, shown in Figure 2.36, and for the non-linear case, shown in Figure 2.72, shows that inclusion of the non-linear effects reduce the maximum predicted stresses with about 25%. It is also seen that the non-linear effects are only influential very close to the ends of the overlap zone. The differences between the linear and non-linear solutions are strongly dependent on the load level. Failure has been predicted to occur at a load level corresponding to σ_N = 80 MPa by use of the ultimate stress criterion.

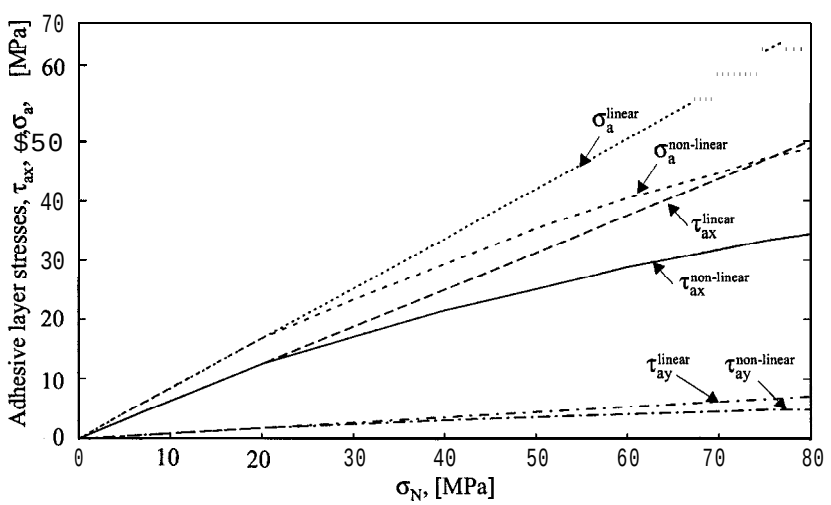

Figure 2.73: Maximum adhesive ***layer*** stresses, τ_{ax}, τ_{ay}, σ_a for a single lap joint using the linear and the non-linear solution procedure as function of the applied in-plane nominal stresses.

Figure 2.73 displays the differences between the linear and non-linear solutions, by showing the maximum adhesive layer stresses as a function of the load level obtained using the same single lap joint configuration.

It is observed from Figure 2.73, that the adhesive non-linearity starts to affect the adhesive layer stresses at very low load levels, and the non-linear effects become increasingly important as the external loading is increased. Thus, prediction of the adhesive stresses using the linear solution procedure will underestimate the load bearing capability of the adhesive joint, except for very brittle adhesives where the non-linear effects are of minor importance. This observation is in close agreement with experimental results, see Hart-Smith (1973a), Hart-Smith (1973c), Hart-Smith (1973b), Adams et al. (1978), Adams (1981) and Harris and Adams (1984).

2.4.4 Summary

From the comparison between the linear elastic solution, shown in Section 2.3, and the non-linear adhesive solution, shown in Section 2.4.2, it can be concluded that the non-linear behaviour shown by many polymeric adhesives exert a strong influence on the adhesive layer stress distribution. The severe stress concentrations, predicted by the linear solution procedure, tend to smooth out when a non-linear solution procedure is applied. The non-linear effects become influential even at low load levels, and become very influential at higher load levels. Thus, in most cases non-linear effects are unavoidable, and a certain degree of plasticity in the adhesive layer close to the ends of the overlap cannot be prevented. Linear elastic solution procedures will therefore underestimate the strength of adhesive bonded joints unless very brittle adhesives with approximately linear elastic properties are considered.

2.5 Validation of the Adhesive Layer Model

As described in the introduction to the chapter on adhesive bonded joints an investigation of the used adhesive layer model has been carried out. To investigate the validity of the adhesive layer model a high-order theory approach developed for the analysis of sandwich structures has been used, see Frostig et al. (1991), Frostig (1992) and Frostig (1993), together with FE-analyses. The investigation is partially presented in the paper: 'Analysis of Adhesive Bonded Joints, Square-end and Spew-Fillet: Closed-Form Higher-Order Theory Approach' by Frostig, Thomsen, and Mortensen (1997). In this section the full and extended validation of the adhesive layer model is presented.

As a consequence of modelling the adhesive layer as continously distributed springs (tension/compression and shear springs) it is not possible to fulfil the condition of zero shear stresses (τ_{ax} = 0) at the free edges of the adhesive layers as assumed in the boundary conditions for all the joints. However, in real adhesive bonded joints no free edges at the ends of the overlap zones are present, since a fillet of surplus adhesive, a so-called spew fillet, is formed at the ends of the overlap. The differences between the model joint and a real joint is illustrated in Figure 2.74.

Consequently, the shear stresses (τ_{ax}) in a real joint will therefore not be zero at the ends of the overlap zone. It can therefore be stipulated that using the spring model approach in some sense is equivalent to assuming the existence of a spew-fillet at the ends of the overlap zone. The actual spew-fillet size, however, is not addressed by adopting the spring model approach.

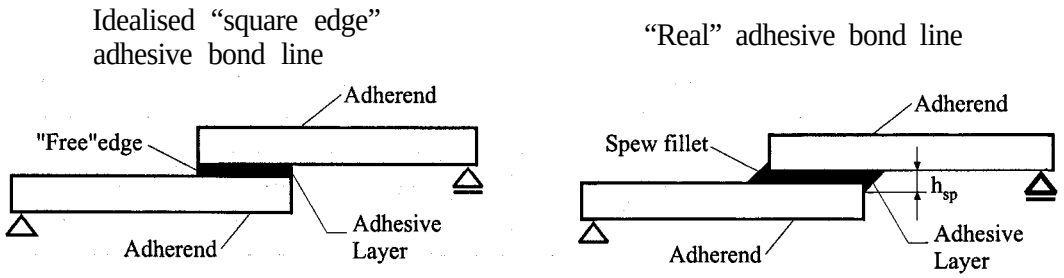

Figure 2.74: Illustration *of a* model joint and a real joint.

The validity of the adhesive layer spring model approach has been investigated by comparison with:

- A high-order theory approach including the presense of a spew-fillet;
- FE-analyses including a spew-fillet;

The comparison has been carried out analysing a single lap joint composed of two identical aluminium adherends with the properties shown in Table 2.9.

Adherend 1 & 2	Aluminium $E_1 = E_2 = 70$ GPa t_1 = 1.62 mm, $b_1 = b_2$ = 25.4 mm
Adhesive	Epoxy $E_a = 4.82$ GPa, ν = 0.4, t_a = 0.25 mm
Lengths	$L_1 = L_2 = 50.8$ mm, L = 12.7 mm
Load & B.C.	Simply supported at both ends, P_N = 1.0 kN $(N = P_N/b)$

Table 2.9: Adherend and adhesive properties, thicknesses, lengths and boundary conditions assumed *for the* single lap joint to investigate *the* validity *of the* spring model approach.

In the following the method described in this chapter is called the 'spring model approach' for simplicity.

2.5.1 Structural Modelling using a High-Order Theory Approach

The high-order theory approach used has been developed by Frostig et al. (1991), Frostig (1993), Frostig and Baruch (1993) and Frostig and Shenhar (1995) for the study of localized effects in sandwich beams and plates. The theory includes the transverse flexibility of the core material. Thus, the core thickness is allowed to change during the deformation of the sandwich panel, and the face sheets are allowed to deflect differently. In the present study the high-order theory approach has been used for the analysis of a single lap joint, since the bonded joint in the overlap zone are comparable with a sandwich plate, i.e the adhesive layer can be seen as the core material and the adherends can be seen at the face sheets.

The structural modelling using the high-order theory approach can be described in the following way (for more details see Frostig et al. (1997)):

- The adherends:
  - Modelled as beams or plates in cylindrical bending.

- The adhesive:
  - Assumed to be a 2-D or 3-D (in case of cylindrical bending) elastic continuum only possessing stiffness in the thickness direction, and therefore only capable of transferring transverse normal and shear stresses. The constitutive relations for the adhesive layer can be written as:

$$\begin{aligned} \tau_{xz}(x, z_a) &= G_a \gamma_{xz} \\ \sigma_{zz}(x, z_a) &= E_a \epsilon_{zz} \end{aligned} \tag{2.63}$$

    where z_a is the local z-coordinate in the adhesive layer. $z_a = 0$ is at the upper interface of the adhesive layer, and $z_a = t_a$ is at the lower interface of the adhesive layer.

    The stress field in the adhesive layer is derived using point equilibrium conditions together with the constitutive relations in Equations 2.63, and are given by (for more detail see Frostig et al. (1997) and Frostig (1992)):

$$\begin{aligned} \tau_{xz}(x, z_a) &= \tau_{xz}(x) = \tau_{ax} \\ \sigma_{zz}(x, z_a) &= -\frac{\tau_{ax,x}(2z_a - t_a)}{2E_a} + \frac{w_2 - w_1}{t_a} \end{aligned} \tag{2.64}$$

    Compared with the stress field for the adhesive layer obtained using the spring model approach, Equations 2.14, it is observed, that the relation for the shear stresses are the same. In the high-order theory approach, however, the transverse normal stresses are not constant across the thickness of the adhesive layer, but are predicted to vary linearly across the the adhesive layer thickness, and are a function of the derivative of the shear stresses with respect to x. Thus, comparing the equation for the transverse normal adhesive layer stresses from the spring model approach, i.e. Equation 2.14, with the same for the high-order theory approach, i.e Equation 2.64, it is seen that the term:

$$\frac{\tau_{a,x}(2z_a - t_a)}{2E_a} \tag{2.65}$$

    has been added.

    Since the adhesive layer is modelled as a continuum it is possible to prescribe the value of the shear stresses at the ends of the overlap.

- The spew-fillet:
  - First approach: $\tau_{ax,x} = 0$ in the adhesive layer at the ends of the overlap. Usually this requirement leads to prediction of non-zero shear stresses at the adhesive edges, thus resembling the presences of a spew-fillet. The size of the spew-fillet is not addressed by this approach, however. By this approach the predicted stress field for the adhesive layer is nearly exactly the same as predicted using the spring model approach.
  - Second approach: The spew-fillet is modelled as an equivalent elastic bar extending between the two adherends. Thus, the capability of the spew-fillet to transfer loads directly between the two adherends is included in the model.

Using the high-order theory approach for the analysis of adhesive bonded joints it is possible to prescribe the shear stresses at the ends of the overlap τ_{ax} to be equal to zero, thus assuming the boundaries of the adhesive layer to be free. Doing this the peeling stresses will be tremendously and unrealistically large at the ends of the overlap zone. Instead the two approaches described above for the modelling of the spew-fillet can ‘be-used.

In the second approach the spew-fillet is modelled as an equivalent elastic bar extending between the two adherends. This concept is based on a practical assumption, indicated by finite element results, see Adams and Peppiatt (1974), Adams et al. (1978), Harris and Adams (1984) and Adams and Wake (1984), that the stress state in the spew-fillet consists mainly of unidirectional stresses that are parallel to the free edge of the spew-fillet, see Figure 2.74. However, using this approach it is necessary to specify the spew-fillet size, which can be very difficult to determine in practice, and is usually unknown in the design phase. Comparison of the two approaches shows, however, that the first approach provides reasonable results for small spew-fillet sizes, and that the second approach provides more meaningful results for larger spew-fillets.

2.5.2 FE-models used for Validation

The aim of this comparison is to investigate the validity of the spring model approach, and to establish to which extent the approach provides reasonably accurate results in predicting the adhesive layer stresses. Therefore, two finite element analyses have been carried out with different spew-fillet sizes. In the first analysis the size of the spew-fillet is $h_{sp} = 2t_a$ and in the second analysis the size is $h_{sp} = 1.2t_a$, where the size of the spew-fillet is defined according to Figure 2.74.

The finite element analysis has been performed using the finite element code ODESSY developed at Aalborg University, see Rasmussen et al. (1993) and Rasmussen and Lund (1997). A zoom of the finite element model at the left end of a single lap joint including a spew-fillet with the size $h_{sp} = 2t_a$ is shown in Figure 2.75.

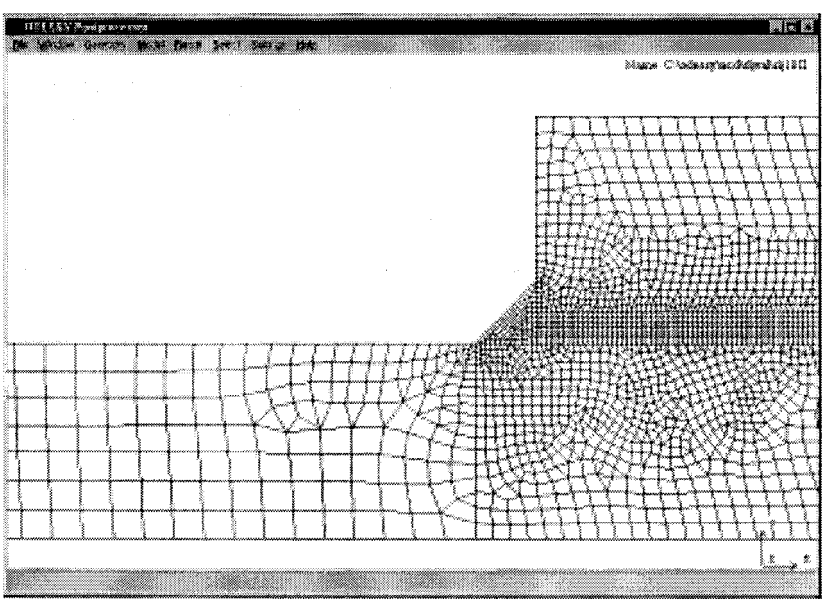

Figure 2.75: Zoom of finite element model at the left end of a single lap joint including a spew-fillet with the size $h_{sp} = 2t_a$.

The structure has been modelled using a mixture of 6 and 8 node isoparametric 2D solid elements. The adhesive layer has been divided into six 8 node isoparametric elements through the thickness.

In the near vicinity of the overlap edges the adhesive layer elements are quadratic, whereas irregular elements are used in the middle of the overlap regions where low stress gradients are present. The finite element model for the single lap joint, including a spew-fillet with the size $h_{sp} = 2t_a$, contains 8525 elements with 26208 nodes. The analysis has been carried out as a plane strain model, since the proposed simple approach is based on the assumption that the laminates behave as plates or wide beams. It should be noted that the prediction of the stresses in the adhesive layer is affected by the singularities present at the corners of the adherends facing the adhesive layer at the ends of the overlap zone.

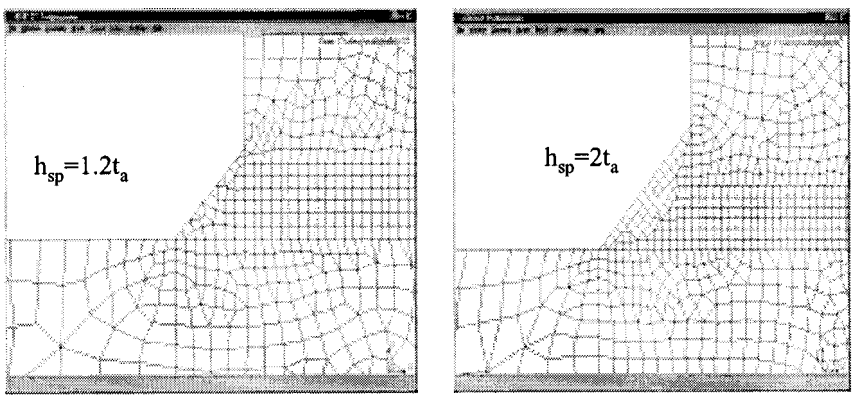

Figure 2.76: Zoom of finite element *models* at the left end *of* a single lap joint including a spew-fillet with the sizes $h_{sp} = 1.2t_a$ and $h_{sp} = 2t_a$.

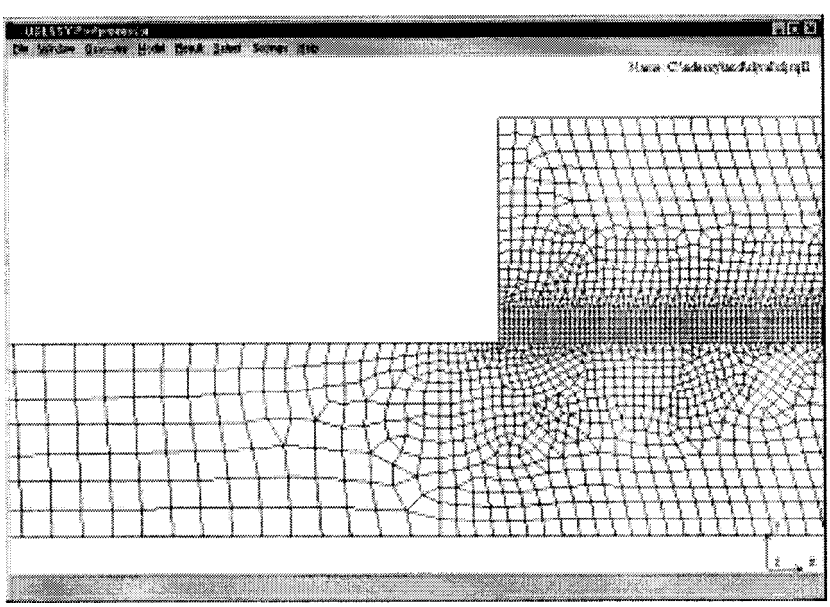

Figure 2.77: Zoom of finite element model at the left *end of* a single lap joint without a *spew*-fillet.

Figure 2.76 displays a zoom of the finite element meshes of the single lap joint with the two

different spew-fillet sizes, i.e. $h_{sp} = 2t_a$ and $h_{sp} = 1.2t_a$.

To support the claim that the presence of a spew-fillet plays a very important structural role as a 'stress reliever' at the ends of the overlap zones, a finite element analysis of the considered single lap joint configuration without a spew-fillet has also been performed. A zoom of the finite element model at the left end of the single lap joint without a spew-fillet is shown in Figure 2.77.

The accuracy of the finite element results obtained near the ends of the overlap zone is of course again affected by the singularity present at the corners of the adherends facing the adhesive layer at the ends of the overlap zone.

2.5.3 Comparison of Results

Analysing the single lap joint problem described in Table 2.9 and using the three different methods: 1) spring model approach, 2) high-order theory approach and 3) the finite element method give the adhesive layer stress distributions shown in Figure 2.78 and 2.79.

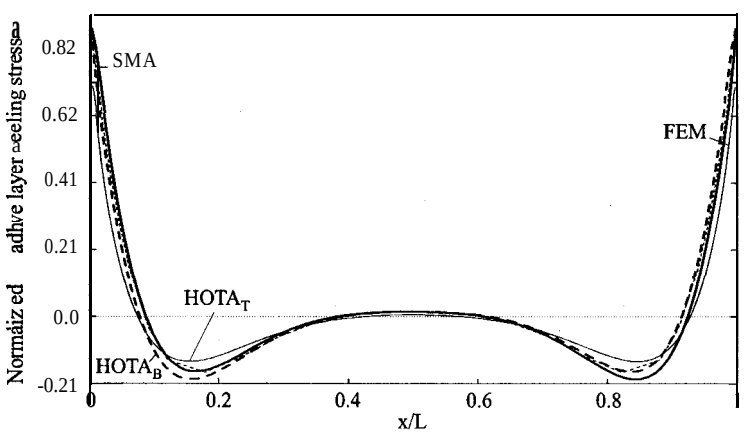

Figure 2.78: Normalized adhesive layer transverse normal stresses, σ_a/σ_N *using* the spring *model* approach *(SMA), the* high-order theory approach *(HOTA,* $\tau_{ax,x}$ = 0 at x = 0, *L)* and the *finite* element method *(FEM) for a single* lap joint *with a* spew-fillet *of size* $h_{sp} = 2t_a$.

From Figure 2.78 and 2.79 it is seen that the stresses calculated by the three methods compare very well and display only small differences. The results calculated by the high-order theory approach, and displayed in the figures, are determined by the assumption that $\tau_{ax,x}$ = 0 at the ends of the overlap zone, i.e. the actual size of the spew-fillet is not addressed. In Figure 2.78 the transverse normal stresses in the adhesive layer are displayed in the top and bottom interfaces of the adhesive layer and are marked by $HOTA_T$ and $HOTA_B$. Only small differencies between the two curves $HOTA_T$ and $HOTA_B$ are observed, however. The stresses calculated by the finite element method and displayed in the figures are determined from the single lap joint configuration with the spew-fillet size $h_{sp} = 2t_a$. It is seen that the stresses determined by the finite element method are a bit lower than the stresses determined by the two other approaches, but if the stresses are determined using the configuration with the spew-fillet size

$h_{sp} = 1.2t_a$, the stresses will be a bit higher than by the two other approaches. Thus, it is concluded that the adhesive layer stresses predicted by the spring model approach essentially equal the stresses predicted by the high-order theory approach including a spew-fillet ($\tau_{ax,x} = 0$ condition at x = 0, L), which again equal the stresses predicted by the finite element method including a spew-fillet with a size h_{sp} between 1 and 2 times the adhesive layer thickness t_a.

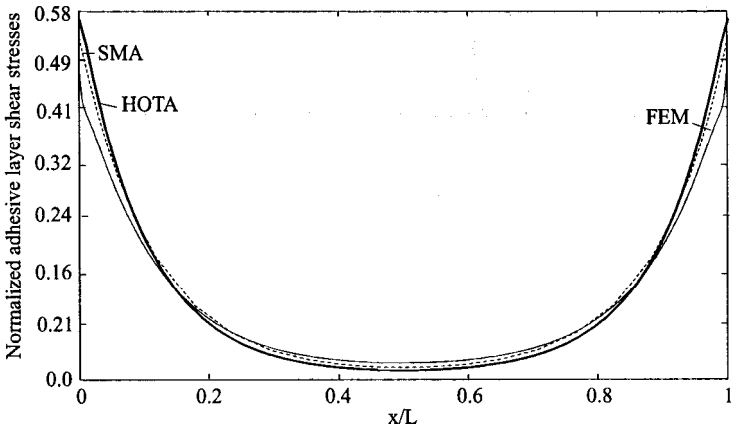

Figure 2.79: *Normalized* adhesive layer shear stresses, τ_{ax}/σ_N *using the* spring model approach *(SMA), the* high-order theory approach *(HOTA,* $\tau_{ax,x} = 0$ *at* x = $0, L$*)* and *the finite* element method (FEM) *for single* lap joint with a spew-fillet of size $h_{sp} = 2t_a$.

In the manufacturing process of real adhesive bonded joints it is unavoidable to have a spew-fillet of at least 1-2 times the adhesive layer thicknesses. However, it is possible to have larger spew-fillet sizes, and in this case the stresses predicted by the spring model approach will overestimate the stresses. Since the real spew-fillet size is usually not known, and, moreover, can be difficult to determine, it is concluded that the stresses predicted by the spring model approach represent reasonable and conservative estimates of the 'real' adhesive layer stresses.

Finally, to emphasize the importance of the presence of a spew-fillet at the ends of the overlap zone, the adhesive layer stresses obtained for the single lap joint configuration without a spew-fillet are displayed in Figures 2.80 and 2.81. The stress distributions displayed have been determined by use of the spring model approach, the high-order theory approach and the finite element method.

From Figure 2.81 it is seen that the adhesive layer shear stresses display the same pattern and almost same peak values as obtained with the presence of spew-fillets. The only exception being that the shear stresses are zero at the adhesive edges when there is no presence of a spew-fillet. Figure 2.80 shows, however, that the transverse normal stresses reach extreme values at the adhesive layer free edges. Furthermore it is seen that the transverse normal stresses at the upper ($HOTA_T$) and lower ($HOTA_B$) adhesive interface have different signs, i.e. tremendous gradients across the adhesive layer thickness are induced. Thus, from this and by comparison with the stresses determined for a single lap joint with a spew-fillet it can be concluded that adhesive bonded joints without spew-fillets will be structurally very weak and useless for any practical applications. Only test will actually reveal that and it is not shown herein.

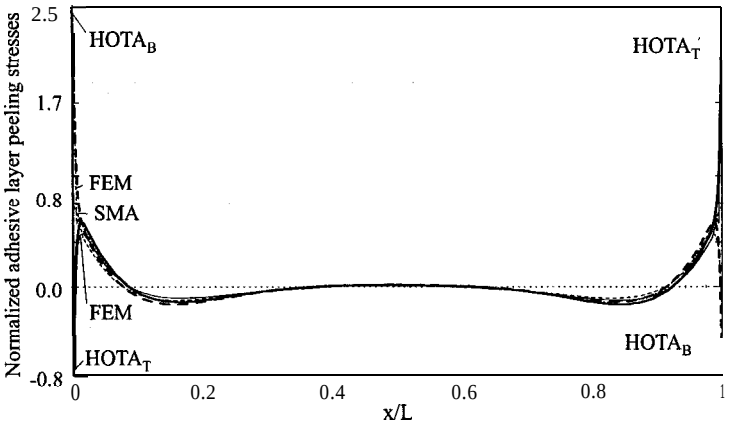

Figure 2.80: Normalized adhesive layer transverse normal stresses, σ_a/σ_N using the spring model approach (SMA), the high-order theory approach $(HOTA,\ \tau_{ax} = 0$ at x = 0, $L)$ and the finite element method (FEM) for a single lap joint without a spew-fillet.

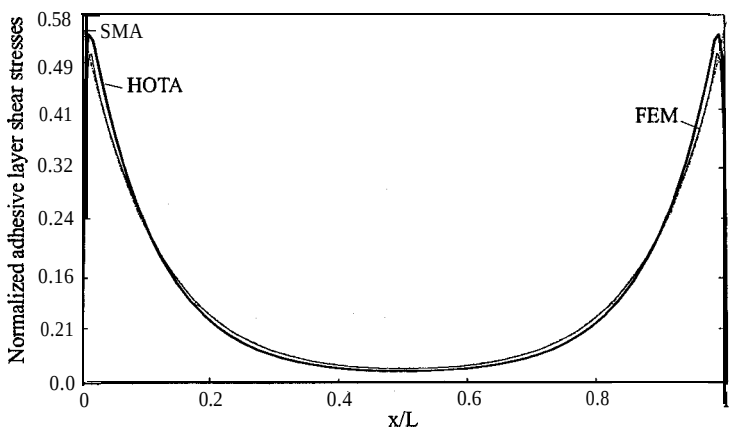

Figure 2.81: *Normalized* adhesive layer shear stresses, τ_a/σ_N using the spring model approach *(SMA), the* high-order theory approach *(HOTA,* $\tau_{ax} = 0$ *at* x = 0, $L)$ and the finite element method (FEM) *for single* lap joint *without* a spew-fillet.

2.5.4 Summary

It has been demonstrated that the results obtained with the spring model approach are in very good agreement with the results obtained using the finite element method and the high-order theory approach including small spew-fillets (i.e. with a spew-fillet size between one and two times the adhesive layer thickness). The stresses predicted using the spring model approach are therefore reliable compared with other methods, since it is unavoidable in the manufacturing process to obtain joints without spew-fillets.

The results obtained from the finite element method and the high-order theory approach also

show that it is senseless from a structural point of view to try to design bonded joints without spew-fillets. In order to fully exploit the stress relieving effect, it is recommended to ensure that the spew-fillets at the ends of the overlap zone become as large as possible.

2.6 Implementation in ESAcomp

The implementation of the Adhesive Bonded Joint Module into ESAComp is planned for the ESAComp version 2.0 (planned to be released in 1999, the implementation will take place in the autumn of 1998 and in the spring 1999). The way that the module will be implemented in ESAComp has been decided already, and with reference to Section 1.1 in Chaper 1, the implementation of the Adhesive Bonded Joint Module into ESAComp is shortly described in this section.

The **Adhesive Bonded Joint Module** will be implemented as an object, see Figure 1.2 and Figure 1.3 in Chaper 1 Section 1.1.1-1.1.2.

Before the analysis module for adhesive bonded joints is called in ESAComp, the laminates which are to be joined must be created. After this is done, the adhesive material must be specified as a homogenous ply or chosen from the ESAComp material database. When this is done, *Joints* is selected in the ESAComp Main Window as shown in Figure 2.82.

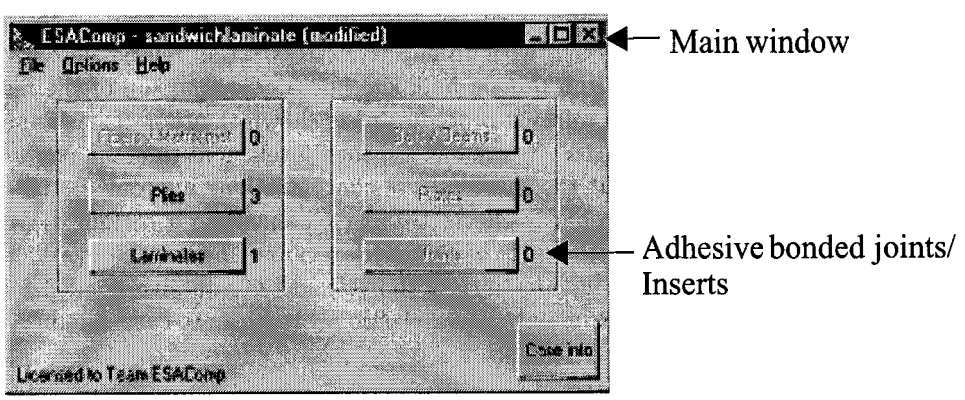

Figure 2.82: Implementation *of the* Adhesive Bonded Joint Module into ESAComp.

After Joints is selected from the main window a new window called *Joints - Case Joints* appears. In the joint window the load and boundary conditions must be specified before the analysis can be performed by selecting *Joint Loads.* After this is done the analysis of adhesive bonded joints is selected under *Analyze* in the joint window, and an *Adhesive* Bonded Joint - analysis specification window will appear. In the *Adhesive Bonded Joint - analysis specification* window the laminates, the adhesives, the joint type, the dimensions the loads etc. can be selected, and the analysis can be performed.

2.7 Conclusions

A general method for the analysis of adhesive bonded joints between composite laminates has been presented. The analysis accounts for coupling effects induced by adherends made as asym-

metric and unbalanced laminates. The analysis allows specification of any combination of boundary conditions and external loading. The analysis can be carried out with the adherends modelled as wide beams or as plates in cylindrical bending. The adhesive layers are as a first approximation assumed to behave as a linear elastic materials. The thickness of the adhesive layer is assumed to be small compared with the thickness of the adherends, and the adhesive layers are modelled as continuously distributed linear tension/compression and shear springs. The results obtained using this approach have been compared with finite element results and results obtained using a high-order theory approach (both including spew-fillets), and the comparison shows that the results are in very good agreement.

For each of the adhesive bonded joint configurations a set of governing equations are derived and solved using the 'Multi-Segment of Integration'. The method is based on a transformation of the original multiple-point boundary value problem into a series of initial value problems, which are solved by direct integration. Continuity of the fundamental variables, as well as fulfilment of the boundary conditions, is ensured by formulating and solving a set of linear algebraic equations. The solution procedures have been used to demonstrate the mechanical responses of several different bonded joint configurations, and for conducting a parametric study. Based on this, a set of general design guidelines has been formulated.

The linear solution procedure has been used together with a modified von Mises criterion and a secant modulus approach for the effective stress/strain relationship of the adhesive, to perform a non-linear solution for the adhesive bonded joint problems. The modified von Mises criterion takes into account that yielding of polymers often depends on both deviatoric as well as hydrostatic stress components. The non-linear solution procedure is based on an iterative use of the linear solution procedure together with an effective stress/strain relationship for the adhesive material, derived empirically from test on bulk specimens. Comparison of the results obtained using the linear and non-linear solution procedures has shown that non-linear adhesive behaviour influences the adhesive layer stresses even at low load levels, and that the non-linear adhesive behaviour tends to smooth out the severe stress concentrations induced at the ends of the overlap zones. In most cases non-linear effects are unavoidable, and a certain degree of plasticity in the adhesive layer close to the ends of the overlap cannot be prevented. The linear elastic solution procedure therefore underestimates the strength of adhesive bonded joints, unless very brittle adhesives with approximately linear elastic properties are considered.

Chapter

3

Ply Drops in Composite and Sandwich Laminates

THE THICKNESS OF the face sheets of sandwich panels is often increased locally to provide for the load transfer around highly loaded locations such as joints or inserts. Such thickness increases are accomplished by adding extra plies to the face laminates, and a taper is produced by dropping off plies away from the area of localised loading. Such ply drops induce local bending effects. These local bending effects, in which the face sheet/core interaction plays an important role, induce interlaminar and bending stresses in the face sheet laminates, as well as stresses in the core/face sheet interface. Thus, the stress concentrations induced in the regions near the dropped plies may initiate delamination, core crushing or direct bending failure of the face sheets.

Ply drops are also used in monolithic/solid composite laminates in areas where the load carried by the laminates decreases, and fewer plies are needed.

3.1 Introduction to Ply Drop Effects

Ply drops in composite and sandwich laminates are used widely. Since abrupt changes in the parameters influencing structural performance appear around a ply drop, as described above, it is very important to be able to predict these changes such that an estimate of the stress and strain level can be determined and evaluated in order to avoid failure. In this section different ply drop types and their modelling will be described and investigated.

3.1.1 Ply Drop Types

The two most commonly used types of ply drops are:

- Exterior ply drops;
- Embedded ply drops;

which also are the ply drops included in the ESAComp Layer Drop-off Module, see Section 1.1.3. The two ply drop types are illustrated in Figure 3.1 and 3.2 as a ‘cut-out’ of a sandwich panel.

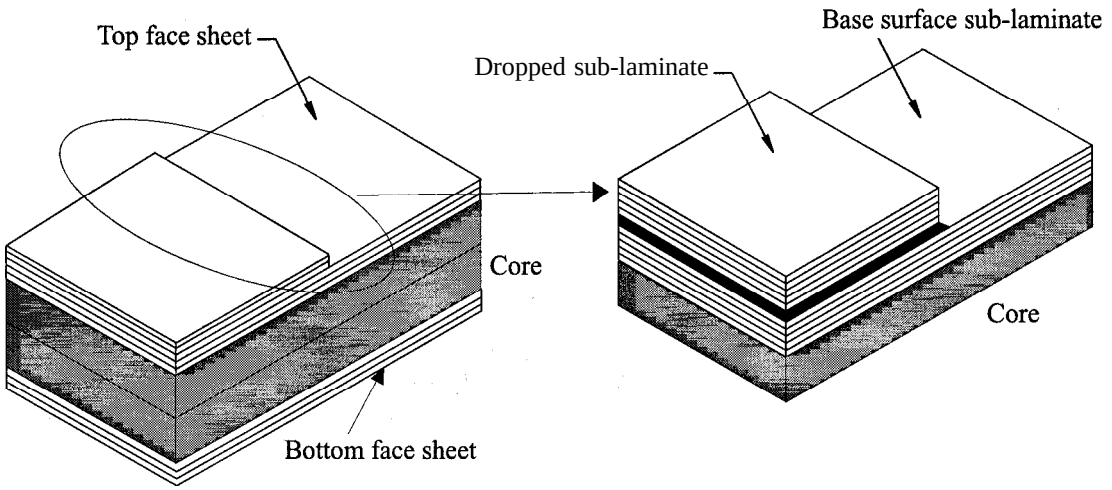

Figure 3.1: Illustration *of* a 'cut-out' *of* an exterior ply *drop* in *the face sheet of* a sandwich panel.

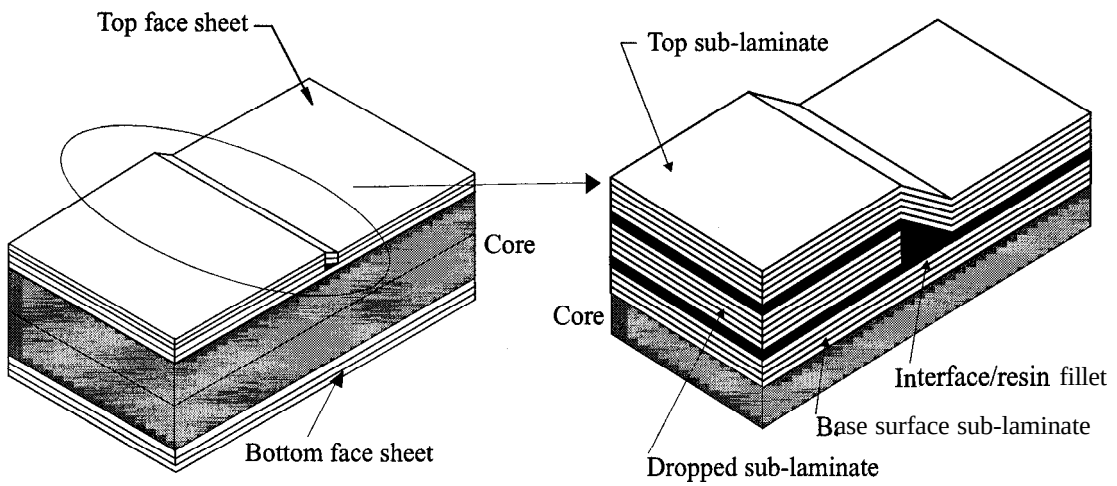

Figure 3.2: Illustration *of* a 'cut-out' *of an* embedded *ply drop in the face sheet of* a sandwich panel.

The embedded ply drops are by far the most efficient type from a structural point of view, but exterior ply drops are also used quite often.

As illustrated in Figures 3.1 and 3.2 the ply drops considered are appearing at one location, the ply drops can also appear by terminating more plies over a distance as illustrated in Figure 3.3.

If several ply drops appear very close to each other in a laminate, the interaction between the different ply drops must be taken into account. In the present work only ply drops appearing at

one location have been considered, but the structural modelling can easily be extended to take into account the interference effects induced when several closely spaced ply drops occur.

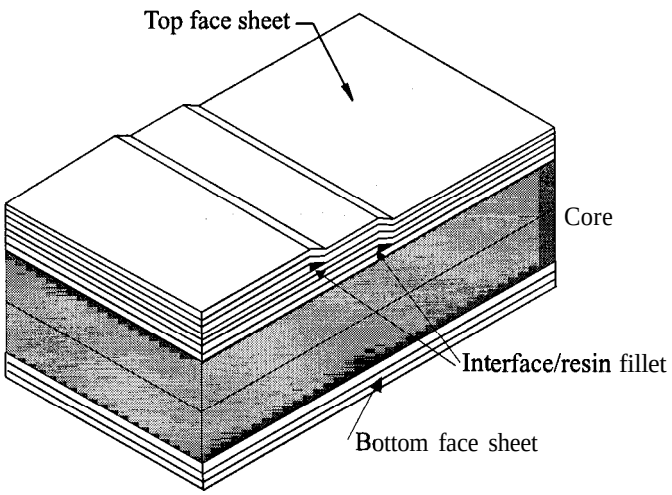

Figure 3.3: Illustration *of* more embedded *ply* drops *in the face sheet of* a sandwich panel.

3.1.2 State-of-the-Art in the Modelling of Ply Drop Effects

The analysis of the ply drop problem as encountered in monolithic composite laminates has been addressed in various references, such as Curry et al. (1987), ESDU, Data Item 91003 (1991), Thomas and Webber (1994), Wisnom and Jones (1995), Vizzini (1995), Botting et al. (1996), Rhim and Vizzini (1997) and Thomsen et al. (1998). In the quoted references analysis methods of varying complexity have‘been adopted, where the most elaborate analyses have been conducted using finite element modelling with refined meshing around the critical interface layers (Vizzini (1995), Botting et al. (1996), Rhim and Vizzini (1997)). A number of authors have investigated the mechanical behaviour of tapered laminates in order to get a basic understanding of the failure mechanisms and to predict delamination. Many of the authors have treated the laminates without taking into account the existence of interface layers between the plies, which then results in singular interlaminar stress fields when plies are dropped. It is therefore not possible to use a simple stress criterion to predict failure. A critical strain energy release rate approach has therefore been adopted for this type of problem (Thomas and Webber (1994) and Wisnom and Jones (1995)). Botting et al. (1996) and Vizzini (1995) introduced an interface/‘resin-rich’ layer between the plies in the modelling, which results in a more realistic prediction of the interface stress level, and they suggested a maximum von Mises or a maximum shear stress criterion as the basis for failure evaluation. Llanos and Vizzini (1992) investigated the effects of the inclusion of an adhesive interface layer between the plies in embedded ply drop problems in sandwich panels. They modelled the problems with and without an adhesive interface layer between the plies in the drop-off zone using finite element analyses, and compared the theoretical results with experimental results. The comparison showed that inclusion of an interface layer is necessary to accurately determine the state of stress in a tapered region. Ply drop problems in sandwich panels with tapered skin laminates (only exterior ply drops) have been treated by Thomsen et al. (1996a), where a simple approach has been proposed, which like Vizzini (1995) and Botting et al. (1996) assumes the existence of an interface/‘resin-rich’ layer between the plies, and which models the interaction between the tapered skin laminate and the core material by using a two-parameter elastic foundation model. The results were verified experimentally in

the elastic range (Thomsen et al. (1996b)). However, ply drop problems in sandwich panels with tapered skin laminates have in general received little attention, even though the short wavelength elastic response encountered in sandwich panels with tapered skin laminates generally induces more severe local bending effects than is the case in monolithic composite laminates with ply drops, see Thomsen et al. (1996a). Thomsen et al. (1998) later used the approach to predict delamination failure in CFRP/sandwich panels with exterior ply drops using a point stress criterion with the stresses calculated some distance away from the ply drop-off edge, and they found that the predicted results compared reasonably well with experimental investigations.

3.1.3 Objectives of The Layer Drop-off Module for ESAComp

The main objective of this module is to provide ESAComp with the capability capable of determining the stress and displacement fields in the most commonly used ply drop types as shown in Figure 3.1 and 3.2, i.e. exterior and embedded ply drops.

The main objective concerning the theoretical work on this topic has been to adopt and extend the principles suggested by Thomsen et al. (1996a) for the analysis of the exterior ply drop problem to the analysis of the corresponding and more complicated embedded ply drop problem. The analysis is carried out by considering a 'cut-out' in the region near a ply drop (see Figures 3.1 and 3.2). The local bending effects only extend a short distance to either side of the ply drop position, and the extension of the considered region is chosen so as to minimize or eliminate interference between the localized bending effects induced at the ply drop position and the imposed boundary conditions. Consequently arbitrary load and boundary conditions can be imposed in the analysis. In addition, the analysis for exterior ply drops suggested by Thomsen et al. (1996a) is extended such that the face sheets are treated as laminates modelled as wide beams including coupling effects.

The validity of the suggested approach for the analysis and design of composite and sandwich laminates with exterior and embedded ply drops is demonstrated through example results, and through comparison with results obtained by finite element analysis. In addition the developed solution procedures are used to conduct a parametric study on the influence of certain parameters influencing the structural performance. Finally, the implementation of the module into ESAComp is demonstrated.

3.2 Structural Modelling

Prepregs/FRP-plies are composed of fibres distributed in a matrix/resin material as illustrated in Figure 3.4.

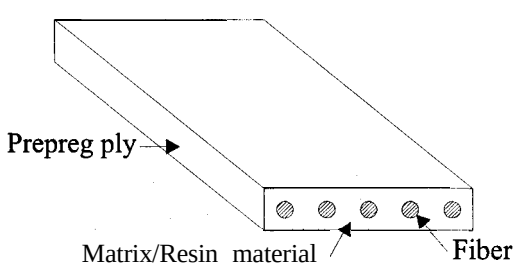

Figure 3.4: Idealised illustration of prepreg fibre reinforced plastic ply.

In the manufacturing process of laminates made of prepregs, the plies are placed on top of each other and subjected to a cure cycle, through which the matrix/resin material surrounding the fibres cures, and a connection between the individual plies is established. If the laminate is investigated in a microscope after the manufacturing process, it can be seen that resin-rich interface layers with no or very few fibres have been created during the curing process. This was demonstrated by, among others, Thomsen et al. (1998) on different CFRP-sandwich panel test specimens. Figure 3.5 shows a microscopic view of an interface layer between two plies in the skin of a sandwich panel test specimen, where the skins are made of the UD-prepreg system SE-84 from SP-systems. SE-84 is a low temperature cure ($80 - 120°C$) carbon/epoxy prepreg system (Thomsen et al. (1998)).

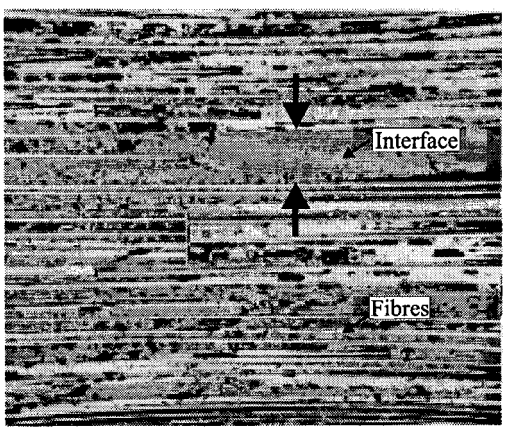

Figure 3.5: Microscopic (magnification: x 200) view of a interface *layer* between two plies *in* the skin *of* a sandwich panel test specimen, with *skins* made *of* the UD-prepreg system ($t_a = 0.03$ mm).

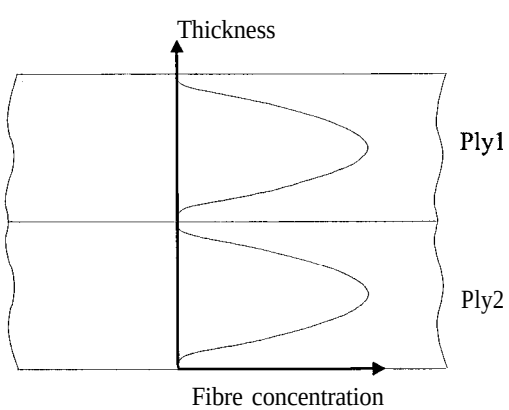

Figure 3.6: Schematic illustration of the fibre distribution within two neighbouring plies in a laminate made of prepregs.

In this case the interface layer thickness was nearly constant and the average thickness was

measured to t_a = 0.03 mm. Thus, it is clear that the fibres within a prepreg laminate are not evenly distributed over the thickness of the laminate, but are instead concentrated within the plies. A high concentration of fibres is seen within the plies, whereas the fibre concentration is very low at the interfaces between the plies. Figure 3.6 presents a schematic illustration of the distribution of fibres in two neighbouring plies in a laminate made of prepregs, based on the observations from Figure 3.5.

Thus, the stiffness of each ply should be determined based on the fibre distribution (unknown in reality) over the thickness as illustrated in Figure 3.6.

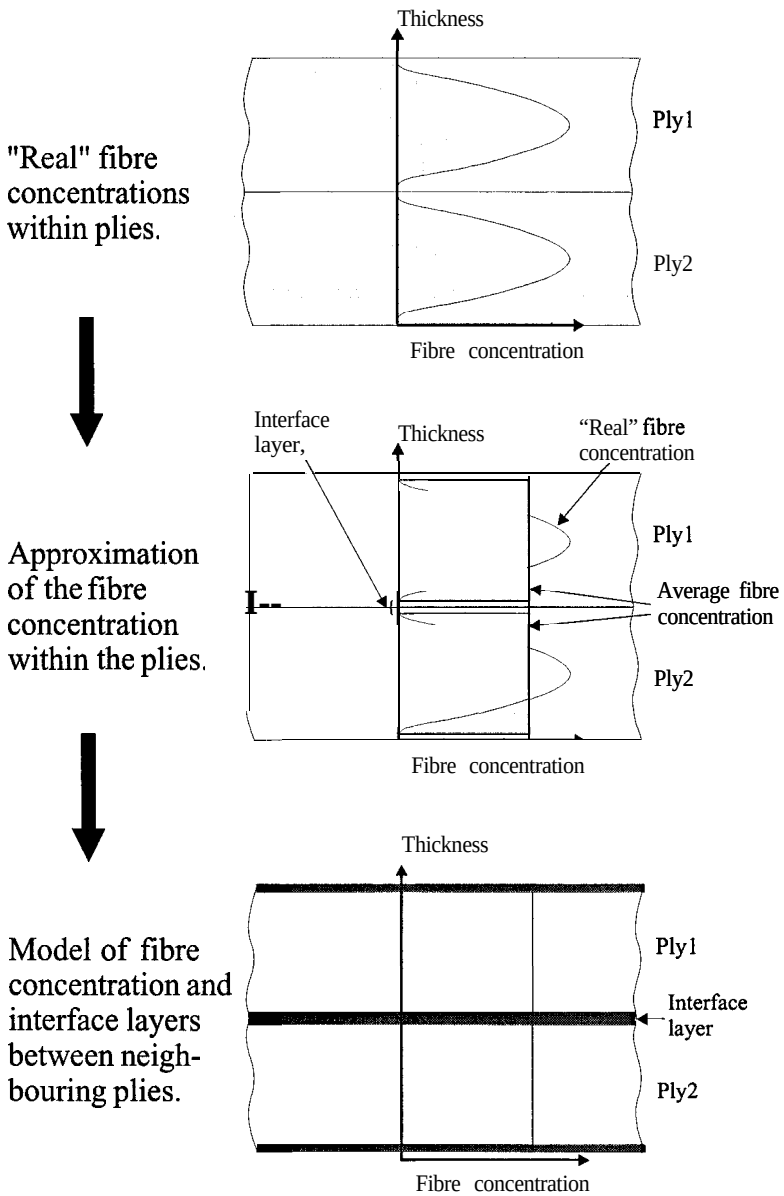

Figure 3.7: Illustration *of the idealization of the* fibre distribution *within* two neighbouring plies *in* a laminate made of prepregs *for* the purposes of the structural modelling.

However, for simplicity in the structural modelling the stiffness within the plies is assumed to be constant over the thickness. This is done by averaging the fibre distribution in the plies, and assuming the existences of a 'resin-rich' interface layer between the plies as illustrated in Figure 3.7

It should be noted here that the idealization shown in Figure 3.7 is only valid for laminates made of prepregs, whereas it is invalid for laminates manufactured by other methods such as Resin Transfer Moulding (RTM) or by wet lay-up, where individual layers are less distinguishable from one anot her.

Based on these considerations, a structural model for the exterior and embedded ply drop problems can be determined. Figure 3.8 illustrates a typical exterior ply drop section subjected to general loading conditions. The model constituent parts are a base-surface sub-laminate, a dropped sub-laminate, an interface/'resin-rich' layer and a core material in cases where the drop occurs in the face sheet laminate of a sandwich panel.

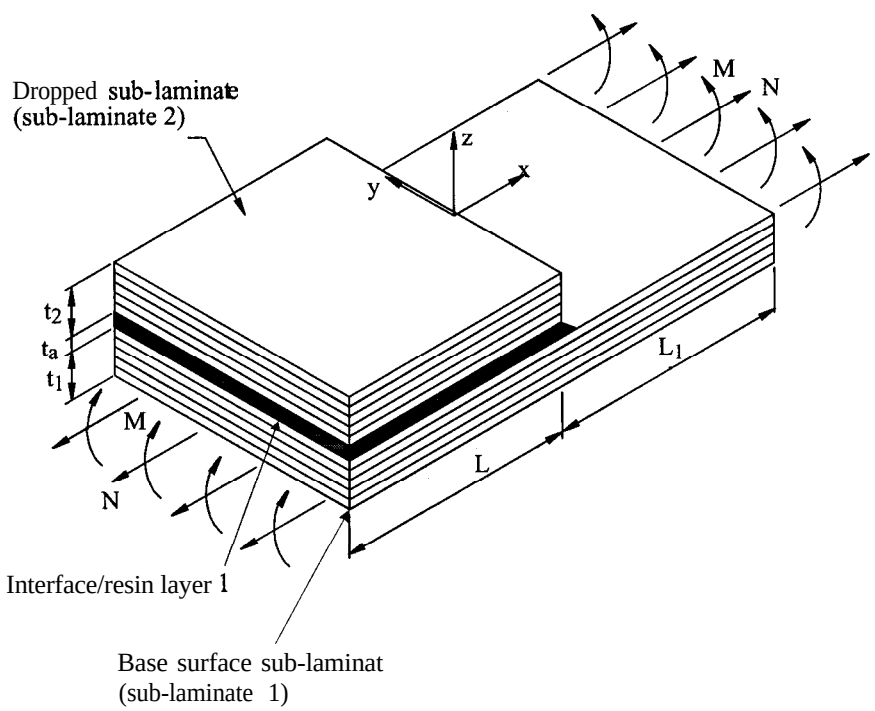

Figure 3.8: *Illustration of exterior* layer drop subjected to general loading conditions.

The sub-laminate thicknesses are t_1 and t_2 and the interface/'resin-rich' layer thickness is t_a.

Figure 3.9 illustrates a typical embedded ply drop subjected to general loading conditions. The model constituent parts are a base-surface sub-laminate, a dropped sub-laminate, a top sub-laminate and three interface/'resin-rich' layers, as well as a core material in cases where the drop occurs in the face laminate of a sandwich panel. The sub-laminates are in both cases considered to be generally orthotropic laminates.

The sub-laminate thicknesses are t_1, t_2 and t_3, and the interface/'resin-rich' layer thicknesses are t_{a1}, t_{a2} and t_{a3}. Within the transition region, i.e. $0 \leq x < L_2$ the interface/'resin-rich' layer thickness is:

$$t_{a3t}(x) = (t_1 + t_{a1} + t_{a2}) - ((t_1 + t_{a1} + t_{a2}) - t_{a3})/L_2) * x; \qquad (3.1)$$

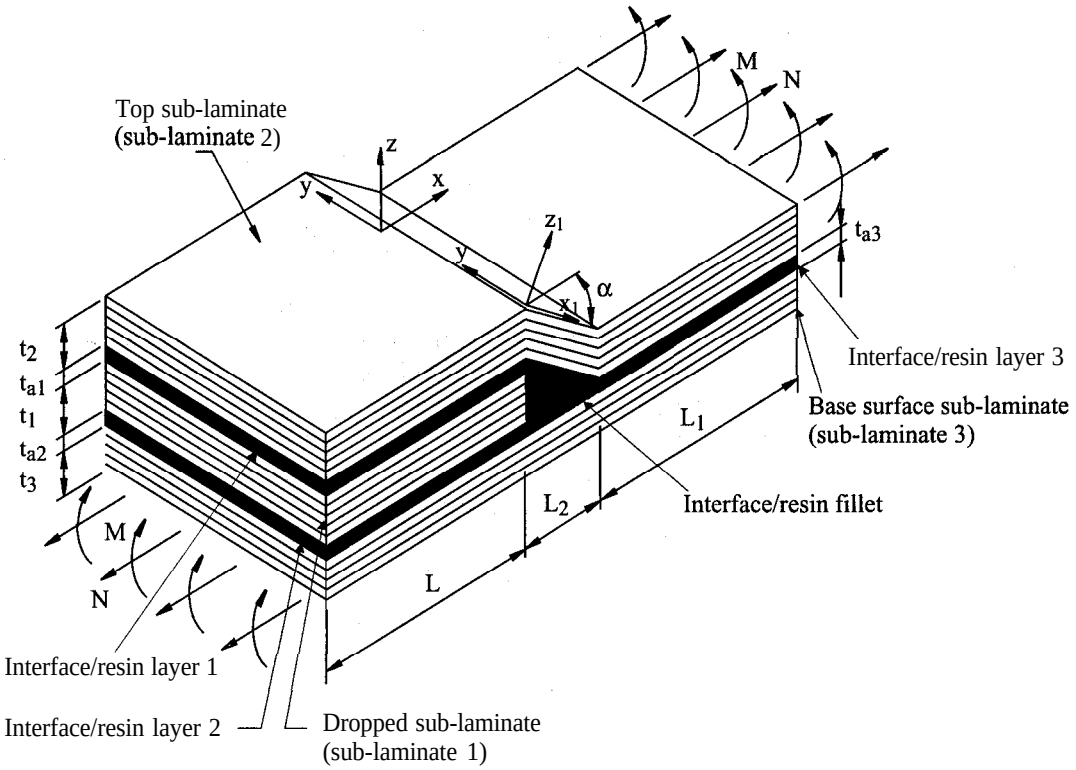

Figure 3.9: Illustration *of* embedded *layer* drop subjected to general loading *conditions.*

After adopting the structural configuration of the ply drop problems, as shown in Figures 3.8 and 3.9 with an interface/'resin-rich' layer between each sub-laminate, the modelling of the ply drop problems can be performed in the same way as the modelling of the adhesive bonded joints. Thus, the basic assumptions for the structural modelling are the same as used for the adhesive bonded joints described in Section 2.2.1, except that the sub-laminates for the ply drop problems have only been modelled as wide beams using the classical 'Bernoulli-Euler' or 'Kirchoff' assumptions. It will involve no principal difficulties to model the sub-laminates in the ply drop problems as plates in cylindrical bending, but this has not been incorporated into the layer drop-off module for ESAComp version 1.0.

The kinematic and constitutive relations used for the sub-laminates are the same as described in Section 2.2.2 and Section 2.2.3, respectively, and the interface/'resin-rich' layers are modelled using the spring model approach described in Section 2.2.4. For the cases where ply drops occur in the face sheets of sandwich panels the interaction between the face laminates and the core material still needs to be described.

Finally, the equilibrium conditions for the two ply drop configurations must be derived to complete the formulation of the set of equations governing the behaviour of the ply drop problems.

3.2.1 Interaction between the face laminates and the core material

In cases where sandwich panels with composite face sheets are considered, the interaction between the face sheets and the core material is modelled using a 'two-parameter' elastic foundation

model, which accounts for the shear interaction between the core and the face sheets. The elastic response of the core material is expressed according to Thomsen (1993), Thomsen (1995) following the approach of Vlasov and Leont'ev (1960) in a slightly modified form, which relates w_i and u_i to the core out-of-plane normal and shear stress components σ_c and τ_c:

$$\begin{aligned} \sigma_c &= K_z w_i \\ \tau_c &= K_x \left\{ u_i \left(x, -\tfrac{t_i}{2}\right) \right\}_{\substack{bending \\ contri.}} = K_x \tfrac{t_i}{2} \beta_i \qquad i = \begin{cases} 1 & for\ exterior\ ply\ drops \\ 3 & for\ embedded\ ply\ drops \end{cases} \end{aligned} \tag{3.2}$$

This two-parameter foundation model, which represents the simplest possible extension of the well-known Winkler foundation model (one-parameter model), Vlasov and Leont'ev (1960), assumes the existence of two elastic foundation moduli:

Ii,: determines the compressive/tensile strain in the foundation (core);

K_x: determines the shearing strain in the foundation (core), and thus defines the load-spreading capacity of the foundation.

Of the two foundation moduli, K_z is of most importance in describing the foundation response, and it is similar to the foundation modulus adopted in the 'classical' Winkler foundation model.

From the above it is recognised that a very essential issue pertaining to the quality of the suggested approach is the accuracy with which K_z and K_x can be expressed in terms of the elastic and geometric properties of the constituent materials (i.e. of the face sheets and the core). Several suggestions for such expressions can be found in the literature (mostly 'soil mechanics' related literature such as Vlasov and Leont'ev (1960), Hètenyi (1946), Kerr (1964) and Zhaohua and Cook (1983)), but unfortunately there are considerable difficulties associated with the establishment of generally valid expressions.

The most thorough approach to the treatment of this problem was presented by Vlasov and Leont'ev (1960) who derived the characteristics of 'single-layer' and 'multiple-layer' foundations from 3-D theory of elasticity. According to this approach, the behaviour of a 'single-layer' foundation characterised by its depth h_c can be described in terms of two constants of which one defines the foundation compressive/tensile strains (corresponding to K_z), and the other defines the foundation shearing strains (corresponding to IL;;). According to Vlasov and Leont'ev (1960), it is necessary a priori to assume a function for the decay of the through-the-thickness core displacement w_c through the elastic foundation (core). The simplest possible way to accomplish this is to assume that the decay is linear, i.e.:

$$w_c(x,z) = w_c(x, z = 0)\psi(z) = w_i(x)\psi(z) \ , \ \psi(z) = \frac{h_c - z}{h_c}, \ (\mathbf{i} = 1,3) \tag{3.3}$$

where z is the through-the-thickness (out-of-plane) coordinate and h_c is the foundation depth (i.e. the core thickness). By adopting the simple linear 'decay function' $\psi(z)$ it can be shown that K_z and K_x can be expressed as follows (Thomsen et al. (1996a)):

$$K_z = \frac{E_0}{h_c(1-\nu_0^2)} \ , \quad K_x = \frac{E_0}{3t^*(1-\nu_0)} \tag{3.4}$$

where

$$E_0 = \frac{E_{zc}}{1-\nu_{zxc}^2} \ , \quad \nu_0 = \frac{\nu_{zxc}}{1-\nu_{zxc}} \tag{3.5}$$

and

$$t^* = \begin{cases} \text{Exterior}: & t_1 \text{ t } t_a \text{ t } t_2 & for \quad -L \le x < 0 \\ & t_1 & for\ 0 \le \text{x} < L_1 \\ \text{Embedded}: & t_1 + t_{a1} \text{ t } t_2 \text{ t } t_{a2} \text{ t } t_3 & \text{for} \quad -L \le x < 0 \\ & t_2 + t_3 \text{ t } t_{a3t}(x) & for\ 0 \le x < L_2 \\ & t_2 \text{ t } t_3 \text{ t } t_{a3} & for \quad L_2 \le x < L_1 \text{ t } L_2 \end{cases} \tag{3.6}$$

E_{zc} and ν_{zxc} are the out-of-plane elastic modulus and Poisson's ratio of the core material. The simple linear decay assumption described above represents a good approximation for foundations of small depth, but for foundations of larger depth it is recommended to use an 'exponential' decay assumption (Vlasov and Leont'ev (1960)). The recommendations pertaining to the distinction between foundations of small depth and foundations of larger depth are not clear, and the choice of decay function often turns out to be a case of 'trial and error' in practice.

3.2.2 Equilibrium Equations

The equilibrium equations are formulated based on equilibrium elements (as for the adhesive bonded joints) within each region of the ply drop configurations, as shown in Figure 3.8 and Figure 3.9. The equilibrium equations are derived based on the assumption that the sub-laminates are face sheets of a sandwich panel. Thus, in case the ply drops occur in a monolithic laminate. the stresses between the laminate and the core will be equal to zero, i.e. $\tau_c = \sigma_c = 0$.

Exterior Ply Drops

The equilibrium equations are derived based on Figure 3.10 and Figure 3.11.

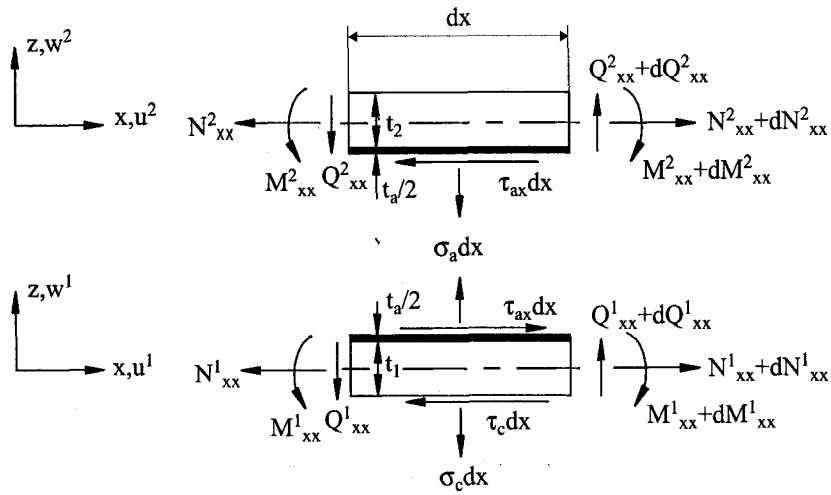

Figure 3.10: Equilibrium elements *of* exterior *ply* drop in *the region* $-L \le x \le 0$.

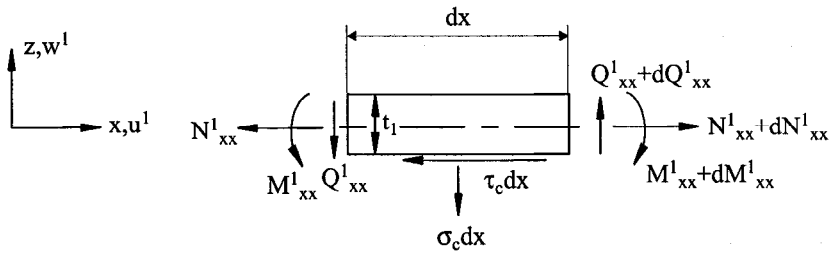

Figure 3.11: Equilibrium *element of exterior ply* drop *in the* region $0 \leq x \leq L_1$.

With reference to Figure 3.8, the equilibrium equations are formulated on each side of the drop as follows:

$$\left.\begin{aligned} N^1_{xx,x} &= \tau_c - \tau_{ax}, & N^2_{xx,x} &= \tau_{ax} \\ Q^1_{x,x} &= \sigma_c - \sigma_a, & Q^2_{x,x} &= \sigma_a \\ M^1_{xx,x} &= Q^1_x - \tau_c \tfrac{t_1(x)}{2} - \tau_{ax} \tfrac{t_1(x)+t_a}{2}, & M^2_{xx,x} &= Q^2_x - \tau_{ax} \tfrac{t_2(x)+t_a}{2} \end{aligned}\right\} -L \leq x \leq 0.$$

$$\left.\begin{aligned} N^1_{xx,x} &= \tau_c - \tau_{ax}, \\ Q^1_{x,x} &= \sigma_c - \sigma_a, \\ M^1_{xx,x} &= Q^1_x - \tau_c \tfrac{t_1(x)}{2} - \tau_{ax} \tfrac{t_1(x)+t_a}{2}, \end{aligned}\right\} 0 \leq x \leq L_1. \tag{3.7}$$

where $N^i_{xx}, Q^i_x, M^i_{xx}$ $(i = 1,2)$ are the normal stress, transverse shear stress and bending moment resultants in the sub-laminates, σ_c is the core transverse normal stress component at the face sheet/core interface, τ_c is the shear stress component at the face sheet/core interface, and finally σ_a, and τ_{ax} are the interface/'resin-rich' layer transverse normal and shear stress components 'for each of the interface layers.

Embedded Ply Drops

Based on Figure 3.12, the equilibrium equations for the first region $(-L \leq x < 0$, see Figure 3.9) are derived:

$$-L \leq x < 0 \left\{ \begin{aligned} N^1_{xx,x} &= \tau_{ax2} - \tau_{ax1} \\ Q^1_{x,x} &= \sigma_{a2} - \sigma_{a1} \\ M^1_{xx,x} &= Q^1_x - \tau_{ax1} \tfrac{t_1+t_{a1}}{2} - \tau_{ax2} \tfrac{t_2+t_{a2}}{2} \\ \\ N^2_{xx,x} &= \tau_{ax1} \\ Q^2_{x,x} &= \sigma_{a1} \\ M^2_{xx,x} &= Q^2_x - \tau_{ax1} \tfrac{t_2+t_{a1}}{2} \\ \\ N^3_{xx,x} &= \tau_c - \tau_{ax2} \\ Q^3_{x,x} &= \sigma_c - \sigma_{a2} \\ M^3_{xx,x} &= Q^3_x - \tau_{ax2} \tfrac{t_3+t_{a3}}{2} - \tau_c \tfrac{t_3}{2} \end{aligned} \right. \tag{3.8}$$

where $N^i_{xx}, Q^i_x, M^i_{xx}$ $(i = 1,2,3)$ are the normal stress, transverse shear stress and bending moment resultants in the sub-laminates, σ_c is the core transverse normal stress component at

the face sheet/core interface, τ_c is the shear stress component at the face sheet/core interface, and finally σ_{ai}, and τ_{axi} $(i = 1,2)$ are the interface/'resin-rich' layer transverse normal and shear stress components for each of the interface layers.

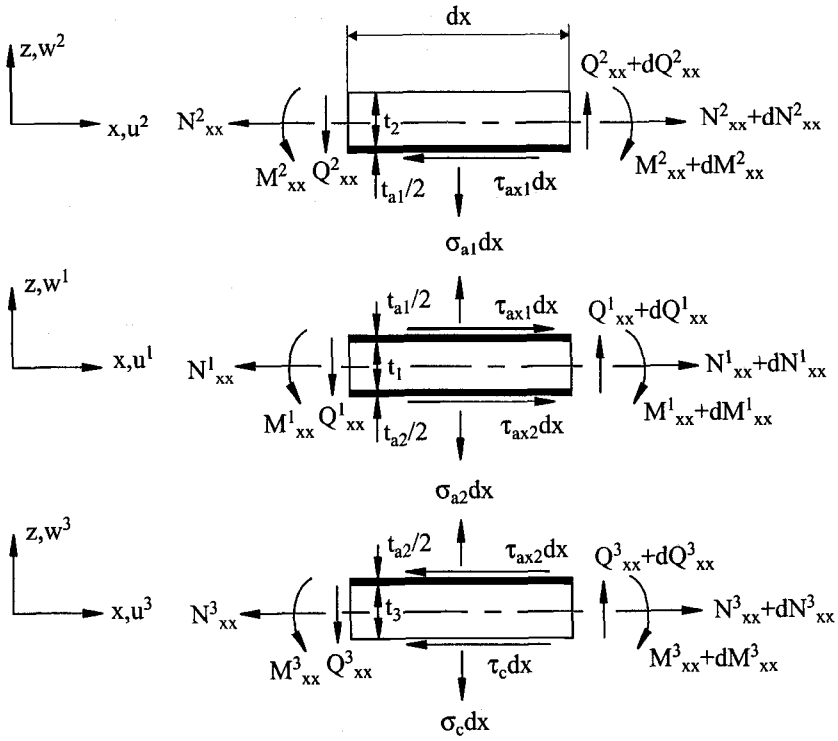

Figure 3.12: Equilibrium *elements of* embedded drop *for* $-L \leq x < 0$.

Within the transition region, i.e. $0 \leq$ x $< L_2$, sub-laminate 2 is described in the local coordinate system (x_1, y, z_1) as shown in Figure 3.9. Within this region it is also assumed that the sub-laminates are fully bonded through the interface/resin fillet and that the fillet thickness varies linearly. The equilibrium equations for the transition region $(0 \leq$ x $< L_2)$ are derived based on Figure 3.13:

$$0 \leq x < L_2 \left| \begin{array}{rcl} N^{2l}_{xxl,xl} & = & \tau^*_{ax3} \\ Q^{2l}_{xl,xl} & = & \sigma^*_{a3} \\ M^{2l}_{xxl,xl} & = & Q_{2l} - \tau^*_{ax3}\frac{t_2+t_{a1}}{2} \\ & & \\ N^3_{xx,x} & = & \tau_c - \tau_{ax3} \\ Q^3_{x,x} & = & \sigma_c - \sigma_{a3} \\ M^3_{xx,x} & = & Q_3 - \tau_{ax3}\frac{t_3+t_{a3t}}{2} - \tau_c\frac{t_3}{2} \end{array} \right. \tag{3.9}$$

where the relationship between τ_{ax3}, σ_{a3} and τ^*_{ax3}, σ^*_{a3} in Equation 3.9 and shown in Figure 3.13, is established through equilibrium of the interface/resin fillet:

$$\tau^*_{ax3} = \tau_{ax3}cos(\alpha) - \sigma_{a3}sin(\alpha), \quad \sigma^*_{a3} = \tau_{ax3}sin(\alpha) \text{ t } \sigma_{a3}cos(\alpha) \tag{3.10}$$

where α is the angle between the x and x_1 axis as shown in Figure 3.9. The equilibrium equations

for the region $L_2 \leq x < L_1 + L_2$ are the same as for the exterior ply drop problem in the region $-L \leq x < 0$, and therefore not shown here.

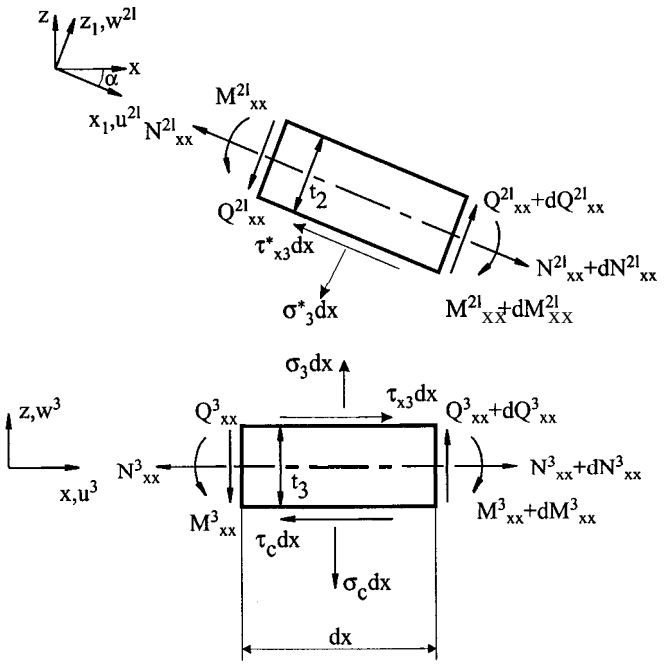

Figure 3.13: Equilibrium elements of embedded drop for $0 \leq x < L_2$.

3.2.3 The Complete Set of System Equations

From the equations derived, the complete set of system equations for the ply drop problems are formed in the same way as for the adhesive bonded joints. Thus, combination of Equations 2.11, 2.13, 2.14 and 3.2, together with the appropriate equilibrium equations, leads to the set of governing equations within each of the regions.

For the exterior ply drop problems the set of governing equations consists of 12 linear coupled first-order ordinary differential equations within the region $-L \leq x < 0$, and of 6 within the region $0 \leq x < L_1$, since only one sub-laminates exist in this region.

For the embedded ply drop problem the set of governing equations consists of 18 linear coupled first-order ordinary differential equations describing the system behaviour within the region $-L \leq x < 0$, and of 12 within the regions $0 \leq x < L_2$ and $L_2 \leq x < L_1 + L_2$. The governing equations for both ply drop types within each of the regions are given in Appendix B.

The solution vector containing the fundamental variables for each of the sub-laminates are:

$$\left\{y^i\right\} = \left\{u_0^i, w^i, \beta_x^i, N_{xx}^i, M_{xx}^i, Q_x^i\right\} \quad i = \begin{cases} 1,2 \textit{ for exterior ply drops} \\ 1,2,3 \textit{ for embedded ply drops} \end{cases} \tag{3.11}$$

As for the adhesive bonded joints, the fundamental variables are those variables, which appear in the boundary conditions on an edge x = constant. These variables will be determined through the analysis.

3.2.4 Boundary Conditions

To solve the problem the boundary and continuity conditions have to be stated.

Exterior Ply Drops

With references to Figure 3.8 the boundary and continuity conditions are defined in the same way as for the bonded doubler joint defined in Section 2.2.3.

Embedded Ply Drops

With references to Figure 3.9 the boundary and continuity conditions are defined as follows:

$$
\begin{aligned}
x = -L: \quad & prescribed: && u_{0i} \text{ or } N_i,\ w_i \text{ or } Q_i,\ \beta_i \text{ or } M_i, \quad \text{i} = 1,2,3 \\
x = 0: \quad & adherend\ 1: && N_1 = M_1 = Q_1 = 0 \\
& adherend\ 2: && u_{02l} = u_{02}cos(\alpha) - w_2 sin(\alpha) \\
& && w_{2l} = u_{02}sin(\alpha) \text{ t } w_2 cos(\alpha) \\
& && \beta_{2l} = \beta_2 \\
& && N_{2l} = N_2 cos(\alpha) - Q_2 sin(\alpha) \\
& && M_{2l} = M_2 \\
& && Q_{2l} = Q_2 cos(\alpha) \text{ t } N_2 sin(\alpha) \\
& adherend\ 3: && Continuity\ across\ junction \\
x = L_2: \quad & adherend\ 2: && u_{02} = u_{02l}cos(\alpha) + w_{2l}sin(\alpha) \\
& && w_2 = -u_{02l}sin(\alpha) \text{ t } w_{2l}cos(\alpha) \\
& && \beta_2 = \beta_{2l} \\
& && N_2 = N_{2l}cos(\alpha) + Q_{2l}sin(\alpha) \\
& && M_2 = M_{2l} \\
& && Q_2 = Q_{2l}cos(\alpha) - N_{2l}sin(\alpha) \\
& adherend\ 3: && Continuity\ across\ junction \\
x = L_1 + L_2: \quad & prescribed: && u_{0i} \text{ or } N_i,\ w_i \text{ or } Q_i,\ \beta_i \text{ or } M_i, \quad i = 2,3
\end{aligned}
\tag{3.12}
$$

The boundary conditions imposed at the ply drop, i.e. at x = 0, are derived from the assumption that the edge of sub-laminate 1 is free, and does not participate in the load transfer, see Figure 3.9.

After the governing equations have been derived and the boundary and continuity conditions have been formulated, the ply drop problems can be solved using the ‘multi-segment method of integration’. The method is implemented and used in exactly the same way as for the adhesive

bonded joint problems, and reference is made to Section 2.2.8 for the details of the 'multi segment method of integration' and its implementation.

3.3 Limitation of the Approach

To conclude the presentation of the mechanical model, some comments concerning the implications and limitations of the suggested approach are given. For ply drops in composite laminates acting as face sheets of a sandwich laminate, the method presented relies heavily upon the assumption that the face sheet/core interaction can be modelled by use of an elastic foundation model (two-parameter foundation model). Obviously, the application of such a model cannot be justified in a general sense, as it is impossible to specify constant values of the elastic foundation moduli K_z and K_x, which are appropriate for deformations of any (arbitrary) deflectional wavelength λ. The elastic wavelength λ can be calculated from the following expressions (Thomsen (1993), Vlasov and Leont'ev (1960)):

$$\lambda = 2\pi L_0, \quad L_0 = \sqrt[4]{\frac{D^*}{K_z}} \tag{3.13}$$

where L_0 is known as the characteristic length, Vlasov and Leont'ev (1960), and D^* is the laminate bending stiffness. For the exterior ply drop configuration D^* is defined by:

$$D^* = \begin{cases} Combined\ bending\ stiffness \\ of\ sub-laminates\ 1\ and\ 2\ for\ -L \le x \le 0 \\ \\ D_{11}^1\ for\ 0 \le x \le L_1 \end{cases} \tag{3.14}$$

For the embedded ply drop configuration D^* is defined by:

$$D^* = \begin{cases} Combined\ bending\ stiffness \\ of\ sub-laminates\ 1,2\ and\ 3\ for\ -L \le x \le 0 \\ \\ Combined\ bending\ stiffness \\ of\ sub-laminates\ 2\ and\ 3\ for\ 0 \le x \le L_1 + L_2 \end{cases} \tag{3.15}$$

The reason why it is impossible to specify values of K_z and K_x that are appropriate for any deflectional wavelengths is that the shearing deformations of the core material (foundation) become very influential for deformations with short wavelengths, thus implying that proper modelling of the face sheet/core interaction can only be achieved by application of a continuum formulation for the core material. For practical sandwich laminates, however, the bounds imposed by the vaguely formulated concept of deformations with short wavelength are not likely to be active, as 'realistic' values of the bending stiffness D^* and the foundation modulus Ii, will ascertain sufficiently large X-values to ensure that the elastic foundation approach will provide good results. As a rule of thumb, the elastic foundation approach will generally provide good results if the following inequality is satisfied (Thomsen (1995)):

$$\begin{gathered} \lambda \gg t_1, \quad if\ t_1 \gg t_2\ for\ exterior\ ply\ drops \\ \\ \lambda \gg t_3, \quad if\ t_3 \gg t_1, t_2\ for\ embedded\ ply\ drops \end{gathered} \tag{3.16}$$

Another important point is that the modelling of the core by application of an elastic foundation model implies that the core material is assumed to support the face laminates continuously. This,

off course, is not strictly true for honeycomb core sandwich laminates, where the face sheets are supported in a discrete manner along the edges of the individual honeycomb cells. Whether the elastic foundation approach provides a good mechanical model for the face sheet/core interaction is determined by the wavelength of the elastic deformations λ, and the cell-size of the honeycomb which is denoted by D_{cell}. The following guidelines are suggested (Thomsen (1995)):

$$\lambda \geq D_{cell}: \quad \left\{ \begin{array}{l} \textit{The elastic foundation model can be expected to} \\ \textit{provide a good description, especially} \text{ if } \lambda >> D_{cell}. \end{array} \right.$$

$$\lambda < D_{cell}: \quad \left\{ \begin{array}{l} \textit{The elastic foundation model is inadequate,} \text{ as } \textit{the face} \\ \textit{sheets will tend to act as plates within the boundaries} \\ \textit{of each honeycomb cell. The quality of the model} \\ \textit{degrades drastically} \text{ if } \lambda \ll D_{cell}. \end{array} \right. \tag{3.17}$$

For most honeycomb cored sandwich laminates the elastic foundation approach will provide a good description. However, sandwich laminates with extremely thin face sheets in combination with relatively large cell size honeycombs are used for certain space craft applications. For such cases, the elastic wavelengths encountered can be very close to (or even violate) the limits imposed by the inequalities of Equations 3.17.

Finally, some comments pertaining to the influence of the core thickness h_c will be given. In the adoption of the elastic foundation approach it is assumed, that the face laminate/core interaction can be treated separately for each side of the sandwich laminate. In other words, the existence of interference effects between the face sheets on opposite sides of the sandwich laminate is ignored. This assumption is only valid if the decay of the local bending effects through the thickness of the core is very steep. Thus, it must be expected that the suggested model will be inadequate for sandwich laminates with very thin core layers, where interaction between the local bending effects induced by dropping layers on each side of the sandwich laminate are likely to contribute significantly to the elastic response characteristics. For cases where the core thickness is small a more appropiate model could be formulated using the 'high-order theory approach' concept as introduced by Frostig et al. (1991), Frostig (1992) and Frostig (1993). In this type of model the core material is modelled as a continuum possesing only out-of-plane stiffness, which allows for an explicit description of the interaction between the face sheets of the considered sandwich panel.

3.4 Examples, Discussion and Comparison with FE-Analysis

In order to show the applicability of the developed solution procedures, two examples will be presented for each of the ply drop types. One example where the ply drop occurs in a sandwich laminate, and one example where the ply drop occurs in a monolithic (or solid) laminate. For the latter, the results obtained are compared with a finite element analysis to evaluate the validity of the approach.

3.4.1 Exterior versus Embedded Ply Drops in a Sandwich Laminate

The basic material properties for the sandwich laminate used in the examples are given by:

Plies	5245C/T-800 UD prepregs: T-800 intermediate modulus carbon fibres in a 120°C to 190°C curing modified bismaleimide resin system. $E_x = 165.0$ GPa, E_y = 9.8 GPa, G_{xy} = 4.8 GPa, ν_{xy} = 0.31, h = 0.152 mm
Core	Hexcel Aluminium honeycomb: 3/16"-5052-1/1000" Core thickness c = 10.0 mm, E_c = 517 MPa, ν_c = 0.3
Interface/Resin-rich layer	Modified bismaleimide resin of prepreg system. $E_a = 3.3$ GPa, ν_a = 0.4, t_a = 0.03 mm

Table 3.1: Specification *of plies,* resin and core material properties used in the example *for* both *ply drop types in* a sandwich panel.

The sub-laminates assumed in the two examples are unsymmetric and unbalanced, which means that laminate coupling effects are included in the analyses.

Exterior Ply Drop Example

The lay-up of the sub-laminates, the dimensions as well as the boundary conditions for the exterior ply drop are shown in Table 3.2.

Lengths	$L = 50$ mm, $L_1 = 50.0$ mm;
Face sheet laminate	$[+45°, 0°, 0°, +45°, 0°, 0°, +45°, 90°, 0°]$, t = 1.064 mm
Core	$h_c = 10$ mm.
Dropped laminate	$[+45°, 0°]$, $t_2 = 0.304$ mm
Base-laminate	$[0°, +45°, 0°, 0°, +45°, 90°, 0°]$, t_1 = 0.760 mm
Load & B.C.	$x = -L$: $u^i = w^i = \beta_x^i = 0$, $(i=1,2)$ $x = L_1 + L_2$: $w^1 = \beta_x^1 = 0$, $N_{xx}^1 = 1$ N/mm;

Table 3.2: Sub-laminate lay-up, thicknesses, lengths and *boundary* conditions *used for* the exterior ply drop in a sandwich panel.

The exterior ply drop configuration used in the example is shown in Figure 3.14.

The boundary conditions of the 'cut-out' of the exterior ply drop example are chosen such that clamping conditions are present at the left end, and such that uniform longitudinal displacements, equivalent to an in-plane normal load of N_{xx}^1= 1 N/mm, are imposed at the right end, i.e. at x = L. Of course, the boundary conditions contain an element of arbitrariness. However, the actual boundary conditions imposed are not very important, as the local bending effects only extend a short distance to each side of the ply drop-off.

The main results, i.e. selected results from the analysis, are shown in Figure 3.15-3.20.

The lateral displacements of the sub-laminates are shown in Figure 3.15.

From Figure 3.15 it is seen that strong local bending effects occur close to the ply drop at x = 0, and that the bending effects are strongly damped due to the presence of a core material. It is also observed that the dropped plies tend to peel of the base-surface laminate at the ends of the drop-off zone, i.e. at x = 0.

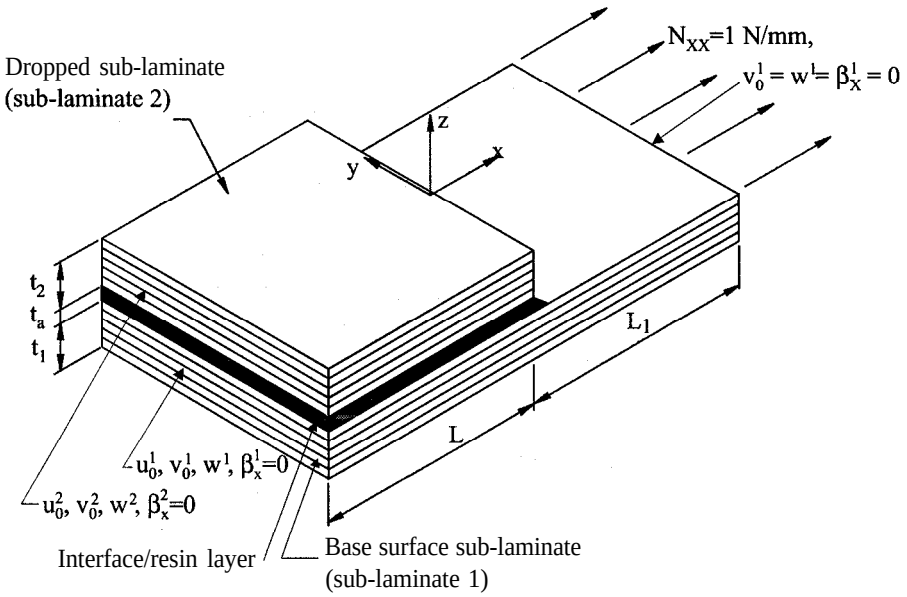

Figure 3.14: Exterior ply drop configuration clamped at *the* left end. A uniform longitudinal displacement is imposed at the right end, i.e. at x = L_1, equivalent to an in-plane normal *force* N = 1 N/mm $\Leftrightarrow \sigma_N = \frac{N}{t_1}$ = 0.94 *MPa*, t_1 = 1.064 mm, t_2 = 0.304 mm, t_a = 0.03 mm, L = 50 mm, L_1 = 50 mm.

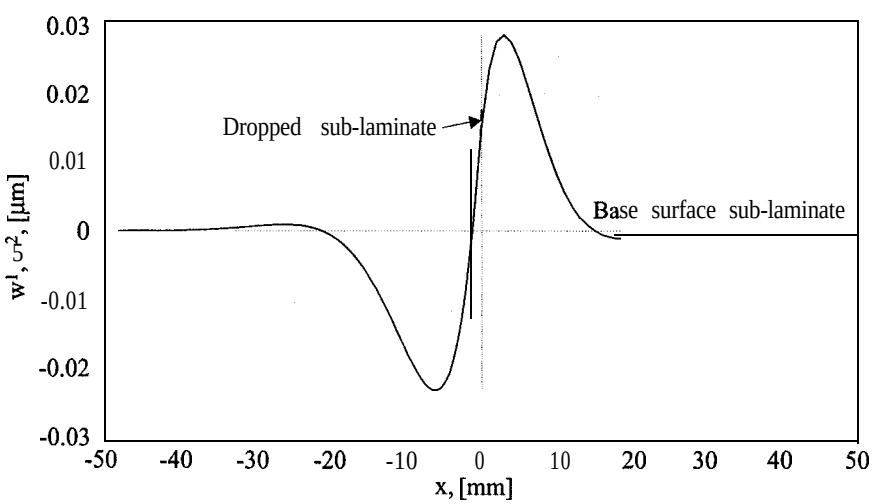

Figure 3.15: Lateral displacements w_1 and w_2 *of the two* sub-laminates of an exterior *ply* drop configuration in a *sandwich laminate*

In Figure 3.16 the predicted interface/'resin-rich' layer stresses are shown.

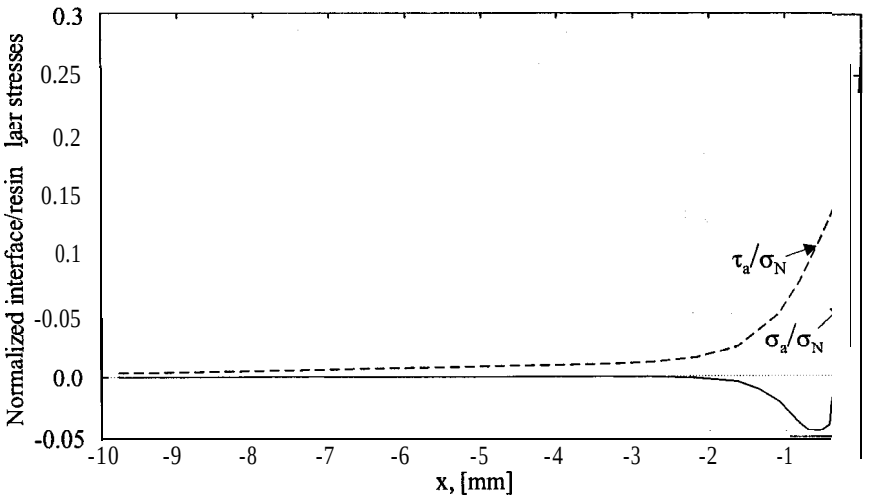

Figure 3.16: *Interface/'resin-rich' layer* stresses in *the* interface *of* the original *face sheet* laminate *of* an exterior *ply drop* configuration in a sandwich laminate.

From Figure 3.16 it is seen that the presence of interface/'resin-rich' transverse normal and shear stresses is very localized. As for the adhesive bonded joints the peak shear stresses appear at the end of the interface/'resin-rich' layer. In the structural model of the exterior ply drop configuration it is implicitly assumed that a free edge of the 'resin-rich' layer exists. This does not correlate well with the results of the analysis, i.e. that the interface shear stresses reach their extremum value exactly at x = 0. However, in the manufacturing process of the ply drop configuration (usually a co curing process) a surplus of resin material will form a 'spew-fillet' of the end of the drop-off zone as for adhesive bonded joints, see Section 2.5. Thus, the prediction of the adopted model that the peak stresses are located at x = 0 correlates well with the nature of the 'physical' drop-off problem. In other words, the discussion of the existence and the effects of the spew-fillet, given in Section 2.5 for adhesive bonded joints, is valid for the exterior ply drop problem as well.

In Figure 3.17 the face laminate/core interface stresses are displayed.

It is seen that the predicted interface transverse normal stresses follows a pattern proportional to the lateral displacements of sub-laminate 1. This is a consequence of the assumption that the transverse normal stresses σ_c at the face laminate/core interface are proportional with the lateral displacements, w_1, of the base-surface sub-laminate. It is seen that two local peaks of σ_c are present, one compressive peak on the left side of the ply drop, and one tensile peak on the right side of the ply drop. The peak values of σ_c and τ_c are very small compared with the stresses in the interface/'resin-rich' layers.

In Figure 3.18 the in-plane normal stress resultants are displayed.

From Figure 3.18 it is seen that the in-plane normal stress resultants N_{xx}^1 and N_{xx}^2 are constant over the length of the considered ply drop configuration, except in the area around the drop-off. In the area $-L \leq$ x < 0 the two sub-laminates share the total in-plane load between them as depicted by their in-plane stiffnesses.

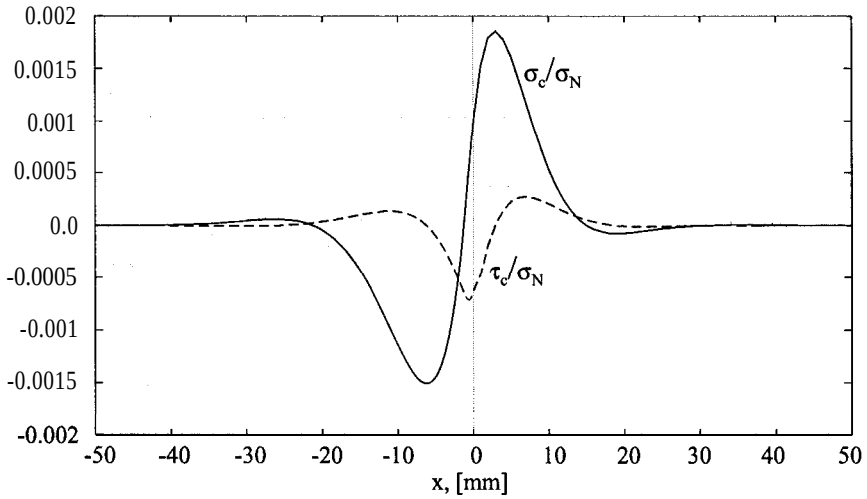

Figure 3.17: The face laminate/core interface stresses of an exterior ply drop configuration in a sandwich laminate.

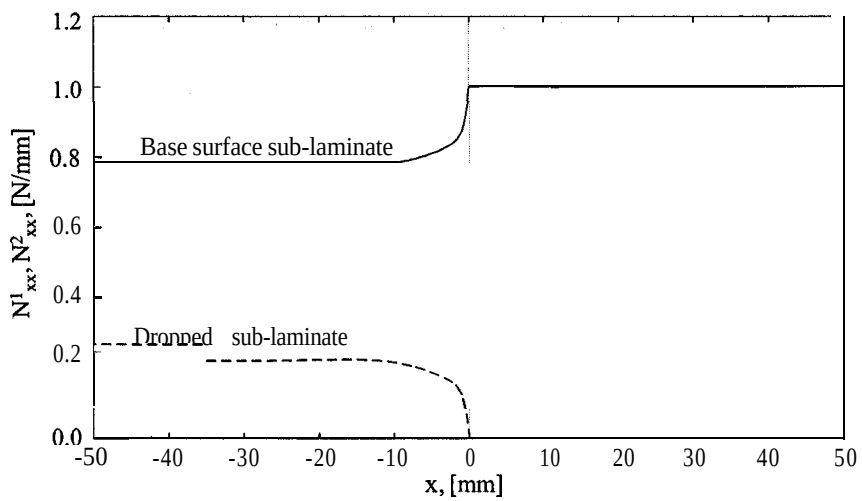

Figure 3.18: In-plane normal stress resultants N^1_{xx} and N^2_{xx} in the sub-laminates of an exterior ply drop configuration in a sandwich laminate

Figure 3.19 shows the distribution of the bending moment resultants M^1_{xx} and M^2_{xx} in the sub-laminates.

It is seen that significant bending moment resultants are present in the area close to the ply drop at $x = 0$, and that the bending moment resultants M^1_{xx} induced in the base-surface sub-laminate are much larger than the bending moment resultants induced in the dropped sub-laminate.

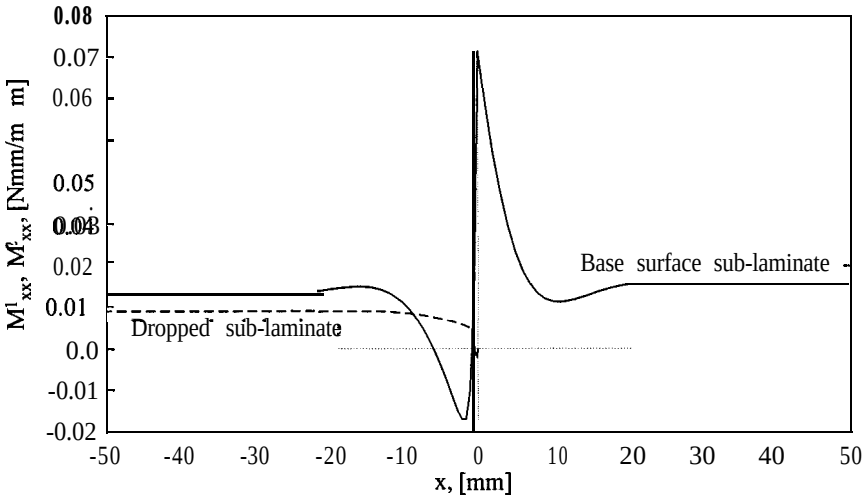

Figure 3.19: Bending moment resultants M_{xx}^{1} and M_{xx}^{2} in the sub-laminates of an exterior ply drop configuration *in* a sandwich laminate

Figure 3.20 shows the distributions of the out-of-plane shear stress resultants Q_x^1 and Q_x^2 in the sub-laminates.

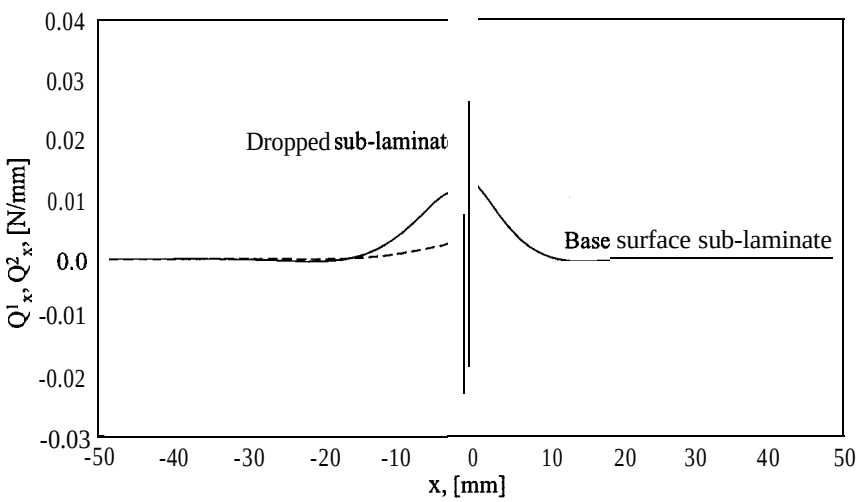

Figure 3.20: Out-of-plane shear stress resultants Q_x^1 *and* Q_{xx}^2 in the sub-laminates *of* an exterior ply drop configuration in a sandwich laminate

It is observed that the out-of-plane shear stress resultants are small compared with the applied loading N_{xx}^1 = 1 N/mm, but that the shear stress resultants are very localised close to the ply drop, thus indicating the presence of strong local bending effects in the ply drop zone.

Embedded Ply drop Example

Instead of dropping the outer plies of the face sheets of the laminates as shown in Figure 3.1 (i.e. exterior ply drop), internal plies can be dropped (i.e. embedded ply drop). Thus, in the following the same sandwich panel configuration as used for the exterior ply drop example will be used to show the output from the analysis obtained for an internal (or embedded) ply drop. In this case two internal plies of the face sheet laminates will be dropped instead of two external plies.

The embedded ply drop configuration assumed in the example is shown in Figure 3.21.

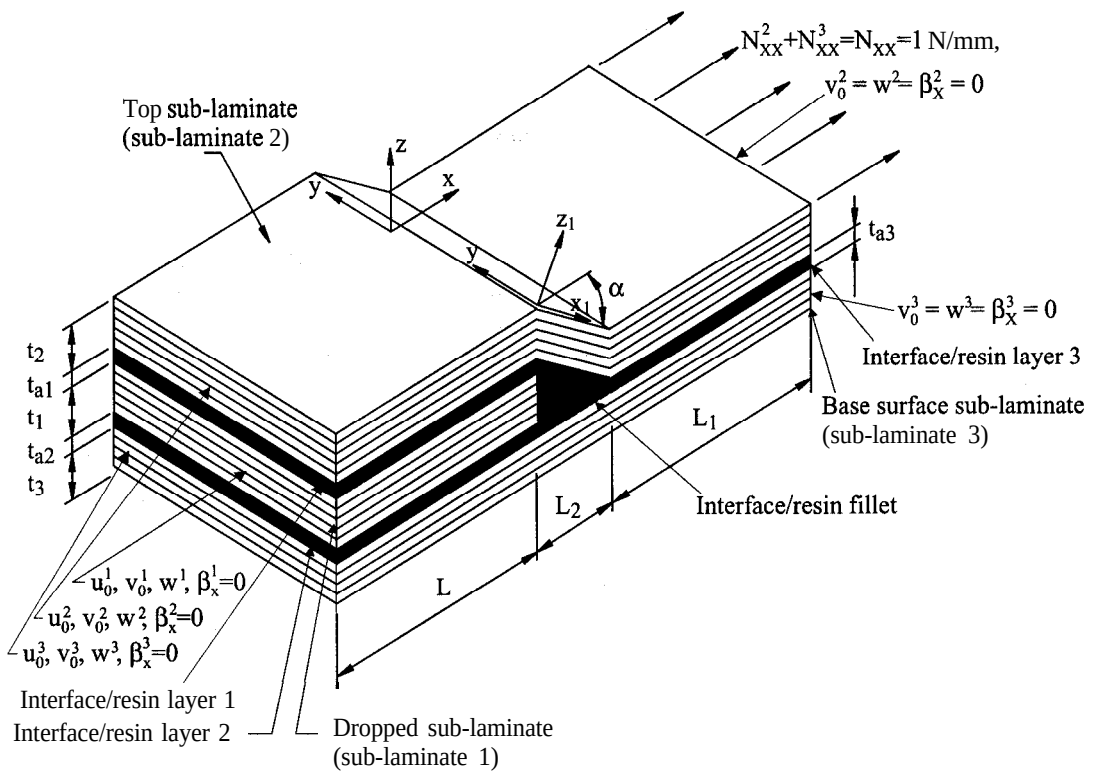

Figure 3.21: Embedded ply drop configuration clamped at the left end. A uniform longitudinal displacement is imposed at the right end, i.e. at x = L, equivalent to an m-plane normal force N = $1\ N/mm \Leftrightarrow \sigma_N = \frac{N}{t_2+t_3} = 0.94\ MPa$, t_1 = t_2 = 0.304 mm, t_3 = 0.760 mm, t_{a1} = t_{a2} = t_{a3} = 0.03 mm, L = 50 mm, L_1 = 49 mm, L_2 = 1.0 mm.

The lay-up of the sub-laminates, the dimensions as well as the boundary conditions for the embedded ply drop example are shown in Table 3.3.

The boundary conditions of the 'cut-out' of the embedded ply drop example are chosen such that clamping conditions are present at the left end, and such that uniform longitudinal displacements, equivalent to an in-plane normal force of N_{xx} = 1 N/mm, are imposed at the right end, i.e. at x = $L_1 + L_2$, as used for the exterior ply drop example.

Lengths	L = 50 mm, L_1 = 49.0 mm, L_2 = 1.0 mm;
Face sheet laminate	$[+45°, 0°, 0°, +45°, 0°, 0°, +45°, 90°, 0°]$, t = 1.064 mm
Core material	$h_c = 10$ mm.
Top laminate	$[+45°, 0°]$, t_2 = 0.304 mm
Dropped laminate	$[0°, +45°]$, t_1 = 0.304 mm
Base-laminate	$[0°, 0°, +45°, 90°, 0"]$, t_3 = 0.760 mm
Load & B.C.	$x = -L$: $u^i = w^i = \beta_x^i = 0$, $(i=1,2,3)$ $x = L_1 + L_2$: $w^i = \beta_x^i = 0$, $N_{xx}^2 + N_{xx}^3 = N_{xx} = 1$ N/mm; $(i=2,3)$

Table 3.3: Sub-laminate lay-up, dimensions and boundary conditions used for the embedded *ply* drop in the sandwich panel.

Selected results from the analysis are shown in Figure 3.22-3.29.

The lateral displacements of the sub-laminates are shown in Figure 3.22.

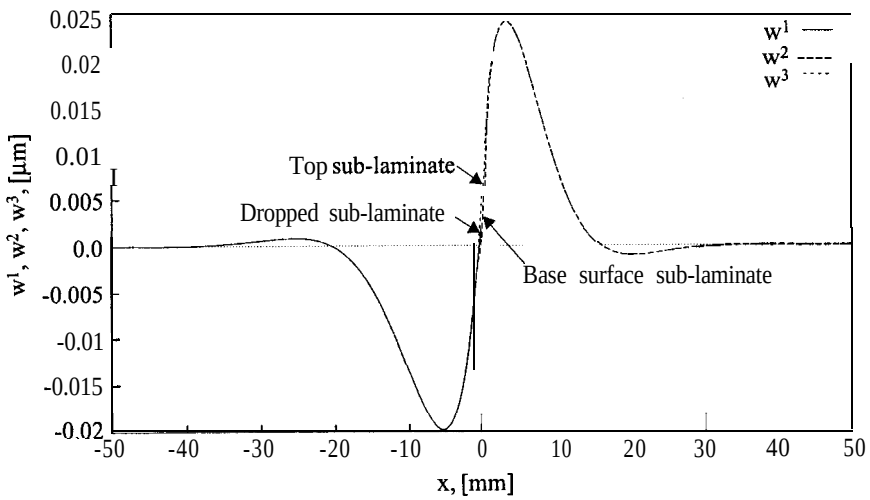

Figure 3.22: Lateral displacements w_1, w_2 and w_3 of the three sub-laminates of the embedded ply drop configuration in a sandwich laminate.

From Figure 3.22 the same pattern of the deflections is seen as for the exterior ply drop-off, i.e. it is observed that strong local bending effects occur close to the ply drop at x = 0, and that the bending effects are strongly damped due to the presence of a core material. Comparison with the lateral deflections for the exterior ply drop in Figure 3.15, shows that the maximum lateral deflection has been reduced by approximately 10% by dropping two internal plies instead of two external plies.

In Figure 3.23, Figure 3.24 and Figure 3.25 the predicted interface/'resin-rich' layer stresses in the three interface/'resin-rich' layers are shown.

Considering Figure 3.22 it is difficult to notice any differences between the deflections of the sub-laminates, but from the interface/'resin-rich' layer stress distributions displayed in Figures 3.23, 3.24 and 3.25 it is seen that significant transverse normal stresses do occur. The presence

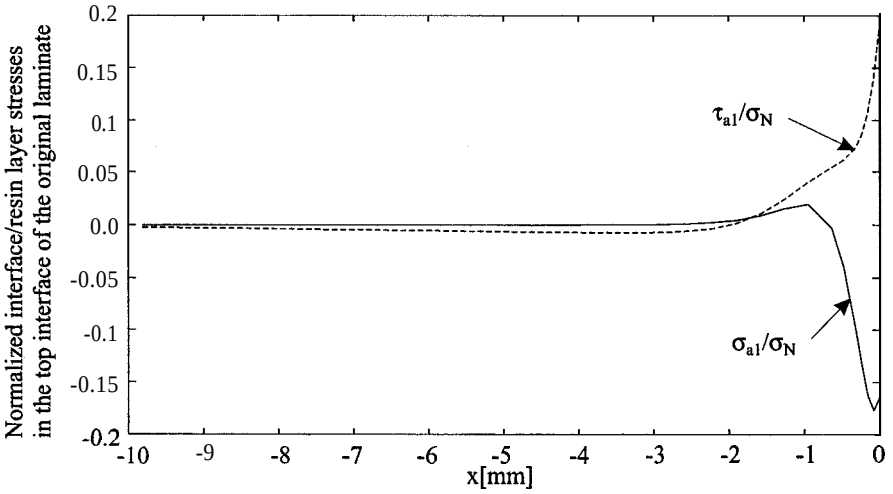

Figure 3.23: Interface/'resin-rich' layer stresses in the top-interface *of the* original sandwich *lam*inate, i.e. interface/'resin-rich' layer 1, of an embedded ply drop configuration in a sandwich laminate.

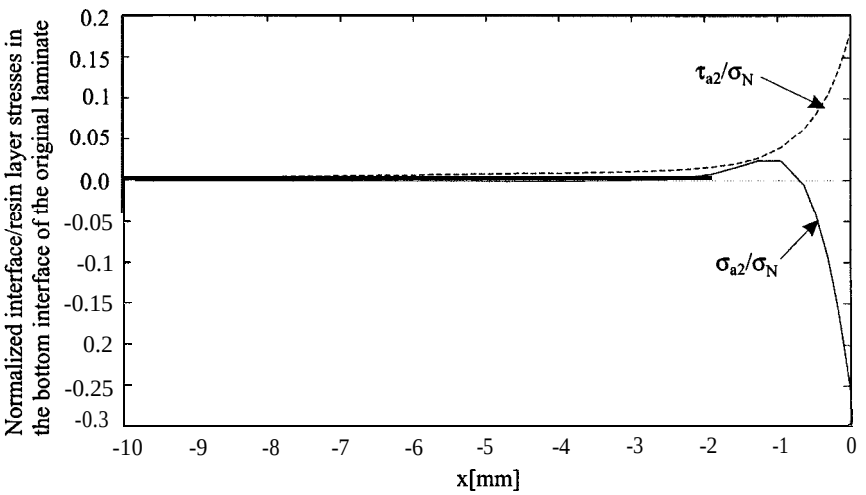

Figure 3.24: Interface/'resin-rich' layer stresses in *the* bottom-interface of the original sandwich laminate, i.e. interface/'resin-rich' layer 2, *of* an embedded *ply* drop configuration in a sandwich laminate.

of these stresses is a consequence of the differences in the lateral deflections of the sub-laminates. From Figures 3.23 and 3.24 it observed that the interface/'resin-rich' layer stresses are localised close to the region near the ply drop at x = 0, and that the stress distributions display almost identical patterns in interface/'resin-rich' layers 1 and 2. It should be noticed that the transverse normal peak stresses in the two layers are both compressive. From Figure 3.25 it seen that interface/'resin-rich' layer stresses in the interface layer 3 are very localised close to the end of

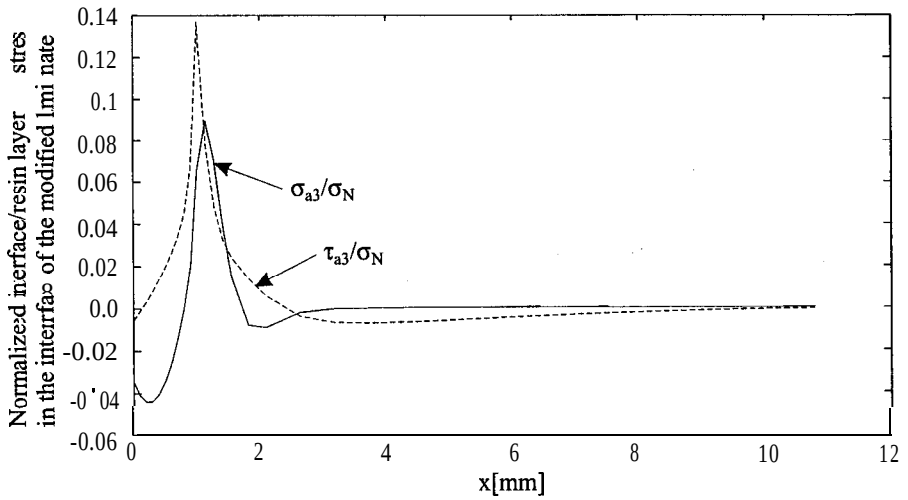

Figure 3.25: *Interface/'resin-rich'* layer stresses in the interface of the modified sandwich laminate, i.e. interface/'resin-rich' *layer* 3, of an embedded ply drop configuration in a sandwich laminate.

the transition region in the modified laminate, i.e. at x = L_2 (x = 1 mm), and that both the shear stresses and the transverse normal stresses reach their maximum values there. Since the peak transverse normal stresses in this area are tensile, this will be the most critical area in the complete laminate assembly. By comparison with the the interface/'resin-rich' layer stresses for the exterior ply drop configuration displayed in Figure 3.16, it is seen that the maximum shear stresses have been reduced by approximately 35%, and that the maximum transverse normal stresses have been reduced by approximately 65%, by dropping two internal plies instead of two external plies. However, since the maximum interface/'resin-rich' layer transverse normal stresses appear in the modified laminate of the embedded ply drop configuration, the achieved reduction of the peak stresses is of course dependent of the transition length, which strongly affects the interface layer stresses.

In Figure 3.26 the face laminate/core interface stresses are shown.

It is seen that the predicted interface transverse normal stresses follow a pattern similar to the lateral displacements of the base-surface laminate, i.e. sub-laminate 3. It is again seen that two local peaks of σ_c are present as for the exterior ply drop example, one compressive peak on the left side of the ply drop, and one tensile peak on the right side of the ply drop. The peak values of σ_c and τ_c are also here very small compared with the stresses in the interface/'resin-rich' layers.

In Figure 3.27 the in-plane normal stress resultants are displayed.

From Figure 3.27 it is seen that the in-plane normal stress resultants N^1_{xx}, N^2_{xx} and N^3_{xx} are constant except in the area adjacent the ply drop. In the area $-L \leq x < 0$ ($-50\ mm \leq x < 0$ mm) the three sub-laminates share the total load between them as depicted by their in-plane stiffnesses. In the transition area, i.e. $0 \leq$ x < L_2 (0 $\leq$ x < 1 mm), the in-plane loads in the top and base-surface sub-laminates increase, due to the reduction of the total laminate thickness. After the transition region, i.e. for x > 1 mm the distribution of the in-plane loads in the two sub-laminates stabilises and approach constant values again.

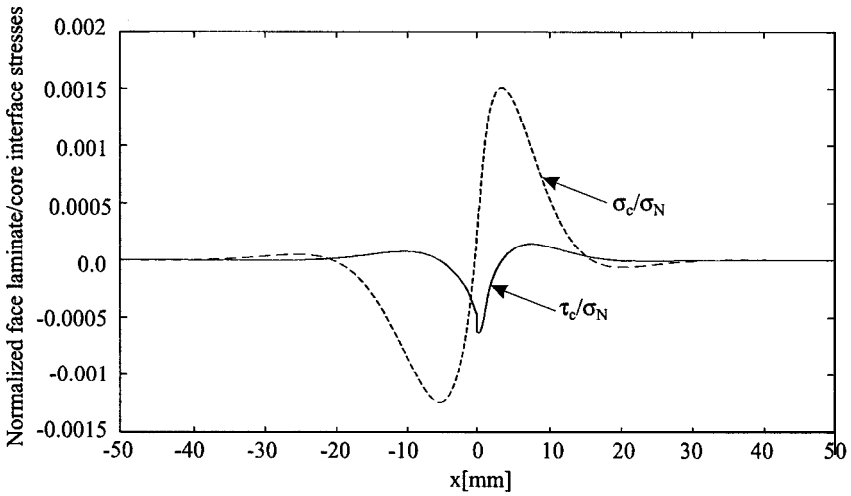

Figure 3.26: *The face* laminate/core interface stresses *of an* embedded *ply* drop configuration in a sandwich laminate.

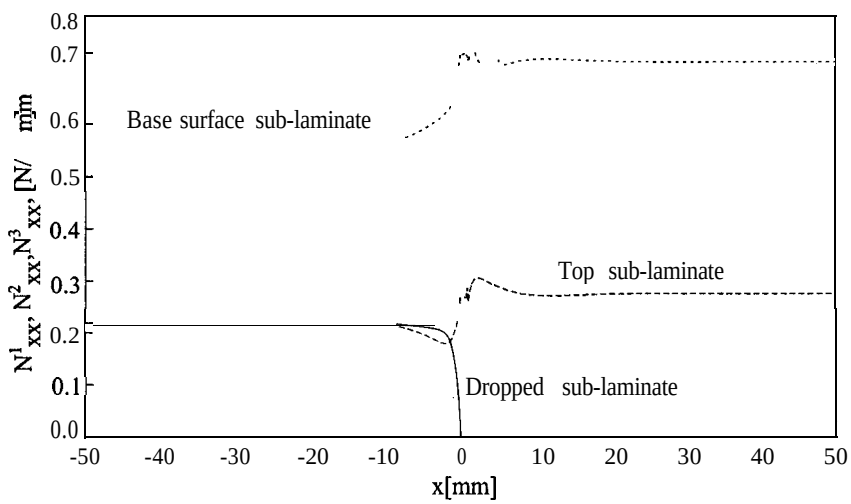

Figure 3.27: In-plane normal stress resultants N^1_{xx}, N^2_{xx} and N^2_{xx} *in the* sub-laminates *of* an embedded *ply* drop configuration *in a* sandwich laminate.

Figure 3.28 shows the distribution of the bending moment resultants M^1_{xx}, M^2_{xx} and M^3_{xx} in the sub-laminates.

It is seen that significant bending moment resultants are present in the area close to the ply drop at x = 0, and that the bending moment resultants M^3_{xx} induced in the base-surface sub-laminate are much larger than the bending moment resultants induced in the dropped and in the top sub-laminate. By comparison with the bending moment resultants for the exterior ply drop problem, shown in Figure 3.19, it is seen that the bending moment resultants display approximately the same pattern and the same magnitudes.

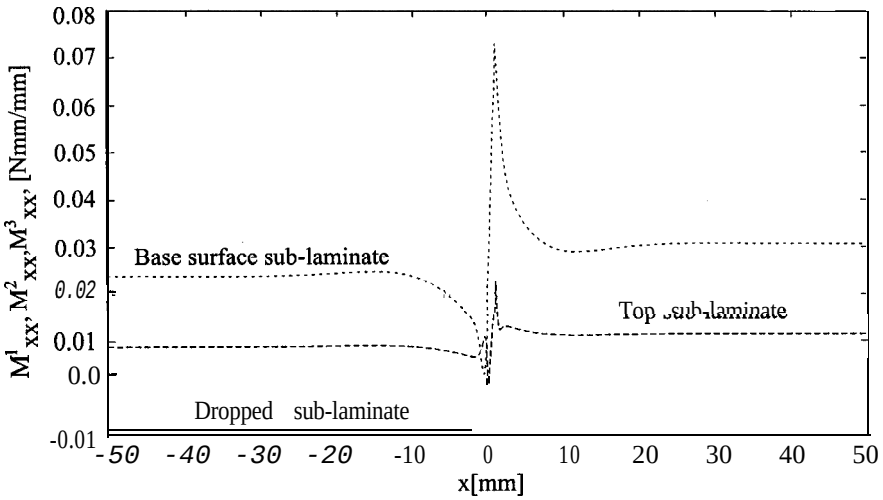

Figure 3.28: Bending moment resultants M^1_{xx}, M^2_{xx} and M^3_{xx} in the three sub-laminates of an embedded ply drop configuration in a sandwich laminate.

Figure 3.29 shows the distribution of the out-of-plane shear stress resultants Q^1_x, Q^2_x and Q^3_x in the sub-laminates.

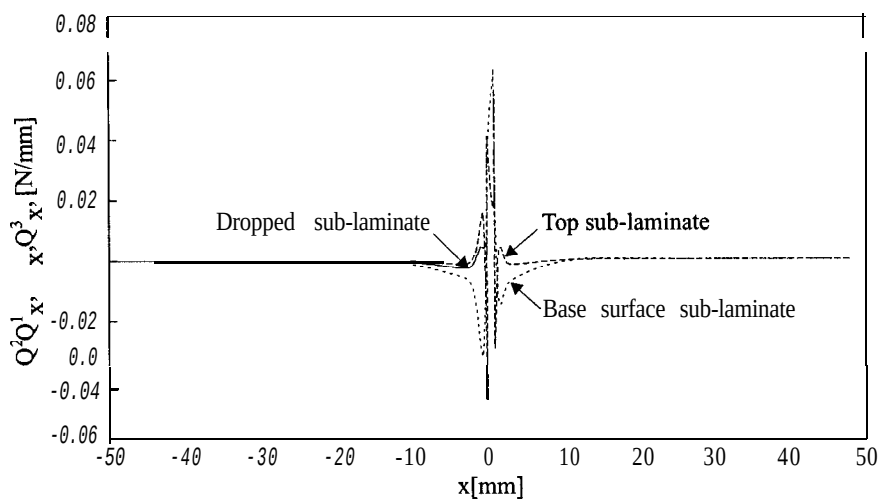

Figure 3.29: Out-of-plane shear stress resultants Q^1_x, Q^2_x and Q^3_x in the three sub-laminates of an embedded ply drop configuration in a sandwich laminate.

It is observed that the out-of-plane shear stress resultants are small compared with the applied loading N = 1 N/mm, but that the shear stress resultants are very localised close to the ply drop.

The examples have shown some of the main output of the analyses. Based on the stress and

bending moment resultants in the sub-laminates, the stress distribution within each of the sub-laminates can be calculated at any location in the longitudinal direction (x-direction). In the same way the displacements or strains can be determined.

3.4.2 Parametric Effects

In the references reviewed, see Section 3.1.2, several investigations of parametric effects have been performed for both exterior and embedded ply drops. Thus, in this section only parametric effects related to the transition length L_2, or the angle α, for the embedded ply drop configuration will be investigated (see Figure 3.9). This is a very important parameter in the prediction of the interface/'resin-rich' layer stresses in the modified laminate, i.e. in interface layer 3 according to Figure 3.21. The investigation will be carried out on the same example as used in Section 3.4.1.

A parametric study of the interface/'resin-rich' layer peak stresses in the modified laminate, i.e. the interface/'resin-rich' layer 3, as a function of the angle α is shown in Figure 3.30. In the example shown in Section 3.4.1 L_2 was chosen to L_2 = 1 mm, which corresponds to α = 18.5'.

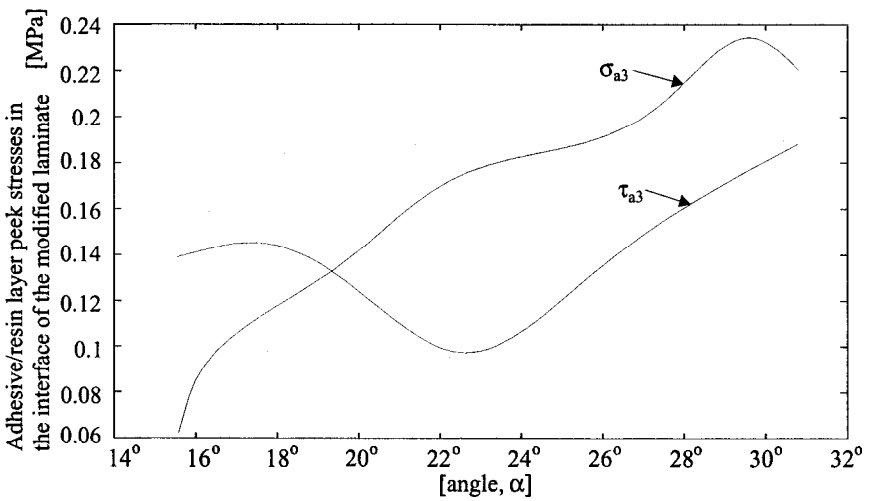

Figure 3.30: *Adhesive/'resin-rich'* layer peak stresses in the interface of the modified sandwich laminate *as a function of the angle* α.

From Figure 3.30 it is seen that the peak transverse normal stresses increase almost linearly as a function of the angle cr. The reason for this is that the top-laminate tends to peel of the base-surface sub-laminate, and that it tends to straighten out in order to provide for a more smooth load flow through the laminate. As the angle α increases this phenomenon becomes more pronounced.

In addition, the parametric study concerning the influence of laminate lay-up variations displayed in Section 2.3.9 for adhesive bonded joints are also valid for the ply drop problems (see Section 2.3.9).

3.4.3 Ply Drops in a Monolithic Laminate and Comparison with Finite Element Analysis Results

To show the validity of the adopted approach by comparison with finite element analysis results a homogenous and isotropic monolithic laminate, composed of aluminium sub-laminates, has been selected. Isotropic laminates made of aluminium have been chosen for simplicity. The fact that embedded ply drops in solid aluminium 'laminates' are unrealistic should be ignored, since the main purpose of the example is to compare the results derived with the developed solution procedure with finite element analysis results.

The basic properties for the monolithic/solid laminate considered are given by:

Plies	Aluminium, $E_{al} = 72.4\ GPa, \nu_a = 0.35, t = 0.5\ mm$
Interface/Resin	Epoxy, $E_a = 3.5\ GPa, \nu_a = 0.4, t_a = 0.1\ mm$

Table 3.4: Specification of plies and resin material properties used in the example for ply drops in a monolithic laminate.

In the following section only selected results will be presented and compared.

Solid/Monolithic Laminate - Exterior Ply Drop Example

The lay-up, dimensions and the boundary conditions for the exterior ply drop example in a monolithic laminate are shown in Table 3.5.

Lengths	$L = 45$ mm, $L_1 = 45.0$ mm
Laminate	$[0°]_8$, $t = 4.0$ mm
Dropped laminate	$[0°]$, $t_2 = 0.5$ mm
Base-laminate	$[0°]_7$, $t_1 = 3.5\ mm$
Load & B.C.	$x = -L$: $u^i = w^i = \beta_x^i = 0$, $(i=1,2)$ $x = L_1 + L_2$: $w^1 = M_{xx}^1 = 0$, $N_{xx}^1 = 120\ N/mm$

Table 3.5: Sub-laminate lay-up, dimensions and boundary conditions used for the exterior ply drop configuration in a monolithic laminate.

The finite element analyses of the ply drop-off problems have been performed using the finite element code ODESSY, as described in Section 2.5.2.

A zoom of the finite element model in the ply drop region of the assumed exterior ply drop configuration is shown in Figure 3.31.

The structure has been modelled using a mixture of 6 and 8 node isoparametric 2D solid elements. The adhesive layer has been modelled using two 8 node isoparametric elements across the adhesive layer thickness. This is a relative crude mesh, and, moreover, a spew-fillet at the end of the drop-off has not been modelled, since this would require a much finer mesh. Still, even with this mesh, the size of the finite element model is quite large: 9399 elements with 29080 nodes. Due to the use of a relatively crude finite element mesh the adhesive layer stresses are not predicted very accurately, and will not be compared with the stresses derived by the developed procedure. The finite element analysis has been carried out as a plane strain model, since the

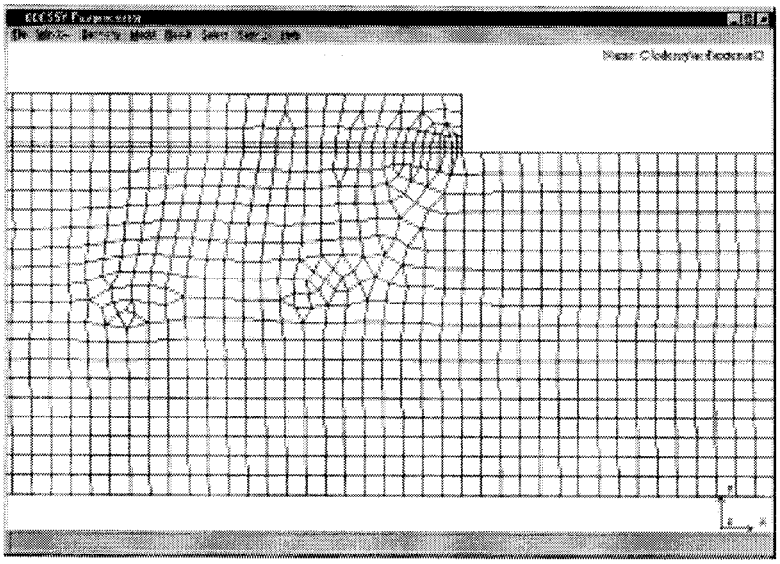

Figure 3.31: *Zoom* of finite element model in the ply drop *region of the* exterior ply drop configuration.

proposed simple approach is based on the assumption that the laminates behave as wide beams. The lateral displacements of the sub-laminates calculated by the proposed simplified approach and the finite element analysis are shown in Figure 3.32.

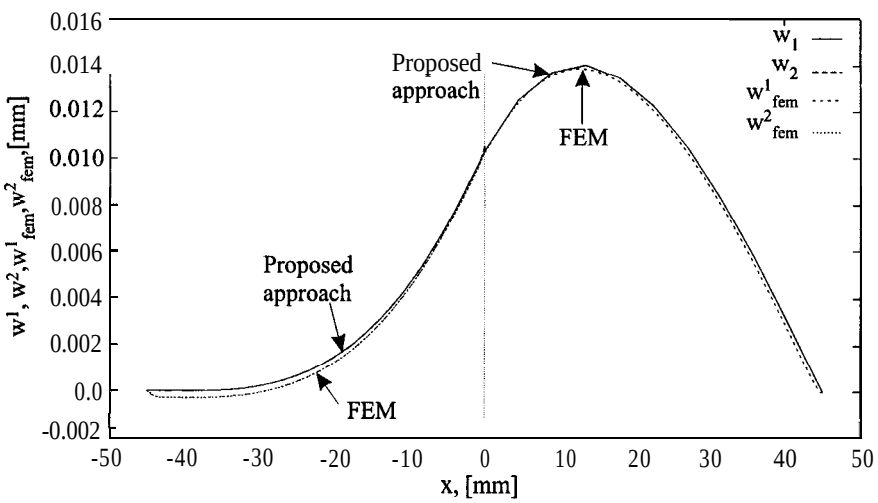

Figure 3.32: Lateral displacements obtained for an exterior ply drop in a monolithic laminate calculated by the proposed simplified approach and by finite element analysis.

Figure 3.32 shows that the lateral displacements calculated by the proposed simplified approach and the finite element analysis compare very well. Comparing the lateral displacements for the

exterior ply drop configuration in a monolithic laminate, as shown in Figure 3.32, with those of the ply drop configuration in a sandwich laminate (see Figure 3.15), shows that the deflection pattern is very different. This of course is due to the presence of a core material in the sandwich laminate.

Solid/Monolithic Laminate - Embedded Ply Drop Example

The lay-up, dimensions and the boundary conditions for the embedded ply drop example in a monolithic laminate are shown in Table 3.6.

Lengths	$L = 45$ mm, $L_1 = 43.0$ mm, $L_2 = 2.0$ mm;
Laminate	$[0°]_8$, $t = 4.0$ mm
Dropped laminate	$[0°]$, $t_1 = 0.5$ mm
Top laminate	$[0°]_2$, $t_2 = 1.0$ mm
Base-laminate	$[0°]_5$, $t_3 = 2.5$ mm
Load & B.C.	$x = -L$: $u^i = w^i = \beta_x^i = 0$, $(i=1,2,3)$, $x = L_1 + L_2$: $w^2 = w^3 = M_{xx}^2 = M_{xx}^3 = 0$, $N_{xx}^2 = 30$ N/mm, $N_{xx}^3 = 90$ N/mm;

Table 3.6: Sub-laminate lay-up, dimensions and boundary conditions *used* for the embedded ply drop configuration in a monolithic laminate.

Figure 3.33 shows a zoom of the finite element model in the ply drop region of the embedded ply drop configuration used for comparison of results.

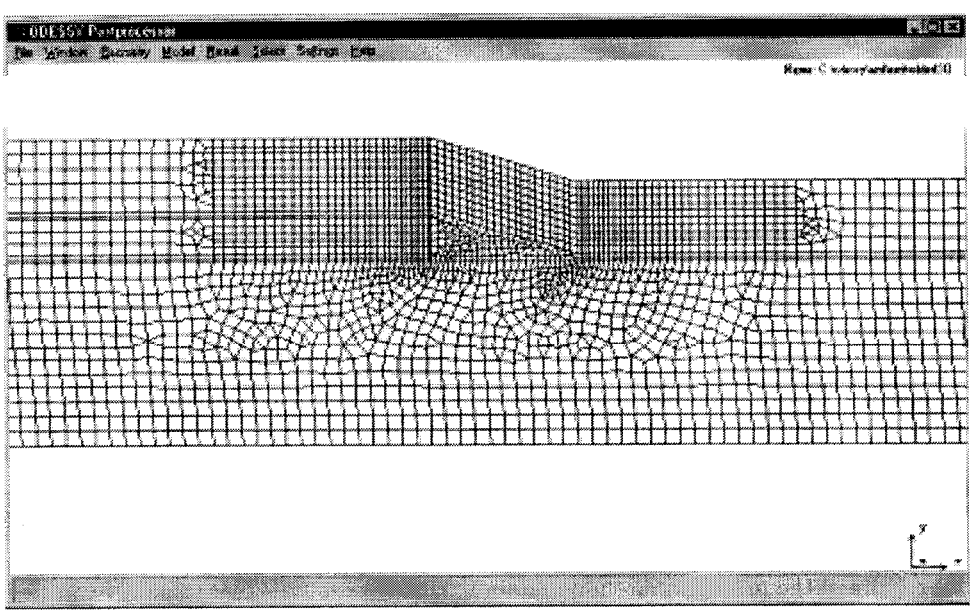

Figure 3.33: Zoom *of finite* element model in the layer drop region of an embedded ply drop configuration.

Again the ply drop assembly has been modelled using a mixture of 6 and 8 node isoparametric 2D solid elements. The interface/'resin-rich' layers have been divided into two 8 node isoparametric elements through the thickness. This is a relatively crude mesh, and consequently the interface/'resin-rich' layer stresses are not predicted very accurately. However, in this case the interface/'resin-rich' layer stresses are comparable, since no free edges of the interface/'resin-rich' layers are present. The finite element model contains 10768 elements with 33113 nodes. The analysis has been carried out as a plane strain model.

The vertical deflections for both analyses are shown in Figure 3.34.

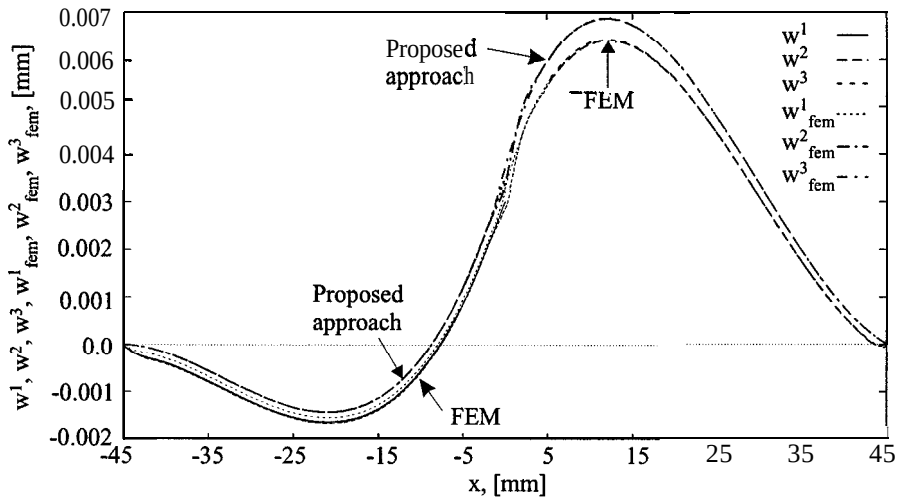

Figure 3.34: Lateral displacements of an embedded ply drop configuration in a monolithic laminate calculated by the proposed simplified approach and by finite element analysis.

From Figure 3.34 it is seen that the deflections calculated by the two methods compare very well, both with respect to the overall pattern as well as the numerical values.

In Figure 3.35 - Figure 3.38 the comparisons of the predicted interface/'resin-rich' layer stresses for the three interface layers are shown. The adhesive layer stresses from the finite element modelled are calculated in the middle of the interface layers.

From the Figures 3.35, 3.36, 3.37 and 3.38 it is seen that the interface/'resin-rich' layer stresses calculated by the proposed simplified approach and the finite element analysis compare very well. Thus, it is seen that the stress distributions display almost identical patterns, and that nearly identical peak values are obtained. As mentioned previously, the finite element model used is based on a rather crude mesh. Furthermore, the finite element model contains points of stress singularities, which will tend to increase the interface/'resin-rich' layer peak stresses if the finite element mesh is refined further close to the ply drop zone. Thus a complete convergence between the results of the proposed method and finite element analysis, with respect to the peak interface/'resin-rich' layer stresses, is impossible to achieve.

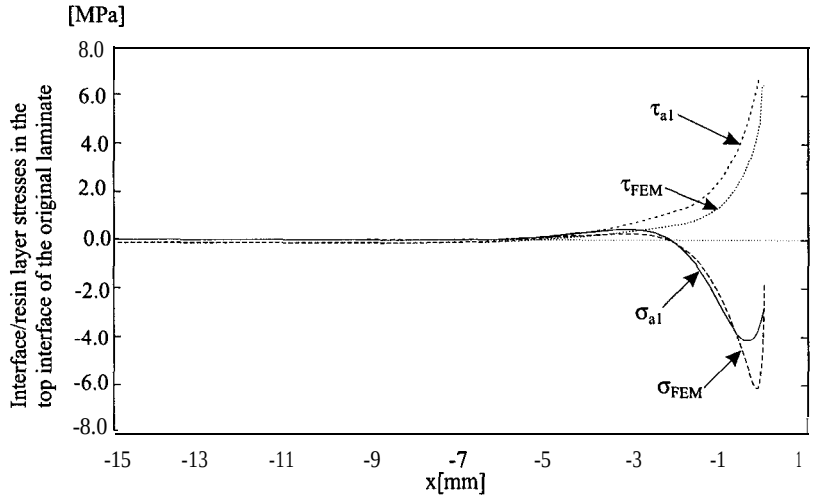

Figure 3.35: *Interface/'resin-rich'* layer stresses in the *top* interface *layer,* i.e. interface layer *1, of* an embedded ply drop configuration in a monolithic laminate, calculated by the proposed simplified approach and by *finite* element analysis.

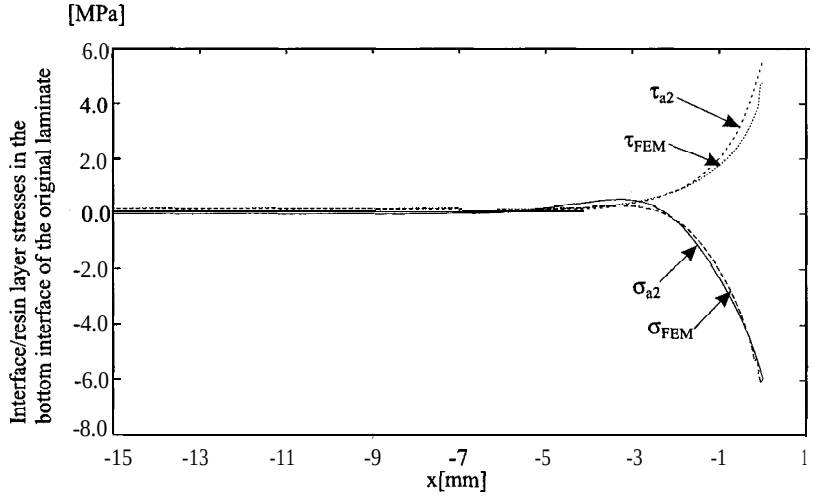

Figure 3.36: *Interface/'resin-rich'* layer stresses in the bottom interface layer *of the original laminate,* i.e. interface layer 2, of an embedded ply drop configuration *in* a monolithic laminate, calculated by *the* proposed simplified approach and by finite element analysis .

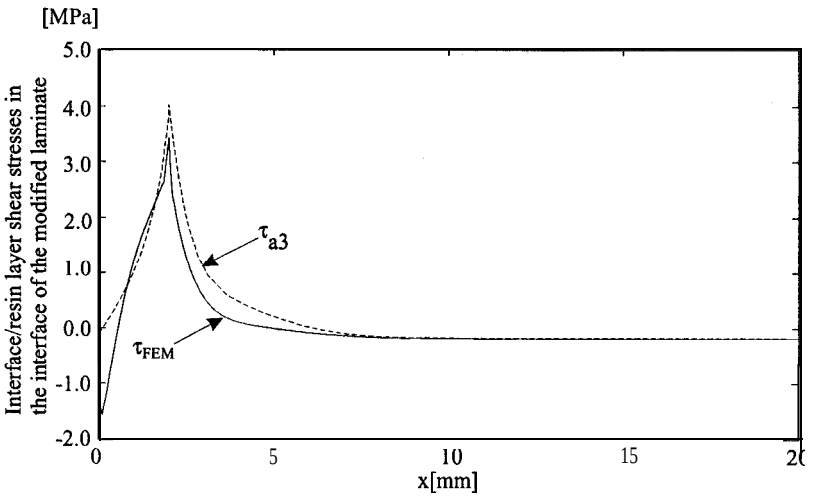

Figure 3.37: Interface/'resin-rich' layer shear stresses in the interface layer of the modified *laminate*, i.e. interface layer 3, *of* an embedded ply drop configuration in a monolithic laminate, calculated by the proposed simplified approach and by finite element analysis.

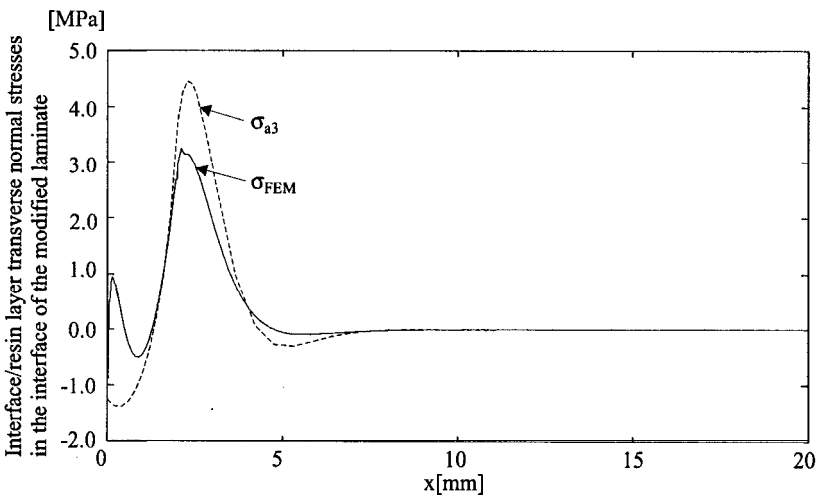

Figure 3.38: *Interface/'resin-rich'* layer transverse *normal stresses in the interface layer of the modified* laminate, *i.e.* interface layer 3, of an *embedded ply drop configuration* in a monolithic laminate, *calculated by the proposed* simplified approach and by finite element analysis.

3.4.4 Summary

The objective of this section has been to show the applicability of the developed linear solution procedure for the analyses of 'exterior' and 'embedded' ply drops, with both asymmetric and unbalanced laminates and homogenous laminates. The different ply drop types have been compared to expose their different performance characteristics, In addition, a parametric study has been performed for embedded ply drops to investigate the influence of the transition length on the interface/'resin-rich' layer stresses in the modified laminate.

For all the ply drop configurations it is observed that the peaks of the bending moment resultants and the transverse shear stress resultants in the laminates appear around the ply drop zone. The same observation is done for the interface/'resin-rich' layer stresses, i.e. the peak layer stresses also appear at the ends of the ply drop zone. The parametric study of the transition length for embedded ply drops shows that the length should be as large as possible in order to minimize the interface/'resin-rich' layer stresses, and to smooth out the load transfer around the drop zone.

The results obtained with the simplified approach are in very good agreement with the results obtained using the finite element method.

3.5 Implementation in ESAcomp

With reference to Section 1.1 in Chaper 1 the implementation of the Layer Drop-off Module into ESAComp version 1.0 is described in this section.

The **Layer Drop-off Module** has been implemented as an **Analysis Tool** for laminate analyses in ESAComp, see Figure 1.2 and Figure 1.3 in Chaper 1 Section 1.1.1-1.1.2.

To show the implementation into ESAComp the Layer Drop-off Module is demonstrated on the sandwich panel used in the examples in Section 3.4.1.

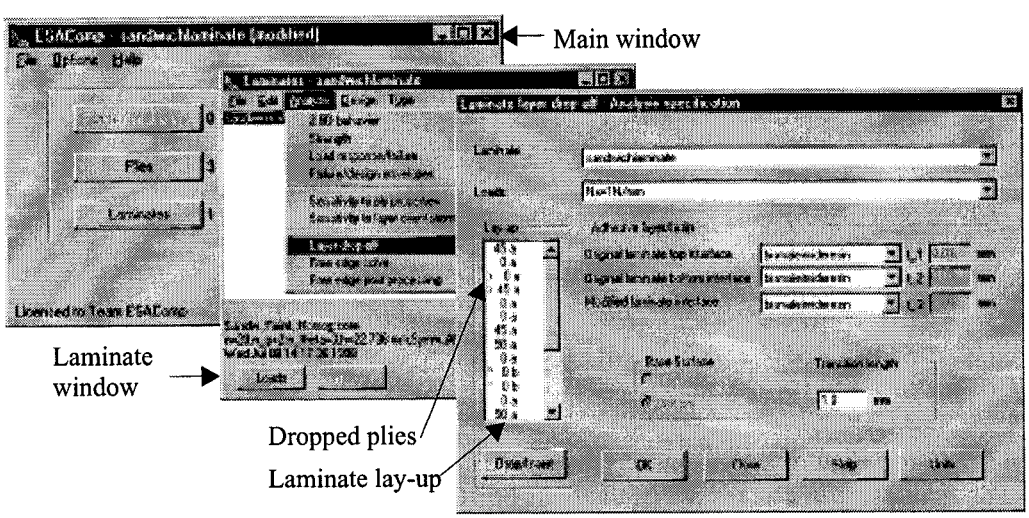

Figure 3.39: Analysis *of* a layer drop-off configuration *in* a sandwich laminate in ESAComp version 1.0.

After a laminate has been created in ESAComp the interface/'resin-rich' layer material must be specified as a homogenous ply before a layer drop-off analysis can be performed. When this has been done, Laminate is selected in the ESAComp *Main Window* as shown in Figure 3.39.

In the laminate window the load must be specified before the layer drop-off analysis can be performed by selecting *Load.* After this the layer drop-off analysis must be selected under Analyze in the laminate window. In the *Laminate layer drop-off* - analysis specification window the laminate and the loading can be selected. After selecting the laminate and the loading, the laminate lay-up appears in the window as shown in Figure 3.39. The plies to be dropped can then be selected. After selection of the plies to be dropped the interface/'resin-rich' material must be specified, and finally the transition length must be selected if the plies dropped are internal (embedded) plies. The analysis can then be performed.

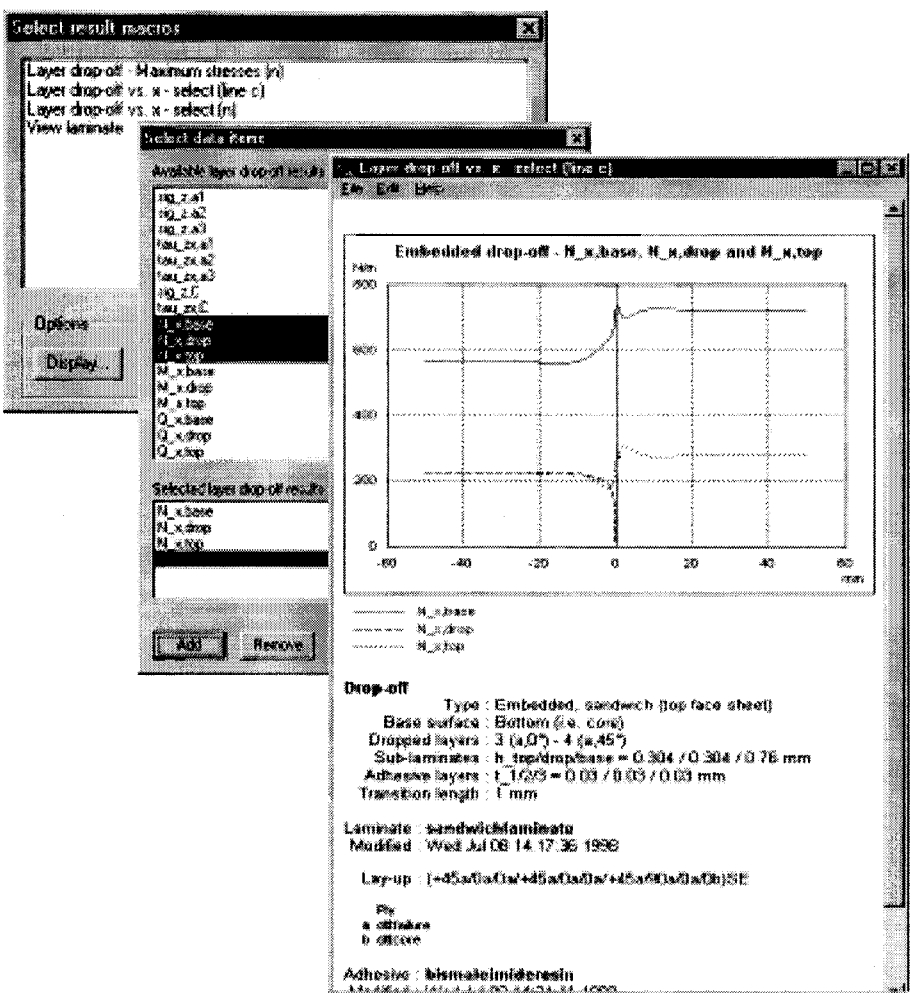

Figure 3.40: Calculation *of* in-plane normal *stress* resultants in an embedded *layer* drop-off *con*figuration *in a* sandwich laminate *in* ESAComp version 1.0.

After the analysis has been carried out the fundamental variables and the interface layer stresses can be selected and displayed as shown in Figure 3.40.

If the ply drop analysis is performed on a monolithic/solid laminate, the user has to specify whether the plies above or below the dropped plies are the base-surface sub-laminate by selecting ***Top*** or ***Bottom*** in the Laminate layer ***drop-off -*** Analysis specification window, see Figure 3.39.

3.6 Conclusions

A simplified method for the analysis of exterior and embedded ply drops in composite and sandwich laminates has been developed. The analysis accounts for coupling effects induced by sub-laminates, which are asymmetric and unbalanced. For ply drops in laminates acting as face sheets in sandwich panels the analysis accounts for the interaction with the core material through a two-parametric elastic foundation model, which includes the shearing interaction between the face laminates and the core material. The analysis allows for specification of any combination of boundary conditions and external loading.

Numerical results have shown that severe local stress concentrations are induced in the interface/ 'resin-rich' layers close to the ply drop zone. From parametric studies it has further been shown that the interface/'resin-rich' layer stresses are strongly dependent on the transition length over which the laminate thickness changes for the embedded layer drop configuration. The results obtained by use of the developed analysis procedures have been compared with finite element analysis, and it has been shown that the results compare very well.

The developed analysis procedures have been implemented in ESAComp version 1.0 (ESAComp System Manual 1998), and can be used for the analysis and design of exterior and embedded ply drops in composite and sandwich laminates.

Chapter

4

Sandwich Plates with Inserts

STRUCTURAL SANDWICH ELEMENTS are used extensively for lightweight spacecraft, aircraft and marine structures. The introduction of loads into such structural elements is often accomplished using inserts. An insert is part of a detachable fixation device, which permits the interconnection of sandwich structures, the connection between such structures and other structural parts (such as frames, profiles, brackets) and the mounting of equipment (such as boxes, feed lines, cable ducts etc.). The system consists of a removable and a fixed structural element. The removable part is either a screw or another threaded element adapted to a fixed 'nut-like' part, the insert.

4.1 Introduction

In this section the different types of inserts used for load introduction into sandwich panels, and their modelling with the objective of predicting the stress and displacement fields in the vicinity of the inserts, will be described.

4.1.1 Insert Types

There are three types of inserts which are most usually used. The three types of inserts are distinguished by the method of integration into the sandwich structure, which are (European Space Agency (1987)):

- by simultaneous bonding during sandwich production;
- by mechanical clamping or screwing into an existing sandwich panel;
- by potting with a curing resin into an existing sandwich panel;

Using the first type of insert, i.e. by simultaneous bonding during sandwich production, it is very difficult to position the insert exactly at the point at which it is required for connection purposes. Therefore the insert must have a large diameter to allow the drilling of a bore hole and cutting thread within a margin to allow for misalignment.

Using the second type of insert, i.e. mechanical clamping or screwing into an existing sandwich panel, also have some significant disadvantages, where the most important is that there is no direct connection with the sandwich core which causes low load-carrying capability. In addition this type of inserts can not transfer any torque, since this requires an adhesive bonding of the insert.

The third type of insert, i.e. inserts fixed into an existing sandwich panel by potting with a curing resin, is the most important type of insert since it can overcome the disadvantages appearing using the two other types of inserts mentioned above. This kind of insert may be of the types: 'through-the-thickness', 'fully potted' or 'partially potted' inserts as illustrated in Figure 4.1.

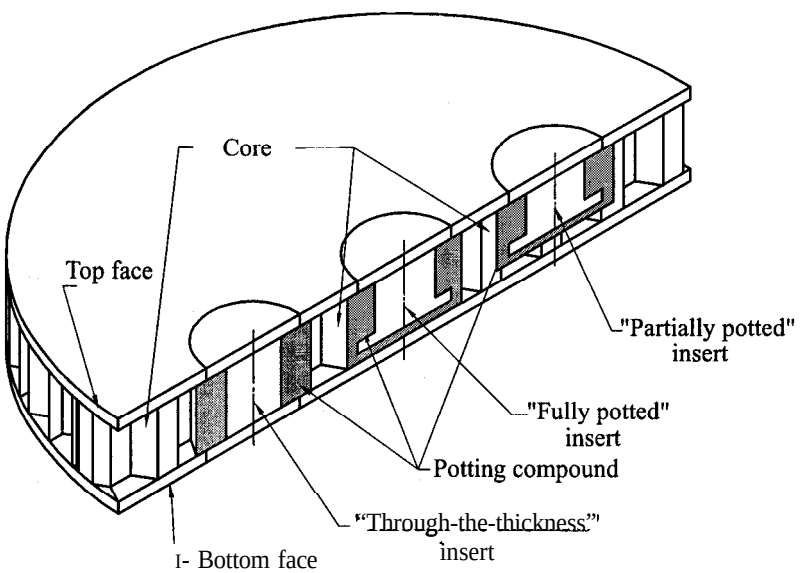

Figure 4.1: Inserts types typically used for structural sandwich plates.

For all the insert types, the ideal load transfer mechanism is disturbed significantly in the regions close to the inserts. In the areas of such disturbances the face sheets will bend locally about their own middle surface rather than about the middle surface of the sandwich plate. This results in severe local stress concentrations in the face sheets, in the core material and in the interface between the face sheets and the core. This again might lead to a premature failure, as sandwich plates with transversely flexible cores such as polymeric foams or honeycombs are susceptible to failure due to local stress concentrations. Sandwich plates with inserts usually fail owing to delamination, to shear rupture of the core or to direct bending of the face sheets. The 'through-the-thickness' inserts are superior compared to the other types of insert with respect to the load carrying capability, since the two face sheets in the sandwich plate with 'through-the-thickness' inserts are forced to deflect together, whereas this is not the case for the other types of insert in sandwich plates (European Space Agency (1987)).

4.1.2 State-of-the-Art in the Modelling of Sandwich Panels

The local bending effects leading to structural failure of sandwich plates with inserts cannot be accounted for using classical 'antiplane' sandwich plate theories, summed up in references such as Plantema (1966), Allen (1969), Stamm and Witte (1974) and Zenkert (1995), as such theories do

not include the transverse flexibility of the core material. A more advanced transverse bending theory for sandwich plates is presented in the monograph by Librescu (1975), in which sandwich plates with 'weak' or 'strong' cores are treated separately. The terms 'weak' or 'antiplane' cores are equivalent concepts, and are used to describe an idealised core in which the stretching and shearing stiffness in planes parallel with the face sheets are zero, but the shear modulus perpendicular to the face sheets is finite. This is in contrast to a sandwich panel with a strong core (or rigid core) which is characterized by the fact that the core inplane stretching and shearing stiffnesses are taken into account, Librescu (1975). For most structural sandwich panel applications the weak core assumptions can be adopted, since very lightweight core materials such as polymeric foams and honeycombs are usually used.

In the theory developed by Librescu (1975) the sandwich panels treated are assumed to be symmetric, and the core material is modelled as a moderately thick plate, where the presence of core transverse normal stresses is included in the modelling. The sandwich plate model presented in Librescu (1975) does not, however, include the transverse flexibility of the core material, since it is assumed a priori that the transverse deflection of the core is uniform through the core thickness (i.e. the core transverse normal strain $\epsilon_z = 0$).

The importance of including the transverse flexibility of the core (i.e. allowing the core thickness to change during deformation of the sandwich panel) when addressing load introduction problems, support problems, and problems involving material and geometric discontinuities in sandwich beams was pointed out by Frostig et al. (1991), Frostig and Baruch (1993), Frostig (1993) and Frostig and Shenhar (1995). This was done by formulating a high-order sandwich beam theory, which include a separate description of each face sheet and a separate description of the core material. The core material is modelled as a special type of transversely isotropic solid where only the transverse stiffness is accounted for, as shortly described in Section 2.5 of this thesis. The high-order sandwich beam theory incorporate both global and localised bending effects, and the basic assumptions as well as the quality of the predictions of the theory was verified experimentally by Thomsen and Frostig (1997).

Thomsen and Rits (1998) and Thomsen (1998) adopted and extended the principles behind the high-order theory developed for sandwich beams (Frostig et al. (1991), Frostig and Baruch (1993), Frostig (1993) and Frostig and Shenhar (1995)), to circular sandwich plates with inserts. The theory can be used for approximate analysis of sandwich plates with 'through-the-thickness' and 'fully potted' inserts subjected to arbitrary external loading and boundary conditions.

4.1.3 Objectives of the ESAComp Insert Module

The main objective of this module is to provide ESAComp with analysis tools capable of determining the stress and displacement fields in sandwich plates with inserts of 'through-the-thickness' and 'fully potted' types as illustrated in Figure 4.1.

The analysis procedures to be implemented in ESAComp are based on the high-order sandwich plate theory approach for sandwich plates with inserts developed by Thomsen (1994a), Thomsen (1994b), Thomsen and Rits (1998) and Thomsen (1998).

The aim of this work has therefore been to prepare the ESAComp implementation of the module for analysis of sandwich paltes with inserts, and to validate the theoretical approach through comparison with results obtained using two alternative methods. The alternative methods in question are electronic speckle pattern interferometry, which is an experimental method for conducting whole field measurements of displacements, and finite element analysis.

Since the high-order sandwich plate theory approach for analysis of inserts in sandwich plates has been developed by others, it will only be described briefly in this section. Elaborate details about the theory including the structural modelling, examples and parametric effects can be found in Thomsen (1994a), Thomsen (1994b), Thomsen and Rits (1998) and Thomsen (1998).

4.2 Structural Modelling and Solution of Field Equations

The structural modelling described briefly in this section is based on the papers: "Analysis of sandwich plates with 'through-the-thickness' inserts using a higher-order sandwich plate theory" by Thomsen (1994b), "Analysis of sandwich plates with 'fully-potted' inserts using a higher-order sandwich plate theory" by Thomsen (1994a), "Analysis and design of sandwich plates with inserts - a high-order sandwich plate theory" by Thomsen and Rits (1998) and "Sandwich plates with 'Through-the-Thickness' and 'Fully Potted' Inserts: Evaluation of Differences in Structural Performance" by Thomsen and Rits (1998).

4.2.1 Model Definitions

In the modelling of the insert/sandwich plate system it is assumed that the interaction between adjacent inserts as well as the interaction between an insert and the plate boundaries or other sources of local disturbances, can be ignored. Figure 4.2 defines the constituent parts, the geometry and the possible external load cases for sandwich plates with 'through-the-thickness' and 'fully potted' inserts.

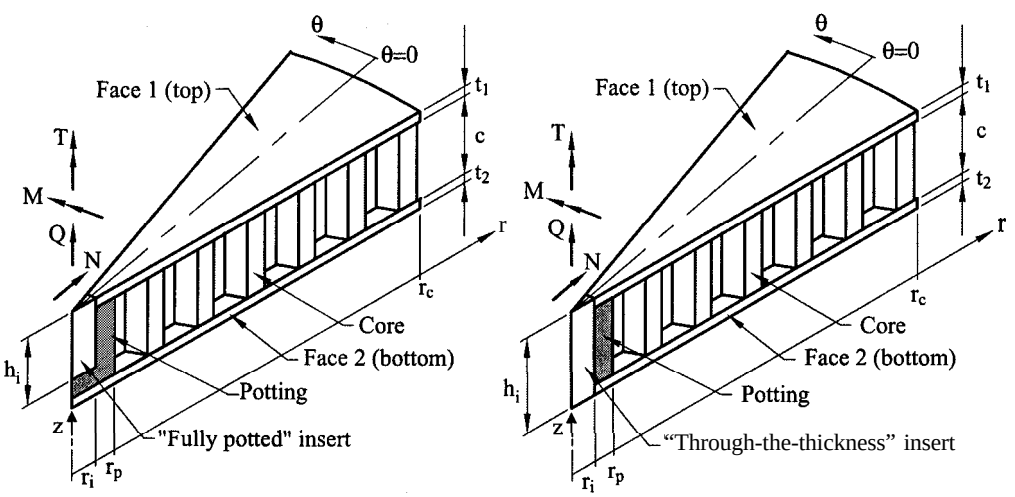

Figure 4.2: *'Cut-outs' of* circular sandwich plates *with* 'fully *potted'* and 'through-the-thickness' *inserts* subjected to arbitrary loading conditions.

If the core is made of honeycomb material (as illustrated in Figure 4.2) the sharp interface between the potting and the core material shown in Figure 4.2 represents a strong idealisation, as the potting/honeycomb intersection is not defined precisely in a geometrical sense.

4.2.2 Modelling of the Core Material

The core material is described as a transversely isotropic solid only possesing stiffness in the through-the-thickness direction (x,-direction according to Figure 4.2). As a consequence of this there can be no transfer of in-plane stresses in the core material, i.e.

$$\sigma_r = \sigma_\theta = \tau_{r\theta} = 0 \tag{4.1}$$

Based on these assumptions the equilibrium equations for the core material can be established and from these it follows, that the core shear stress components are independent of the z_c-coordinate.

Combination of the core equilibrium equations, with the core kinematic and constitutive relations yields a set of equations describing the complete core stress and displacement fields in terms of the transverse core coordinate z_c and in terms of the face sheet displacement components. The core material response is coupled with the face sheet responses by requiring continuity of the displacement field across the core/face sheet interfaces.

The core equilibrium equations, the complete core stress and displacement fields, as well as the continuity of the displacement field across the core/face sheet interfaces are shown in Appendix C

4.2.3 Modelling of the Face Sheets

The face sheets are modelled as elastic plates, with the possibility of including transverse shearing effects in the modelling. The face sheets are treated as homogeneous, isotropic and linear elastic in the modelling. Obviously, this is a simplifying assumption as the face sheets are often made as FRP-laminates. However, the adopted approximation is quite reasonable in reality, since strongly orthotropic face-laminates are hardly ever used around inserts or other areas of load introduction. Instead, if the surrounding sandwich structure is made with strongly orthotropic face-laminates, the zones around the inserts will be reinforced locally such that the resulting laminates appear as nearly quasi isotropic with respect to the in-plane properties.

4.2.4 Derivation of the Complete Set of Governing Equations

Formulation of the equilibrium, kinematic and constitutive equations for the top and bottom face sheets, and combination of those with the core equations and continuity requirements, yields the governing set of partial differential equations. In the formulation, the order of the set of governing equations is 24, and consequently the governing equations can be reduced to 24 first order partial differential equations with 24 unknowns. If the 24 unknowns, the fundamental variables, are those quantities that appear in the natural boundary conditions at an edge r=constant, then the boundary value problem can be stated completely in terms of these variables. The solution vector containing the fundamental variables can be written as

$$\begin{aligned}\{y(r,\theta)\} \;=\; \{&u^1_{0r}, u^1_{0\theta}, w^1, \beta^1_r, \beta^1_\theta, N^1_r, N^1_{r\theta}, M^1_r, M^1_{r\theta}, Q^1_r, \tau_{rz}, q_r,\\ &\tau_{\theta z}, q_\theta, u^2_{0r}, u^2_{0\theta}, w^2, \beta^2_r, \beta^2_\theta, N^2_r, N^2_{r\theta}, M^2_r, M^2_{r\theta}, Q^2_r\}\end{aligned} \tag{4.2}$$

where u^i_{0r}, $u^i_{0\theta}$ are the in-plane displacements of the face sheet midplanes, w^i is the lateral deflection of the face sheets, β^i_r, β^i_θ are rotations of normals to the face sheet midsurfaces, N^i_r, $N^i_{r\theta}$ are the face sheet in-plane stress resultants, M^i_r, $M^i_{r\theta}$ are the face sheet moment resultants, and

Q_r^i are the face sheet radial transverse shear stress resultants $(i = 1, 2)$, τ_{rz} and $\tau_{\theta z}$ are the core shear stress components. q_r, q_θ are two new 'core variables' defined by:

$$q_r(r,\theta) = \tau_{rz,r}, \quad q_\theta(r,\theta) = \tau_{r\theta,r} \tag{4.3}$$

The complete set of governing equations is given in Appendix C. The dependency of the θ-coordinate is eliminated by Fourier series expansion of the fundamental variables thus reducing the problem to two sets of 24 first order ordinary differential equations.

4.2.5 Specification of Boundary Conditions

The boundary conditions prescribed for sandwich plates with 'through-the-thickness' and 'fully potted' inserts are not identical, as the support conditions for the face sheets and the core material adjacent to the insert are different for the two cases.

'Through-the-thickness' inserts

The actual statement of the boundary conditions varies somewhat from load case to load case (Q, *T*, *M* or N, see Figure 4.2), but with reference to Figure 4.2 the imposed boundary conditions are generally derived from the following assumptions:

$r = r_i$: The 'through the thickness' insert is considered as an infinitely rigid body to which the face sheets and the potting material are rigidly connected.

$r = r_p$: Continuity of the fundamental variables across the potting/honeycomb interface.

$r = r_c$: It is assumed that the face sheet and honeycomb core midsurfaces are simply supported.

The boundary conditions at $r = r_i$, $r = r_p$ and $r = r_c$ are stated by specifying linear combinations of the fundamental variables.

'Fully Potted' inserts

The 'fully potted' insert is modelled as a thick top face sheet (plate), although it is recognised, that this is a crude approximation. However, the insert will appear as a rigid body compared with the core and the thin face sheets, and the results obtained for the insert itself are therefore of no interest.

The system of governing equations contains elements of the type r^{-1}, r^{-2} and r^{-3}, see Appendix C, and therefore shows singular behaviour for $r \to 0$. To avoid this, the problem is rephrased slightly, assuming that the plate centre defined by a small radius $r = r_{im}$ (an imaginary 'inner rim') is removed. If $r = r_{im}$ is sufficiently small, this hardly influences the solution away from the plate centre. The actual statement of the boundary conditions varies somewhat from load case to load case (Q, *T*, *M* or N, see Figure 4.2), but with reference to Figure 4.2 the imposed boundary conditions are generally derived from the following assumptions:

$r = r_{im}$:
- Bottom face (face 2) : Free edge conditions are imposed.
- Potting (core) material : Free edge conditions are imposed.
- Top face (face 1) : The external loading is applied to the insert as surface loading distributed over the top surface of the insert.

$r = r_i$: Continuity of the fundamental variables, except for u_{0r}^1 and τ_{rz} which change discontinously.

$r = r_p$: Continuity of the fundamental variables across the potting/honeycomb interface,

$r = r_c$: It is assumed that the face sheets and honeycomb core midsurface are simply supported.

The boundary conditions at $r = r_i$, $r = r_p$ and $r = r_c$ are stated by specifying linear combinations of the fundamental variables.

4.2.6 Numerical Solution Procedure

The sets of governing equations, together with the statement of the boundary conditions constitutes a boundary value problem, which is solved using the 'multi-segment method of integration' as described in Section 2.2.8.

4.3 Examples

To show the applicability of the developed solution procedures, and to illustrate the differences in the mechanical behaviour between the 'through-the-thickness' and 'fully potted' insert types, two examples are presented. The first example is a sandwich plate with a 'through-the-thickness' insert, and the second one is a sandwich plate with a 'fully potted' insert. In both cases the inserts are subjected to axisymmetric transverse compressive loading, see Figure 4.2. Both examples are based on a symmetric insert/sandwich plate system defined by the geometrical and material properties shown in Table 4.1.

Face 1	Aluminium face sheet, $E_1 = 70.0$ GPa, $\nu_1 = 0.3$
Face 2	Same as Face 1, i.e. $E_2 = E_1$, $\nu_2 = \nu_1$
Insert	Same material properties as the face sheets, i.e. aluminium
Potting	Araldite AW106, $E_p = 1.5$ GPa, $\nu_p = 0.45$
Core	Divinycell H130, $E_c = 140$ MPa, $\nu_c = 0.33$
Geometry	$r_i = 5.0$ mm, $r_p = 10.0$ mm, $r_c = 100.0$ mm, c = 10.0 mm, $t_1 = t_2 = 1.0$ mm
Through-the-thickness ins.	$h_i = t_1 + c + t_2 = 12.0$ mm
Fully potted ins.	$h_i = 6.0$ mm
Load	Q = -10 N (compressive transverse load)

Table 4.1: Specification *of face sheets,* inserts, potting and core material and geometrical properties for sandwich plates *with* inserts.

The insert/sandwich plate problems shown in the examples and defined in Table 4.1, are the test specimens used for the experimental investigation described in the Section 4.4.1. This is the reason for the choise of a very small transverse loading.

4.3.1 'Through-the-thickness' Insert

The external load Q = -10 N has been applied by assuming a rigid body transverse motion of the insert, and results in the transverse deflections of the face sheets as well as the midsurface lateral displacement of the core material w_c as shown in Figure 4.3.

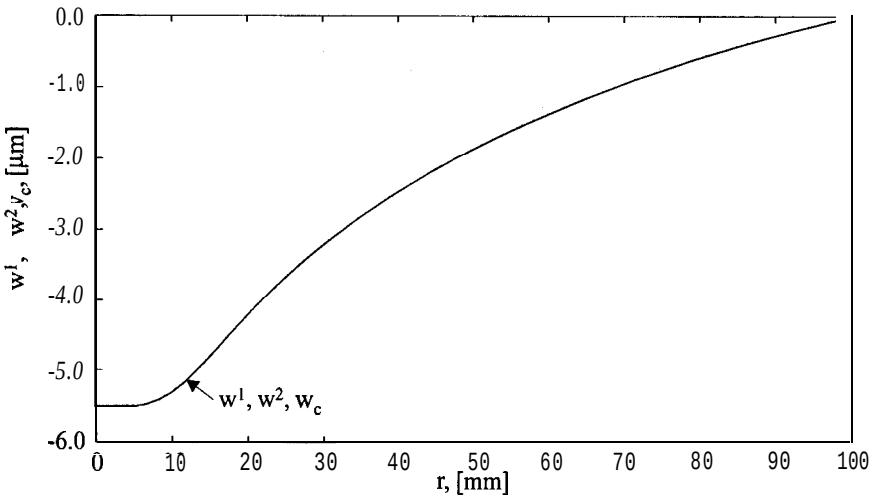

Figure 4.3: Radial distribution *of the* transverse deflections *of the face sheets* w^1, w^2 and *the core* midsurface w_c ofsymmetric sandwich plate *with* a 'through-the-thickness'insert subjected to *a* transverse loading Q = -10 N.

The interval $r \leq 5$ mm corresponds to the insert, and the interval $5 \leq r \leq 10$ mm corresponds to the potting region and $r \geq 10$ mm corresponds to the core region. Due to symmetry about the sandwich plate midplane the transverse deflection of the two face sheets are identical, but the deflections of the midplane of the core material w_c are slightly different from w^1, w^2 (difficult to see from the figure).

The radial distribution of the stresses in the core are shown in Figure 4.4.

The transverse normal core stresses are shown in the top and bottom interfaces between the core and the face sheets, i.e. σ_c^{top} and σ_c^{bottom}. From Figure 4.4 it is seen that the transverse normal stresses are very localized in and close to the potting region ($5 \leq r \leq 10$ mm). It is observed that σ_c^{top} and σ_c^{bottom} are of opposite signs, and that they change between tension and compression. The shear stresses, which are constant over the core thickness, decrease as r is increased.

Figure 4.5 displays the distributions of the radial bending moment resultants M_r^1, M_r^2.

It is seen from Figure 4.5 that the bending moment resultants are identical and display peak values at the intersection between the insert and the face sheets, which of course is owing to the assumption that the insert and the face sheets are rigidly connected. At the intersection between the potting and the core region a local peak of the bending moment resultants is observed. This is caused by the changes of the core stiffnesses at this location.

Figure 4.6 displays the radial distributions of the transverse shear stress resultants Q_r^1, Q_r^2.

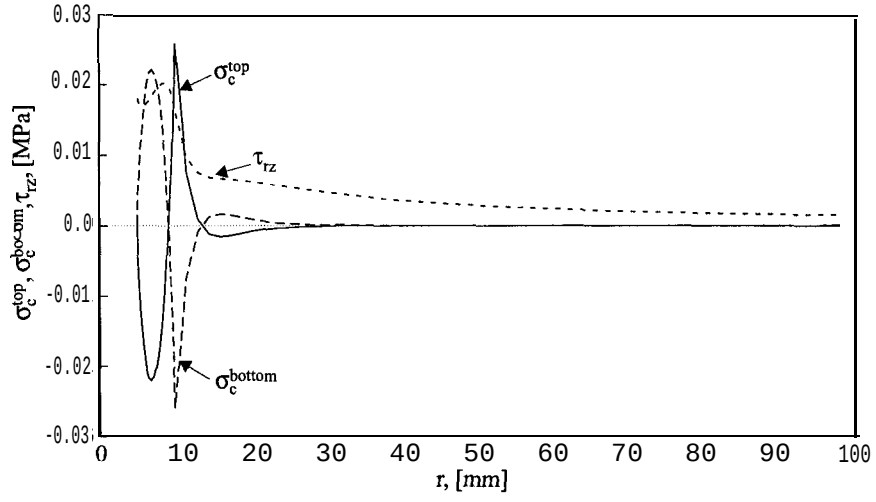

Figure 4.4: Core stresses τ_{rz}, σ_c^{top}, σ_c^{bottom} in symmetric sandwich plate *with* a *'through-the-*thickness' insert subjected to a transverse loading Q = -10 N.

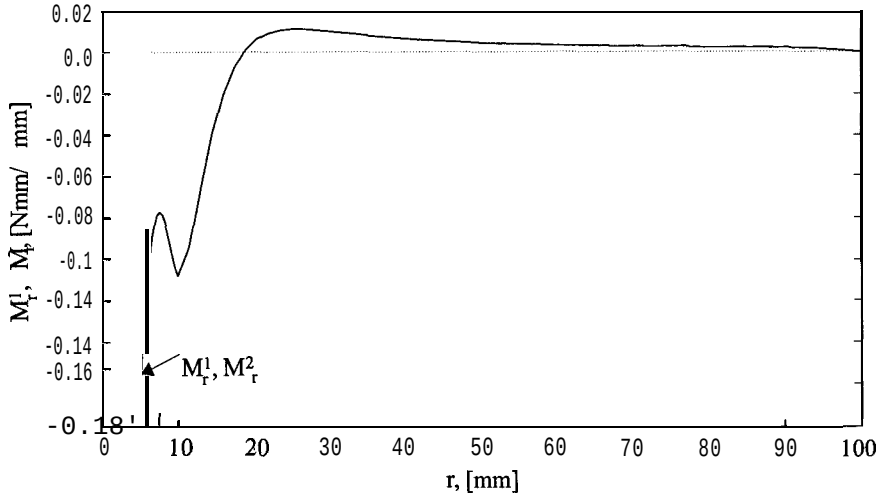

Figure 4.5: Radial bending moment resultants M_r^1, M_r^2 in *the face* sheets *of* symmetric sandwich plate *with* a 'through-the-thickness'insert subjected to a transverse loading Q = -10 N.

The results shown in Figure 4.6 are closely related to the results shown in Figure 4.5. Therefore, Q_r^1 and Q_r^2 are identical, and display the same pattern as M_r^1 and M_r^2 except the opposite sign. The peak values appear in the same positions as for M_r^1 and M_r^2.

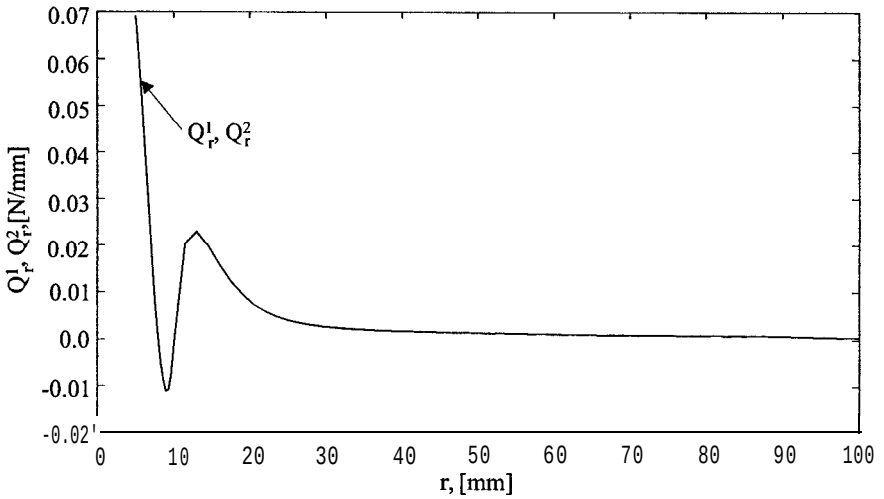

Figure 4.6: Radial transverse shear stress resultants Q_r^1, Q_r^2 *in the face sheets of* symmetric sandwich plate *with* a 'through-the-thickness'insert subjected to *a* transverse loading Q = -10 N.

4.3.2 'Fully Potted' Insert

The external load Q = -10 N has been applied as a transverse normal load distributed uniformly over the top surface of the insert.

Applying the external load gives the transverse deflections w^1, w^2 of the face sheets and the midsurface lateral displacement of the core material w_c shown in Figure 4.7.

In the interval r $\leq$ 5 the insert w^1 deflects as a rigid body and is indented into the potting compound, and it is observed that the deflection of the insert w^1 is larger than the midplane deflection of the potting material $w_c(z_c = 0)$ and the bottom face sheet w^2. This is owing to the circumstance that the insert is 'indented' into the potting compound through the action of the compressive transverse load on the insert. It is also observed that the deflection of the top face sheet (w') in the potting region (5 $\leq$ r $\leq$ 10 mm) is larger than the deflection of the bottom face sheet (w^2), since the insert is assumed to be rigidly connected to the top face sheet. In the interval $r \geq 10$ mm w^1 and w^2 are almost identical. Compared with the transverse deflections for the 'through-the-thickness' insert, see Figure 4.3, it is seen that the deflection pattern in the potting region is very different.

The radial distribution of the core stresses is shown in Figure 4.8.

The transverse normal core stresses are again shown in the top and bottom interfaces between the core and the face sheets, i.e. σ_c^{top} and σ_c^{bottom}. From Figure 4.8 it is seen that large compressive stresses (σ_c^{top}) appear underneath the insert, since the insert is indented into the potting compound. The transverse normal stresses in the bottom interface (σ_c^{bottom}) are tensile in the potting region under the insert, and compressive in the rest of the potting region. The core shear stresses increase in the entire potting region, whereas a discontinuity in the shear stresses appear'at r = 5.0 mm where the insert ends, since the core thickness changes at this location. After the potting region the shear stresses decrease with increasing values of r, as was also seen for the 'through-the-thickness' insert case

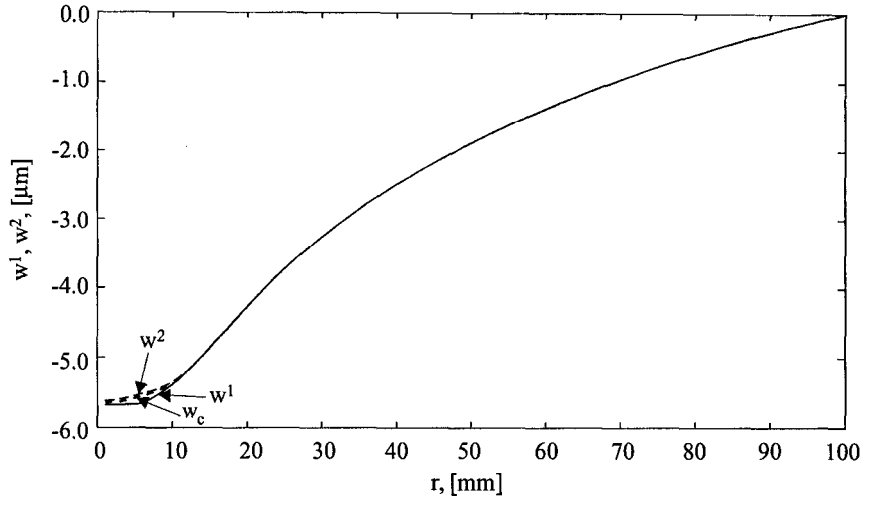

Figure 4.7: Radial distribution *of the* transverse deflection of the face sheets w^1, w^2 *of* symmetric sandwich plate with a *'fully* potted'insert *subjected to* a transverse loading Q = -10 N.

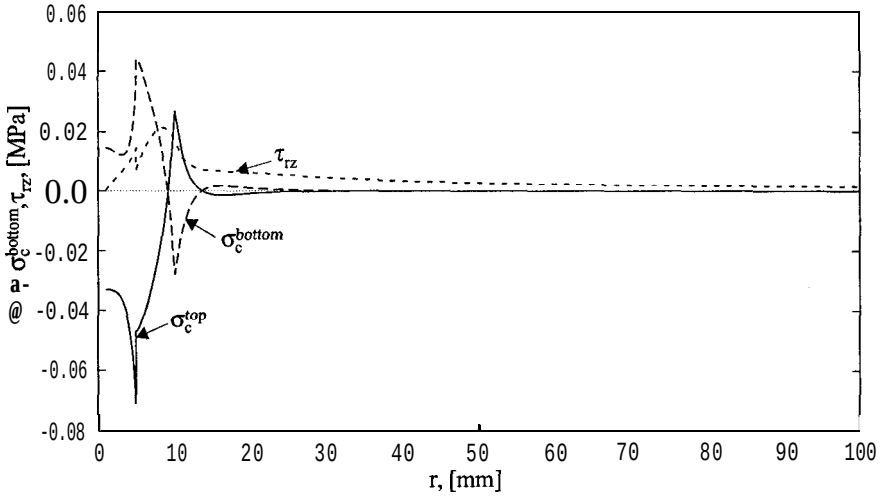

Figure 4.8: Core stresses $\tau_r z$, σ_c^{top}, σ_c^{bottom} in symmetric sandwich plate *with a 'fully* potted' *insert* subjected to a transverse loading Q = -10 N.

Figure 4.9 displays the radial distributions of the radial bending moment resultants M_r^1, M_r^2.

It is seen that large bending moment resultants appear in the top face close to the insert, whereas only small bending moment resultants are induced in the bottom face sheet. The reason for this is that the insert is only attached directly to the top face sheet, whereas the loads acting on the bottom face sheet have been transferred through the relatively flexible potting material. Thus, the load introduction in the bottom face sheet has been 'smoothed' considerbly, which again causes inducement of small bending moment resultants. Compared with the bending moment

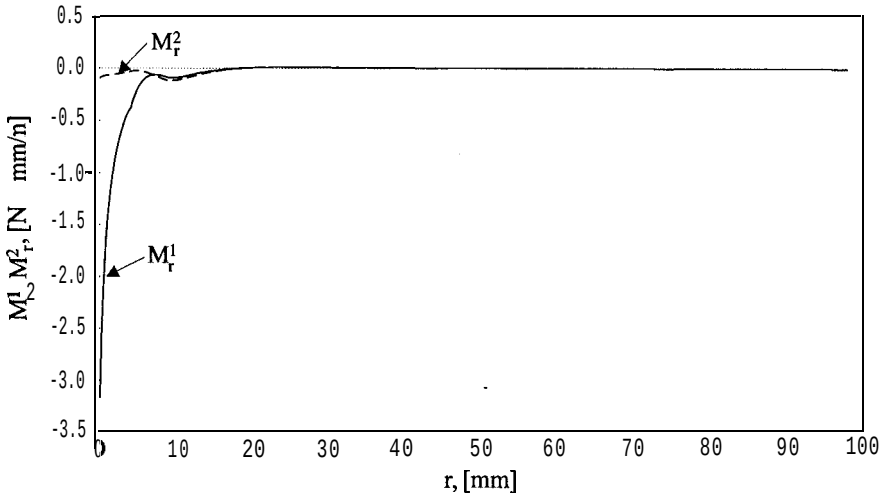

Figure 4.9: Radial bending moment *resultants* M_r^1, M_r^2 *in the face sheets of symmetric* sandwich plate with a 'fully *potted' insert* subjected to a transverse loading Q = -10 N.

resultants induced in the face sheets of the 'through-the-thickness' insert problem, see Figure 4.5, it is seen that the peak bending moment resultant induced in the face sheets of the 'fully potted' insert problem is about 17 times larger.

Figure 4.10 displays the radial distributions of the radial shear stress resultants Q_r^1, Q_r^2.

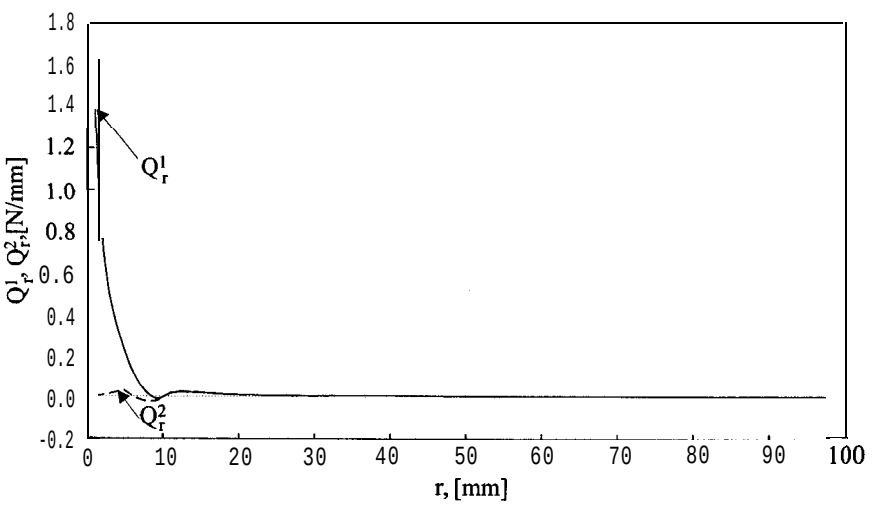

Figure 4.10: Radial transverse shear stress resultants Q_r^1, Q_r^2 *in the* face sheets of symmetric *sandwich plate with a 'fully potted' insert subjected to a transverse loading Q =* -10 N.

The results shown in Figure 4.10 are closely related to the results shown in Figure 4.9, and large shear stress resultants therefore only appear in the top face sheet. Compared with the shear stress resultants induced in the face sheets of the 'through-the-thickness' insert problem, see Figure 4.5, it is seen that the maximum shear stress resultant induced in the top face sheets of the 'fully potted' insert problem is about 23 times larger.

4.3.3 Summary

The objective of this section has been to show the applicability of the developed solution procedure for the analysis of sandwich plates with 'through-the-thickness' and 'fully-potted' inserts.

For both insert types it is observed that very localized effects appear in the area around the inserts, and that stresses, which cannot be predicted by application of a 'classical' antiplane sandwich plate theory, appear in the core and potting material.

The examples have revealed significant differences in the sandwich plate responses induced by the two insert types.

4.4 Investigation of the Validity of the Approach

The work reported by Thomsen (1994a), Thomsen (1994b), Thomsen and Rits (1998) and Thomsen (1998) on the analysis of sandwich plates with inserts using a high-order sandwich plate theory approach has not been validated thoroughly before, and it was decided to investigate the validity of the approach by comparison with results obtained from an experimental investigation and with results obtained from finite element analysis. The objectives of the comparative investigations have been limited to:

- Evaluation of the theoretical approach for sandwich plates with 'through-the-thickness' and 'fully potted' inserts subjected to transverse loading Q, by comparison of the predicted face sheet deflections with experimental measurements on test specimens.
- Evaluation of the high-order sandwich plate theory approach by comparison with finite element analysis results. The comparative study focuses on the boundary/continuity conditions between the insert and the face sheets/potting material for sandwich plates subjected to transverse loading Q.

4.4.1 Experimental Investigation

The experimental investigation of the transverse deflections of the face sheets in a sandwich plate with an insert has been performed using *Electronic Speckle Pattern Interferometry*, abbreviated ESPI. The reason for chosing this type of measurement is that the ESPI technique (or other optical methods such as holographic interferometry - HI) is a whole field measurement method. This means that it is possible from just one experiment to obtain information about the complete displacement field of the surface area considered.

Electronic Speckle Pattern Interferometry - ESPI

When an object is illuminated by a laser, it is covered with a very fine granular structure. All the points of the object illuminated by the laser are coherent, and the waves that they transmit are capable of interfering. The image from each object point produces a diffraction image, and the interference between these diffraction images is responsible for the granular structure known as the speckle pattern.

In ESPI the basic idea is to use the speckle pattern correlation to create fringes. This is the same idea as used in classical holographic interferometric (HI), where a wavefront emanating from an object (the test specimen) are made to interfere with a wavefront from the same object recorded on a photosensitive plate at an earlier time and thus creating fringes. In ESPI the fringe pattern is created by digital image subtraction of two subsequent video recordings of different speckle patterns. The first recording displays the speckle pattern of an unloaded specimen, known as the reference image, and the second one displays the speckle pattern of the loaded specimen (the recording can be made in reverse order). The stored images are manipulated using digital image processing techniques to create an image, known as a specklegram, displaying interferometric data as fringe patterns. The data produced by ESPI are similar to the data produced by a holographic recording, as each fringe represents a line of constant deflection amplitude. The information displayed in the specklegram only represents relative displacements with respect to the surface shape stored in the reference picture.

The main difference between HI and ESPI is the image quality. The resolution of the recording medium used for ESPI needs only to be relatively low, compared to the requirements for the recording of a HI-image.

The only disadvantage of ESPI, compared with HI, is that the fringe patterns contain an unavoidable amount of speckle noise, which can make the fringe pattern obscured, and reduces the maximum number of fringes as the technique can determine. As a consequence of this there is a limit on the maximum displacements the system can determine, since each fringe represents a line of constant deflection amplitude. For further details of the features of HI and ESPI techniques, reference is made to Fracon (1979) and Maas (1991).

The interferometric measurements, carried out as part of this thesis work, were performed using the SD-10-S ESPI system from Newport Instruments AG with image processing software from GOM - Gesellschaft für Optische Messtechnik. The system is only capable of determining the displacements in one direction at a time. Thus, if the entire displacement field must be determined, i.e. in all three space directions x, y and z, then three measurements must be performed. The characteristics of the used ESPI system in terms of measuring range and accuracy are:

- Measuring range:
  - Out-of-plane: up to 25 μm
  - In-plane: up to 50 μm
- Accuracy:
  - Out-of-plane: 0.04 μm
  - In-plane: 0.1 μm
- Up to 30 recordings per second

The experimental set-up of the ESPI system is shown in Figure 4.11.

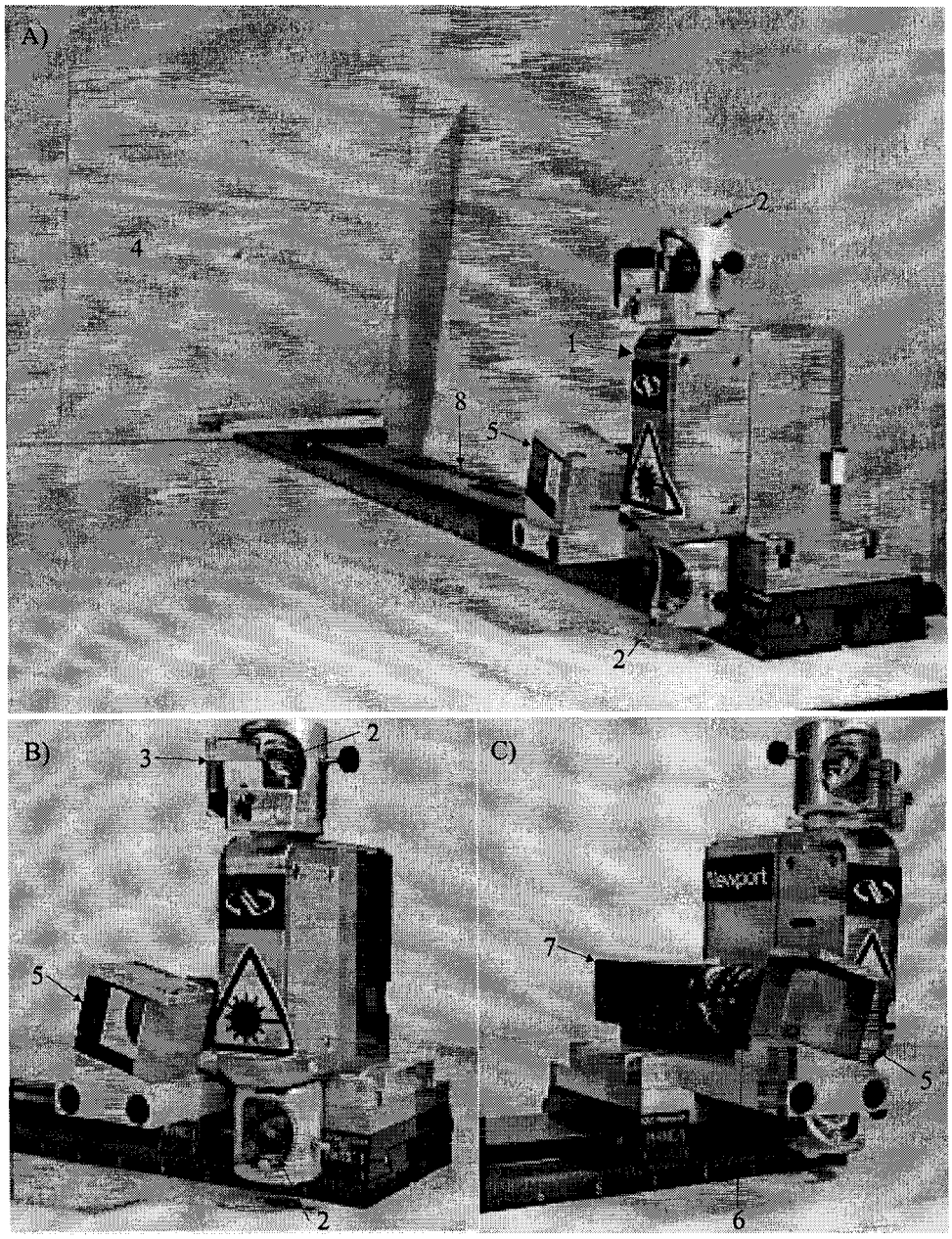

Figure 4.11: *ESPI* system from Newport Instruments AG. A) The entire set-up of *the ESPI* system for measurements of transverse deformations, B) and *C)* Zoom *of the ESPI* head.

Figure 4.11-A) displays the entire set-up of the ESPI system for measurements of transverse deformations, and Figure 4.11-B) and C) display a zoom of the ESPI head. The system consists of (1) a 50 mW laser diode, (2) two satellite mirrors, (3) one regular mirror, (4) a reference plane, (5) a beamsplitter, (6) a lens, (7) a CCD camera and (8) an optical rail.

The ESPI system shown in Figure 4.11 is, as previously mentioned, capable of measuring the

displacements in all three space directions, i.e. in the x, y and z-directions. The laser beam from the laser diode is internally divided in two beams with a phase shift device (realized with a piezo element), which allows to modify the optical path length of one of the laser beams, and each of these laser beams illuminate the satellite mirrors (2). If the system is used for measuring in-plane displacements the two satellite mirrors (2) are used to reflect the laser light onto the object and thereby illuminating the object. For measuring the displacements in the vertical direction the satellite mirrors (2) are placed as shown in Figure 4.11 above and below each other, and the beamsplitter (5) is removed from the set-up. For measuring the displacements in the horizontal direction, the satellite mirrors (2) are rotated such that they are placed in the same horizontal plane, and the beamsplitter (5) is removed from the set-up as for the measurement of displacements in the vertical direction. For measurements the transverse displacements, as shown in Figure 4.11, the beamsplitter (5) is mounted in front of the lens, and the reference plane (4) is mounted on the optical rail (8). The upper satellite mirror (2) is now directed to illuminate the reference plane (4) by use of a regular mirror (3), and the CCD camera (7) will now see both the object and the reference plane (4). After the set-up has been arranged, the measurements can be made. Deformations of the illuminated object will change the speckle pattern, which can can be measured by the system.

Test Specimens, Test Set-up and Experimental Procedure

Two test specimens were manufactured for the investigation, one with a 'through-the-thickness' insert and one with a 'fully potted' insert. The test specimens are based on a symmetric insert/sandwich plate system defined by the geometrical and material properties shown in Table 4.2, which are the same as shown in Table 4.1 in Section 4.3 assumed for the numerical examples.

Face 1 Face 2 Insert	Aluminium face sheet, E_1 = 70.0 GPa, ν_1 = 0.3 Same as Face 1, i.e. $E_2 = E_1$, $\nu_2 = \nu_1$ Same material properties as the face sheets, i.e. aluminium
Potting/Adhesive	Araldite AW106, E_p = 1.5 GPa, ν_p = 0.45
Core	Divinycell H130, E_c = 140 MPa, ν_c = 0.33
Geometry	$r_i = 5.0$ mm, $r_p = 10.0$ mm, $r_c = 104.0$ mm, c = 10.0 mm, $t_1 = t_2 = 1.0$ mm
Through-the-thickness ins,	$h_i = t_1 + c + t_2$ = 12.0 mm
Fully potted ins.	$h_i = 6.0$ mm
Load	Q = -10 N (compressive transverse load)

Table 4.2: Specification *of face sheets,* insert, potting, core material and geometrical properties *for* sandwich *plates* with inserts.

The test specimens are shown in Figure 4.12, where $d_i = 2r_i = 10$ mm, d_0 = 11 mm, $d_p = 2r_p =$ 20 mm, $d_c = 2r_c$ = 208 mm, $t_1 = t_2 =$ 1.0 mm and t_c = 10 mm, in accordance with Table 4.2. The diameter d_0 shown in 4.12 is the diameter of the hole in the face sheets for the insert and accounts for the tolerances on the insert and the face sheets, and for misalignments during bonding of the face sheets and the core material.

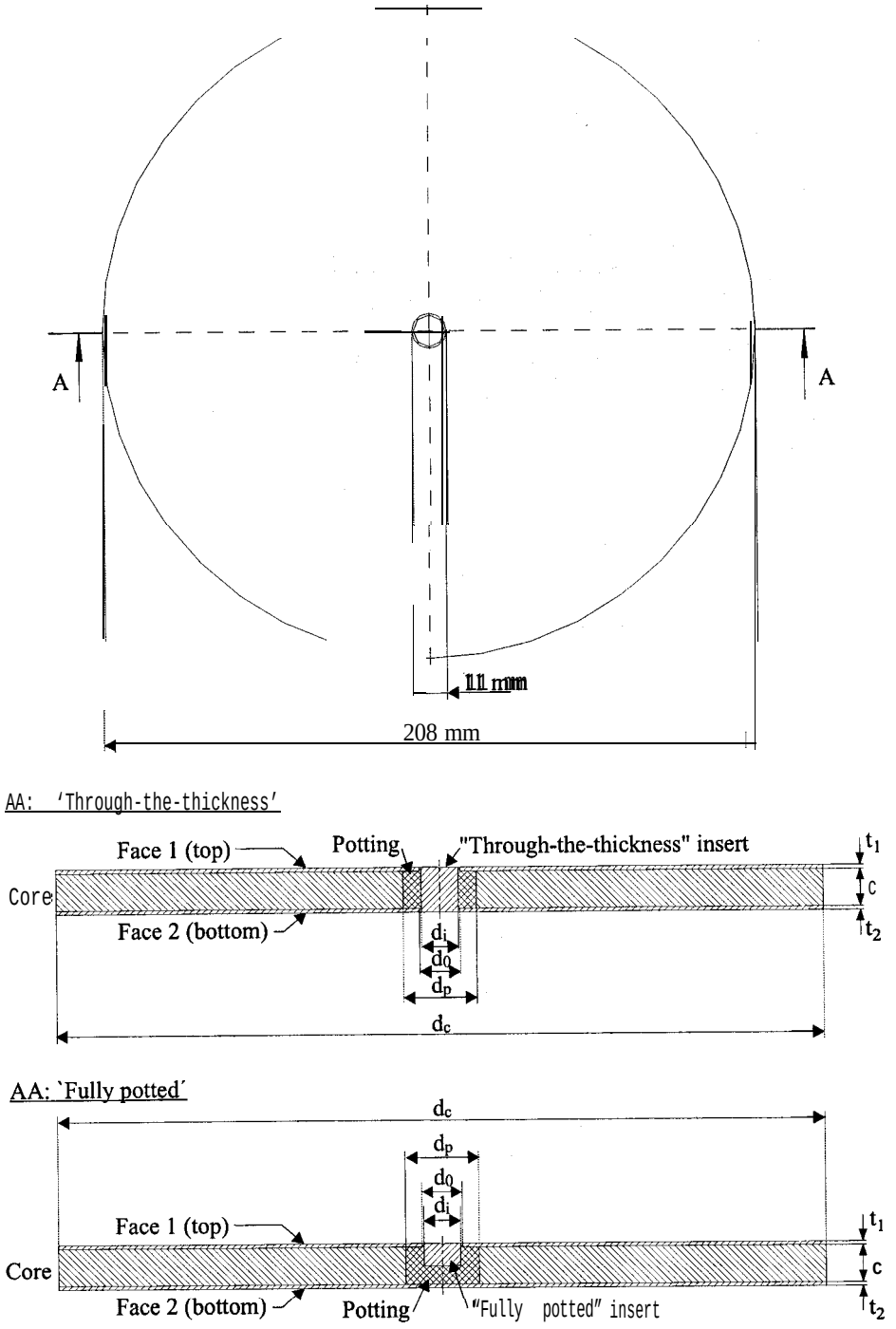

Figure 4.12: Circular sandwich plate test specimens *with* 'through-the-thickness' and *'fully potted' inserts.*

The test rig shown in Figure 4.13 was used for the experiments. The device has been used previously for the investigation of local bending effects in sandwich plates, see Thomsen (1995).

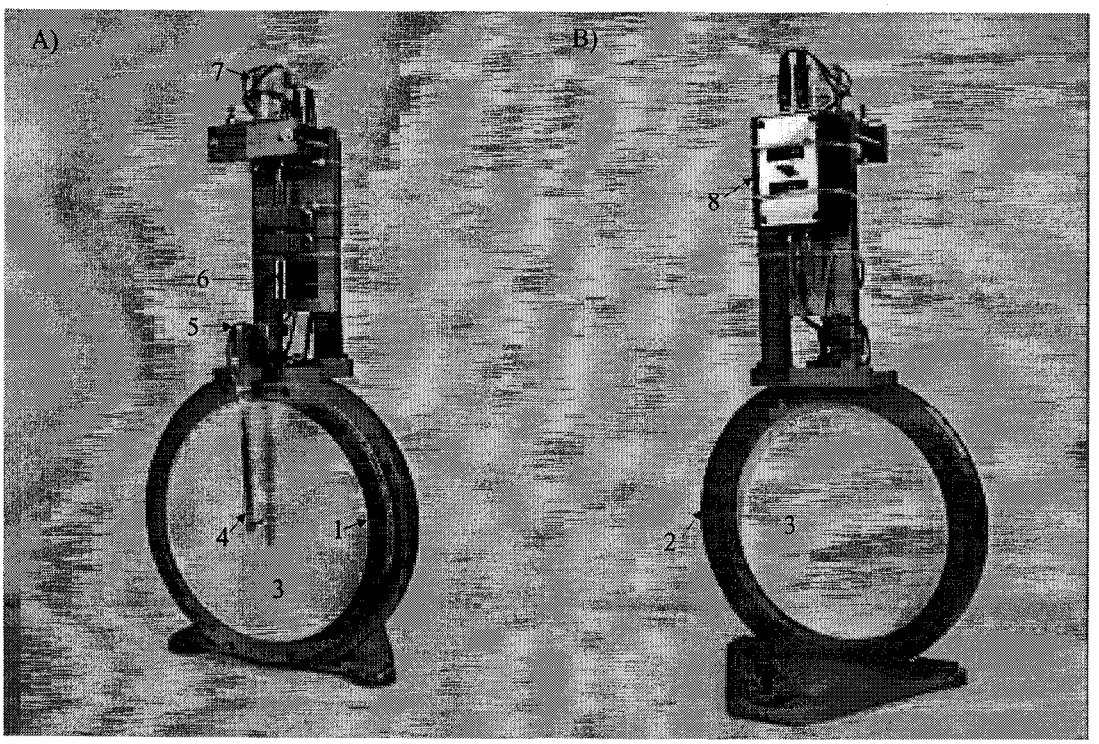

Figure 4.13: *Test rig for loading and clamping of circular sandwich plate with an insert.*

The test rig is designed such that it is possible to see both the top and bottom face sheets of the sandwich plate test specimens from exterior positions. Thereby it is possible to make ESPI measurements on both sides of the test specimens. With references to Figure 4.13, the test rig consists of two rings (1), (2) between which the circular sandwich plate with an insert (3) is clamped. On top of the ring arrangement, a loading device is placed consisting of a loading arm (4), which can rotate about a hinge (5). The loading arm is activated through a spindle arrangement (6), which again is driven by a 24 V DC motor (7) mounted with a gearbox (gear ratio 1:150; loading arm travelling speed; 0.1 mm/s). Start/stop of the DC motor is controlled through a switch box (8).

The load is transferred from the loading arm (4) to the centre of the insert in the sandwich plate (3) through a small pin. The pin is sharpened at both ends to simulate a point load and to avoid the transfer of bending moment loading between the pin and the loading arm (4). To measure the actual load applied to the insert, the loading arm (4) is mounted with two strain gauges, which are connected to a HBM UMP 60 strain gauge amplifier in a Wheatstone half-bridge. The maximum load to which the loading device was designed is 50 N, but in the actual experiments the maximum load was $Q_{max} =$ IO N. If the load is increased further, the number of fringes also increases, and it becomes impossible to distinguish between the individual fringes.

The inner radius of the ring (1) and (2) is R = 100 mm, and the ESPI system is therefore only capable of determining the deflection of the face plates/inserts within in this radius. The boundaries at R = 100 mm of the sandwich plate are assumed to be simply supported in the

analysis, i.e r_c = 100 mm in the numerical examples. The real boundary conditions within the test rig will be somewhere between clamped and simple supported conditions. However, clamping of the sandwich plate at the circumference at $r_c = R$ = 100 mm in the analysis, gives almost the same results. Thus in the numerical examples used for comparison the outer circumference of the sandwich plate is chosen to be r_c = 100 mm. Figure 4.14 shows the test rig placed in front of the ESPI system used.

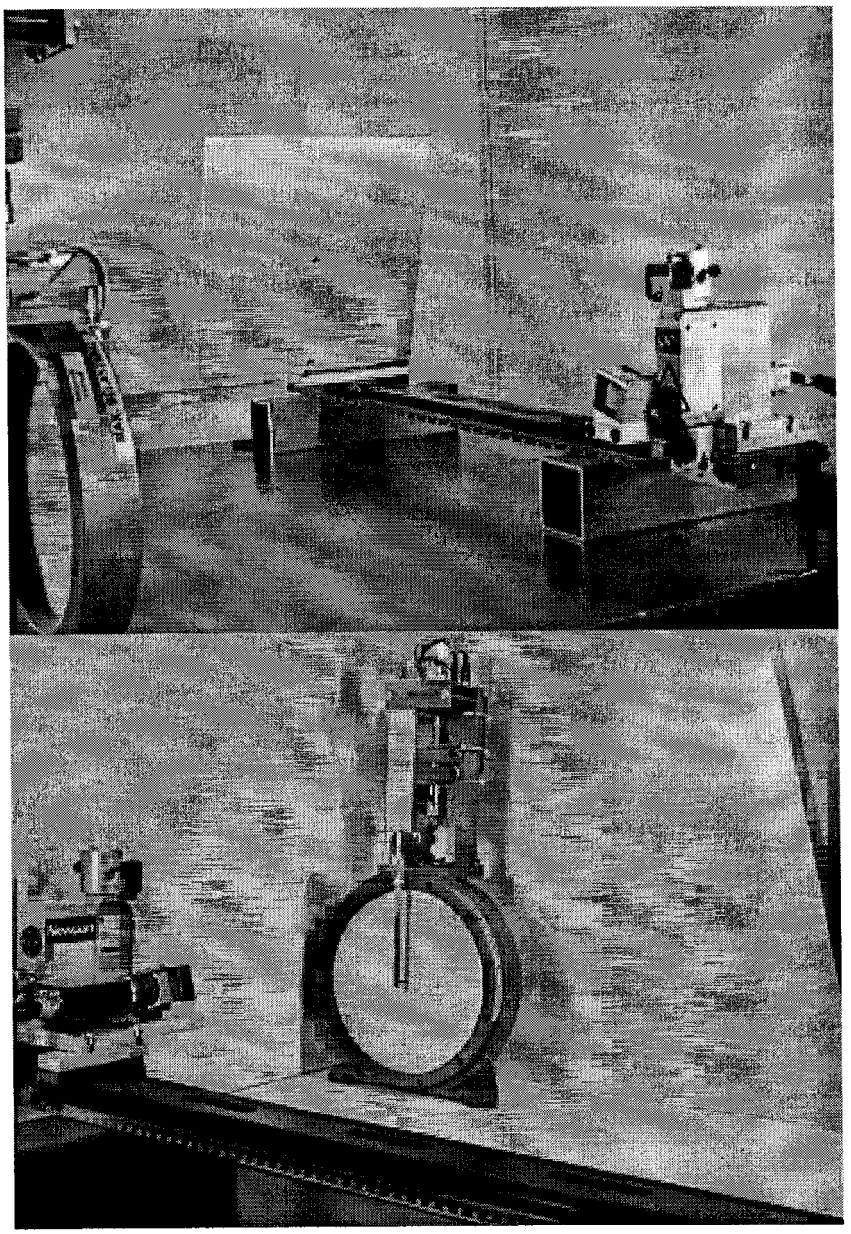

Figure 4.14: Experimental set-up for measuring the *face* sheet transverse displacements of sandwich plates *with an* insert *using the ESPI technique.*

After the test specimen has been positioned in the test rig, the following test procedure was

followed in the recording of interferometric images:

- The test rig is positioned such that the lower part of the sandwich plate and the test rig, from the insert and downwards, can be recorded by the CCD camera.
- The size of the images recorded is determined.
- A reference picture is captured where the insert is unloaded.
- The load is applied to the insert, and a new picture is captured.
- A phase difference image is computed from the two images captured by the system. Each phase image contains 768 x 512 pixels.
- From the phase difference image the ESPI system determines the transverse displacements within the entire recorded area.
- After the displacements have been determined for the insert and the top face sheet, the test rig is turned around, a reference picture is captured, the load is removed, a new picture is captured, and a phase image containing 768 x 512 pixels is computed. From this phase image the bottom face sheet transverse displacements are determined. This procedure ensures that the displacements of the top and bottom face sheets are measured at the exact same load.

Measurements, Results and Discussion: 'Through-the-thickness' Insert

The phase image of the top face sheet of the sandwich plate with a 'through-the-thickness' insert loaded with (approximately) Q = -10.0 N is shown in Figure 4.15.

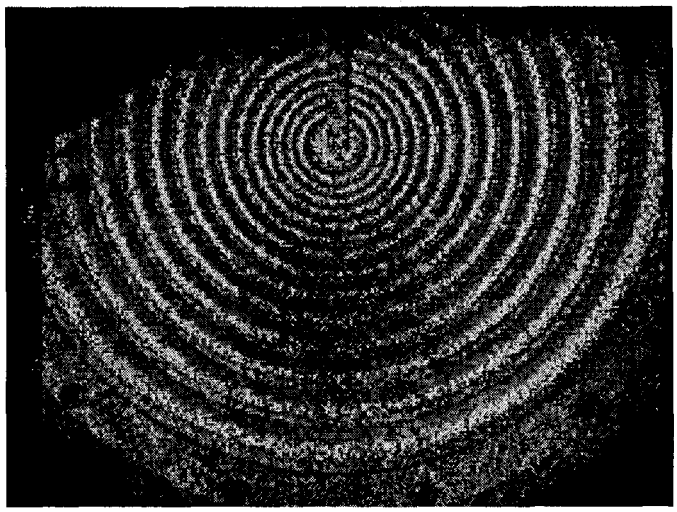

Figure 4.15: Phase image *of top face sheet of sandwich plate with a 'through-the-thickness' insert.*

The phase image shown in Figure 4.15 is, as described previously, obtained by subtracting the speckle pattern images of the test specimen captured in its unloaded and loaded configurations, respectively. The size of the image shown in Figure 4.15 is 200 mm x 150 mm. Right below the loading arm and the insert there is an area where the speckle pattern is a bit indistinct, which is due to an insufficient illumination of the sandwich plate.

After the phase image, shown in Figure 4.15, has been determined the image is unwrapped, which means that the phase image is converted into a new image containing information about the actual displacements. The unwrapped image of the phase image (Figure 4.15) is shown in Figure 4.16.

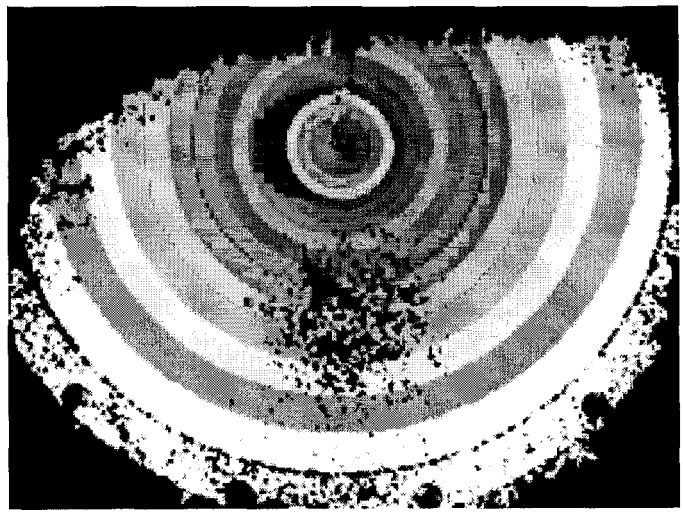

Figure 4.16: Unwrapped phase image of top face sheet of sandwich plate with a *'through-the-*thickness' insert.

The fringe pattern observed in Figure 4.15 and Figure 4.16 shows a system of circular rings. The circular fringe rings are nearly concentric, which indicates that the support of the sandwich plate along the outer boundary is almost uniform, and that the loaded insert is placed very near the exact centre of the sandwich plate. Each of the rings shown in the unwrapped image in Figure 4.16 are level curves representing equal magnitudes of the transverse displacements. The consequences of having areas with indistinct speckle patterns, caused by insufficient illumination as described above, are seen from Figure 4.16 as areas with little or no information about the displacements.

The information about the displacements shown in Figure 4.16, can be displayed as shown in Figure 4.17, which shows the transverse displacements of half (approximately) of the top face sheet of the sandwich plate test specimen with a 'through-the-thickness' insert.

Figure 4.17 also displays the 'iso'-displacement curves of the face sheet, which form a pattern of nearly concentric circles. In areas where little information about the displacements are obtained from the measurements owing to pour illumination, the displacements are interpolated and thus a continuous displacement surface is shown in Figure 4.17.

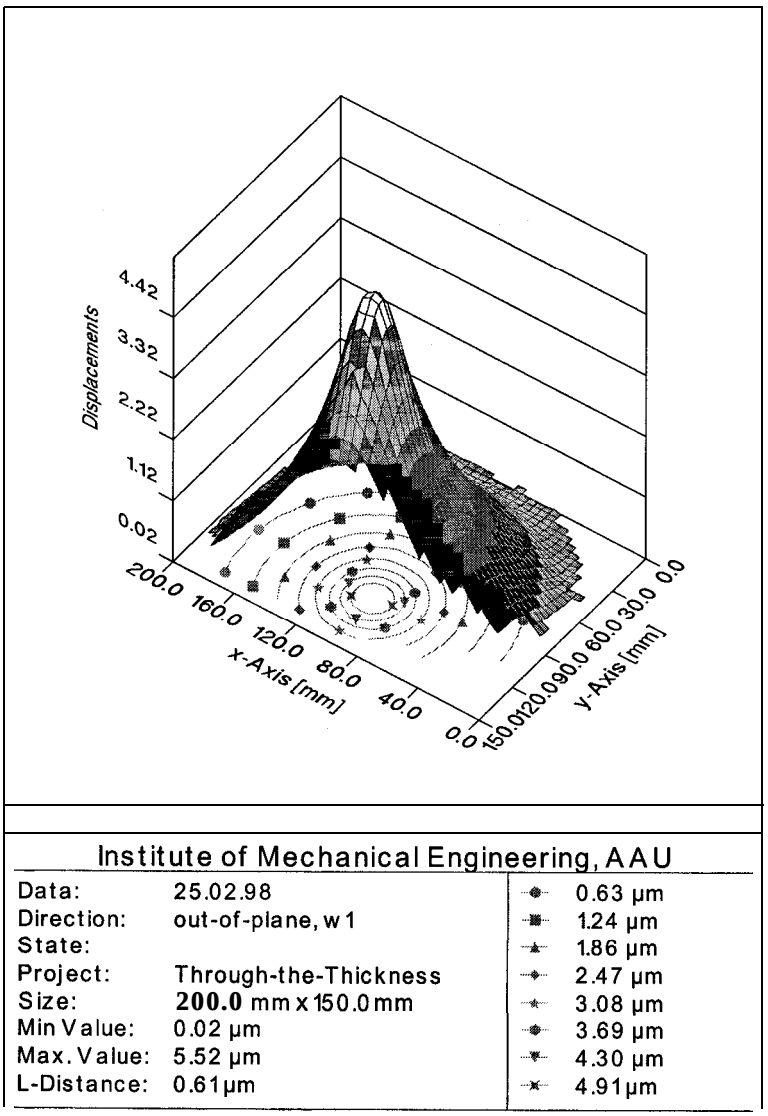

Figure 4.17: Transverse displacements *of the top face sheet (Face* 1) *of the* sandwich plate *test* specimen with a 'through-the-thickness'insert $(Q = -10\ N)$.

In the same way the displacements of the bottom face sheet (Face 2) are displayed in Figure 4.18.

By picking out the displacements along three radial sections, and by averaging the measured displacements along these sections, an average radial displacement distribution is derived. In

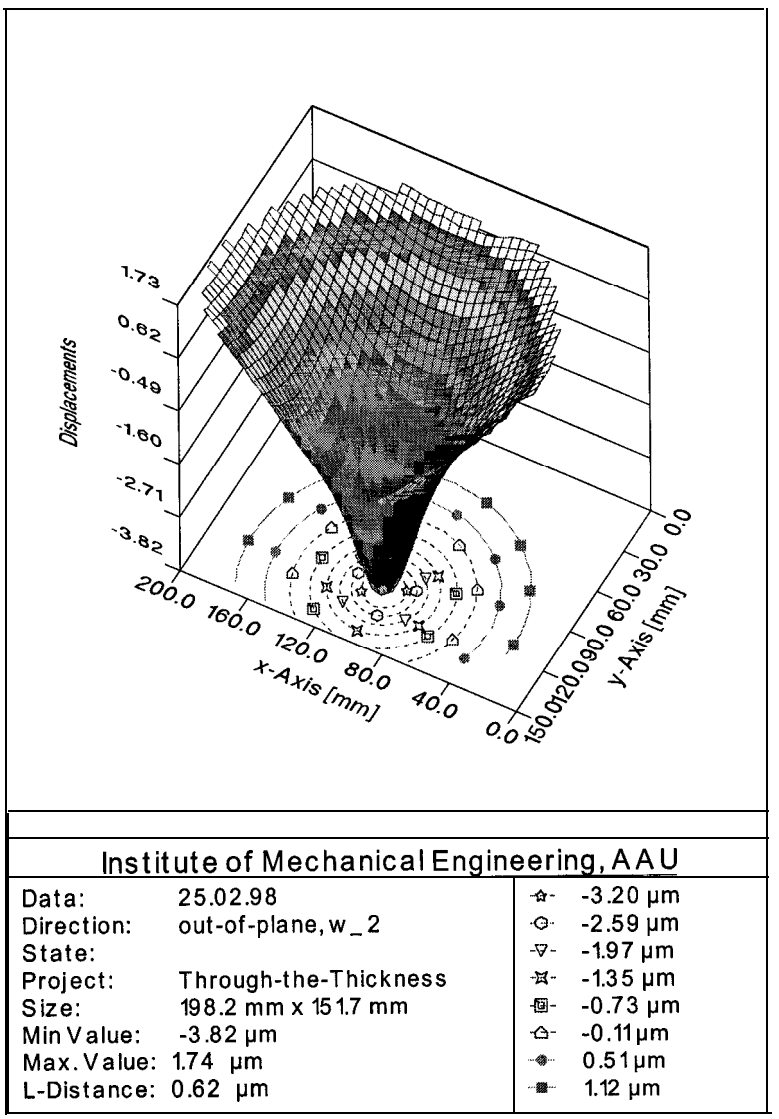

Figure 4.18: Transverse displacements of the bottom face sheet (Face 2) of the sandwich plate test specimen with a 'through-the-thickness'insert (Q = -10 N).

this average displacement distribution, the effects of a slight misalignment of the insert and slightly non-axisymmetric boundary conditions are reduced considerably. The derived radial distributions of the transverse displacements of the face sheets are shown in Figures 4.19 and 4.20.

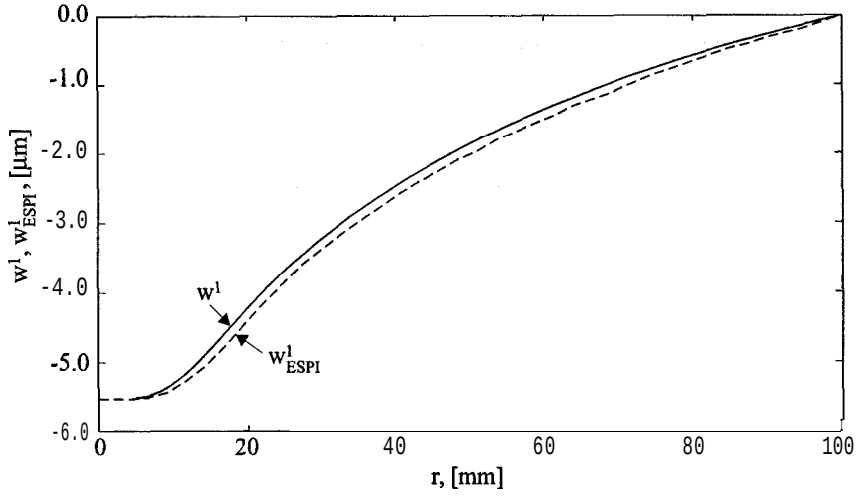

Figure 4.19: Radial distribution of *the* transverse displacements *of the top face sheet (Face 1) of the* sandwich plate *test* specimen *with* a 'through-the-thickness' insert, determined *by ESPI* measurements and compared *with* high-order theory prediction (Q = -10 *N).*

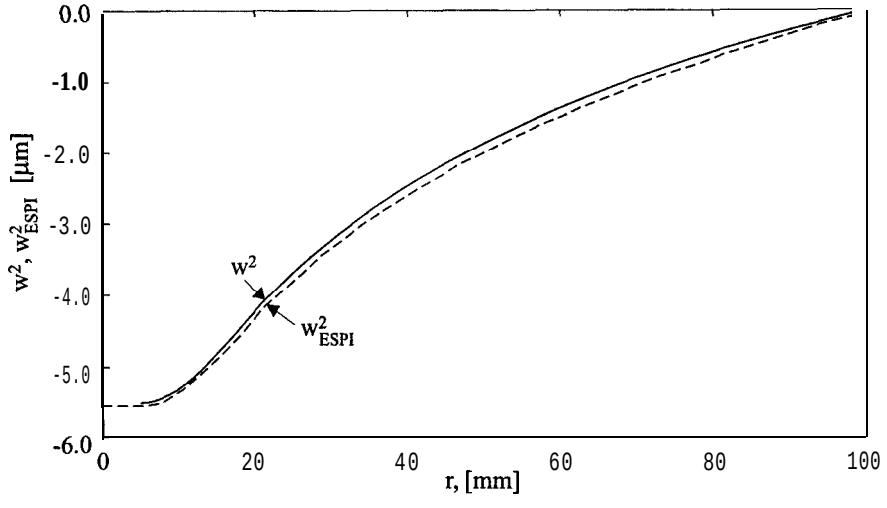

Figure 4.20: Radial distribution *of* transverse displacements *of the* bottom *face sheet (Face 2) of* the sandwich plate test specimen with a 'through-the-thickness' insert, determined *by ESPI* measurements and compared *with* high-order theory prediction (Q = -10 *N).*

From Figure 4.19 and Figure 4.20, it is seen that the results obtained for the transverse displacements using the high-order theory approach for the sandwich plate with a 'through-the-thickness' insert compare very well with the measurements. From Figure 4.19 and Figure 4.20 it is seen that the measured displacements of the top and bottom face sheet are identical (or nearly identical).

This result was also predicted by the high-order sandwich plate theory (see Figure 4.3), and in fact the same result could have been achieved by application of classical 'antiplane' sandwich plate theory. The reason for this is that the 'through-the-thickness' insert forces the two face sheets to deflect together, thus effective suppressing the effect of the transverse core flexibility on the displacements of the face sheets. However, in sandwich plates with 'fully potted' inserts subjected to transverse loading the face sheets are not directly attached to each other through the rigid insert, and the displacements predicted by using the high-order theory (which accounts for the transverse core flexibility) will differ from the displacements predicted using a classical antiplane sandwich theory.

Measurements, Results and Discussion: 'Fully Potted' Insert

Figure 4.21 shows the transverse displacements of half (approximately) of the top face sheet of the sandwich plate test specimen with a 'fully potted' insert.

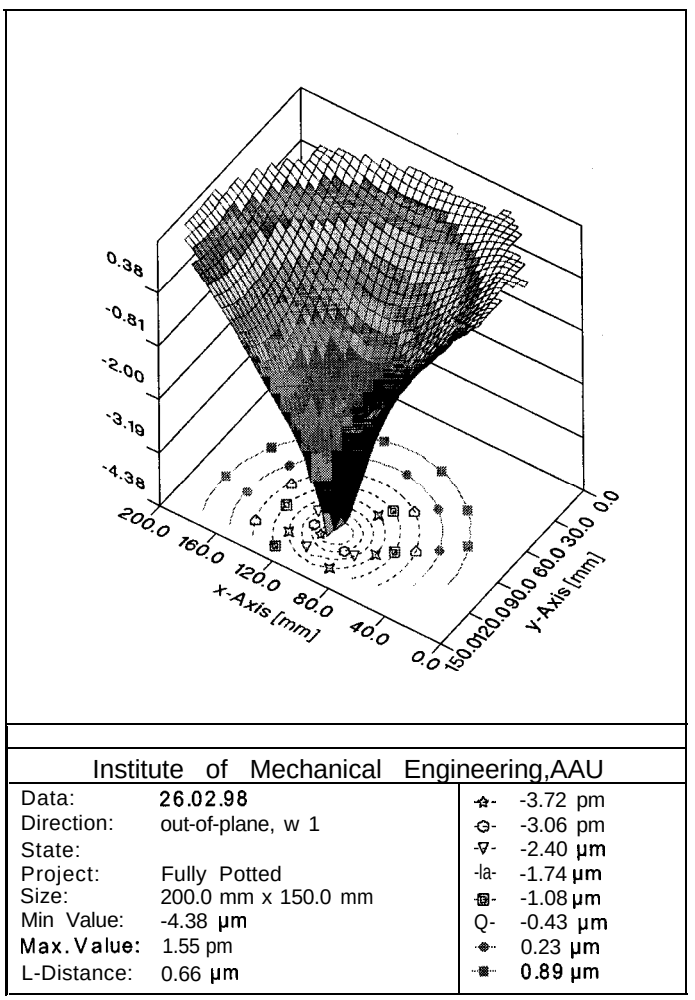

Figure 4.21: Transverse displacements of the top face sheet (Face 1) of the sandwich plate test specimen with a 'fully potted'insert (Q = -10 N).

Figure 4.22 shows the transverse displacements of half (approximately) of the bottom face sheet of the sandwich plate test specimen with a 'fully potted' insert.

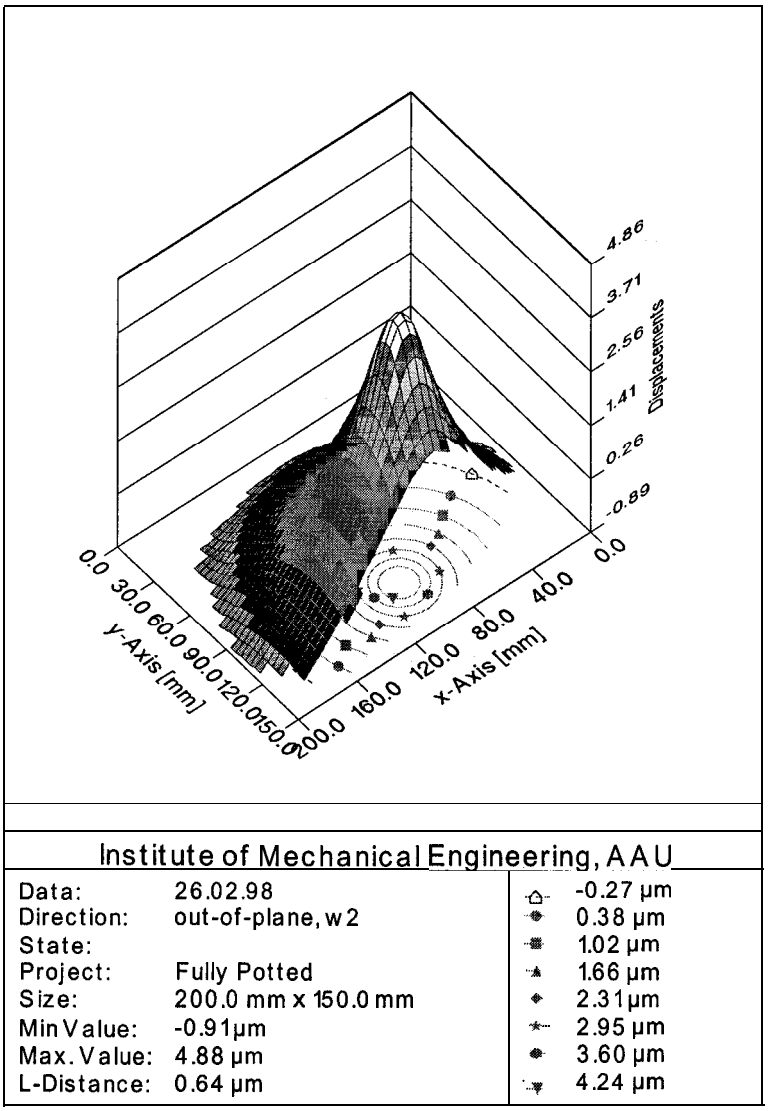

Figure 4.22: Transverse displacements *of* the bottom face sheet *(Face* 2) of the sandwich plate test specimen with a 'fully potted' insert $(Q = -10\ N)$.

Picking out the displacements along three radial sections of the surface plots of the two face sheets and averaging the results, as for the 'through-the thickness' insert problem, gives the average radial displacements distribution for the 'fully potted' insert problem. The resulting transverse displacement distribution are shown in Figure 4.23 and Figure 4.24 for the top and bottom face sheets, respectively.

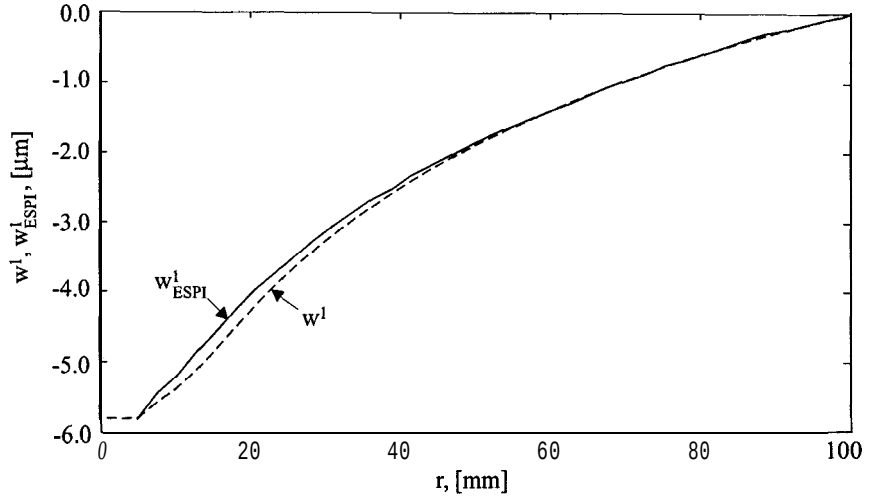

Figure 4.23: Radial distribution of the transverse displacements of the top face sheet (Face 1) of the *sandwich* plate test *specimen* with a 'fully potted' insert, determined by *ESPI* measurements and by high-order theory prediction (Q = -10 *N).*

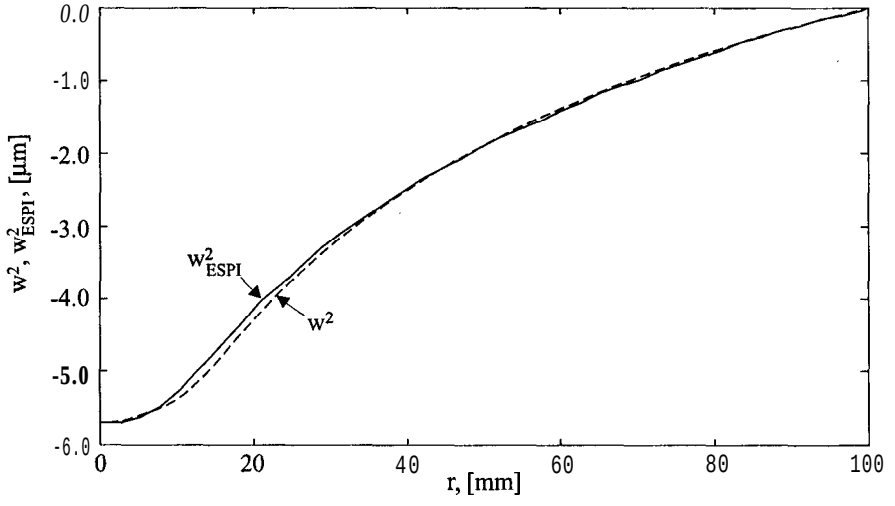

Figure 4.24: Radial distribution *of* the transverse displacements *of the* bottom *face* sheet (Face 2) of *the* sandwich plate test specimen with a 'fully potted' insert, determined by *ESPI* measurements and *by high-order* theory prediction (Q = -10 *N).*

From Figure 4.23 and Figure 4.24 it is seen that the results obtained by the experimental measurements and by the high-order theory approach compare very well. Moreover, the experimental measurements also show that there is an indentation of the insert and the face sheets in the area around the insert (see also Figure 4.7). This phenomenon cannot be predicted using a classical antiplane sandwich plate theory, since such theories assume a priori that the sandwich plate thickness remains constant during deformation.

Thus, for sandwich plates with inserts subjected to transverse loading, the displacement fields predicted by use of the high-order sandwich plate theory correlates very well with the experimental measurements for both the 'through-the-thickness' and 'fully pottede' inserts.

4.4.2 Comparison with Finite Element Analysis

As illustrated in Figure 4.12 there is a small amount of potting material between the insert and the face sheets, owing to the differences between the diameter of the insert d_i and the diameter of the hole in the face sheets d_0. In the formulation of the the high-order theory approach it was assumed, that the face sheets are rigidly connected to the insert (see Section 4.2.5). To investigate the validity of this assumption two finite element models were prepared, one with inclusion of the potting material between the insert and the face sheets and one without. Figure 4.25 illustrates the model of the 'through-the-thickness' insert problem including the potting material between the insert and the face sheets, and the finite element model of the same problem. Again an transverse load of Q = -10 N is assumed.

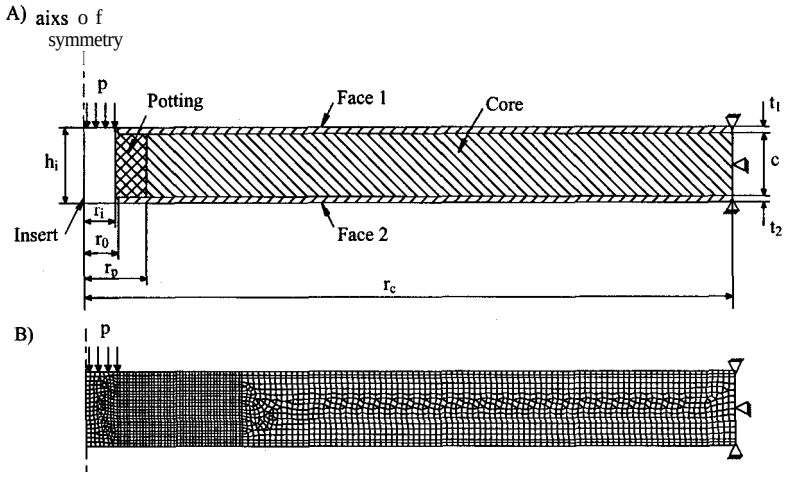

Figure 4.25: Model *of* sandwich plate *with* 'through-the-thickness' *insert* and *finite* element model.

The results obtained using the high-order theory approach, and the finite element analyses with and without the potting material between the insert and the face sheets are shown in Figure *4.26.*

In Figure 4.26 w^1 is the transverse displacements determined by the high-order theory approach, $w_{FEM}^{1-rigid}$ is the transverse displacements determined by finite element analysis assuming a rigid connection between the insert and the face sheets, and w_{FEM}^{1-pot} is the transverse displacements determined by finite element analysis including the potting material between the insert and the face sheets. Figure 4.26 displays a very close match between the results of the high-order theory and the finite element analysis, and it is seen that the influence on the transverse displacements of including the potting material between the insert and the face sheets is very small.

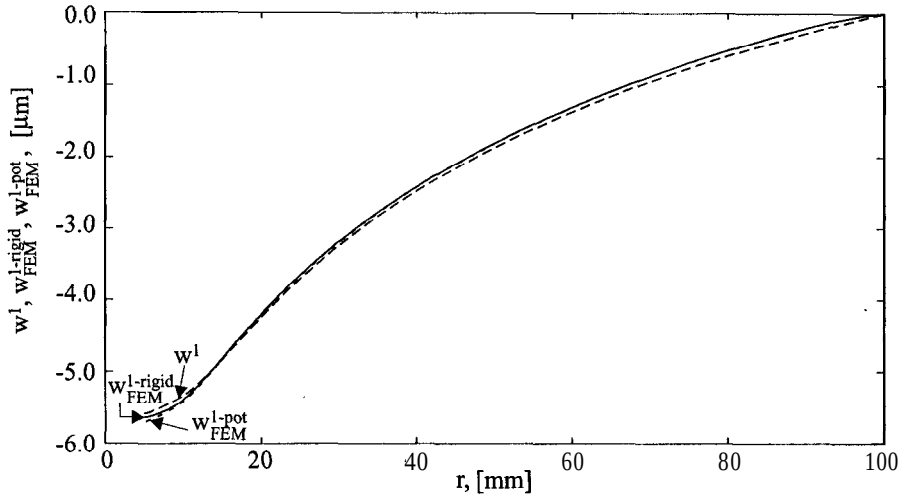

Figure 4.26: Radial distribution *of* the transverse displacements *of* the top *face* sheet (Face 1) *of* the sandwich plate test specimen with a 'through-the-thickness' insert, determined *by the high-order sandwich plate theory and compared finite element results with* and without inclusion *of* potting material between the *face* sheets and the insert.

However, the predicted peak values of the bending moment and transverse shear stress resultants in the face sheets will be much smaller in the case where a flexible potting material is present between the face sheets and the insert, than if a rigid insert/face sheet interface is assumed as described in Section 4.2.5. However, the high-order sandwich plate theory allows for the specification of arbitray boundary conditions, and it involves no principal difficulties to include finite stiffness boundary conditions at the insert/face sheet interfaces.

In the comparison between the results of the high-order sandwich plate theory and the finite element analyses, it could be of relevance to compare the stress distributions predicted by the different methods. However, the finite element models contain several singular points where the stresses are undetermined. In these singular points, and in their near vicinity, the predicted stresses will tend to increase when the finite element meshes are refined, and no convegence will be experienced. The high-order sandwich plate theory predicts stress peaks of finite magnitude. Moreover, as the stress component of interest, in the context of evaluating the quality of the high-order sandwich plate theory, are induced in the material interfaces where the finite element stress singularities appear, it is not very meaningful to conduct a comparison of the peak stresses obtained from the two methods.

In the regions of the sandwich plates away from the insert and the material interfaces, the results of the high-order theory coincide with the results obtainable using classical antiplane sandwich theories, which have been validated elsewhere (Plantema (1966), Allen (1969) and Zenkert (1995)). Thus, no further comparison between the high-order sandwich plate theory results and finite element results will be presented.

4.4.3 Summary

The objective of this section has been to compare the results obtained for the analyses of sandwich plates with inserts using the high-order sandwich plate theory approach with results obtained from an experimental investigation using electronic speckle pattern interferometry and obtained from finite element analysis.

The comparison between the high-order theory approach and the experimental investigation shows that the results compare very well.

Investigation of the boundary conditions between the inserts and the face sheets using finite element analysis, shows that changes in the modelling of the boundary conditions do not affect the transverse displacements significantly. Such changes can be anticipated to influence the face sheet stresses significantly, but the high-order theory does in fact allow for the specification of any type of boundary conditions.

However, the investigation of the approach shown in this section, should not be seen as a full validation, since only the transverse displacement field for one out of four possible load cases has been investigated. A more comprehensive evaluation of the high-order theory, as applied for studying sandwich plates with inserts, requires further investigations.,

4.5 Implementation in ESAcomp

The implementation of the Insert Module into ESAComp has not yet been settled, but it is planned for a later version of ESAComp. However, the actural way that the module will be implemented in ESAComp has been decided, and with references to Section 1.1 in Chaper 1 the implement&ion of the Insert Module into ESAComp is shortly described in this section.

The **Insert Module** will be implemented as an object, see Figure 1.2 and Figure 1.3 in Chaper 1 Section 1.1.1-1.1.2.

Before the analysis module for inserts in sandwich plates is called in ESAComp, a sandwich laminate must be created. After this is done the potting material used for fixing the insert in the sandwich laminate must be specified as a homogenous ply in the same way as the core material is specified or chosen from the ESAComp material database. When this is done, *Joints* is selected in the ESAComp Main Window as shown in Figure 4.27.

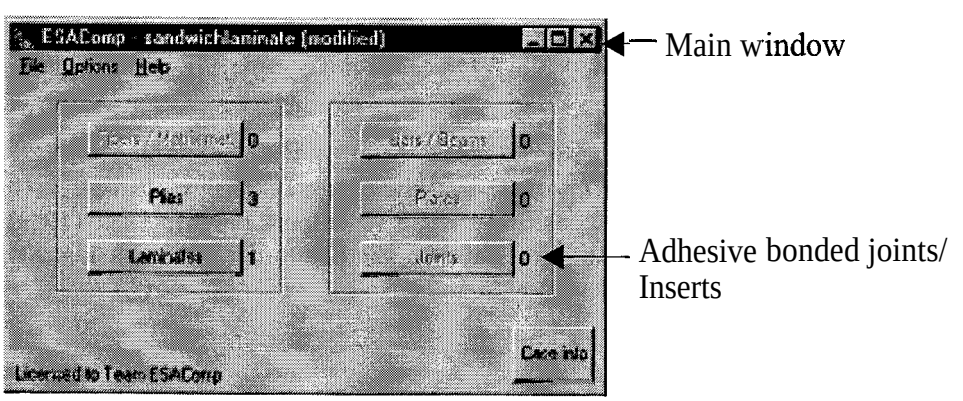

Figure 4.27: Implementation *of the* Insert Module *in* ESAComp.

After Joints is selected from the main window a new window called *Joints - Case Joints* appears. From this window *Inserts* is selected and a new window called *Inserts* appears. In the insert window the load and boundary conditions must be specified before the analysis can be performed by selecting *Insert Loads*. After this is done the analysis of sandwich plates with inserts is selected under *Analyze* in the Insert window, and an *Insert - analysis specification* window will appear. In the Insert - *analysis* specification window the sandwich laminate, the insert and potting type, the dimensions and the loads to be investigated can be selected, and the analysis can be performed.

4.6 Conclusions

It has been decided to include a tool for analysis of sandwich plates with inserts in ESAComp. This analysis tool will be based on a high-order sandwich plate theory, which has been developed and adopted especially for the study of sandwich plates with inserts of the 'through-the-thickness' and 'fully potted' types for implementation in ESAComp.

A brief description of the theory has been presented, and it includes separate descriptions of the structural responses of each of the face sheets, separate description of the core response including specification of different properties in the 'potting' and the 'honeycomb' regions, and general specification of external loading and boundary conditions.

Examples have shown the importance in using the high-order theory approach to capture the localized effects around loaded inserts in sandwich plates.

The high-order theory approach has been evaluated by comparison with experimental measurements on test specimens using electronic speckle pattern interferometry, and by comparison with finite element results. The predictions have compared well with the experimental data as well as with the finite element analysis results.

Chapter

5

Conclusions

A number of tools for engineering analysis and design of high-performance FRP-composite structural elements have been treated in this thesis. The outcome is a variety of analysis tools implemented in the computerized analysis and design software program ESAComp. The results are summarized and conclusions are drawn in the following.

5.1 Adhesive Bonded Joints

A general method for the analysis of adhesive bonded joints between composite laminates has been developed. The analysis accounts for coupling effects induced by adherends made as asymmetric and unbalanced laminates. The analysis allows specification of any combination of boundary conditions and external loading. The analysis can be carried out with the adherends modelled as wide beams or plates in cylindrical bending. The adhesive layers are as a first approach assumed to behave as a linear elastic material.

Solution procedures have been developed for the analysis of the following joint types:

- Single lap joint with straight and scarfed adherends in the overlap zone;
- Bonded doubler joint;
- Double lap joint;
- Single sided stepped and scarfed lap joint;
- Double sided stepped and scarfed lap joint;

The results obtained have been compared with finite element results and results from a high-order theory approach, and the comparison shows that the results are in very good agreement.

Example results have been presented with the objective of demonstrating the applicability of the developed algorithms. Furthermore, a parametric study has been carried out, and the results of this study have exposed the influence of coupling effects, as experienced with laminated composite adherends. Based on this, a set of general design guidelines has been given in order to improve the structural performance of bonded joints with laminated adherends.

In order to perform a non-linear solution for the adhesive bonded joint problems, the linear solution procedures have been used together with a modified von Mises criterion and a secant modulus approach for the effective stress/strain relationship for the adhesive material. The modified von Mises criterion takes into account the fact that yielding of polymers often depends on both deviatoric as well as hydrostatic stress components. The non-linear solution procedure is based on an interactive use of the linear solution procedure for the problems together with an effective stress/strain relationship for the adhesive material, derived empirically from test on bulk specimens. Comparison of the results obtained using the linear and non-linear solution procedure has shown that the non-linear adhesive behaviour influences the adhesive layer stresses even at low load levels. Thus, in most cases non-linear effects are unavoidable and a certain degree of plasticity in the adhesive layer close to the ends of the overlap cannot be prevented.

The developed analysis procedures are planned for implementation in ESAComp version 2.0.

5.2 Ply Drops in Composite and Sandwich Laminates

A simplified method for the analysis of 'exterior' and 'embedded' ply drops in composite and sandwich laminates has been developed. The analysis accounts for coupling effects induced by adherends made as asymmetric and unbalanced laminates. For ply drops in laminates acting as face sheets in sandwich panels the analysis accounts for the interaction with the core material through a two-parametric elastic foundation model, which includes the shearing interaction between the face laminates and the core material. The analysis allows for specification of any combination of boundary conditions and external loading.

Numerical results have shown that severe local stress concentrations are induced at the interface/ 'resin-rich' layers close to the ply drop zone. From parametric studies it has further been shown that the interface/'resin-rich' layer stresses are strongly dependent on the transition length over which the laminate thickness changes for 'embedded' layer drop-off configuration. The results obtained by use of the developed analysis procedures have been compared with finite element analyses, and it has been shown that the results compare well.

The developed analysis procedures have been implemented in ESAComp version 1.0 (ESAComp System Manual (1998)), and can be used for the analysis and design of 'exterior' and 'embedded' ply drops in composite and sandwich laminates.

5.3 Sandwich Plates with Inserts

It has been decided to include a tool for analysis of sandwich plates with inserts in ESAComp. This analysis tool will be based on a high-order sandwich plate theory, which has been developed and adopted especially for the study of sandwich plates with inserts of the 'through-the-thickness' and 'fully potted' types for implementation in ESAComp.

A brief description of the theory has been presented, and it includes separate descriptions of the structural responses of each of the face sheets, separate description of the core response including specification of different properties in the 'potting' and the 'honeycomb' regions, and general specification of external loading and boundary conditions.

Examples have shown the importance of using the high-order theory approach to capture the localized effects around loaded inserts in sandwich plates.

The high-order theory approach has been evaluated by comparison with experimental measurements on test specimens using electronic speckle pattern interferometry, and by comparison with finite element results. The predictions have compared well with the experimental data as well as with the finite element analysis results.

The implementation of the Insert Module into ESAComp has not been settled, but is planned for a later version of ESAComp.

5.4 Further Work

The developed analysis modules are or will be implemented in the ESAComp design software system. The analysis modules presented in this thesis do not necessarily represent the final versions, since ESAComp is an open system, and since future updates of ESAComp are planned. Thus, the analysis modules presented in this work can be extended if so desired, and it is already foreseeable at this time that a number of additional analysis features would be highly relevant for implementation in ESAComp. In the following some of these additional analysis and design features are mentioned

5.4.1 Adhesive Bonded Joints

The module for analysis of adhesive bonded joints, described in Chapter 2 of this thesis, already contains procedures which allow for failure load estimation. These procedures are based on approximate non-linear analysis, and account for adhesive plasticity. For the non-linear solution procedure a tangent modulus approach should be implemented as an alternative approximation to the secant modulus approach used for the non-linear adhesive behaviour. Other failure modes than adhesive layer failure (i.e. cohesive failure) due to plastic yielding are possible, however, and other failure criteria may be implemented in ESAComp. Possibilities in this context could be point stress criteria for brittle adhesives, failure criteria based on the critical strain energy release rate, or other criteria. Evaluation of the different laminate (adherend) failure modes can already be carried out in ESAComp version 1.0.

5.4.2 Ply Drops in Composite and Sandwich Laminates

The module for analysis of ply drops in composite and sandwich laminates described in Chapter 3 of this thesis does not include, in its present form, any facilities for failure load estimation. The ply drop module should be extended, however, with appropriate failure criteria, such that ESAComp will be able to provide failure load predictions. In the context of ply drop problems the modes related to laminate failure can already be evaluated in ESAComp version 1.0, since various composite failure criteria have been implemented. Interface/'resin-rich' layer failure cannot be predicted at the present time. Possible failure criteria for implementation in ESAComp in this context could be point stress criteria (Thomsen et al. (1998), Botting et al. (1996), Vizzini (1995)), or criteria based on evaluation of the critical strain energy release rate.

5.4.3 Sandwich Plates with Inserts

The module for analysis of sandwich plates with inserts described in Chapter 4 of this thesis should be extended such that analysis of sandwich plates with 'partially potted' insert (see Figure

4.1) is enabled in ESAComp. This will require that a theoretical approach for this type of insert problems is developed. Such a theory would be more complicated than the high-order theory presented briefly in Section 4.2, since it would be necessary to extend the analysis to include a multi-layer core description. Furthermore, it would be of importance to include face sheets modelled as orthotropic laminates in the modelling. Failure criteria could also be implemented in the module, thus enabling failure load prediction. Finally, further experimental investigations should be performed to evaluate the high-order theory approach for the analysis of sandwich plates with inserts.

Bibliography

Adams, R. D. (1981). Stress analysis: a finite element analysis approach. *Developments* in *Adhesives, Applied* Science Publishers, *London, 2 ed.*

Adams, R. D., J. Coppendale, and N. A. Peppiatt (1978). Failure analysis of aluminium-aluminium bonded joints. *Adhesion,* 2, pp. 105-119.

Adams, R. D. and N. A. Peppiatt (1974). Stress analysis of adhesive-bonded lap joints. Journal *of* Strain *Analysis, 9,* pp. 185-196.

Adams, R. D. and W. C. Wake (1984). Structural adhesive joints in engineering. *Elsevier Applied* Science *Publishers,* 1. ed.,(ISBN O-85334-263-6).

Allen, H. G. (Oxford, 1969). Analysis and design of structural sandwich panels. *Pergamon Press,.*

Botting, A. D., A. J. Vizzini, and S. W. Lee (1996). Effect of ply-drop configuration on delamination strength of tapered composite structures. *AIAA* Journal, *43*(8), pp. 1650-1656.

Crocombe, A. D. and R. D. Adams (1981). An effective stress/strain concept in mechanical characterization of structural adhesive bonding. Journal *of Adhesion, 13*(2), pp. 141-155.

Curry, J. M., E. R. Johnson, and J. H. Starnes (1987). Effect of dropped plies on the strength of graphite/epoxy laminates. *Proc. of AIAA/ASME/ASCE/AHS 28th* Structures, *Structural* Dynamics *and Materials Conference, Monterey,* (Paper No. AIAA 87-0874), pp. 737-747.

ESAComp System Manual, . (1998). ESAComp user's guide. Version 1.0, pp. 1.1–1.3,3.1–3.7.

ESDU, Data Item 91003,. (1991). Delamination of tappered composites. *ESDU* International *plc. London.*

European Space Agency, . (1987). Insert design handbook. *ESA PSS-03-1202 Issue 1.*

Fracon, M. (1979). Laser speckle and application in optics. *ACADEMIC PRESS,* (ISBN 0-12-265760-s).

Frostig, Y. (1992). Behaviour of delaminated sandwich beam with transversely flexible core - high order theory. *Composite* Structures, 20, pp. l-16.

Frostig, Y. (1993). On stress concentration in the bending of sandwich beams with transversely flexible core. *Composite* Structures, 24, pp. 161-169.

Frostig, Y. and M. Baruch (1993). High-order buckling analysis of sandwich beams with transversely flexible core. Journal *of ASCR, EM, 119*(5), pp. 476-495.

Frostig, Y., M. Baruch, 0. Vilnay, and I. Sheinman (1991). Bending of nonsymmetric sandwich beams with transversely flexible core. *ASCE* Journal *of* Engineering *Mechanics, 117*(9), pp. 1931-1952.

Frostig, Y. and Y. Shenhar (1995). High-order bending of sandwich beams with transversely flexible core and unsymmetrical laminated composite skins. Composite Engineering, *5*, pp. 405-414.

Frostig, Y., 0. T. Thomsen, and F. Mortensen (1997). Analysis of adhesive bonded joints, square-end and spew-fillet: Closed-form higher-order theory approach. Report No. *81,* Institute *of Mechanical Engineering, Aalborg* University, Denmark, *submitted.*

Gali, S., G. Dolev, and 0. Ishai (1981). An effective stress/strain concept in mechanical characterization of structural adhesive bonding. International *Journal of Adhesion* and *Adhesives, 1,* pp. 135-140.

Gali, S. and 0. Ishai (1978). Interlaminar stress distribution within an adhesive layer in the nonlinear range. Journal *of Adhesion, 9,* pp. 253-266.

Goland, M. and E. Reissner (1944). The stresses in cemented joints. Journal *of Applied Me*chanics, 1, pp. A17–A27.

Harris, J. A. and R. D. Adams (1984). Strength prediction of bonded single lap joints by non-linear finite element methods. International *Journal of Adhesion and Adhesives, 4,* pp. 65-78.

Hart-Smith, L. J. (1973.a). Adhesive bonded double lap joints. *Technical report NASA CR* 112237, Douglas Aircraft Company, McDonnell *Douglas* Corporation, *USA.*

Hart-Smith, L. J. (1973.b). Adhesive bonded scarf and stepped-lap joints. *Technical report NASA CR 112235,* Douglas *Aircraft* Company, McDonnell *Douglas Corporation, USA.*

Hart-Smith, L. J. (1973.c). Adhesive bonded single lap joints. *Technical* **report** *NASA CR 112236,* Douglas *Aircraft Company, McDonnell* Douglas Corporation, *USA.*

Hètenyi, M. (1946). Beams on elastic foundations. *The* University *of Michigan Press,* Ann Arbor, Michigan, *USA.*

Jones, R. M. (1975). Mechanics of composite materials. *Scripta Book* Company, Whashington.

Kalnins, A. (1964a). Analysis of shell of revolution subjected to symmetrical and non-symmetrical loads. Journal *of Applied Mechanics, 31* (Trans. ASME), pp. 467-476.

Kalnins, A. (1964b). Free vibration of rotationally symmetric shells. *The* Journal *of the Acous*tical *Society of America, 36*(7), pp. 1355-1365.

Kalnins, A. (1965). 0n free and forced vibration of rotationally symmetric layered shells. *Journal of Applied Mechanics, 32,* pp. 941-943.

Kerr, A. D. (1964). Elastic and viscoelastic foundation models. *Journal of Applied Mechanics, 32,* pp. 491-498.

Librescu, L. (1975). Elastostatics and kinetic of anistropic and heterogeneous shell-type structures. *Noordhoff, Leyden,.*

Lilleheden, L. (1994). Properties of adhesive in situ and in bulk. International Journal *of Adhesion and Adhesive, 14*(1), pp. 31-37.

Llanos, A. S. and A. J. Vizzini (1992). The effect of film adhesive on the delamination strength of tapered composites. *Composite Materials, 26*(13), pp. 1968-1983.

Maas, A. M. (1991). Phase shifting speckle interferometry. *Ph.D. Thesis,* Technical University *of Delft, The Netherlands.*

Mortensen, F. and 0. T. Thomsen (1997a). Facilities in ESAComp for analysis and design of adhesive joints between composite laminates. *Proc.* Composite and *Sandwich Structures, (NESCOII), ISBN 0 94781794 8, Ch*ameleon *Press Ltd., London, UK,* pp. 247-266.

Mortensen, F. and 0. T. Thomsen (1997b). Simplified linear and non-linear analysis of stepped and scarfed lap adhesive joints between composite laminates. *Composite Structures, 38*(1-4), pp. 281-294.

Pickett, A. K. (1983.). Stress analysis of adhesive bonded lap joints. Ph.D. *thesis, University of* Surrey.

Pickett, A. K. and L. Hollaway (1985). The analysis of elasto-plastic adhesive stress in adhesive bonded lap joints in FRP-structures. Composite Structures, *4*, pp. 135-160.

Plantema, F. (1966). Sandwich construction. *John Wiley & Sons, New York,*, pp. 135–160.

Press, W. H., S. A. Teukolsky, W. T. Vetterling, and B. P. Flannery (1992). Numerical recipes in *C. The Art* of *Scientific* Computing, *2.ed.*

Rasmussen, J. and E. Lund (1997). The issue of generality in design optimization systems. Engineering *Optimization,* 29, pp. 23-37.

Rasmussen, J., E. Lund, and N. Olhoff (1993). Integration of parametric modeling and structural analysis for optimum design. in *Proc. of Advances* in *Design Automation, The* American Society of Mechanical Engineers, *(Eds. Gilmore et* al), *Albequerque, New Mexico, USA.*

Renton, W. J. and J. R. Vinson (1975a). The efficient design of adhesive bonded joints. *Journal of Adhesion,* 7, pp.175–193.

Renton, W. J. and J. R. Vinson (1975b). On the behavior of bonded joints in composite material structures. *Engineering Fracture Mechanics,* 7, pp.41–60.

Rhim, J. and A. J. Vizzini (1997). Analysis of interlaminar stressses in an internally-dropped ply region. *Proc.* of Eleventh *International Conference on* Composite Materials, 5, pp. 652-662.

Stamm, K. and H. Witte (1974). Sandwichkonstruktionen (in german). *Springer- Verlag, Wien,* Austria,.

Thomas, D. M. and J. P. H. Webber (1994). A design-study into the delamination behaviour of tappered composites. *Composite Structures, 27,* pp. 379-388.

Thomsen, 0. T. (1989). Analysis of adhesive bonded generally orthotropic circular cylindrical shells. *Ph.D.-thesis,* Institute *of* Mechanical *Engineering, Aalborg University, Den*mark, Special *Report No. 4.*

Thomsen, 0. T. (1992). Elasto-static and elasto-plastic stress analysis of adhesive bonded tubular lap joints. Composite Structures, 21, pp. 2499259.

Thomsen, 0. T. (1993). Analysis of local bending effects in sandwich plates with orthotropic face layers subjected to localised loads. Composite Structures, 25, pp. 511–520.

Thomsen, 0. T. (1994a). Analysis of sandwich plates with fully potted inserts using a high-order sandwich plate theory. *ESA/ESTEC Report EWP-1827, European Space Agency, The Netherlands,.*

Thomsen, 0. T. (1994b). Analysis of sandwich plates with through-the-thickness inserts using a high-order sandwich plate theory. *ESA/ESTEC Report EWP-1807,* European Space Agency, *The* Netherlands,.

Thomsen, 0. T. (1995). Theoretical and experimental investigation of local bending effects in sandwich plates. Composite Structures, 30, pp. 85-101.

Thomsen, 0. T. (1998). Sandwich plates with 'through-the-thickness' and 'fully potted' inserts: Evaluation of differences in structural performance. Composite *Structures, 40*(2), pp. 159-174.

Thomsen, 0. T. and Y. Frostig (1997). Localized bending of sandwich beams: photoelastic investigation versus high-order sandwich theory results. *Composite* Structures, *37*(1), pp. 97-108.

Thomsen, 0. T., Y. Frostig, and F. Mortensen (1998). Ply drop-off effects in CFRP/sandwich panels: Theoretical prediction and experimental investigation of delamination failure. *Report No. 100, Institute of Mechanical* Engineering, *Aalborg University, Denmark, submitted,*.

Thomsen, 0. T. and W. Rits (1998). Analysis and design of sandwich plates with inserts - a high-order sandwich plate theory. Composites, *Part B(6).*

Thomsen, 0. T., W. Rits, D. C. G. Eaton, and S. Brown (1996a). Ply drop-off effects in CFRP/Honeycomp sandwich panels - theory. Composites *Science and Technology, 56,* pp. 407-422.

Thomsen, 0. T., W. Rits, D. C. G. Eaton, and S. Brown (1996b). Ply drop-off effects in CFRP/Honeycomp sandwich panels - experimental results. Composites Science *and Technology, 56,* pp. 423-437.

Tong, L. (1996). Bond strength for adhesive-bonded single-lap joints. *Acta* Mechanic, *Springer-Verlag, 117,* pp. 101-113.

Vizzini, A. J. (1995). Influence of realistic ply-drop geometries on interlaminar stresses in tapered laminates. *Composite Material: Fatique* and Fracture, *5*(ASTM STP 1230, R.H. Martin, Ed., American Society for Testing and Materials, Philadelphia), pp. 467-485.

Vlasov, V. Z. and N. N. Leont'ev (Moscow, 1960). Beams, plates and shells on elastic foundations. *Composite Material: Fatique and* Fracture, *5,*(English translation by Israel Programme for Scientific Translation, Jerusalem, 1966).

Volkersen, 0. (1938). Die nietkraftverteilung in zugbeanspruchten nietverbindungen mit konstanten laschenquerschnitten. *Luftfahrtforschung, 15,* pp. 41-47.

Whitney, J. M. (1987). Structural analysis of laminated anisotropic plates. Technomic *Publishing Company. Inc.,* Lancaster.

Wisnom, M. R. and M. I. Jones (1995). Delamination due to interaction between overall interlaminar shear and stresses at terminating plies. *Composite* Structures, 31, pp. 39-47.

Yuceoglu, U. and D. P. Updike (1975.a). The effect of bending on the stresses in adhesive joints. *Lehigh University, Bethlehem,* Pensylvania, *NASA NGR-39-007-011,*.

Yuceoglu, U. and D. P. Updike (1975.b). Stress analysis of adhesive bonded stiffener plates and double joints. *Lehigh* University, *Bethlehem, Pensylvania, NASA NGR-39-007-011.*

Yuceoglu, U. and D. P. Updike (1981). Bending and shear deformation effects in lap joints. *Journal of* Engineering *Mechanics, 107,* pp. 55-76.

Zenkert, D. (1995). An introduction to sandwich construction. *EMAS* Publishing, *West Midlands,*.

Zhaohua, F. and R. D. Cook (1983). Beam elements on two-parameter elastic foundations. *ASCE Journal of Engineering Mechanics, 109,* pp. 1390–1402.

APPENDIX

Appendix

A

Governing Equations for the Adhesive Bonded Joints

The set of governing equations for all the considered adhesive bonded joint types are presented in this appendix. The governing equations presented are those where the adherends are modelled as plates in cylindrical bending. The case where the adherends are modelled as wide beams can be considered as a special case of cylindrical bending, and results in a reduced set of the governing equations. However, to demonstrate that this is true the governing equations for the case of adherends modelled as beams are also shown for the single lap joint.

A.1 Single Lap joint

From the equations derived it is possible to form the complete set of system equations for the problem. Thus combination of Equations 2.9, 2.11 and 2.16 yields for laminate 1 and 2 in the areas $-L_1 \leq x \leq 0$ and $L \leq x \leq L + L_2$ (outside of overlap):

$$\left.\begin{aligned} u^i_{0,x} &= k_{1i}N^i_{xx} + k_{2i}N^i_{xy} + k_{3i}M^i_{xx} \\ w^i_{,x} &= -\beta^i_x \\ \beta^i_{x,x} &= -k_{4i}N^i_{xx} - k_{5i}N^i_{xy} - k_{6i}M^i_{xx} \\ v^i_{0,x} &= k_{7i}N^i_{xx} + k_{8i}N^i_{xy} + k_{9i}M^i_{xx} \\ N^i_{xx,x} &= 0 \\ N^i_{xy,x} &= 0 \\ M^i_{xx,x} &= Q^i_x \\ Q^i_{x,x} &= 0 \end{aligned}\right\} \quad \text{i} = 1, 2. \qquad \text{(A.1)}$$

Equation A.1 constitute a set of eight linear coupled first-order ordinary differential equations. The coefficients $k_{1i} - k_{9i}$ (i = $1, 2$) contain laminate stiffness parameters and are a result of isolating $u^i_{0,x}$, $v^i_{0,x}$ and $w^i_{,xx}$ from N^i_{xx}, N^i_{xy} and M^i_{xx} in Equations 2.9:

$$\begin{aligned} k_{1i} &= \frac{1}{m_{1i}} \\ k_{2i} &= -\frac{m_{3i}}{m_{1i}} \end{aligned}$$

$$
\begin{aligned}
k_{3i} &= \frac{m_{2i}}{m_{1i}} \\
k_{4i} &= h_{1i}k_{1i} \\
k_{5i} &= h_{1i}k_{2i} + h_{3i} \\
k_{6i} &= h_{1i}k_{3i} + h_{2i} \\
k_{7i} &= -\frac{c_{1i}}{c_{2i}}k_{1i} \\
k_{8i} &= \frac{1}{c_{2i}} - \frac{c_{1i}}{c_{2i}}k_{2i} \\
k_{9i} &= -\frac{c_{1i}}{c_{2i}}k_{3i} - \frac{c_{3i}}{c_{2i}}
\end{aligned}
\tag{A.2}
$$

where the coefficients c_{ji}, h_{ji} and m_{ji} $(j = 1,2,3)$ are:

$$
\begin{aligned}
c_{1i} &= A^i_{16} - \frac{B^i_{16}B^i_{11}}{D^i_{11}} \\
c_{2i} &= A^i_{66} - \frac{B^i_{16}B^i_{16}}{D^i_{11}} \\
c_{3i} &= \frac{B^i_{16}}{D^i_{11}} \\
h_{1i} &= \frac{B^i_{11}}{D^i_{11}} - \frac{B^i_{16}c_{1i}}{D^i_{11}c_{2i}} \\
h_{2i} &= -\frac{B^i_{16}c_{3i}}{D^i_{11}c_{2i}} - \frac{1}{D^i_{11}} \\
h_{3i} &= \frac{B^i_{16}}{D^i_{11}c_{2i}} \\
m_{1i} &= A^i_{11} - B^i_{11}h_{1i} - \frac{A^i_{16}c_{1i}}{c_{2i}} \\
m_{2i} &= -\frac{A^i_{16}c_{3i}}{c_{2i}} - B^i_{11}h_{2i} \\
m_{3i} &= \frac{A^i_{16}}{c_{2i}} - B^i_{11}h_{3i}
\end{aligned}
\tag{A.3}
$$

Within the overlap zone, i.e. for $0 \leq x \leq L$, combination of Equation 2.9, 2.11, 2.14 and 2.18 yields for laminate 1 and 2:

$$
\begin{aligned}
u^1_{0,x} &= k_{11}N^1_{xx} + k_{21}N^1_{xy} + k_{31}M^1_{xx} \\
w^1_{,x} &= -\beta^1_x \\
\beta^1_{x,x} &= -k_{41}N^1_{xx} - k_{51}N^1_{xy} - k_{61}M^1_{xx} \\
v^1_{0,x} &= k_{71}N^1_{xx} + k_{81}N^1_{xy} + k_{91}M^1_{xx} \\
N^1_{xx,x} &= \frac{G_a}{t_a}u^1_0 + \frac{G_a t_1}{2t_a}\beta^1_x - \frac{G_a}{t_a}u^2_0 + \frac{G_a t_2}{2t_a}\beta^2_x \\
N^1_{xy,x} &= \frac{G_a}{t_a}v^1_0 - \frac{G_a}{t_a}v^2_0
\end{aligned}
$$

$$
\begin{aligned}
M^1_{xx,x} &= Q^1_x + \frac{G_a(t_1+t_a)}{2t_a}u^1_0 + \frac{G_a t_1(t_1+t_a)}{4t_a}\beta^1_x - \frac{G_a(t_1+t_a)}{2t_a}u^2_0 + \frac{G_a t_2(t_1+t_a)}{4t_a}\beta^2_x \\
Q^1_{x,x} &= \frac{E_a}{t_a}w^1 - \frac{E_a}{t_a}w^2
\end{aligned}
\tag{A-4}
$$

$$
\begin{aligned}
u^2_{0,x} &= k_{12}N^2_{xx} + k_{22}N^2_{xy} + k_{32}M^2_{xx} \\
w^2_{,x} &= -\beta^2_x \\
\beta^2_{x,x} &= -k_{42}N^2_{xx} - k_{52}N^2_{xy} - k_{62}M^2_{xx} \\
v^2_{0,x} &= k_{72}N^2_{xx} + k_{82}N^2_{xy} + k_{92}M^2_{xx} \\
N^2_{xx,x} &= -\frac{G_a}{t_a}u^1_0 - \frac{G_a t_1}{2t_a}\beta^1_x + \frac{G_a}{t_a}u^2_0 - \frac{G_a t_2}{2t_a}\beta^2_x \\
N^2_{xy,x} &= -\frac{G_a}{t_a}v^1_0 + \frac{G_a}{t_a}v^2_0 \\
M^2_{xx,x} &= Q^2_x + \frac{G_a(t_2+t_a)}{2t_a}u^1_0 + \frac{G_a t_1(t_2+t_a)}{4t_a}\beta^1_x - \frac{G_a(t_2+t_a)}{2t_a}u^2_0 + \frac{G_a t_2(t_2+t_a)}{4t_a}\beta^2_x \\
Q^2_{x,x} &= -\frac{E_a}{t_a}w^1 + \frac{E_a}{t_a}w^2
\end{aligned}
$$

Equations A.4 constitute a set of 16 linear coupled first-order ordinary differential equations.

A.1.1 Single Lap joint - Beam Case

For laminate 1 and 2 in the areas $-L_1 \leq x \leq 0$ and $L \leq x \leq L + L_2$ (outside of overlap) combination Equations 2.11, 2.13, 2.14 together with the equilibrium equations yields:

$$
\left.
\begin{aligned}
u^i_{0,x} &= k_{1i}N^i_{xx} + k_{2i}M^i_{xx} \\
w^i_{,x} &= -\beta^i_x \\
\beta^i_{x,x} &= -k_{3i}N^i_{xx} - k_{4i}M^i_{xx} \\
N^i_{xx,x} &= 0 \\
M^i_{xx,x} &= Q^i_x \\
Q^i_{x,x} &= 0
\end{aligned}
\right\} \quad i = 1,2. \tag{A.5}
$$

Equation A.5 constitute a set of six linear coupled first-order ordinary differential equations. The coefficients $k_{1i} - k_{4i}$ $(i = 1,2)$ contain the laminate stiffness parameters and are determined by isolating of $u^i_{0,x}$ and $w^i_{,xx}$ from N^i_{xx} and M^i_{xx} in Equation 2.13:

$$
\begin{aligned}
k_{1i} &= \frac{1}{A^i_{11} - \frac{(B^i_{11})^2}{D^i_{11}}} \\
k_{2i} &= -\frac{B^i_{11}}{D^i_{11}\left(A^i_{11} - \frac{(B^i_{11})^2}{D^i_{11}}\right)} \\
k_{3i} &= k_{2i} \\
k_{4i} &= \frac{1}{D^i_{11}} + \frac{(B^i_{11})^2}{(D^i_{11})^2\left(A^i_{11} - \frac{(B^i_{11})^2}{D^i_{11}}\right)}
\end{aligned}
\tag{A.6}
$$

By comparison with the coefficients for the cylindrical bending case it is seen that the coefficients for the beam case are strongly reduced and only contain few of the laminate stiffness parameters.

Within the overlap zone, i.e. for $0 \leq x \leq L$, the governing for laminate 1 and 2 are:

$$
\begin{aligned}
u^1_{0,x} &= k_{11}N^1_{xx} + k_{21}M^1_{xx} \\
w^1_{,x} &= -\beta^1_x \\
\beta^1_{x,x} &= -k_{31}N^1_{xx} - k_{41}M^1_{xx} \\
N^1_{xx,x} &= \frac{G_a}{t_a}u^1_0 + \frac{G_a t_1}{2t_a}\beta^1_x - \frac{G_a}{t_a}u^2_0 + \frac{G_a t_2}{2t_a}\beta^2_x \\
M^1_{xx,x} &= Q^1_x + \frac{G_a(t_1+t_a)}{2t_a}u^1_0 + \frac{G_a t_1(t_1+t_a)}{4t_a}\beta^1_x - \frac{G_a(t_1+t_a)}{2t_a}u^2_0 + \frac{G_a t_2(t_1+t_a)}{4t_a}\beta^2_x \\
Q^1_{x,x} &= \frac{E_a}{t_a}w^1 - \frac{E_a}{t_a}w^2
\end{aligned}
\tag{A.7}
$$

$$
\begin{aligned}
u^2_{0,x} &= k_{12}N^2_{xx} + k_{22}M^2_{xx} \\
w^2_{,x} &= -\beta^2_x \\
\beta^2_{x,x} &= -k_{32}N^2_{xx} - k_{42}M^2_{xx} \\
N^2_{xx,x} &= -\frac{G_a}{t_a}u^1_0 - \frac{G_a t_1}{2t_a}\beta^1_x + \frac{G_a}{t_a}u^2_0 - \frac{G_a t_2}{2t_a}\beta^2_x \\
M^2_{xx,x} &= Q^2_x + \frac{G_a(t_2+t_a)}{2t_a}u^1_0 + \frac{G_a t_1(t_2+t_a)}{4t_a}\beta^1_x - \frac{G_a(t_2+t_a)}{2t_a}u^2_0 + \frac{G_a t_2(t_2+t_a)}{4t_a}\beta^2_x \\
Q^2_{x,x} &= -\frac{E_a}{t_a}w^1 + \frac{E_a}{t_a}w^2
\end{aligned}
$$

Equations A.7 constitute a set of 12 linear coupled first-order ordinary differential equations. By comparison with the equations for the cylindrical bending case it is seen that the equations display the same overall appearance except that all variables associated with the width direction are nil in Equations A.7.

A.2 Single Lap Joint with Scarfed Adherends

The governing equations outside the overlap zone are the same as for the single lap joint with straight adherends. Within the overlap zone, i.e. for $0 \leq x \leq L$, the governing equations for laminate 1 and 2 are derived by combination of Equation 2.9, 2.11, 2.14 and 2.20:

$$
\begin{aligned}
u^1_{0,x} &= k_{11}N^1_{xx} + k_{21}N^1_{xy} + k_{31}M^1_{xx} \\
w^1_{,x} &= -\beta^1_x \\
\beta^1_{x,x} &= -k_{41}N^1_{xx} - k_{51}N^1_{xy} - k_{61}M^1_{xx} \\
v^1_{0,x} &= k_{71}N^1_{xx} + k_{81}N^1_{xy} + k_{91}M^1_{xx} \\
N^1_{xx,x} &= \frac{G_a}{t_a}u^1_0 + \frac{G_a t_1(x)}{2t_a}\beta^1_x - \frac{G_a}{t_a}u^2_0 + \frac{G_a t_2(x)}{2t_a}\beta^2_x \\
N^1_{xy,x} &= \frac{G_a}{t_a}v^1_0 - \frac{G_a}{t_a}v^2_0 \\
M^1_{xx,x} &= Q^1_x + \frac{G_a(t_1(x)+t_a)}{2t_a}u^1_0 + \frac{G_a t_1(x)(t_1(x)+t_a)}{4t_a}\beta^1_x - \frac{G_a(t_1(x)+t_a)}{2t_a}u^2_0 \\
&\quad + \frac{G_a t_2(x)(t_1(x)+t_a)}{4t_a}\beta^2_x - \frac{t_1 - t_{1end}}{2L}N^1_{xx} \\
Q^1_{x,x} &= \frac{E_a}{t_a}w^1 - \frac{E_a}{t_a}w^2
\end{aligned}
$$

(A.8)

$$
\begin{aligned}
u^2_{0,x} &= k_{12}N^2_{xx}\,\mathrm{t}\;k_{22}N^2_{xy}\,\mathrm{t}\;k_{32}M^2_{xx}\\
w^2_{,x} &= -\beta^2_x\\
\beta^2_{x,x} &= -k_{42}N^2_{xx} - k_{52}N^2_{xy} - k_{62}M^2_{xx}\\
v^2_{0,x} &= k_{72}N^2_{xx}\,\mathrm{t}\;k_{82}N^2_{xy}\,\mathrm{t}\;k_{92}M^2_{xx}\\
N^2_{xx,x} &= -\frac{G_a}{t_a}u^1_0 - \frac{G_a t_1(x)}{2t_a}\beta^1_x + \frac{G_a}{t_a}u^2_0 - \frac{G_a t_2(x)}{2t_a}\beta^2_x\\
N^2_{xy,x} &= -\frac{G_a}{t_a}v^1_0 + \frac{G_a}{t_a}v^2_0\\
M^2_{xx,x} &= Q^2_x + \frac{G_a(t_2(x)\,\mathrm{t}\,t_a)}{2t_a}u^1_0 + \frac{G_a t_1(x)(t_2(x)+t_a)}{4t_a}\beta^1_x - \frac{G_a(t_2(x)+t_a)}{2t_a}u^2_0\\
&\quad + \frac{G_a t_2(x)(t_2(x)+t_a)}{4t_a}\beta^2_x - \frac{t_2 - t_{2end}}{2L}N^2_{xx}\\
Q^2_{x,x} &= -\frac{E_a}{t_a}w^1 + \frac{E_a}{t_a}w^2
\end{aligned}
$$

Equation A.8 constitute a set of 16 linear coupled first-order ordinary differential equations.

A.3 Bonded Doubler Joint

The governing equations for the bonded doubler joint are exactly the same as for the single lap joint in the overlap zone and outside the overlap zone in the region $L \leq x \leq L + L_2$.

A.4 Double Lap Joint

The governing equations for the double lap joint are exactly the same as for the single lap joint in the region $-L_1 \leq x \leq 0$.

The governing equations for laminate 1, 2 and 3 within the overlap zone, i.e. for $0 \leq x \leq L$, are derived by combination of Equation 2.9, 2.11, 2.14 and 2.25:

$$
\begin{aligned}
u^1_{0,x} &= k_{11}N^1_{xx} + k_{21}N^1_{xy} + k_{31}M^1_{xx}\\
w^1_{,x} &= -\beta^1_x\\
\beta^1_{x,x} &= -k_{41}N^1_{xx} - k_{51}N^1_{xy} - k_{61}M^1_{xx}\\
v^1_{0,x} &= k_{71}N^1_{xx} + k_{81}N^1_{xy}\,\mathrm{t}\;k_{91}M^1_{xx}\\
N^1_{xx,x} &= \left(\frac{G_{a1}}{t_{a1}} + \frac{G_{a2}}{t_{a2}}\right)u^1_0 + \left(\frac{t_1 G_{a1}}{2t_{a1}} + \frac{t_1 G_{a2}}{2t_{a2}}\right)\beta^1_x - \frac{G_{a1}}{t_{a1}}u^2_0 + \frac{G_{a1}t_2}{2t_{a1}}\beta^2_x - \frac{G_{a2}}{t_{a2}}u^3_0 + \frac{G_{a2}t_3}{2t_{a2}}\beta^3_x\\
N^1_{xy,x} &= \left(\frac{G_{a1}}{t_{a1}} + \frac{G_{a2}}{t_{a2}}\right)v^1_0 - \frac{G_{a1}}{t_{a1}}v^2_0 - \frac{G_{a2}}{t_{a2}}v^3_0\\
M^1_{xx,x} &= Q^1_x + \left(\frac{G_{a1}(t_1+t_{a1})}{2t_{a1}} - \frac{\text{".''I;\$}\ t_{a2})}{}\right)u^1_0 + \left(\frac{G_{a1}(t_1+t_{a1})t_1}{4t_{a1}} + \frac{G_{a2}(t_1+t_{a2})t_1}{4t_{a2}}\right)\beta^1_x\\
&\quad - \frac{G_{a1}(t_1+t_{a1})}{2t_{a1}}u^2_0 + \frac{G_{a1}(t_1+t_{a1})t_2}{4t_{a1}}\beta^2_x - \frac{G_{a2}(t_1+t_{a2})}{2t_{a2}}u^3_0 + \frac{G_{a2}(t_1+t_{a2})t_3}{4t_{a2}}\beta^3_x\\
Q^1_{x,x} &= \left(\frac{E_{a1}}{t_{a1}} + \frac{E_{a2}}{t_{a2}}\right)w^1 - \frac{E_{a1}}{t_{a1}}w^2 - \frac{E_{a2}}{t_{a2}}w^3
\end{aligned}
$$

(A.9)

$$
\begin{aligned}
u^2_{0,x} &= k_{12}N^2_{xx} \text{ t } k_{22}N^2_{xy} \text{ t } k_{32}M^2_{xx} \\
w^2_{,x} &= -\beta^2_x \\
\beta^2_{x,x} &= k_{42}N^2_{xx} + k_{52}N^2_{xy}\mathbf{t}\ k_{62}M^2_{xx} \\
v^2_{0,x} &= k_{72}N^2_{xx}\mathbf{t}\ k_{82}N^2_{xy}\mathbf{t}\ k_{92}M^2_{xx} \\
N^2_{xx,x} &= -\frac{G_{a1}}{t_{a1}}u^1_0 - \frac{G_{a1}t_1}{2t_{a1}}\beta^1_x + \frac{G_{a1}}{t_{a1}}u^2_0 - \frac{G_{a1}t_2}{2t_{a1}}\beta^2_x \\
N^2_{xy,x} &= -\frac{G_{a1}}{t_{a1}}v^1_0 + \frac{G_{a1}}{t_{a1}}v^2_0 \\
M^2_{xx,x} &= Q^2_x \quad \frac{G_{a1}(t_2 \text{ t } t_{a1})}{2t_{a1}}u^1_0 + \frac{G_{a1}t_1(t_2 \text{ t } t_{a1})}{4t_{a1}}\beta^1_x \quad \frac{G_{a1}(t_2 \text{ t } t_{a1})}{2t_{a1}}u^2_0 + \frac{G_{a1}t_2(t_2 \text{ t } t_{a1})}{4t_{a1}}\beta^2_x \\
Q^2_{x,x} &= -\frac{E_{a1}}{t_{a1}}w^1 + \frac{E_{a1}}{t_{a1}}w^2
\end{aligned}
$$

$$
\begin{aligned}
u^3_{0,x} &= k_{13}N^3_{xx} \text{ t } k_{23}N^3_{xy} + k_{33}M^3_{xx} \\
w^3_{,x} &= -\beta^3_x \\
\beta^3_{x,x} &= k_{43}N^3_{xx} \text{ t } k_{53}N^3_{xy} \text{ t } k_{63}M^3_{xx} \\
v^3_{0,x} &= k_{73}N^3_{xx} \text{ t } k_{83}N^3_{xy} + k_{93}M^3_{xx} \\
N^3_{xx,x} &= -\frac{G_{a2}}{t_{a2}}u^1_0 + \frac{G_{a2}t_1}{2t_{a2}}\beta^1_x + \frac{G_{a2}}{t_{a2}}u^3_0 + \frac{G_{a2}t_3}{2t_{a2}}\beta^3_x \\
N^3_{xy,x} &= -\frac{G_{a2}}{t_{a2}}v^1_0 + \frac{G_{a2}}{t_{a2}}v^3_0 \\
M^3_{xx,x} &= Q^3_x + \frac{G_{a2}(t_3 \text{ t } t_{a2})}{2t_{a2}}u^1_0 + \frac{G_{a2}t_1(t_3 + t_{a2})}{4t_{a2}}\beta^1_x + \frac{G_{a2}(t_3 \text{ t } t_{a2})}{2t_{a2}}u^3_0 + \frac{G_{a2}t_3(t_3 \text{ t } t_{a2})}{4t_{a2}}\beta^3_x \\
Q^3_{x,x} &= -\frac{E_{a2}}{t_{a2}}w^1 + \frac{E_{a2}}{t_{a2}}w^2
\end{aligned}
$$

Equation A.10 constitute a set of 24 linear coupled first-order ordinary differential equations within the overlap zone.

The governing equation for laminate 2 and 3 in the region $L \leq x \leq L$ t L_2 (outside of overlap) are derived by combination of Equation 2.9, 2.11 and 2.16:

$$
\begin{aligned}
u^2_{0,x} &= k_{12}N^2_{xx} \text{ t } k_{22}N^2_{xy} \text{ t } k_{32}M^2_{xx} \\
w^2_{,x} &= -\beta^2_x \\
\beta^2_{x,x} &= -k_{42}N^2_{xx} - k_{52}N^2_{xy} - k_{62}M^2_{xx} \\
v^2_{0,x} &= k_{72}N^2_{xx} \text{ t } k_{82}N^2_{xy} \text{ t } k_{92}M^2_{xx} \\
N^2_{xx,x} &= 0 \\
N^2_{xy,x} &= 0 \\
M^2_{xx,x} &= Q^2_x \\
Q^2_{x,x} &= 0
\end{aligned}
\qquad \text{(A.lO)}
$$

$$
\begin{aligned}
u^3_{0,x} &= k_{13}N^3_{xx} \text{ t } k_{23}N^3_{xy} \text{ t } k_{33}M^3_{xx} \\
w^3_{,x} &= -\beta^3_x \\
\beta^3_{x,x} &= -k_{43}N^3_{xx} - k_{53}N^3_{xy} - k_{63}M^3_{xx} \\
v^3_{0,x} &= k_{73}N^3_{xx} \text{ t } k_{83}N^3_{xy} \text{ t } k_{93}M^3_{xx} \\
N^3_{xx,x} &= 0
\end{aligned}
$$

$$
\begin{aligned}
N^3_{xy,x} &= 0 \\
M^3_{xx,x} &= Q^3_x \\
Q^3_{x,x} &= 0
\end{aligned}
$$

Equation A.10 constitute a set of 16 linear coupled first-order ordinary differential equations.

A.5 Single Sided Stepped Lap Joint

The governing equations for the single-sided stepped lap joint are the same as for the single lap joint outside the overlap zone, i.e. Equations A.l. Inside the overlap zone the governing equations are also the same as for the single lap joint within each step zone, but the stiffness coefficients change from step to step, owing to the changes in thicknesses and laminate parameters. Within each gap in the overlap zone (i.e. in the transition zone between adjacent steps) it is assumed, that there is no interaction between the adherends through the adhesive layer. Consequently, the governing equations are the same as those of the individual adherends outside the overlap zone, i.e. as given by Equations A.1 where i = $1, 2$.

A.6 Single Sided Scarfed Lap Joint

The governing equations outside the overlap zone are the same as for the single lap joint, i.e. Equations A.l. Within the overlap zone, i.e. for $0 \leq x \leq L$, the governing equations for laminate 1 and 2 are derived by combination of Equation 2.9, 2.11, 2.14 and 2.22:

$$
\begin{aligned}
u^1_{0,x} &= k_{11}N^1_{xx} + k_{21}N^1_{xy} + k_{31}M^1_{xx} \\
w^1_{,x} &= -\beta^1_x \\
\beta^1_{x,x} &= -k_{41}N^1_{xx} - k_{51}N^1_{xy} - k_{61}M^1_{xx} \\
v^1_{0,x} &= k_{71}N^1_{xx} + k_{81}N^1_{xy} + k_{91}M^1_{xx} \\
N^1_{xx,x} &= \frac{G_a}{t_a}u^1_0 + \frac{G_a t_1(x)}{2t_a}\beta^1_x - \frac{G_a}{t_a}u^2_0 + \frac{G_a t_2(x)}{2t_a}\beta^2_x \\
N^1_{xy,x} &= \frac{G_a}{t_a}v^1_0 - \frac{G_a}{t_a}v^2_0 \\
M^1_{xx,x} &= Q^1_x + \frac{G_a(t_1(x)\ \mathrm{t}\ t_a)}{2t_a}u^1_0 + \frac{G_a t_1(x)(t_1(x)\ \mathrm{t}\ t_a)}{4t_a}\beta^1_x - \frac{G_a(t_1(x)+t_a)}{2t_a}u^2_0 \\
&\quad + \frac{G_a t_2(x)(t_1(x)\ \mathrm{t}\ t_a)}{4t_a}\beta^2_x + \frac{t_1 - t_{1end}}{2L}N^1_{xx} \\
Q^1_{x,x} &= \frac{E_a}{t_a}w^1 - \frac{E_a}{t_a}w^2
\end{aligned}
\qquad \text{(A.1.1)}
$$

$$
\begin{aligned}
u^2_{0,x} &= k_{12}N^2_{xx} + k_{22}N^2_{xy} + k_{32}M^2_{xx} \\
w^2_{,x} &= -\beta^2_x \\
\beta^2_{x,x} &= -k_{42}N^2_{xx} - k_{52}N^2_{xy} - k_{62}M^2_{xx} \\
v^2_{0,x} &= k_{72}N^2_{xx} + k_{82}N^2_{xy} + k_{92}M^2_{xx} \\
N^2_{xx,x} &= -\frac{G_a}{t_a}u^1_0 - \frac{G_a t_1(x)}{2t_a}\beta^1_x + \frac{G_a}{t_a}u^2_0 - \frac{G_a t_2(x)}{2t_a}\beta^2_x
\end{aligned}
$$

$$
\begin{aligned}
N^2_{xy,x} &= -\frac{G_a}{t_a}v^1_0 + \frac{G_a}{t_a}v^2_0 \\
M^2_{xx,x} &= Q^2_x + \frac{G_a(t_2(x)+t_a)}{2t_a}u^1_0 + \frac{G_a t_1(x)(t_2(x)+t_a)}{4t_a}\beta^1_x - \frac{G_a(t_2(x)+t_a)}{2t_a}u^2_0 \\
&\quad + \frac{G_a t_2(x)(t_2(x)+t_a)}{4t_a}\beta^2_x + \frac{t_2 - t_{2end}}{2L}N^2_{xx} \\
Q^2_{x,x} &= -\frac{E_a}{t_a}w^1 + \frac{E_a}{t_a}w^2
\end{aligned}
$$

Equation A.11 constitute a set of 16 linear coupled first-order ordinary differential equations.

A.7 Double Sided Stepped Lap Joint

The governing equations for the double sided stepped lap joint are the same as for the single lap joint outside the overlap zone, i.e. Equations A.l. Inside the overlap zone the governing equations are the same as for the double lap joint within each step, but the coefficients change from step to step due to the changes of thicknesses and laminate parameters. Within each gap in the overlap zone it is assumed that there is no interaction between the adherends through the adhesive layers. Consequently, and the governing equations are the same as those of the individual adherends outside the overlap region, i.e. Equations A.1 with $i = 2a, 2b$.

A.8 Double Sided Scarfed Lap Joint

The governing equations for the double sided scarfed lap joint are the same as for the single lap joint outside the overlap zone.

The governing equations for the laminates within the overlap zone, i.e. for $0 \leq x \leq L$, are derived by combination of Equation 2.9, 2.11, 2.14 and 2.27:

$$
\begin{aligned}
u^1_{0,x} &= k_{11}N^1_{xx} + k_{21}N^1_{xy} + k_{31}M^1_{xx} \\
w^1_{,x} &= -\beta^1_x \\
\beta^1_{x,x} &= -k_{41}N^1_{xx} - k_{51}N^1_{xy} - k_{61}M^1_{xx} \\
v^1_{0,x} &= k_{71}N^1_{xx} + k_{81}N^1_{xy} + k_{91}M^1_{xx} \\
N^1_{xx,x} &= \left(\frac{G_{a1}}{t_{a1}} + \frac{G_{a2}}{t_{a2}}\right)u^1_0 + \left(\frac{t_{1a}(x)G_{a1}}{t_{a1}} + \frac{t_{1a}(x)G_{a2}}{t_{a2}}\right)\beta^1_x \\
&\quad - \frac{G_{a1}}{t_{a1}}u^{2a}_0 + \frac{G_{a1}t_{2a}(x)}{2t_{a1}}\beta^{2a}_x - \frac{G_{a2}}{t_{a2}}u^{2b}_0 + \frac{G_{a2}t_{2b}}{2t_{a2}}\beta^{2b}_x \\
N^1_{xy,x} &= \left(\frac{G_{a1}}{t_{a1}} + \frac{G_{a2}}{t_{a2}}\right)v^1_0 - \frac{G_{a1}}{t_{a1}}v^{2a}_0 - \frac{G_{a2}}{t_{a2}}v^{2b}_0 \\
M^1_{xx,x} &= Q^1_x + \left(\frac{G_{a1}(t_{1a}(x)+t_{a1}/2)}{t_{a1}} - \frac{G_{a2}(t_{1b}(x)+t_{a2}/2)}{t_{a2}}\right)u^1_0 \\
&\quad + \left(\frac{G_{a1}(t_{1a}(x)+t_{a1}/2)t_{1a}(x)}{t_{a1}(x)} + \frac{G_{a2}(t_{1b}(x)+t_{a2})t_{1b}(x)}{t_{a2}}\right)\beta^1_x \\
&\quad - \frac{G_{a1}(t_{1a}(x)+t_{a1}/2)}{t_{a1}(x)}u^{2a}_0 + \frac{G_{a1}(t_{1a}(x)+t_{a1}/2)t_{2a}(x)}{2t_{a1}}\beta^{2a}_x \\
&\quad - \frac{G_{a2}(t_{1b}(x)+t_{a2}/2)}{t_{a2}}u^{2b}_0 + \frac{G_{a2}(t_{1b}(x)+t_{a2}/2)t_{2b}(x)}{2t_{a2}}\beta^{2b}_x
\end{aligned}
$$

$$
\begin{aligned}
Q^1_{x,x} &= \left(\frac{E_{a1}}{t_{a1}} + \frac{E_{a2}}{t_{a2}}\right) w^1 - \frac{E_{a1}}{t_{a1}} w^{2a} - \frac{E_{a2}}{t_{a2}} w^{2b} \\
u^{2a}_{0,x} &= k_{12} N^{2a}_{xx} + k_{22} N^{2a}_{xy} + k_{32} M^{2a}_{xx} \\
w^{2a}_{,x} &= -\beta^{2a}_x \\
\beta^{2a}_{x,x} &= k_{42} N^{2a}_{xx} + k_{52} N^{2a}_{xy} + k_{62} M^{2a}_{xx} \\
v^{2a}_{0,x} &= k_{72} N^{2a}_{xx} + k_{82} N^{2a}_{xy} + k_{92} M^{2a} 2_{xx} \\
N^{2a}_{xx,x} &= -\frac{G_{a1}}{t_{a1}} u^1_0 - \frac{G_{a1} t_{1a}(x)}{t_{a1}} \beta^1_x + \frac{G_{a1}}{t_{a1}} u^{2a}_0 - \frac{G_{a1} t_{2a}(x)}{t_{a1}} \beta^{2a}_x \\
N^{2a}_{xy,x} &= -\frac{G_{a1}}{t_{a1}} v^1_0 + \frac{G_{a1}}{t_{a1}} v^{2a}_0 \\
M^{2a}_{xx,x} &= Q^{2a}_x + \frac{G_{a1}(t_{2a}(x) + t_{a1})}{2t_{a1}} u^1_0 + \frac{G_{a1} t_{1a}(x)(t_{2a}(x) + t_{a1})}{2t_{a1}} \beta^1_x - \frac{G_{a1}(t_{2a}(x) + t_{a1})}{2t_{a1}} u^{2a}_0 + \\
&\quad \frac{G_{a1} t_{2a}(x)(t_{2a}(x) + t_{a1})}{4t_{a1}} \beta^{2a}_x + \frac{t^{end,R}_{2a} - t^{end,L}_{2a}}{2L} N^{2a}_{xx} \\
Q^2_{x,x} &= -\frac{E_{a1}}{t_{a1}} w^1 + \frac{E_{a1}}{t_{a1}} w^{2a}
\end{aligned}
\tag{A.12}
$$

$$
\begin{aligned}
u^{2b}_{0,x} &= k_{13} N^{2b}_{xx} + k_{23} N^{2b}_{xy} + k_{33} M^{2b}_{xx} \\
w^{2b}_{,x} &= -\beta^{2b}_x \\
\beta^{2b}_{x,x} &= k_{43} N^{2b}_{xx} + k_{53} N^{2b}_{xy} + k_{63} M^{2b}_{xx} \\
v^{26}_{0,x} &= k_{73} N^{2b}_{xx} + k_{83} N^{2b}_{xy} + k_{93} M^{2b}_{xx} \\
N^{2b}_{xx,x} &= -\frac{G_{a2}}{t_{a2}} u^1_0 + \frac{G_{a2} t_{1b}}{t_{a2}} \beta^1_x + \frac{G_{a2}}{t_{a2}} u^{2b}_0 + \frac{G_{a2} t_{2b}}{2t_{a2}} \beta^{2b}_x \\
N^{2b}_{xy,x} &= -\frac{G_{a2}}{t_{a2}} v^1_0 + \frac{G_{a2}}{t_{a2}} v^{2b}_0 \\
M^{2b}_{xx,x} &= Q^{2b}_x + \frac{G_{a2}(t_{2b}(x) + t_{a2})}{2t_{a2}} u^1_0 + \frac{G_{a2} t_{1b}(x)(t_{2b}(x) + t_{a2})}{2t_{a2}} \beta^1_x + \frac{G_{a2}(t_{2b}(x) + t_{a2})}{2t_{a2}} u^{2b}_0 + \\
&\quad \frac{G_{a2} t_{2b}(x)(t_{2b}(x) + t_{a2})}{4t_{a2}} \beta^{2b}_x - \frac{t^{end,R}_{2b} - t^{end,L}_{2b}}{2L} N^{2b}_{xx} \\
Q^{26}_{x,x} &= -\frac{E_{a2}}{t_{a2}} w^1 + \frac{E_{a2}}{t_{a2}} w^{26}
\end{aligned}
$$

Equation A.12 constitute a set of 24 linear coupled first-order ordinary differential equations within the overlap zone.

A.9 Number of Equations and Variables for the Bonded Joint Problems

The number of equations and unknown variables, within each of the regions (Region 1: $-L_1 \leq x \leq 0$, Region 2: $0 \leq x \leq L$, Region 3: $L \leq x \leq L + L_2$) as well as in total, for all the joints are:

- Single lap joint with and without scarfed adherends, Single sided scarfed lap joint:
  - Region 1: 2 M_1 *(m/2,1)* matrix equations with $(2M_1 + 1)$ unknown (m/2,1) matrices.
  - Region 2: 4 M_2 *(m/2,1)* matrix equations with $4M_2$ unknown (m/2,1) matrices.

- Region 3: 2 Ms (m/2,1) matrix equations with $(2M_3 - 1)$ unknown (m/2,1) matrices.
- Total: $(2M_1 + 4M_2$ t $2M_3)$ (m/2,1) matrix equations with $(2M_1 + 4M_2 + 2M_3)$ unknown (m/2,1) matrices.

- Bonded doubler joint:
  - Region 2: 4 M_2 (m/2,1) matrix equations with $4M_2 + 1$ unknown (m/2,1) matrices.
  - Region 3: 2 M_3 (m/2,1) matrix equations with $(2M_3 - 1)$ unknown (m/2,1) matrices.
  - Total: $(4M_2 + 2M_3)$ (m/2,1) matrix equations with $(4M_2 + 2M_3)$ unknown (m/2,1) matrices.

- Double lap joint:
  - Region 1: 2 M_1 *(m/2,1)* matrix equations with $(2M_1 + 1)$ unknown (m/2,1) matrices.
  - Region 2: 6 M_2 matrix equations with $(6M_2 + 1)$ unknown (m/2,1) matrices.
  - Region 3: 4 M_3 (m/2,1) matrix equations with $(4M_3 - 2)$ unknown (m/2,1) matrices.
  - Total: $(2M_1 + 6M_2 + 4M_3)$ (m/2,1) matrix equations with $(2M_1 + 6M_2$ •t $2M_3)$ unknown (m/2,1) matrices.

- Single sided stepped lap joint:
  - Region 1: 2 M_1 (m/2,1) matrix equations with $(2M_1$ t 1) unknown (m/2,1) matrices.
  - Region 2: 4 M_2 (m/2,1) matrix equations with $4M_2$ unknown (m/2,1) matrices. To fulfil the continuity conditions between each step the number of equations and unknown is increased with 4 *(m/2,1)* matrix equations and unkown matrices.
  - Region 3: 2 Ms (m/2,1) matrix equations with $(2M_3 - 1)$ unknown (m/2,1) matrices.
  - Total: $(2M_1 + 4M_2 + 2M_3)$ (m/2,1) matrixequations with $(2M_1 + 4(M_2 + n_{step}) + 2M_3)$ unknown (m/2,1) matrices.

- Double sided stepped lap joint:
  - Region 1: 2 M_1 *(m/2,1)* matrix equations with $(2M_1 + 1)$ unknown (m/2,1) matrices.
  - Region 2: 6 M_2 (m/2,1) matrix equations with $6M_2$ unknown (m/2,1) matrices. To fulfil the continuity conditions between each step the number of equations and unknown is increased with 6 (m/2,1) matrix equations and unkown matrices.
  - Region 3: 2 M_3 (m/2,1) matrix equations with $(2M_3 - 1)$ unknown (m/2,1) matrices.
  - Total: $(2M_1 + 4M_2 + 2M_3)$ (m/2,1) matrix equations with $(2M_1 + 6(M_2 + (n_{step} - 1))$ t $2M_3)$ unknown (m/2,1) matrices.

- Double sided scarfed lap joint:
  - Region 1: 2 M_1 (m/2,1) matrix equations with $(2M_1 + 1)$ unknown (m/2,1) matrices.
  - Region 2: 6 M_2 (m/2,1) matrix equations with $4M_2$ unknown (m/2,1) matrices.
  - Region 3: 2 M_3 *(m/2,1)* matrix equations with $(2M_3 - 1)$ unknown *(m/2,1)* matrices.
  - Total: $(2M_1 + 4M_2 + 2M_3)$ (m/2,1) matrix equations with $(2M_1 + 6M_2$ ♦ $2M_3)$ unknown (m/2,1) matrices.

Appendix

B

Governing Equations for the Ply Drop Problems

The set of governing equations for the two types of ply drops are presented in this appendix. The derivation of the governing equations presented is based on the assumptions that the sub-laminates behave as wide beams, and that they act as the face sheets of a sandwich panel. In case the ply drop occurs in a monolithic laminate, the differential equations are the same except that the mechanical properties of the core material are set equal to zero, i.e. $E_c = G_c = 0$, which implies that the foundation moduli K_x and K_z are nil.

B.l Exterior Ply Drop

The governing equations in the region $-L \leq x < 0$ (see Figure 3.8) are derived by combination of Equations 2.11, 2.13, 2.14, 3.2 and 3.7:

$$
\begin{aligned}
u^1_{0,x} &= k_{11}N^3_{xx} + k_{21}M^3_{xx} \\
w^1_{,x} &= -\beta^1_x \\
\beta^3_{,x} &= k_{31}N^1_{xx} + k_{41}M^1_{xx} \\
N^1_{xx,x} &= \frac{G_a}{t_a}u^1_0 + \left(\frac{G_a t_1}{2t_a} - \frac{K_x t_1}{2}\right)\beta^1_x - \frac{G_a}{t_a}u^2_0 + \frac{G_a t_2}{2t_a}\beta^2_x \\
M^1_{xx,x} &= \frac{G_a(t_1+t_a)}{2t_a}u^1_0 + \left(\frac{G_a(t_2+t_a)t_1}{4t_a} + \frac{K_x t_1^2}{4}\right)\beta^1_x - \\
&\quad \frac{G_a(t_1+t_a)}{2t_a}u^2_0 + \frac{G_a(t_1+t_a)t_2}{4t_a}\beta^2_x + + Q^1_x \\
Q^1_{x,x} &= \left(\frac{E_a}{t_a} + K_z\right)w^1 - \frac{E_a}{t_a}w^2
\end{aligned}
\qquad \text{(B.1)}
$$

$$
\begin{aligned}
u^2_{0,x} &= k_{12}N^2_{xx} + k_{22}M^2_{xx} \\
w^2_{,x} &= -\beta^2_x \\
\beta^2_{x,x} &= k_{32}N^2_{xx} + k_{42}M^2_{xx} \\
N^2_{xx,x} &= -\frac{G_a}{t_a}u^1_0 - \frac{G_a t_1}{2t_a}\beta^1_x + \frac{G_a}{t_a}u^2_0 - \frac{G_a t_2}{2t_a}\beta^2_x
\end{aligned}
$$

$$
\begin{aligned}
M^2_{xx,x} &= \frac{G_a(t_2+t_a)}{2t_a}u^1_0 + \frac{G_a(t_2+t_a)t_1}{4t_a}\beta^1_x - \frac{G_a(t_2+t_a)}{2t_a}u^2_0 + \frac{G_a(t_2+t_a)t_2}{4t_a}\beta^2_x + Q^2_x \\
Q^2_{x,x} &= -\frac{E_a}{t_{a3}}w^1 + \frac{E_a}{t_a}w^2
\end{aligned}
$$

where the coefficients $k_{1i} - k_{4i}$ $(i = 1, 2)$ contain laminate stiffness parameters and are defined by Equations A.6 in Appendix A.

The governing equations in the region $0 \leq x < L_1$ (see Figure 3.9) are derived by combination of Equations 2.11, 2.13, 2.14, 3.2 and 3.7:

$$
\begin{aligned}
u^1_{0,x} &= k_{11}N^3_{xx} + k_{21}M^3_{xx} \\
w^1_{,x} &= -\beta^1_x \\
\beta^3_{,x} &= k_{31}N^1_{xx} + k_{41}M^1_{xx} \\
N^1_{xx,x} &= -\left(\frac{K_x t_1}{2}\right)\beta^1_x \\
M^1_{xx,x} &= \left(\frac{K_x t^2_1}{4}\right)\beta^1_x + +Q^1_x \\
Q^1_{x,x} &= (K_z)\,w^1
\end{aligned}
\tag{B.2}
$$

B.2 Embedded Ply Drop

The governing equations for the sub-laminates 1,2 and 3 in the region $-L \leq x < 0$ (see Figure 3.9) are derived by combination of Equations 2.11, 2.13, 2.14, 3.2 and 3.8:

$$
\begin{aligned}
u^1_{0,x} &= k_{11}N^1_{xx} \text{ t } k_{21}M^1_{xx} \\
w^1_{,x} &= -\beta^1_x \\
\beta^1_{,x} &= k_{31}N^1_{xx} + k_{41}M^1_{xx} \\
N^1_{xx,x} &= \left(\frac{G_{a1}}{t_{a1}} + \frac{G_{a2}}{t_{a2}}\right)u^1_0 + \left(\frac{G_{a1}}{t_{a1}} - \frac{G_{a1}}{t_{a2}}\right)\frac{t_1}{2}\beta^1_x - \frac{G_{a1}}{t_{a1}}u^2_0 + \frac{G_{a1}t_2}{2t_{a1}}\beta^2_x - \frac{G_{a2}}{t_{a2}}u^3_0 - \frac{G_{a2}t_3}{2t_{a2}}\beta^3_x \\
M^1_{xx,x} &= \left(\frac{G_{a1}(t_1+t_{a1})}{2t_{a1}} \quad \frac{G_{a2}(t_1+t_{a2})}{2t_{a2}}\right)u^1_0 + \left(\frac{G_{a1}(t_1+t_{a1})t_1}{4t_{a1}} + \frac{G_{a1}(t_1+t_{a2})t_1}{4t_{a2}}\right)\beta^1_x - \\
&\quad \frac{G_{a1}(t_1 \text{ t } t_{a1})}{4t_{a2}\ t_{a1}}{}^{,2}\ {}_{0} \frac{G_{a1}(t_1 \text{ t } t_{a1})t_2}{4t_{a1}}\ \beta^{\cdot}_{x} + \frac{(t_1 \text{ t } t_{a2})}{2t_{a2}}u^3_0 + \frac{G_{a2}(t_1 \text{ t } t_{a2})t_3}{}^{3} + Q^1_x \\
Q^1_{x,x} &= \left(\frac{E_{a1}}{t_{a1}} + \frac{E_{a2}}{t_{a2}}\right)w^1 \frac{E_{a1}}{t_{a1}}w^2 - \frac{E_{a2}}{t_{a2}}w^3
\end{aligned}
$$

$$
\begin{aligned}
u^2_{0,x} &= k_{12}N^2_{xx} + k_{22}M^2_{xx} \\
w^2_{,x} &= -\beta^2_x \\
\beta^2_{x,x} &= k_{32}N^2_{xx} + k_{42}M^2_{xx} \\
N^2_{xx,x} &= -\frac{G_{a1}}{t_{a1}}u^1_0 - \frac{G_{a1}t_1}{2t_{a1}}\beta^1_x + \frac{G_{a1}}{t_{a1}}u^2_0 - \frac{G_{a1}t_2}{2t_{a1}}\beta^2_x \\
M^2_{xx,x} &= -\frac{G_{a1}(t_2+t_{a1})}{2t_{a1}}u^1_0 + \frac{G_{a1}(t_2+t_{a1})t_1}{4t_{a1}}\beta^1_x - \frac{G_{a1}(t_2+t_{a1})}{2t_{a1}}u^2_0 + \frac{G_{a1}(t_2+t_{a1})t_2}{4t_{a1}}\beta^2_x + Q^2_x \\
Q^2_{x,x} &= -\frac{E_{a1}}{t_{a1}}w^1 + \frac{E_{a1}}{t_{a1}}w^2
\end{aligned}
\tag{B.3}
$$

$$
u^3_{0,x} = k_{13}N^3_{xx} + k_{23}M^3_{xx}
$$

$$
\begin{aligned}
w^3_{,x} &= -\beta^3_x \\
\beta^3_{,x} &= k_{33}N^3_{xx} \text{ t } k_{43}M^3_{xx} \\
N^3_{xx,x} &= -\frac{G_{a2}}{t_{a2}}u^1_0 + \frac{G_{a2}t_1}{2t_{a2}}\beta^1_x + \frac{G_{a2}}{t_{a2}}u^3_0 + \left(\frac{G_{a2}t_3}{2t_{a2}} - K_x\frac{t_3}{2}\right)\beta^3_x \\
M^3_{xx,x} &= -\frac{G_{a2}(t_1 \text{ t } t_{a2})}{2t_{a2}}u^1_0 + \frac{G_{a2}(t_3+t_{a2})t_1}{4t_{a2}}\beta^1_x + \frac{G_{a2}(t_3+t_{a2})}{2t_{a2}}u^3_0 + \\
&\quad \left(\frac{G_{a2}(t_3+t_{a2})t_3}{4t_{a2}} + K_x\frac{t_3^2}{4}\right)\beta^3_x + Q^3_x \\
Q^3_{x,x} &= -\frac{E_{a2}}{t_{a2}}w^1 + \left(K_z - \frac{E_{a2}}{t_{a2}}\right)w^2
\end{aligned}
$$

The **governing** equations in the region Cl $\leq x < L_2$ (i.e. in the transistion region, see Figure 3.9) are in the same way derived by combination of Equations 2.11, 2.13, 2.14, 3.2 and 3.9:

$$
\begin{aligned}
u^{2l}_{0,x} &= k_{12}N^{2l}_{xx} + k_{22}M^{2l}_{xx} \\
w^{2l}_{,x} &= -\beta^{2l}_x \\
\beta^{2l}_{x,x} &= k_{32}N^{2l}_{xx} + k_{42}M^{2l}_{xx} \\
N^{2l}_{xx,x} &= \left(\frac{G_{a3}}{t_{a3t}}cos^2(\alpha) - \frac{E_{a3}}{t_{a3t}}sin^2(\alpha)\right)u^{2l}_0 - \frac{G_{a3}t_2}{2t_{a3t}}cos^2(\alpha)\beta^{2l}_x - \frac{G_{a3}}{t_{a3t}}cos(\alpha)u^3_0 - \\
&\quad \frac{G_{a3}t_3}{2t_{a3t}}cos(\alpha)\beta^3_x - \left(\frac{G_{a3}}{t_{a3t}} + \frac{E_{a3}}{t_{a3t}}\right)cos(\alpha)sin(\alpha)w^{2l} + \frac{E_{a3}}{t_{a3t}}sin(\alpha)w^3 \\
M^{2l}_{xx,x} &= \left(\frac{E_{a3}(t_2+t_{a3t})}{2t_{a3t}}sin^2(\alpha) - \frac{G_{a3}(t_2+t_{a3t})}{2t_{a3t}}cos^2(\alpha)\right)u^{2l}_0 + \frac{G_{a3}(t_2+t_{a3t})t_2}{4t_{a3t}}cos^2(\alpha)\beta^{2l}_x \\
&\quad + \frac{G_{a3}(t_2 \text{ t } t_{a3t})}{2t_{a3t}}cos(\alpha)u^3_0 \text{ t } \frac{G_{a3}(t_2 \text{ t } t_{a3t})t_3}{4t_{a3t}}cos(\alpha)\beta^3_x \text{ t} \\
&\quad \left(\frac{G_{a3t}(t_2 \text{ t } t_{a3t})}{2t_{a3t}} + \frac{E_{a3}(t_2 \text{ t } t_{a3t})}{2t_{a3t}}\right)cos(\alpha)sin(\alpha)w^{2l} - \frac{E_{a3}(t_2 \text{ t } t_{a3t})}{2t_{a3t}}sin(\alpha)w^3 \\
Q^{2l}_{x,x} &= \left(\frac{G_{a3}}{t_{a3t}} + \frac{E_{a3}}{t_{a3t}}\right)cos(\alpha)sin(\alpha)u^{2l}_0 - \frac{G_{a3}t_2}{2t_{a3t}}sin(\alpha)cos(\alpha)\beta^{2l}_x - \frac{G_{a3}}{t_{a3t}}sin(\alpha)u^3_0 \\
&\quad - \frac{G_{a3}t_3}{2t_{a3t}}sin(\alpha)\beta^3_x + \left(-\frac{E_{a3}}{t_{a3t}}sin^2(\alpha) + \frac{E_{a3}}{t_{a3t}}cos^2(\alpha)\right)w^{2l} - \frac{E_{a3}}{t_{a3t}}cos(\alpha)w^3
\end{aligned}
\tag{B.4}
$$

$$
\begin{aligned}
u^3_{0,x} &= k_{13}N^3_{xx} + k_{23}M^3_{xx} \\
w^3_{,x} &= -\beta^3_x \\
\beta^3_{,x} &= k_{33}N^3_{xx} + k_{43}M^3_{xx} \\
N^3_{xx,x} &= -\frac{G_{a3}}{t_{a3t}}cos(\alpha)u^{2l}_0 + \frac{G_{a3}t_2}{2t_{a3t}}cos(\alpha)\beta^{2l}_x + \\
&\quad \frac{G_{a3}}{t_{a3t}}u^3_0 + \left(\frac{G_{a3}t_3}{2t_{a3t}} - \frac{K_x t_3}{2}\right)\beta^3_x + \frac{G_{a3}}{t_{a3t}}sin(\alpha)w^{2l} \\
M^3_{xx,x} &= -\frac{G_{a3}(t_3 \text{ t } t_{a3t})}{2t_{a3t}}cos(\alpha)u_{02l} \text{ t } \frac{G_{a3}(t_3 \text{ t } t_{a3t})t_2}{4t_{a3t}}cos(\alpha)\beta^{2l}_x \text{ t } \frac{G_{a3}(t_2 \text{ t } t_{a3t})}{2t_{a3t}}sin(\alpha)w^{2l} + \\
&\quad \frac{G_{a3}(t_2 \text{ t } t_{a3t})}{2t_{a3t}}u^3_0 + \left(\frac{G_{a3}(t_2+t_{a3t})t_3}{4t_{a3t}} + \frac{K_x t_3^2}{4}\right)\beta^3_x + Q^3_x \\
Q^3_{x,x} &= -\frac{E_{a3}}{t_{a3t}}cos(\alpha)w^{2l} - \frac{E_{a3}}{t_{a3t}}sin(\alpha)u^{2l}_0 + \left(K_z + \frac{E_{a3}}{t_{a3t}}\right)w^3
\end{aligned}
$$

The governing equations in the region $L_2 \leq$ x < $L_1 + L_2$ (see Figure 3.2) are derived by

combination of Equations 2.11, 2.13, 2.14, 3.2 and 3.7:

$$
\begin{aligned}
u^2_{0,x} &= k_{12}N^2_{xx} + k_{22}M^2_{xx} \\
w^2_{,x} &= -\beta^2_x \\
\beta^2_{x,x} &= k_{32}N^2_{xx} + k_{42}M^2_{xx} \\
N^2_{xx,x} &= \frac{G_{a3}}{t_{a3}}u^2_0 - \frac{G_{a3}t_2}{2t_{a3}}\beta^2_x - \frac{G_{a3}}{t_{a3}}u^3_0 - \frac{G_{a3}t_3}{2t_{a3}}\beta^3_x \qquad \text{(B.5)} \\
M^2_{xx,x} &= -\frac{G_{a3}(t_2+t_{a3})}{2t_{a3}}u^2_0 + \frac{G_{a3}(t_2+t_{a3})t_2}{4t_{a3}}\beta^2_x + \frac{G_{a3}(t_2+t_{a3})}{2t_{a3}}u^3_0 + \frac{G_{a3}(t_2+t_{a3})t_3}{4t_{a3}}\beta^3_x + Q^2_x \\
Q^2_{x,x} &= \frac{E_{a3}}{t_{a3}}w^2 - \frac{E_{a3}}{t_{a3}}w^3
\end{aligned}
$$

(B.6)

$$
\begin{aligned}
u^3_{0,x} &= k_{13}N^3_{xx} + k_{23}M^3_{xx} \\
w^3_{,x} &= -\beta^3_x \\
\beta^3_{,x} &= k_{33}N^3_{xx} + k_{43}M^3_{xx} \\
N^3_{xx,x} &= -\frac{G_{a3}}{t_{a3}}u^2_0 + \frac{G_{a3}t_2}{2t_{a3}}\beta^2_x + \frac{G_{a3}}{t_{a3}}u^3_0 + \left(\frac{G_{a3}t_3}{2t_{a3}} - \frac{K_x t_3}{2}\right)\beta^3_x \\
M^3_{xx,x} &= -\frac{G_{a3}(t_3+t_{a3})}{2t_{a3}}u^2_0 + \frac{G_{a3}(t_3+t_{a3})t_2}{4t_{a3}}\beta^2_x + \\
&\quad \frac{G_{a3}(t_3+t_{a3})}{2t_{a3}}u^3_0 + \left(\frac{G_{a3}(t_2+t_{a3})t_3}{4t_{a3}} + \frac{K_x t_3^2}{4}\right)\beta^3_x + Q^3_x \\
Q^3_{x,x} &= -\frac{E_{a3}}{t_{a3}}w^2 + \left(\frac{E_{a3}}{t_{a3}} + K_z\right)w^3
\end{aligned}
$$

The coefficients $k_{1i} - k_{4i}$ $(i = 1, 2, 3)$ contain laminate stiffness parameters and are defined by Equations A.6 in Appendix A.

Appendix

C

Matematical Formulation - Circular Sandwich Plates

The core equilibrium equations, the set of equations describing the the core stress and displacement field in terms of the transverse core coordinate z_c, as well as the entire set of governing equations for the sandwich plate/insert problems shown in this appendix are based on Thomsen (1994a), Thomsen (1994b), Thomsen and Rits (1998) and Thomsen (1998).

C.1 Modelling of the Core Material

Considering the conditions of equilibrium in the core material the following relation can be established based on the assumption that $\sigma_r = \sigma_\theta = \tau_{r\theta} = 0$:

$$\begin{aligned} &\tau_{rz,z} = 0 \\ &\tau_{\theta r,z} = 0 \\ &\sigma_{c,z} + \tau_{rz,r} + \tfrac{1}{r}\tau_{rz} + \tfrac{1}{r}\tau_{\theta z,\theta} = 0 \end{aligned} \tag{C.1}$$

In Equation C.1 σ_c is the core transverse normal stress, and τ_{rz}, $\tau_{\theta z}$ are the core shear stress components. From the first two of Equation C.1 it follows, that the core shear stress components are independent of the z_c-coordinate.

Combination of the core equilibrium equations, Equation C.1, and the core kinematic and constitutive relations yield a set of equations describing the core stress and displacement field in terms of the transverse core coordinate z_c and the face sheets displacements:

$$\begin{aligned}
\tau_{rz}(r,\theta,z_c) &= \tau_{rz}(r,\theta) \\
\tau_{\theta z}(r,\theta,z_c) &= \tau_{\theta z}(r,\theta) \\
\sigma_c(r,\theta,z_c) &= \frac{E_c}{c}\{w^1 - w^2\} - \left\{\tau_{rz,r} + \frac{1}{r}\tau_{rz} + \frac{1}{r}\tau_{\theta z,\theta}\right\} z_c \\
w_c(r,\theta,z_c) &= w^1 + \frac{\{w^1 - w^2\}}{c}\left\{z_c - \frac{c}{2}\right\} - \frac{1}{2E_c}\left\{\tau_{rz,r} + \frac{1}{r}\tau_{rz} + \frac{1}{r}\tau_{\theta z,\theta}\right\}\left\{z_c^2 - \frac{c^2}{4}\right\} \\
u_c(r,\theta,z_c) &= u_{0r}^1 - \frac{\beta_r^1}{2}\left\{t_1 - \frac{z_c^2}{c} - z_c + \frac{3c}{4}\right\} - \frac{\beta_r^2}{2}\left\{\frac{z_c^2}{c} - z_c + \frac{c}{4}\right\} + \frac{\tau_{rz}}{G_c}\left\{z_c - \frac{c}{2}\right\} +
\end{aligned}$$

$$
\begin{aligned}
& \frac{1}{2E_c}\left\{\tau_{rz,rr}+\frac{1}{r}\tau_{rz,r}-\frac{1}{r^2}\tau_{rz}+\frac{1}{r}\tau_{\theta z,\theta r}-\frac{1}{r^2}\tau_{\theta z,\theta}\right\}\left\{\frac{z_c^3}{c}-\frac{c^2 z_c}{4}+\frac{c^3}{12}\right\} \\
v_c(r,\theta,z_c) \;=\; & u_{0\theta}^1-\frac{\beta_\theta^1}{2}\left\{t_1-\frac{z_c^2}{c}-z_c+\frac{3c}{4}\right\}-\frac{\beta_\theta^2}{2}\left\{\frac{z_c^2}{c}-z_c+\frac{c}{4}\right\}+\frac{\tau_{\theta z}}{G_c}\left\{z_c-\frac{c}{2}\right\}+ \\
& \frac{1}{r2E_c}\left\{\tau_{rz,r\theta}+\frac{1}{r}\tau_{rz,\theta}+\frac{1}{r}\tau_{\theta z,\theta\theta}\right\}\left\{\frac{z_c^3}{c}-\frac{c^2 z_c}{4}+\frac{c^3}{12}\right\}
\end{aligned}
\tag{C.2}
$$

where E_c, G_c are the core elastic constants, u_r^c, u_θ^c, w^c are the core displacement components, and u_{0r}^i, $u_{0\theta}^i$, w^i $(i=1,2)$ are the displacement components of the top and bottom faces, see Figure C.l. From Equation C.2 it is seen that τ_{rz} and $\tau_{\theta z}$ are constant, that σ_c varies linearly, that w^c varies quadratically, and that u_r^c and u_θ^c varies cubically over the thickness of the core.

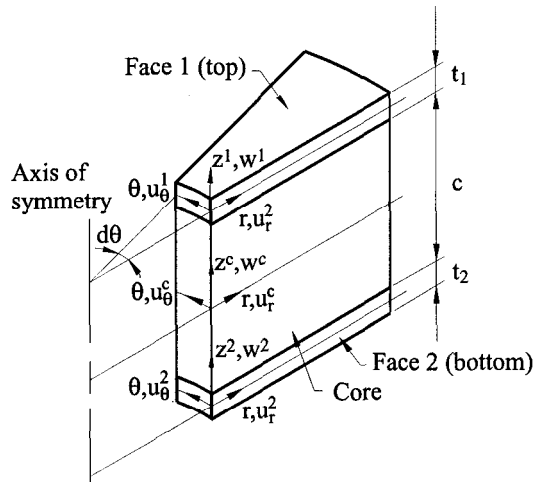

Figure C.l: Geometrical definition *of* sandwich plate element.

The elastic responce of the core material is coupled with the elastic responces of the face sheets by requiring continuity of the displacement field across the core/face sheet interfaces. This implies that the following surface tractions and shear stresses are transferred between the core and the face sheets:

$$
\begin{aligned}
&\textit{Top face/core interface} && \begin{cases} \sigma_c^{top} &= \sigma_c(r,\theta,\frac{c}{2}) \\ \tau_{rz} &= \tau_{rz}(r,\theta) \\ \tau_{\theta z} &= \tau_{\theta z}(r,\theta) \end{cases} \\
&\textit{Bottom face/core interface} && \begin{cases} \sigma_c^{Bottom} &= \sigma_c(r,\theta,-\frac{c}{2}) \\ \tau_{rz} &= \tau_{rz}(r,\theta) \\ \tau_{\theta z} &= \tau_{\theta z}(r,\theta) \end{cases}
\end{aligned}
\tag{C.3}
$$

C.2 Governing Equations

Formulation of the equilibrium equations, and the kinematic and constitutive relations for the top and bottom face sheets, and combination of those with the core equations and continuity requirements, yields the governing set of partial differential equations.

Governing equations for the top face sheet:

$$
\begin{aligned}
u^1_{0r,r} &= -\frac{\nu_1}{r}u^1_{0r} - \frac{\nu_1}{r}u^1_{0\theta,\theta} + \frac{N^1_r}{A_1} \\
u^1_{0\theta,r} &= -\frac{1}{r}u^1_{0r,\theta} - \frac{1}{r}u^1_{0\theta} + \frac{N^1_{r\theta}}{A_1(1-\nu_1)} \\
w^1_{,r} &= -\beta^1_r \\
\beta^1_{r,r} &= -\frac{\nu_1}{r}\beta^1_r - \frac{\nu_1}{r}\beta^1_{\theta,\theta} + \frac{M^1_r}{D_1} \\
\beta^1_{\theta,r} &= \frac{M^1_{r\theta}}{D_1(1-\nu_1)} \\
N^1_{r,r} &= \frac{A_1(1-\nu_1^2)}{r^2}u^1_{0r} + \frac{A_1(1-\nu_1^2)}{r^2}u^1_{0\theta,\theta} - \frac{(1-\nu_1)}{r}N^1_r - \frac{1}{r}N^1_{r\theta,\theta} + \tau_{rz} \\
N^1_{r\theta,r} &= -\frac{A_1(1-\nu_1^2)}{r^2}u^1_{0r,\theta} - \frac{A_1(1-\nu_1^2)}{r^2}u^1_{0\theta,\theta\theta} - \frac{\nu_1}{r}N^1_{r,\theta} - \frac{2}{r}N^1_{r\theta} + \tau_{z\theta} \\
M^1_{r,r} &= \frac{D_1(1-\nu_1^2)}{r^2}\beta^1_r + \frac{D_1(1-\nu_1^2)}{r^2}\beta^1_{\theta,\theta} - \frac{(1-\nu_1)}{r}M^1_r - \frac{1}{r}M^1_{\theta r,\theta} + Q^1_r - \frac{t_1}{2}\tau_{rz} \\
M^1_{r\theta,r} &= -\frac{D_1(1-\nu_1)\nu_1}{r^2}\beta^1_{r,\theta} - \frac{D_1(1-\nu_1)\nu_1}{r^2}\beta^1_{\theta,\theta\theta} + \frac{(1-\nu_1)}{r}M^1_{r,\theta} - \frac{2}{r}M^1_{\theta r} - \frac{t_1}{2}\tau_{z\theta} \\
Q^1_{r,r} &= \frac{E_c}{c}w^1 - \frac{D_1(1-\nu_1)}{r^3}\beta^1_{r,\theta\theta} - \frac{D_1(1-\nu_1)}{r^3}\beta^1_{\theta,\theta\theta\theta} - \frac{1}{r^2}M^1_{r,\theta\theta} - \frac{1}{r}Q^1_r - \\
&\quad \frac{c}{2r}\tau_{rz} - \frac{c}{2}q_r - \frac{c}{2r}\tau_{\theta z,\theta} - \frac{E_c}{c}w^2
\end{aligned}
\tag{C.4}
$$

Governing equation for the core:

$$
\begin{aligned}
\tau_{rz,r} &= q_r \\
q_{r,r} &= -\frac{12E_c}{c^3}u^1_{0r} + \frac{6E_c(t_1+c)}{c^3}\beta^1_r + \left\{\frac{1}{r^2} + \frac{12E_c}{c^2G_c}\right\}\tau_{rz} - \frac{1}{r}q_r + \frac{1}{r^2}\tau_{\theta z,\theta} - \frac{1}{r}q_{\theta,\theta} \\
&\quad + \frac{12E_c}{c^3}u^2_{0r} + \frac{6E_c(t_2+c)}{c^3}\beta^2_r \\
\tau_{\theta z,r} &= q_\theta \\
q_{\theta,r} &= -\frac{G_c(3-\nu_1)}{cr^2}u^1_{0r,\theta} - \frac{G_c(2-\nu_1)}{cr^2}u^1_{0\theta} - \frac{G_c(1-\nu_1)}{cr^2}u^1_{0\theta,\theta\theta} - \frac{\nu_1}{crA_1(1-\nu_1)}N^1_{r,\theta} \\
&\quad + \frac{G_c}{crA_1(1-\nu_1)}N^1_{r\theta} + \frac{1}{r}q_{r,\theta} + \frac{G_c}{c}\left\{\frac{1}{A_1(1-\nu_1)} + \frac{1}{A_2(1-\nu_2)}\right\}\tau_{z\theta} - \frac{1}{r}q_\theta \\
&\quad + \frac{G_c(3-\nu_2)}{cr^2}u^2_{0r,\theta} - \frac{2G_c}{cr^2}u^2_{0\theta} + \frac{G_c(1-\nu_2)}{cr^2}u^2_{0\theta,\theta\theta} + \\
&\quad \frac{G_c(2-\nu_2)}{crA_2(1-\nu_2)}N^2_{r,\theta} - \frac{G_c}{crA_2(1-\nu_2)}N^2_{r\theta}
\end{aligned}
\tag{C.5}
$$

Governing equations for the bottom face sheet:

$$
u^2_{0r,r} = -\frac{\nu_2}{r}u^2_{0r} - \frac{\nu_2}{r}u^2_{0\theta,\theta} + \frac{N^2_r}{A_2}
$$

$$
\begin{aligned}
u^2_{0\theta,r} &= -\frac{1}{r}u^2_{0r,\theta} + \frac{1}{r}u^2_{0\theta} + \frac{N^2_{r\theta}}{A_2(2-\nu_2)} \\
w^2_{,r} &= -\beta^2_r \\
\beta^2_{r,r} &= -\frac{\nu_2}{r}\beta^2_r - \frac{\nu_2}{r}\beta^2_{\theta,\theta} + \frac{M^2_r}{D_2} \\
\beta^2_{\theta,r} &= \frac{M^2_{r\theta}}{D_2(1-\nu_2)} \\
N^2_{r,r} &= \frac{A_2(1-\nu_2^2)}{r^2}u^2_{0r} + \frac{A_2(1-\nu_2^2)}{r^2}u^2_{0\theta,\theta} - \frac{(1-\nu_2)}{r}N^2_r - \frac{1}{r}N^2_{r\theta,\theta} - \tau_{rz} \\
N^2_{r\theta,r} &= \frac{A_2(1-\nu_2^2)}{r^2}u^2_{0r,\theta} - \frac{A_2(1-\nu_2^2)}{r^2}u^2_{0\theta,\theta} - \frac{\nu_2}{r}N^2_{r,\theta} - \frac{2}{r}N^2_{\theta r} - \tau_{z\theta} \\
M^2_{r,r} &= \frac{D_2(1-\nu_2^2)}{r^2}\beta^2_r + \frac{D_2(1-\nu_2^2)}{r^2}\beta^2_{\theta,\theta} - \frac{(1-\nu_2)}{r}M^2_r - \frac{1}{r}M^2_{\theta r\,\theta} + Q^2_r - \frac{t_2}{2}\tau_{rz} \\
M^2_{r\theta,r} &= -\frac{D_2(1-\nu_2)\nu_2}{r^2}\beta^2_{r,\theta} - \frac{D_2(1-\nu_2^2)\nu_2}{r^2}\beta^2_{\theta\,\theta\theta} + \frac{(1-\nu_2)}{r}M^2_{r,\theta} - \frac{2}{r}M^2_{\theta r} - \frac{t_2}{2}\tau_{z\theta} \\
Q^2_{r,r} &= -\frac{E_c}{c}w^1 + \frac{E_c}{c}w^2 - \frac{D_2(1-\nu_2)}{r^3}\beta^2_{r,\theta\theta} - \frac{D_2(1-\nu_2)}{r^3}\beta^2_{\theta,\theta\theta\theta} - \frac{1}{r^2}M^2_{r,\theta\theta} - \frac{1}{r}Q^2_r - \\
&\quad \frac{c}{2r}\tau_{rz} - \frac{c}{2}q_r - \frac{c}{2r}\tau_{\theta z,\theta}
\end{aligned}
\tag{C.6}
$$

where ν^i $(i=1,2)$ is the Poisson's ratio of the face sheets, and A_i, D_i are the face sheets extensional and bending stiffnessses defined by:

$$
A_i = \frac{E_i t_i}{(1-\nu_i^2)},\quad D_i = \frac{E_i t_i^3}{12(1-\nu_i^2)},\quad (\mathrm{i} = 1,2) \tag{C.7}
$$

Appendix

D

List of Publications by F. Mortensen related to the Thesis

D.l Primary Author

Mortensen, F., Development of tools for engineering analysis and design of high-performance FRP-composite structural elements, Institute of Mechanical Engineering, Aalborg *University, Denmark,* Report No. 67, November 1995.

Mortensen, F. & Thomsen, O.T., A Simple Unified Approach for the Analysis and Design of Adhesive Bonded Composite Laminates, In *Proc.* 11^{th} *International Conference on Composite Materials (ICCM-11)*, Gold Coast, Australia, 14-18 July, 1997, Vol VI, pp. 129-137.

Mortensen, F. & Thomsen, O.T., Simplified linear and non-linear analysis of Analysis of Stepped and Scarfed Adhesive-bonded Lap-joints between Composite Laminates, Composite *Structures,* Vol. 38, No. l-4, 1997, pp.383-394, ISSN 0263-8223.

Mortensen, F. & Thomsen, O.T., Facilities in ESAComp for Analysis and Design of Adhesive Joints Between Composite Laminates, *in Proc. Composite* and Sandwich *Structures (NESCO II) (ed. J Bäcklund, D. Zenkert, B.T. Åström)*, ISBN 0 94 7817 94 8, Chameleon Press Ldt., London, UK, 1997, pp.247-266.

Mortensen, F. & Thomsen, O.T., A Simple Approach for the Analysis of Embedded Ply Drops in Composite and Sandwich Laminates, Institute *of* Mechanical *Engineering,* Aalborg *University, Denmark,* Report No. 99, 1998, (To appear in *Composite Science and Technology).*

Mortensen, F. & Thomsen, O.T., Simplified Analysis of Embedded Ply Drop-offs in Composite and Sandwich Laminates, *In Proc. of* American *Society for Composites, Thirteenth* Annual *Technical* Conference, September 21-23, 1998, Baltimore, Maryland, USA.

D.2 Co-author

Frostig, Y., Thomsen, 0. T. & Mortensen, F., Analysis of Adhesive Bonded Joints, Square-end and Spew-Fillet: Closed-Form Higher-Order Theory Approach, *Institute of* Mechanical *Engi*neering, *Aalborg* University, Denmark, Report *No.* 81, 1997, *submitted.*

Thomsen, O.T., Mortensen, F. & Frostig, Y., Interface Failure at Ply Drops in CFRP/ Sandwich Panels: Stress Analysis, Failure Load Prediction and Experimental Investigation, *Institute of* Mechanical Engineering, *Aalborg University*, Denmark, Report No. 100, 1998, submitted.

Thomsen, O.T., Mortensen, F. & Frostig, Y., Simple Stress Analysis and Point Stress Criterion for Prediction of Delamination Failure at Ply-Drops in CFRP/Sandwich Panels, In *Proc.* of American *Society for Composites, Thirteenth* Annual *Technical* Conference, September 21-23, 1998, Baltimore, Maryland, USA.